

**GRAPHOL AND VANADIA-LINKED ZINC DOPED LITHIUM
MANGANESE SILICATE NANOARCHITECTONIC PLATFORMS
FOR SUPERCAPATTERIES**



By

MIRANDA MENGWI NDIPINGWI

BSc. Chemistry (University of Buea), BSc. Honours Chemistry (University of the Western Cape), MSc. Nanoscience – Cum Laude (University of the Western Cape)

A thesis submitted in fulfilment of the requirements for the degree of

PHILOSOPHIAE DOCTOR

In the

**Department of Chemistry
Faculty of Science
University of the Western Cape, South Africa**

**Supervisor: Professor Emmanuel Iwuoha
Co-supervisor: Dr. Chinwe Ikpo**

December 2019

ABSTRACT

Energy storage technologies are rapidly being developed due to the increased awareness of global warming and growing reliance of society on renewable energy sources. Among various electrochemical energy storage technologies, high power supercapacitors and lithium ion batteries with excellent energy density stand out in terms of their flexibility and scalability. However, supercapacitors are handicapped by low energy density and batteries lag behind in power. Supercapatteries have emerged as hybrid devices which synergize the merits of supercapacitors and batteries with the likelihood of becoming the ultimate power sources for multi-function electronic equipment and electric/hybrid vehicles in the future. But the need for new and advanced electrodes is key to enhancing the performance of supercapatteries. Leading-edge technologies in material design such as nanoarchitectonics become very relevant in this regard. This work involves the preparation of vanadium pentoxide (V_2O_5), pristine and zinc doped lithium manganese silicate (Li_2MnSiO_4) nanoarchitectures as well as their composites with hydroxylated graphene (G-ol) and carbon nanotubes (CNT). The nanoarchitected electrode materials were characterized by various morphological, physical and electrochemical techniques and tested as symmetric and asymmetric electrodes for supercapatteries and supercapacitors. G-ol nanosheets with single layers of 14 - 23 nm thick delivered specific capacitance of 137.7 F g^{-1} , high specific energy of 47.8 Wh Kg^{-1} and specific power of 377 W kg^{-1} as symmetric supercapacitor cells. V_2O_5 -based electrode materials with particle sizes of 10.4 – 22.9 nm were also assembled as asymmetric supercapacitors with activated carbon. AC// V_2O_5 -CNT-G-ol asymmetric device delivered a specific capacitance of 173.4 F g^{-1} , high specific energy of 63.2 W h kg^{-1} and good cycle stability over 4,000 cycles. Supercapattery devices were further assembled with activated carbon and zinc doped Li_2MnSiO_4 in 1 M Na_2SO_4 electrolyte. The devices delivered good capacitance retention and specific energies of

38.4 W h kg⁻¹ - 21.3 W h kg⁻¹, capacitance retention of 72.5 % - 84.5 % and excellent coulombic efficiency of 99.6 – 99.7 % over 3000 cycles. With regards to new electrode designs, nanoarchitectures of Li₂Mn_{1-x}Zn_xSiO₄/V₂O₅-CNT/G-ol_{10%} (N₁) and Li₂Mn_{1-x}Zn_xSiO₄/V₂O₅-CNT/G-ol_{5%} (N₂) were fabricated and applied as supercapattery electrodes with activated carbon in 1 M Na₂SO₄ electrolyte. The AC//N₂ supercapattery device delivered a maximum specific capacitance of 205 F g⁻¹, excellent specific energy of 92.3 W h kg⁻¹ at a specific power of 769.8 W kg⁻¹ and excellent coulombic efficiency of 98.8 % over 5000 cycles. The various nanostructured electrode materials demonstrated good electrochemical performance and cycling stability as supercapattery and supercapacitor electrode designs. This study may serve as a facile and low cost broad-spectrum approach towards the design of high performance nanoarchitectonic electrodes for energy storage devices.



KEYWORDS

Aqueous electrolytes

Battery-supercapacitor hybrids

Carbon nanotubes

Composite nanoarchitectures

Capacitance retention

Hydroxylated graphene

Lithium manganese silicate

Mechanochemical reactions

Nanoarchitectonics

Specific capacitance

Specific energy

Specific power

Supercapatteries

Vanadia

Zinc doping



ABBREVIATIONS

AC	Activated carbon
CIF	Crystallographic information files
CNTs	Carbon nanotubes
CPE	Constant phase element
C_{sp}	Specific capacitance
C_T	Total capacitance
CV	Cyclic Voltammetry
E	Specific energy
E°	Standard electrode potential
EDLC	Electrochemical double-layer capacitors
EDS	Energy dispersive spectroscopy
EIS	Electrochemical impedance spectroscopy
ESR	Equivalent series resistance
FTIR	Fourier transform infrared spectroscopy
FWHM	Full width at half maximum
GCD	Galvanostatic charge-discharge
GO	Graphene oxide
G-ol	Hydroxylated graphene



HESD	Hybrid Energy Storage Devices
HRSEM	High resolution scanning electron microscopy
HRTEM	High resolution transmission electron microscopy
IR_{drop}	Ohmic drop
$\text{Li}_2\text{MnSiO}_4$	Lithium manganese silicate
N_1	Nanoarchitectonic platform 1
N_2	Nanoarchitectonic platform 2
OCV	Open circuit voltage
P	Specific power
R_{ct}	Charge transfer resistance
SAED	Selected area electron diffraction
SAXS	Small angle x-ray scattering
SDG	Stoichiometric derivatives of graphene
SS-NMR	Solid state nuclear magnetic resonance spectroscopy
TMOs	Transition metal oxides
V_2O_5	Vanadium pentoxide
XRD	X-ray diffraction
Z_{img}	Imaginary impedance
Z_{re}	Real impedance



DECLARATION

I declare that **Graphol and vanadia-linked zinc doped lithium manganese silicate nanoarchitectonic platforms for supercapatteries** is my own work, that it has not been submitted before for any degree or examination in any other university, and that all the sources I have used or quoted have been indicated and acknowledged as complete references.

Signature -----  -----

Miranda Mengwi Ndipingwi

December 2019



DEDICATION

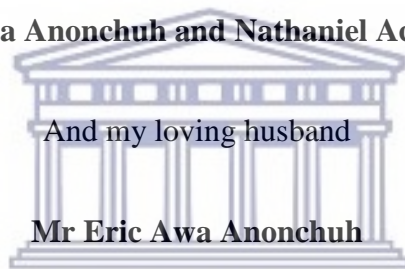
This thesis is dedicated to

My beloved parents

Mrs Suzan Ndipingwi and late Mr Awafor Ndipingwi

My lovely children

Felix-Ryan Awa Anonchuh and Nathaniel Achu Anonchuh



And my loving husband

Mr Eric Awa Anonchuh

UNIVERSITY *of the*
WESTERN CAPE

ACKNOWLEDGEMENTS

First and above all, to the **Almighty God**, for your goodness and mercy that has destined my life for good works, I glorify thee, I praise thee, I give thee all the honor and adoration. Thank you Lord for your garland of Grace and wisdom that has continuously led my path and has brought me to the successful completion of this work.

Supervisors and mentors: My heartfelt gratitude goes to my supervisor Professor Emmanuel Iwuoha for his academic guidance, unconditional support, continuous encouragements, advice, generosity and kindness. Thank you Prof. for your patience, uncommon disposition and the numerous sacrifices. I can't thank you enough for your support especially all you have continuously done during my greatest times of need throughout my time as your student. It has been a great privilege and enriching experience to be mentored by the best role model, father and supervisor. You are indeed "a living legend". May the good Lord richly bless you sir.

To my co-supervisor, Dr. Chinwe Ikpo, I am extremely grateful for your academic guidance, encouragements, advice, very fruitful discussions and kind gestures. Thank you Dr. for being an amazing role model and big sister to me. Your mentorship was truly invaluable and I could not have done it without you. May God bless you always.

Family: I am deeply thankful to my beloved mom Mrs Suzan Ndipingwi, my late dad Mr Awafor Ndipingwi and the entire Ndipingwi's family for their ever felt love, prayers and constant support.

Special thanks to my sister, my mother, my role model and friend, Mrs Rosaline Kuja. Thank you very much 'mummy' for believing in me and committing to do whatever it takes to see that I am who that I am today. Your love, prayers, constant encouragements and support over these years have finally paid off. I love you. I am also grateful for the support from my in-law

Mr Adolf Kuja as well as my brothers and sisters; Mr Linus Ndipingwi, Mr Julius Ndipingwi, Patrick Ndipingwi, Davidson Ndipingwi, Fidelis Ndipingwi, Irene Kuja and Nicoline Ndipingwi. Thank you all for your love, prayers and constant words of encouragement.

To my lovely husband Mr Eric Awa Anonchuh and my caring boys; Felix-Ryan Awa Anonchuh and Nathaniel Achu Anonchuh, you all have been a huge blessing in my life. Thank you for your unfailing love, patience, care, understanding and your continuous support. You have been so amazing.

My gratitude is also extended to the entire Anonchuh's family for their love, support and encouragements especially Mrs Martha Anonchuh, Claudette Anonchuh, Lessly Anonchuh, Elvis Anonchuh and Divine Anonchuh.

Special thanks to my dear friends that have truly become sisters over the course of this work. Dr. Anne Djourmessi, Dr. Florence Tikum, Mrs Candice Franke and Bih Fonkem. Thank you all for your love, continuous support and encouragements. May the Lord richly bless you.

SensorLab: My gratitude also goes to Prof. Priscilla Baker, Prof. Fanelwa Ajayi, Dr. Natasha Ross and Dr. Tesfaye Waryo. Thank you for your support and encouragements. To my friends and colleagues; Dr. Keagan Pokpas, Dr. Usisipho Feleni, Dr. Nomaphelo Ntsongoshi, Dr. Samantha Dومان, Penny Mathumba, Ninon Etsassala, Onyinyechi Uhuo, Precious Ekwere and Emmanuel Ramoroka, many thanks for your friendship, advice and inspiration. It was lovely working with you all.

Department of Chemistry: To Mrs. Wilma Jackson, Prof. Edith Beukes, Mr. Timothy Lesch, Prof. Salam Titinchi and Mrs. Dawn McMahon, thank you for your very instrumental academic and technical support. You all are so kind.

Sponsorship: I am grateful to the National Research Foundation (NRF) of South Africa for the award of a PhD Scholarship, enabled by Professor Emmanuel Iwuoha's South African Research Chair Initiative (SARChI) for NanoElectrochemistry and Sensor Technology.



LIST OF PUBLICATIONS

- 1 **M.M. Ndipingwi**, C.O. Ikpo, N.W. Hlongwa, N. Dywili, A.L. Djoumessi Yonkeu, E.I. Iwuoha, Crystal chemistry and lithium-ion intercalation properties of lithium manganese silicate cathode for aqueous rechargeable Li-ion batteries, *J. Appl. Electrochem.* 49 (2019) 465–474.
- 2 **M.M. Ndipingwi**, C.O. Ikpo, N.W. Hlongwa, Z. Myalo, Orthorhombic Nanostructured $\text{Li}_2\text{MnSiO}_4/\text{Al}_2\text{O}_3$ Supercapattery Electrode with Efficient Lithium-Ion Migratory Pathway, *Batteries & Supercaps* 1 (2018) 223–235.
- 3 A.C. Nwanya, **M.M. Ndipingwi**, N. Mayedwaa, L.C. Razanamahandry, C.O. Ikpo, T. Waryo, S.K.O. Ntwampe, E. Malenga, E. Fosso-Kankeu, F.I. Ezema, E.I. Iwuoha, M. Maaza, Maize (*Zea mays* L.) fresh husk mediated biosynthesis of Copper Oxides: Potentials for Pseudo Capacitive Energy Storage, *Electrochim. Acta.* 301 (2019) 436–448.
- 4 N.R. Dywili, A. Ntziouni, C. Ikpo, **M. Ndipingwi**, N.W. Hlongwa, A.L.D. Yonkeu, M. Masikini, K. Kordatos, E.I. Iwuoha, Graphene oxide decorated nanometal-poly(anilino-dodecylbenzene sulfonic acid) for application in high performance supercapacitors, *Micromachines.* 10 (2019) 115.
- 5 N.W. Hlongwa, C.O. Ikpo, N. Ross, M. Nzaba, **M.M. Ndipingwi**, P.G.L. Baker, et al., Electrochemical Studies on Novel LiMnPO_4 ; Coated with Magnesium Oxide-Gold Composite Thin Film in Aqueous Electrolytes, *J. Nano Res.* 44 (2016) 90–99.

-
- 6 N. Ross, C.O. Ikpo, N.W. Hlongwa, **M.M. Ndipingwi**, et al., Electrochemical Studies on Novel LiMnPO₄ Coated with Magnesium Oxide-Gold Composite Thin Film in Aqueous Electrolytes, *J. Nano Res.* 44 (2016) 90–99.
- 7 S.V. John, N. Mayedwa, C. Ikpo, L.Y. Molefe, **M.M. Ndipingwi**, N.R. Dywili, et al., Photoluminescence quenching of poly(octylfluorenylbenzothiadiazole) luminophore by n-type cobalt(II) salicylaldimine metallodendrimer, *Synth. Met.* 220 (2016) 114-122.
- 8 N. Matinise, N. Mayedwa, C.O. Ikpo, N.W. Hlongwa, **M.M. Ndipingwi**, L. Molefe, et al., Bimetallic Nanocomposites of Palladium (100) and Ruthenium for Electrooxidation of Ammonia, *J. Nano Res.* 44 (2016) 100–113.
- 9 **Miranda Mengwi Ndipingwi**, Chinwe O. Ikpo, Anne Lutgarde Djoumessi Yonkeu, Precious Ekwere, Nolly Christopher, Emmanuel I. Iwuoha, Fabrication of Zinc doped Lithium Manganese Silicate/Vanadium Pentoxide/Graphol Composite Nanoarchitectures for Supercapattery Energy Storage (**Manuscript prepared for Journal of Energy Storage Materials**)
- 10 **Miranda Mengwi Ndipingwi**, Chinwe O. Ikpo, Emmanuel I. Iwuoha, Zinc Doped Lithium Manganese Silicate Mixed Spherical and Rhombohedrally-Shaped Nanocrystals as battery-type Electrodes for Supercapattery Applications (**Manuscript prepared for ACS Applied Materials & Interfaces**)

11 **Miranda Mengwi Ndipingwi**, Chinwe O. Ikpo, Emmanuel I. Iwuoha, Vanadia-Hydroxylated Graphene Nanocapsules as Scherbinaite Active Supercapacitor Electrodes (**Manuscript prepared for Journal of Power Sources**)

12 **Miranda Mengwi Ndipingwi**, Chinwe O. Ikpo, Emmanuel I. Iwuoha, High Voltage and Freestanding Hydroxylated Graphene Films for Supercapacitors with Aqueous Electrolytes (**Manuscript prepared for Carbon**)



LIST OF CONFERENCES

1. **Miranda M. Ndipingwi**, Chinwe O. Ikpo, Emmanuel I. Iwuoha, Lithium Manganese Silicate Supercapatteries with Efficient Lithium ion Storage. 5th International Symposium on Electrochemistry titled “Electrochemistry at Nanostructured Interfaces”. University of the Western Cape, Bellville, South Africa, 11-14 August 2019. **Oral presentation**
2. **M. M. Ndipingwi**, C. O. Ikpo and E. I. Iwuoha. High Power Li-Ion Capacitor Electrodes Based on Nanoporous Vanadia/hydroxylated graphene Nanocomposites. NANOSMAT-AFRICA 2018 International Conference on Surfaces, Coatings and Nanostructured Materials – 19-23 November 2018, Cape Town, South Africa. **Poster presentation**
3. **Miranda M. Ndipingwi**, Chinwe O. Ikpo, Ntuthuko W. Hlongwa, Zolani Myalo and Emmanuel I. Iwuoha. Crystal Chemistry and Lithium-ion Intercalation Properties of Lithium Manganese Silicate cathode for Rechargeable Li-Ion Batteries. The 4th International Symposium on Electrochemistry titled (Pure and Applied Electrochemistry), University of Johannesburg, South Africa. 3-5 April 2018. **Poster presentation.**
4. **Miranda Ndipingwi**, Chinwe Ikpo, Ntuthuko Hlongwa, Lerato Molefe, Natasha Ross and Emmanuel Iwuoha. Alumina-Li₂MnSiO₄-C Nanocomposite Hybrid as High Energy Density Cathode for Lithium-ion Batteries. The 2nd International Conference

on Composites, Biocomposites and Nanocomposites (ICCBN 2015). DUT, Durban, South Africa. 28-30 October 2015. **Oral Presentation.**

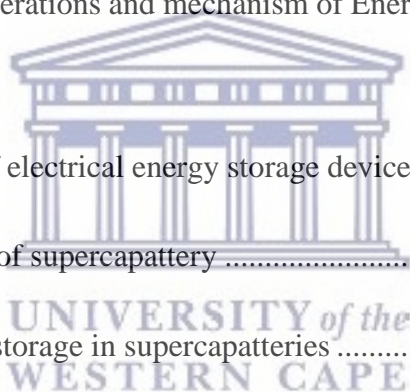
5. **Miranda Ndipingwi**, Chinwe Ikpo, Ntuthuko Hlongwa, Natasha Ross, Emmanuel Iwuoha, Anne Djoumessi and Priscilla Baker. Designing Next Generation High Energy Density Lithium-ion Battery with Manganese Orthosilicate-capped Alumina- nanofilm. The 3rd International Symposium on Electrochemistry (Materials, Analytical and Physical Electrochemistry Today-MAPET 2015). University of the Western Cape, South Africa. 26-28 May 2015. **Poster presentation.**



TABLE OF CONTENTS

ABSTRACT.....	i
KEYWORDS.....	iii
ABBREVIATIONS.....	iv
DECLARATION.....	vi
DEDICATION.....	vii
ACKNOWLEDGEMENTS.....	viii
LIST OF PUBLICATIONS.....	xi
LIST OF CONFERENCES.....	xiv
TABLE OF CONTENTS.....	xvi
LIST OF FIGURES.....	xxvi
LIST OF TABLES.....	xl
CHAPTER ONE.....	1
BACKGROUND INFORMATION, AIMS AND OBJECTIVES OF THE STUDY.....	1
The Role of Electrochemical Energy Storage in the Global Energy Transformation.....	1
1.1 Introduction.....	1
1.2 The Global Energy Mix.....	2
1.3 Electrical Energy Storage.....	4
1.4 Research Problem and Motivation.....	5
1.5 Research aim and objectives.....	7

1.6 Thesis outline	8
References.....	9
CHAPTER TWO	13
LITERATURE REVIEW	13
Development Trends and Performance Metrics of Supercapatteries. Recent Advances in Materials, Device Performance and Future Prospects	13
2.1 . Introduction.....	13
2.2 . Supercapatteries among electrochemical energy storage devices: Ragone Plot.....	15
2.3. Components, design considerations and mechanism of Energy storage in Supercapatteries	17
2.3.1. Typical components of electrical energy storage devices.....	17
2.3.2. Design considerations of supercapattery	18
2.3.3. Mechanism of energy storage in supercapatteries	20
2.3.3a. Non-faradaic capacitive charge storage	21
2.3.3b. Capacitive faradaic charge storage (pseudocapacitive)	21
2.3.3c. Non-capacitive faradaic charge storage (Nernstian)	22
2.4. Measurement of key performance parameters	24
2.4.1 Capacitance.....	26
2.4.2 Energy and Power.....	27
2.4.3 Cycle Stability and capacitance retention.....	28
2.5. Recent advances in materials and performance of supercapattery electrodes	28



2.5.1.	Activated carbon (AC).....	30
2.5.2.	Doped Graphenes (Hydroxylated graphene- Graphol).....	32
2.5.3.	Carbon nanotubes (CNTs).....	36
2.5.4.	Vanadium pentoxide (V ₂ O ₅).....	37
2.5.5.	Lithium manganese silicate (Li ₂ MnSiO ₄).....	41
2.5.6	Electrochemical Performance of reported Hybrid Energy Storage Devices (HESD) 48	
2.6	Conclusion and Future Prospects.....	50
	References.....	51
	CHAPTER THREE	68
	RESULTS AND DISCUSSION – MANUSCRIPT 1	68
	High Voltage and Freestanding Hydroxylated Graphene Films for Supercapacitors with Aqueous Electrolytes (Prepared for Carbon).....	68
	Abstract.....	68
	Key words: Hydroboration, Hydroxylated graphene, symmetric supercapacitor, high specific energy69	
3.1	Introduction.....	69
3.2	Experimental details.....	74
3.2.1	Materials	74
3.2.2a.	Synthesis of Graphene oxide (GO)	74
3.2.2b.	Synthesis of hydroxylated graphene (graphol /G-ol) nanosheets	75

3.2.3.1	Material Characterization.....	76
3.2.3.2	Electrode preparation and electrochemical measurements	77
3.3	Results and Discussion	78
3.3.1	High-resolution Scanning and Transmission Electron Microscopic Analysis	78
3.3.2	X-ray diffraction Studies	80
3.3.3	Small-angle X-ray scattering experiments	84
3.3.4	Fourier transform Infrared (FTIR) Spectroscopic Analysis	86
3.3.5	Raman Spectroscopic Studies.....	89
3.3.6	Solid state ¹³ C Magic Angle Spinning Nuclear Magnetic Resonance Spectroscopic Studies (SS- ¹³ C-MAS NMR).....	91
3.3.7	Electrochemical Performance of graphite, GO and G-ol	92
i)	Cyclic Voltammetric (CV) studies.....	93
ii)	Galvanostatic charge-discharge (GCD) studies	95
iii)	Electrochemical impedance spectroscopic (EIS) measurements	97
3.3.8	Fabrication and Electrochemical Performance of flexible supercapacitor devices 101	
i)	Voltage window determination via Cyclic Voltammetric Studies	102
ii)	Galvanostatic charge-discharge studies	104
iii)	Electrochemical cycling/stability studies	108
iv)	Electrochemical Impedance studies before and after cycling	109
3.3.9	Specific Energy and Specific Power	113

3.4	Conclusion	115
	References.....	117
	CHAPTER FOUR.....	125
	RESULTS AND DISCUSSION – MANUSCRIPT 2	125
	Vanadia-Hydroxylated Graphene Nanocapsules as Scherbinaite Active Supercapacitor Electrodes (Prepared for ACS Applied Materials & Interfaces)	125
	Abstract.....	125
	Keywords: V ₂ O ₅ nanorods, Graphol, Nanocapsules, Activated carbon, Asymmetric supercapacitor, High specific energy	126
4.1	Introduction.....	126
4.2	Experimental details.....	129
4.3	Materials.....	130
4.3.1	Functionalization of CNTs by acid oxidation.....	130
4.3.2	Synthesis of V ₂ O ₅ nanorods and V ₂ O ₅ -CNT nanonetwork	131
4.3.3	Synthesis of hydroxylated graphene (graphol /G-ol)	131
4.3.4	Synthesis of V ₂ O ₅ -CNT-G-ol nanocapsules.....	132
4.3.5	Material Characterization	132
4.3.6	Electrode preparation and electrochemical measurements.....	133
4.4	Results and Discussion	134
4.4.1	Structure and morphological Analysis by Scanning and Transmission Electron Microscopies (SEM and HRTEM)	134



4.4.2	Particle size distribution by Small Angle X-ray Scattering (SAXS).....	142
4.4.3	Crystallography by X-ray Diffraction Studies (XRD)	145
4.4.3 (a)	Crystal structure and phase identification	145
4.4.3 (b)	Crystal geometry and atom connectivity.....	149
4.4.5	Functional group Analysis by Fourier transform Infrared (FTIR) Spectroscopy	152
4.4.6	Raman Spectroscopy	156
4.4.7 (a)	Electrochemical Performance	157
i)	Cyclic Voltammetric (CV) studies.....	158
ii)	Galvanostatic charge-discharge (GCD) studies	161
iii)	Electrochemical impedance spectroscopic (EIS) measurements	164
4.4.7 (b)	Electrochemical Performance of the fabricated asymmetric supercapacitor devices	168
i)	Electrochemical cycling / stability studies.....	173
4.4.7 (c)	Specific Energy and Specific Power.....	175
4.5	Conclusion	179
	References.....	180
	CHAPTER FIVE	188
	RESULTS AND DISCUSSION – MANUSCRIPT 3	188
	Zinc Doped Lithium Manganese Silicate Mixed Spherical and Rhombohedrally-Shaped Nanocrystals as battery-type Electrodes for Supercapattery Applications (Prepared for ACS Applied Materials & Interfaces)	188

Abstract	188
Keywords: Nanocrystals, Zn-doping, $\text{Li}_2\text{MnSiO}_4$, supercapattery, high specific energy	189
5.1 Introduction.....	189
5.2 Experimental details.....	192
5.2.1 Materials	192
5.2.2. Synthesis of pristine and Zn doped $\text{Li}_2\text{MnSiO}_4$ nanomaterials	193
5.2.3.1 Material Characterization.....	194
5.2.3.2 Electrode preparation and electrochemical measurements	194
5.3 Results and Discussion	195
5.3.1 Structure and morphological Analysis by Scanning and Transmission Electron Microscopies (SEM and HRTEM)	195
5.3.2 Particle size distribution by Small Angle X-ray Scattering (SAXS).....	204
5.3.3 Crystallography by X-ray Diffraction Studies (XRD)	209
5.3.3 (a) Crystal structure and phase identification	209
5.3.3 (b) Crystal structure models and atom connectivity	212
5.3.4 Functional group Analysis by Fourier transform Infrared (FTIR) Spectroscopy	216
5.3.5 (a) Electrochemical characterization	218
i) Cyclic Voltammetric (CV) studies.....	218
ii) Electrochemical impedance spectroscopic (EIS) measurements	225
5.3.5 (b) Electrochemical Performance of the fabricated supercapattery devices.....	229
i) Cyclic Voltammetric studies of supercapattery devices	229

ii)	Galvanostatic charge-discharge (GCD) studies of supercapattery devices.....	232
iii)	Electrochemical cycling / stability studies	235
5.3.5 (c)	Specific Energy and Specific Power	238
5.4	Conclusion	241
	References.....	242
	CHAPTER SIX.....	251
	RESULTS AND DISCUSSION – MANUSCRIPT 4	251
	Fabrication of Zinc doped Lithium Manganese Silicate/Vanadium Pentoxide/Graphol Composite Nanoarchitectures for Supercapattery Energy Storage (Prepared for Energy Storage Materials)	251
	Abstract.....	251
	Keywords: Vanadium pentoxide, graphol, doped $\text{Li}_2\text{MnSiO}_4$, nanoarchitectures, supercapattery, naoarchitectonics, high specific energy.....	252
6.1	Introduction.....	252
6.2	Experimental details.....	255
6.2.1	Materials	255
6.2.2.	Synthesis of $\text{Li}_2\text{Mn}_{1-x}\text{Zn}_x\text{SiO}_4/ \text{V}_2\text{O}_5\text{-CNT/ G-ol}$ Nanoarchitectures.....	256
6.2.3	Material Characterization	257
6.2.4	Electrode preparation and electrochemical measurements.....	258
6.3	Results and Discussion	259
6.3.1	Structure and morphological Analysis by Scanning and Transmission Electron Microscopies (SEM and HRTEM)	259

6.3.2	Particle size distribution by Small Angle X-ray Scattering (SAXS).....	265
6.3.3	Crystallography by X-ray Diffraction Studies (XRD)	269
6.3.3 (a)	Crystal structure and phase identification	269
6.3.3 (b)	Crystal structure models and atom connectivity	272
6.3.4	Functional group Analysis by Fourier transform Infrared (FTIR) Spectroscopy	275
6.4	Raman Spectroscopy	277
6.5 (a)	Electrochemical Performance	278
i)	Cyclic Voltammetric (CV) studies.....	279
ii)	Electrochemical impedance spectroscopic (EIS) measurements	281
6.5 (b)	Electrochemical Performance of the fabricated asymmetric supercapacitor devices	285
iv)	Cyclic Voltammetric studies of supercapattery devices	286
v)	Galvanostatic charge-discharge (GCD) studies of supercapattery devices.....	289
vi)	Electrochemical cycling / stability studies	293
vii)	Electrochemical Impedance studies before and after cycling	295
6.5 (c)	Specific Energy and Specific Power	298
6.6	Conclusion	300
	References.....	302
	CHAPTER SEVEN	309
	CONCLUSION AND RECOMMENDATIONS	309
7.1	Summary of main thesis results	309

7.2	Recommendations for Future work	312
-----	---------------------------------------	-----



LIST OF FIGURES

	Title	page
Figure 1.1	Historical and Projected data for global energy consumption by fuel type	2
Figure 2.1	Comparing the energy and power densities of hybrid supercapacitors, batteries and fuel cells	16
Figure 2.2	Schematic representation of a single cell of a typical electrical energy storage device	17
Figure 2.3	General design of a supercapattery.	19
Figure 2.4	Different hybridization approaches between battery and supercapacitor-type electrodes and materials	20
Figure 2.5	Scheme demonstrating similarities between capacitive and faradaic charge storage in EDL capacitor, pseudocapacitor, battery and supercapattery (a) Voltammetric representation of Nernstian (b1, b2), mixed Nernstian and capacitive (b3) and capacitive (b4) charge storage mechanisms (b).	23
Figure 2.6:	Outline of the band model for chemical bonding between metal atoms (c); that are separated and non-interactive (i), and forming clusters of 2 (ii), 5 (iii), 20 (iv) and 10^{20} atoms (v). Energy levels of the valence electrons as a function of the degree (or zone size) of delocalisation of valence electrons in the respective clusters of metal atoms (d)	24
Figure 2.7	Scheme showing key performance parameters, characterisation techniques and factors affecting the evaluation of supercapatteries	25

Figure 2.8	physical activation of AC from wood (a), changes in pore size with activation time and electrochemical performance of AC negative electrode (b)	31
Figure 2.9	Recent developments and applications of graphene and graphene-based composites	32
Figure 2.10:	Synthesis route of hydroxylated graphene; A- Formation of oxylfluorinated graphene via hydroxyl substitution of fluorine atoms, B-Further substitution to graphol	34
Figure 2.11	Formation of hydroxylated graphene (graphol) through hydroboration	35
Figure 2.12	Electrochemical characterisation of hydroxylated graphene-sulfur nanocomposites: cyclic voltammograms of the Li-S cell with nanocomposite as cathode (a), cyclic performance of the Li-S cell	36
Figure 2.13	Crystal structure of V_2O_5	38
Figure 2.14	Comparison of Li insertion voltage of M^{2+}/M^{3+} and M^{3+}/M^{4+} redox couples in Li_2MSiO_4	43
Figure 2.15	Crystal structures of the four orthorhombic and monoclinic polymorphs of Li_2MnSiO_4 : (a) $Pmn2_1$, (b) $Pmnb$, (c) $P2_1/n$ and (d) Pn space groups	44
Figure 3.1	Schematic illustration of the synthesis pathway of graphol	76
Figure 3.2.1	SEM image of GO (a), G-ol (b), HRTEM image of GO (c), G-ol (d), SAED image of GO (e), G-ol (f)	80
Figure 3.2.2	EDS spectra of Graphite, GO and G-ol (g)	80
Figure 3.3	XRD pattern of graphite, GO and G-ol	81

Figure 3.4	Model structures of graphite, GO and G-ol showing the position of all atoms obtained simulated using Match and Endeavour softwares. A = oxidation, B = hydroboration/ oxidation	84
Figure 3.5 (a)	Intensity particle size distribution of Graphite, GO and G-ol nanosheets	85
Figure 3.5 (b):	Volume particle size distribution of Graphite, GO and G-ol nanosheets	86
Figure 3.6 (a)	FTIR spectra of graphite, GO and G-ol nanosheets	87
Figure 3.6 (b)	FTIR spectrum of GO nanosheets (enlarged)	88
Figure 3.7	Raman spectra of graphite, GO and G-ol nanosheets excited by 514.9 nm laser	90
Figure 3.8	¹³ C MAS SS-NMR spectra of graphite, GO and G-ol nanosheets.	92
Figure 3.9 (a)	CV curves of graphite, GO and G-ol at a scan rate of 40 mV s ⁻¹ in 0.5 M LiClO ₄ -aqueous electrolyte at a potential window of -0.2 – 0.8 V	94
Figure 3.9 (b)	CV curves of G-ol at scan rates of 10 – 50 mV s ⁻¹ in 0.5 M LiClO ₄ - aqueous electrolyte	95
Figure 3.9 (c)	Variation of specific capacitance with scan rate for graphite, GO and G-ol	96
Figure 3.10 (a)	GCD profiles of G-ol at different current loads	98
Figure 3.10 (b)	Variation of specific capacitances with the current load of G-ol	99
Figure 3.11 (a)	Nyquist plot of Graphite, GO and G-ol	100

Figure 3.11 (b)	Circuit models used to fit EIS data	101
Figure 3.11 (c)	Phase angle Bode plots of Graphite, GO and G-ol	101
Figure 3.11 (d)	Total impedance Bode plots of Graphite, GO and G-ol	102
Figure 3.12	Symmetric and asymmetric supercapacitor designs	104
Figure 3.13 (a)	CV curves of G-ol//G-ol and AC//G-ol devices at a scan rate of 80 mV s ⁻¹ in 0.5 M LiClO ₄ aqueous electrolyte at a voltage window of 1.6 V.	105
Figure 3.13 (b)	CV curves of G-ol//G-ol devices at different voltage windows of 1.0 – 1.8 V in 0.5 M LiClO ₄ aqueous electrolyte	106
Figure 3.14 (a)	GCD profiles of symmetric device - G-ol//G-ol at current loads of 0.07 A g ⁻¹ - 1.5 A g ⁻¹	108
Figure 3.14 (b)	GCD profiles of asymmetric device - AC//G-ol at current loads of 0.07 A g ⁻¹ - 1.5 A g ⁻¹	109
Figure 3.14 (c)	Comparative plot of G-ol//G-ol and AC//G-ol at a current load of 0.07 A g ⁻¹	110
Figure 3.14 (e)	Variation of discharge capacitance with current load for G-ol//G-ol and AC//G-ol.	110
Figure 3.15	Cycling stability of G-ol//G-ol and AC//G-ol supercapacitors over 5000 cycles.	111
Figure 3.16 (a)	Nyquist plots of G-ol//G-ol and AC//G-ol devices before and after cycling at OCV	113
Figure 3.16 (b)	Phase angle Bode plots of G-ol//G-ol and AC//G-ol devices before and after cycling at OCV	114

Figure 3.16 (c)	Total impedance Bode plots of G-ol//G-ol and AC//G-ol devices before and after cycling at OCV	115
Figure 3.16 (d)	EIS data fitting circuit models of G-ol//G-ol device before and after cycling	116
Figure 3.16 (e)	EIS data fitting circuit models of AC//G-ol device before and after cycling	116
Figure 3.17	Ragone plot of G-ol//G-ol and AC//G-ol supercapacitors at different current loads	118
Figure 4.1 (a)	SEM image of V ₂ O ₅	139
Figure 4.1 (b)	SEM image of CNTs with the HRTEM and SAED images as insets	140
Figure 4.1 (c)	SEM image of V ₂ O ₅ -CNT nanonetwork	141
Figure 4.1 (d)	SEM image of V ₂ O ₅ -CNT-G-ol nanocomposite with SEM image of G-ol as the inset	142
Figure 4.1 (e)	HRTEM image of V ₂ O ₅ nanorods, with its lattice fringes and SAED image as insets	143
Figure 4.1 (f)	HRTEM image of V ₂ O ₅ -CNT nanonetwork with lattice fringes and SAED images as insets	144
Figure 4.1 (g)	HRTEM image of V ₂ O ₅ -CNT-G-ol nanocomposite with lattice fringes and SAED images as insets	145
Figure 4.1 (h)	EDS maps of V ₂ O ₅ -CNT-G-ol with relative elemental intensities: carbon (red), vanadium (yellow) and oxygen (blue)	146
Figure 4.2 (a)	SAXS pair distance distribution function by physical volume of scattered particles	148

Figure 4.2 (b)	SAXS pair distance distribution function by number of particles scattered	149
Figure 4.3 (a)	XRD pattern of V ₂ O ₅ , V ₂ O ₅ -CNT and V ₂ O ₅ -CNT-G-ol nanomaterials	152
Figure 4.3 (b)	XRD pattern of G-ol nanosheets	153
Figure 4.4 (a)	Crystal structure models of V ₂ O ₅ nanorods simulated from Match and Endeavour	154
Figure 4.4 (b)	Crystal structure models of V ₂ O ₅ -CNT nanonetwork simulated from Match and Endeavour	155
Figure 4.4 (c)	Crystal structure models of V ₂ O ₅ -CNT-G-ol nanocapsules simulated from Match and Endeavour	156
Figure 4.5 (a)	FTIR spectrum (overlaid) of V ₂ O ₅ nanorods, V ₂ O ₅ -CNT nanonetwork and V ₂ O ₅ -CNT-G-ol nanocapsules	158
Figure 4.5 (b)	FTIR spectrum of V ₂ O ₅ -CNT-G-ol nanocapsules illustrating all bond vibrations	159
Figure 4.6	Raman spectra of V ₂ O ₅ , V ₂ O ₅ -CNT and V ₂ O ₅ -CNT-G-ol nanomaterials with excitation laser of 514.9 nm.	161
Figure 4.7 (a)	CV curves of V ₂ O ₅ nanorods, V ₂ O ₅ -CNT nanonetwork, and V ₂ O ₅ -CNT-G-ol nanocapsules at 10 mV s ⁻¹ in 1 M LiNO ₃ aqueous electrolyte at potential window of -0.2 – 0.8 V	164
Figure 4.7 (b)	CV curves of V ₂ O ₅ -CNT-G-ol at scan rates of 10 – 60 mVs ⁻¹ in 1 M LiNO ₃ aqueous electrolyte at potential window of -0.2 – 0.8 V	165
Figure 4.7 (c)	Variation of specific capacitance with scan rate for V ₂ O ₅ , V ₂ O ₅ -CNT and V ₂ O ₅ -CNT-G-ol nanomaterials in 1 M LiNO ₃ aqueous electrolyte at potential window of -0.2 – 0.8 V	166

Figure 4.8 (a)	GCD profiles of V_2O_5 nanorods, V_2O_5 -CNT nanonetwork and V_2O_5 -CNT-G-ol nanocapsules at 1 A g^{-1} in 1 M LiNO_3 aqueous electrolyte at potential window of $-0.2 - 0.8 \text{ V}$	168
Figure 4.8 (b)	GCD curves of V_2O_5 -CNT-G-ol at different current loads in 1 M LiNO_3 aqueous electrolyte at potential window of $-0.2 - 0.8 \text{ V}$	169
Figure 4.8 (c)	Variation of discharge capacitance with current load of V_2O_5 -CNT-G-ol	170
Figure 4.9 (a)	Nyquist plots of V_2O_5 , V_2O_5 -CNT and V_2O_5 -CNT-G-ol nanomaterials obtained at OCV	172
Figure 4.9 (b)	Circuit models used to fit EIS data	172
Figure 4.9 (c)	Phase angle Bode plots of V_2O_5 , V_2O_5 -CNT and V_2O_5 -CNT-G-ol	173
Figure 4.9 (d)	Total impedance Bode plots of V_2O_5 , V_2O_5 -CNT and V_2O_5 -CNT-G-ol	174
Figure 4.10 (a)	comparative CV plots of AC and V_2O_5 -CNT-G-ol electrodes at scan rate of 50 mV s^{-1} in 1.0 M LiNO_3 aqueous electrolyte at different potential windows	177
Figure 4.10 (b)	Comparative plot of the GCD profiles of AC// V_2O_5 , AC// V_2O_5 -CNT and AC// V_2O_5 -CNT-G-ol asymmetric devices at a current load of 0.25 A g^{-1} in 1.0 M LiNO_3 aqueous electrolyte.	178
Figure 4.10 (c)	GCD profiles of AC// V_2O_5 -CNT-G-ol asymmetric device at different current loads in 1.0 M LiNO_3 aqueous electrolyte	179
Figure 4.10 (d)	Variation of charge and discharge capacitance values with current load of AC// V_2O_5 -CNT-G-ol device in 1.0 M LiNO_3 aqueous electrolyte at voltage window of 1.6 V	180
Figure 4.11 (a)	Cycling stability of AC// V_2O_5 , AC// V_2O_5 -CNT, AC// V_2O_5 -CNT-G-ol supercapacitor devices over 4000 cycles	182

Figure 4.11 (b)	Coulombic efficiency of AC//V ₂ O ₅ , AC//V ₂ O ₅ -CNT, AC//V ₂ O ₅ -CNT-G-ol supercapacitor devices over 4000 cycles	183
Figure 4.12	Ragone plot of AC//V ₂ O ₅ , AC//V ₂ O ₅ -CNT, AC//V ₂ O ₅ -CNT-G-ol supercapacitor devices at different current loads in 1.0 M LiNO ₃ aqueous electrolyte at voltage window of 1.6 V	186
Figure 5.1 (a)	SEM and HRTEM micrographs of Li ₂ MnSiO ₄ with SAED and lattice fringes as insets	206
Figure 5.1 (b)	SEM and HRTEM micrographs of Li ₂ Mn _{0.98} Zn _{0.02} SiO ₄ with SAED and lattice fringes as insets	207
Figure 5.1 (c)	SEM and HRTEM micrographs of Li ₂ Mn _{0.96} Zn _{0.04} SiO ₄ with SAED and lattice fringes as insets	208
Figure 5.1 (d)	SEM and HRTEM micrographs of Li ₂ Mn _{0.94} Zn _{0.06} SiO ₄ with SAED and lattice fringes as insets	209
Figure 5.1 (e)	SEM and HRTEM micrographs of Li ₂ Mn _{0.92} Zn _{0.08} SiO ₄ with SAED and lattice fringes as insets	210
Figure 5.1 (f)	EDS spectra of undoped and Zn-doped Li ₂ MnSiO ₄ nanomaterials	211
Figure 5.1 (g)	EDS maps of Li ₂ Mn _{0.96} Zn _{0.04} SiO ₄ nanocrystals	212
Figure 5.2 (a ₁)	SAXS pair distance distribution functions of undoped and Zn-doped Li ₂ MnSiO ₄ nanocrystals by intensity of scattered particles	214
Figure 5.2 (a ₂)	SAXS pair distance distribution functions of undoped and Zn-doped Li ₂ MnSiO ₄ nanocrystals by intensity of scattered particles (enlarged lower section of a ₁)	215

Figure 5.2 (b ₁)	SAXS pair distance distribution functions of undoped and Zn-doped Li ₂ MnSiO ₄ nanocrystals by physical volume of particles scattered	216
Figure 5.2 (b ₂)	SAXS pair distance distribution functions of undoped and Zn-doped Li ₂ MnSiO ₄ nanocrystals by physical volume of particles scattered (enlarged lower section of b ₁)	217
Figure 5.3	XRD spectra of Li ₂ MnSiO ₄ (a), Li ₂ Mn _{0.98} Zn _{0.02} SiO ₄ (b), Li ₂ Mn _{0.96} Zn _{0.04} SiO ₄ (c), Li ₂ Mn _{0.94} Zn _{0.04} SiO ₄ (d), and Li ₂ Mn _{0.92} Zn _{0.08} SiO ₄ (e)	220
Figure 5.4 (a)	Crystal structure models of Li ₂ MnSiO ₄ nanocrystals	222
Figure 5.4 (b)	Crystal structure models of Li ₂ Mn _{0.98} Zn _{0.02} SiO ₄ nanocrystals	222
Figure 5.4 (c)	Crystal structure models of Li ₂ Mn _{0.96} Zn _{0.04} SiO ₄ nanocrystals	223
Figure 5.4 (d)	Crystal structure models of Li ₂ Mn _{0.94} Zn _{0.06} SiO ₄ nanocrystals	223
Figure 5.4 (e)	Crystal structure models of Li ₂ Mn _{0.92} Zn _{0.08} SiO ₄ nanocrystals	224
Figure 5.5 (a)	FTIR spectra of undoped and Zn-doped Li ₂ MnSiO ₄ electrode materials	225
Figure 5.5 (b)	FTIR spectrum of Li ₂ Mn _{0.96} Zn _{0.04} SiO ₄ nanocrystals	226
Figure 5.6 (a)	Comparative CV curves of pure and Zn-doped Li ₂ MnSiO ₄ nanomaterials at a scan rate of 20 mV s ⁻¹ in 1 M sodium sulfate (Na ₂ SO ₄) aqueous electrolyte	230
Figure 5.6 (b)	CV curves of Li ₂ Mn _{0.96} Zn _{0.04} SiO ₄ at scan rates of 10 – 150 mV s ⁻¹ in 1 M sodium sulfate (Na ₂ SO ₄) aqueous electrolyte	231

Figure 5.6 (c)	Linear relationship between the peak current (I_{pa} and I_{pc}) versus the square root of the scan rate of $\text{Li}_2\text{Mn}_{0.96}\text{Zn}_{0.04}\text{SiO}_4$ electrode material	232
Figure 5.6 (d)	Variation of specific capacity with scan rate of $\text{Li}_2\text{Mn}_{0.96}\text{Zn}_{0.04}\text{SiO}_4$ electrode material in 1 M sodium sulfate (Na_2SO_4) aqueous electrolyte at a potential window of 0.1 – 0.8 V	233
Figure 5.7 (a)	Nyquist plots of pure and Zn-doped $\text{Li}_2\text{MnSiO}_4$ electrode materials	236
Figure 5.7 (b)	Circuit models used to fit EIS data of pure and Zn-doped $\text{Li}_2\text{MnSiO}_4$ electrode	236
Figure 5.7 (c)	Phase angle Bode plots of pure and Zn-doped $\text{Li}_2\text{MnSiO}_4$ electrodes	237
Figure 5.7 (d)	Total impedance Bode plots of pure and Zn-doped $\text{Li}_2\text{MnSiO}_4$ electrode materials	238
Figure 5.8 (a)	CV curves of activated carbon and $\text{Li}_2\text{Mn}_{0.96}\text{Zn}_{0.04}\text{SiO}_4$ at a scan rate of 50 mV s^{-1} in 1 M Na_2SO_4 aqueous electrolyte	240
Figure 5.8 (b)	CV curves of AC// $\text{Li}_2\text{MnSiO}_4$ and AC// $\text{Li}_2\text{Mn}_{1-x}\text{Zn}_x\text{SiO}_4$ supercapattery devices in 1 M Na_2SO_4 aqueous electrolyte at a potential window of 0.1 – 0.8 V	241
Figure 5.9 (a)	GCD profiles of AC// $\text{Li}_2\text{MnSiO}_4$ and AC// $\text{Li}_2\text{Mn}_{1-x}\text{Zn}_x\text{SiO}_4$ supercapattery devices at a current load of 0.1 A g^{-1} at a voltage window of 1.6 V	243
Figure 5.9 (b)	GCD profiles of AC// $\text{Li}_2\text{Mn}_{0.96}\text{Zn}_{0.04}\text{SiO}_4$ device at varying current loads $0.1 - 2 \text{ A g}^{-1}$ in 1 M Na_2SO_4 aqueous electrolyte	244

Figure 5.9 (c)	Variation of specific capacitance with current load of AC//Li ₂ MnSiO ₄ and AC// Li ₂ Mn _{1-x} Zn _x SiO ₄ supercapattery devices in 1 M Na ₂ SO ₄ aqueous electrolyte and voltage window of 1.6 V	245
Figure 5.10 (a)	Cycling stability of AC//Li ₂ MnSiO ₄ and AC// Li ₂ Mn _{1-x} Zn _x SiO ₄ supercapattery devices over 1000 and 3000 cycles	246
Figure 5.10 (b)	Coulombic efficiency of AC//Li ₂ MnSiO ₄ and AC// Li ₂ Mn _{1-x} Zn _x SiO ₄ supercapattery devices	248
Figure 5.11	Ragone plot of AC//Li ₂ MnSiO ₄ and AC// Li ₂ Mn _{1-x} Zn _x SiO ₄ supercapattery devices in 1 M Na ₂ SO ₄ aqueous electrolyte and voltage window of 1.6 V	250
Figure 6.1	Synthesis scheme of N ₁ and N ₂ nanoarchitectonic electrode materials	267
Figure 6.2 (a)	SEM and HRTEM micrographs of N ₁ with SAED and lattice fringes as insets	271
Figure 6.2 (b)	SEM and HRTEM micrographs of N ₂ with SAED and lattice fringes as insets	272
Figure 6.2 (c)	EDS spectra and EDS maps of N ₁ with elemental mass ratios overlaid on the electron images	273
Figure 6.2 (d)	EDS spectra and EDS maps of N ₂ with elemental mass ratios overlaid on the electron images	274
Figure 6.3 (a)	SAXS pair distance distribution functions of G-ol, V ₂ O ₅ -CNT, Li ₂ Mn _{1-x} Zn _x SiO ₄ , N ₁ and N ₂ nanomaterials by intensity of scattered particles	277

Figure 6.3 (b ₁)	SAXS pair distance distribution functions of G-ol, V ₂ O ₅ -CNT, Li ₂ Mn _{1-x} Zn _x SiO ₄ , N ₁ and N ₂ nanomaterials by physical volume of particles scattered	278
Figure 6.3 (b ₂)	SAXS pair distance distribution functions of G-ol, V ₂ O ₅ -CNT, Li ₂ Mn _{1-x} Zn _x SiO ₄ , N ₁ and N ₂ nanomaterials by physical volume of particles scattered	279
Figure 6.4	XRD spectra of G-ol, V ₂ O ₅ -CNT, Li ₂ Mn _{1-x} Zn _x SiO ₄ nanomaterials and N ₁ and N ₂ nanohybrids	282
Figure 6.5 (a)	Crystal structure model of N ₁ nanohybrid electrode material	284
Figure 6.5 (b)	Crystal structure model of N ₂ nanohybrid electrode material	285
Figure 6.6	FTIR spectra of G-ol, V ₂ O ₅ -CNT, Li ₂ Mn _{1-x} Zn _x SiO ₄ , N ₁ and N ₂ electrode nanomaterials	286
Figure 6.7	Raman spectra of G-ol, V ₂ O ₅ -CNT, Li ₂ Mn _{1-x} Zn _x SiO ₄ , N ₁ and N ₂ electrode nanomaterials with excitation laser of 514.9 nm.	288
Figure 6.8 (a)	Comparative CV curves of Li ₂ Mn _{1-x} Zn _x SiO ₄ , N ₁ and N ₂ electrodes with G-ol and V ₂ O ₅ -CNT as inset at a scan rate of 80 mV s ⁻¹ in 1 M sodium sulfate (Na ₂ SO ₄) aqueous electrolyte	290
Figure 6.8 (b)	CV curves of N ₂ nanohybrid electrode at scan rates of 5 – 100 mV s ⁻¹ in 1 M sodium sulfate (Na ₂ SO ₄) aqueous electrolyte	291
Figure 6.9 (a)	Nyquist plots of N ₁ and N ₂ nanohybrid electrodes at OCV	293
Figure 6.9 (b)	Circuit models used to fit EIS data	293
Figure 6.10 (a)	Phase angle Bode plots of N ₁ and N ₂ nanohybrid electrode materials	294
Figure 6.10 (b)	Total impedance Bode plots of N ₁ and N ₂ nanohybrid electrode materials	295

Figure 6.11 (a)	.CV curves of activated carbon and N ₂ nanohybrid electrodes at a scan rate of 50 mV s ⁻¹ in 1 M Na ₂ SO ₄ aqueous electrolyte	297
Figure 6.11 (b)	CV curves of AC//N ₂ supercapattery at various potential ranges from 0 – 1.8 V at a scan rate of 80 mV s ⁻¹ in 1 M Na ₂ SO ₄ aqueous electrolyte	297
Figure 6.11 (c)	Comparative plot of AC// N ₁ and AC//N ₂ supercapattery devices at 50 mVs ⁻¹ in 1 M Na ₂ SO ₄ aqueous electrolyte at voltage window of 1.8 V	298
Figure 6.11 (d)	CV curves of AC//N ₂ supercapattery at scan rates of 10 -120 mVs ⁻¹ in 1 M Na ₂ SO ₄ aqueous electrolyte at voltage window of 1.8 V	299
Figure 6.12 (a)	Comparative GCD profiles of AC//N ₂ and AC// N ₁ supercapattery devices at voltage range of 1.8 V and current load of 0.1 A g ⁻¹ (i) and 1.6 V and 0.05 A g ⁻¹ (ii)	301
Figure 6.12 (b)	GCD curves of AC//N ₂ (i) and AC// N ₁ (ii) supercapattery devices at various current loads at voltage range of 1.8 V	302
Figure 6.12 (c)	GCD curves of AC//N ₂ (i) and AC// N ₁ (ii) supercapattery devices at various current loads at voltage range of 1.6 V	302
Figure 6.12 (d)	Variation of discharge capacitance with current load of AC//N ₂ device in 1 M Na ₂ SO ₄ aqueous electrolyte at voltage window of 1.8 V	303
Figure 6.13 (a)	Cycling stability of AC//N ₁ and AC//N ₂ supercapattery devices over 5000 cycles in 1 M Na ₂ SO ₄ aqueous electrolyte at voltage window of 1.8 V	304
Figure 6.13 (b)	Coulombic efficiency of AC//N ₁ and AC//N ₂ supercapattery devices over 5000 cycles in 1 M Na ₂ SO ₄ aqueous electrolyte at voltage window of 1.8 V	305

Figure 6.14 (a)	Nyquist plots of AC//N ₁ and AC//N ₂ supercapattery devices before and after cycling with circuit model used to fit EIS data as inset	307
Figure 6.14 (b)	Total impedance Bode plots of AC//N ₁ and AC//N ₂ supercapattery devices before and after cycling	308
Figure 6.14 (c)	Phase angle Bode plots of AC//N ₁ and AC//N ₂ supercapattery devices before and after cycling	309
Figure 6.15	Ragone plot of AC//N ₁ and AC//N ₂ supercapattery devices in 1 M Na ₂ SO ₄ aqueous electrolyte at voltage window of 1.8 V	311



LIST OF TABLES

Table 2.1	Comparison between batteries and supercapacitors based on 14 operational Parameters	
Table 2.2	Synthesis methods, morphology, size of particle and electrochemical properties of V ₂ O ₅ - based electrodes reported in literature.	41
Table 2.3	Method of synthesis, physical and electrochemical properties of Li ₂ MnSiO ₄ - based electrodes reported in literature	47
Table 2.4	Summary of the performance of different hybrid energy storage devices	49
Table 3.1	Structural properties of graphite, GO and G-ol nanosheets	83
Table 3.2	Functional groups/ bonds present in graphite, GO and G-ol	88
Table 3.3	Raman active modes of graphite, GO and G-ol	90
Table 3.4	EIS curve fitting data of graphite, GO and G-ol	103
Table 3.5	EIS simulation data of G-ol//G-ol and AC//G-ol supercapacitor devices before and after cycling	116
Table 3.6	Electrochemical performance data of G-ol//G-ol and AC//G-ol flexible supercapacitors	119
Table 4.1	Structural properties of V ₂ O ₅ , V ₂ O ₅ -CNT, V ₂ O ₅ -CNT-G-ol nanomaterials obtained from XRD studies	151
Table 4.2	Functional groups/ bonds vibrations in V ₂ O ₅ nanorods, V ₂ O ₅ -CNT nanonetwork and V ₂ O ₅ -CNT-G-ol nanocapsules	159
Table 4.3	EIS curve fitting data of V ₂ O ₅ -based electrode materials	174

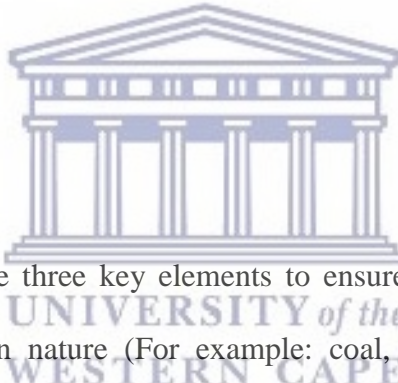
Table 4.4	Charge and discharge capacities of Asymmetric AC//V ₂ O ₅ -CNT-G-ol device	180
Table 4.5	Comparison of V ₂ O ₅ -CNT-G-ol supercapacitor with other devices assembled with V ₂ O ₅ -based electrode materials and composites with different carbon forms.	185
Table 5.1	Nanocrystallite sizes of Li ₂ MnSiO ₄ and Li ₂ Mn _{0.98} Zn _{0.02} SiO ₄ , Li ₂ Mn _{0.96} Zn _{0.04} SiO ₄ , Li ₂ Mn _{0.94} Zn _{0.04} SiO ₄ , and Li ₂ Mn _{0.92} Zn _{0.08} SiO ₄ obtained from HRTEM analysis	205
Table 5.2	Crystallographic data of Li ₂ MnSiO ₄ , Li ₂ Mn _{0.98} Zn _{0.02} SiO ₄ , Li ₂ Mn _{0.96} Zn _{0.04} SiO ₄ , Li ₂ Mn _{0.94} Zn _{0.04} SiO ₄ , and Li ₂ Mn _{0.92} Zn _{0.08} SiO ₄ electrode materials	219
Table 5.3	Redox and charge storage properties of undoped and Zn-doped Li ₂ MnSiO ₄ electrode materials obtained from CV investigations	229
Table 5.4	EIS curve fitting data of pure and Zn-doped Li ₂ MnSiO ₄ electrode materials	235
Table 6.1	Average crystallite sizes of N ₁ and N ₂ nanohybrid electrodes obtained from SEM micrographs	270
Table 6.2	Structural parameters of N ₁ and N ₂ nanohybrids obtained from XRD analysis	281
Table 6.4	EIS curve fitting data of N ₁ and N ₂ nanohybrid electrodes	292
Table 6.5	EIS simulation data of AC//N ₁ and AC//N ₂ supercapattery devices before and after 5000 cycles	306

CHAPTER ONE

BACKGROUND INFORMATION, AIMS AND OBJECTIVES OF THE STUDY

The Role of Electrochemical Energy Storage in the Global Energy Transformation

1.1 Introduction



Energy, water and food are the three key elements to ensure human survival and growth. Energy can either be found in nature (For example: coal, crude oil, wind, solar, tidal, geothermal, biomass and natural gas) or can be subjected to conversion and transformation processes for direct consumption by humankind (For example: electricity, petroleum products, fuel and gases). Worldwide energy consumption continues to increase significantly over the years due to economic and population growth. The advent of a low-carbon society has initiated the inevitable transformation from traditional fossil fuels to non-fossil new energy [1,2].

1.2 The Global Energy Mix

Global energy supply is dominated by carbon-based fossil fuels and their demand increases at a rapid rate due to progress of society and economic development. Consumption of fossil fuels by 2011 globally, emitted about 31 Giga tonnes of carbon dioxide (which represents two-thirds of greenhouse gases) with coal contributing the largest emission share [3,4]. It is projected that average global temperatures will rise above 3.5 °C by 2035 and about 5 – 6 °C by the end of this century if the consumption of fossil fuels increases at the current rate. This is regarded as a serious scenario that will lead to very severe damage on the environment. It is therefore imperative that the emission of greenhouse gases are reduced substantially and urgently for effective climate change mitigation. According to a framework for Sustainable Development Goals (SDGs) adopted in 2015 by the United Nations General Assembly (UNGA) for international cooperation for realisation of a sustainable future for the planet, clean energy is central to the success of this framework [5]. The global goal on energy aims to ensure affordable, reliable and universal access to modern energy services, increase the share of renewable energy in the global energy mix and double the rate of improvement in energy efficiency.

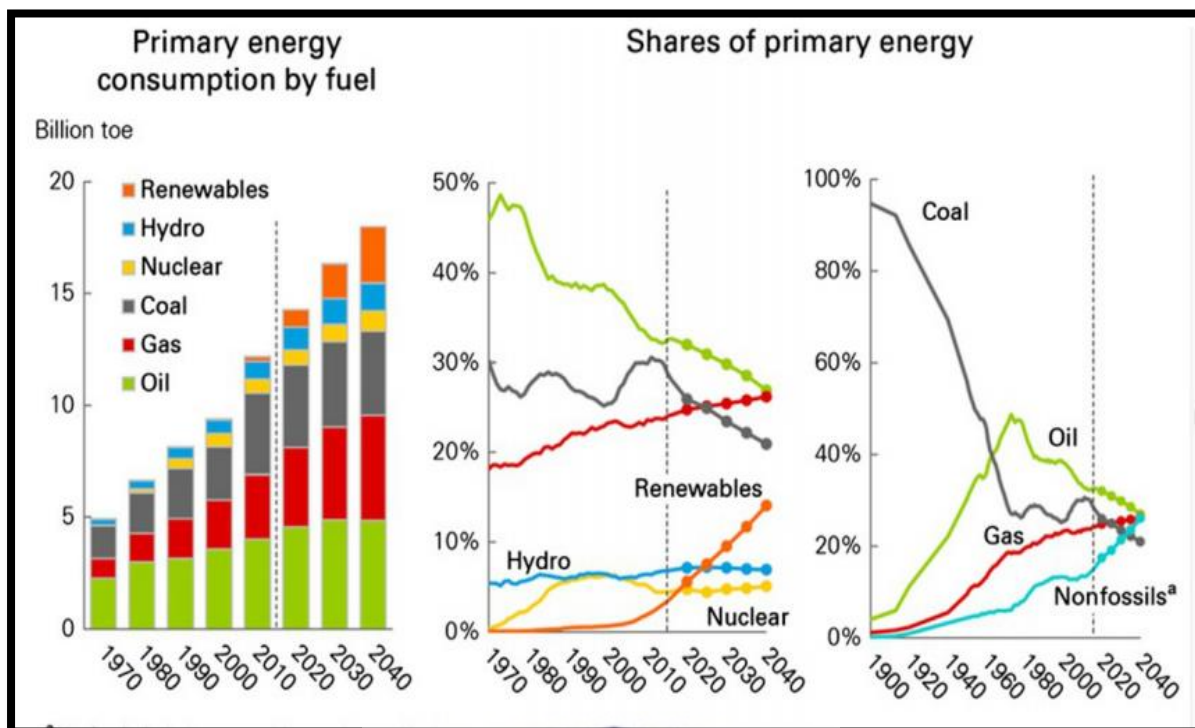


Figure 1.1: Historical and Projected data for global energy consumption by fuel type [3].



UNIVERSITY of the
WESTERN CAPE

Global energy demand is predicted to reach 18 Billion tons of oil equivalent (toe) by 2030 and by 2040 (regardless of the increase in demand), natural gas and new energy as clean energy resources will take up a higher share in the primary energy mix as shown in Figure 1.1. Moreover, coal, oil, gas and new energy resources will each account for a quarter of global energy consumption [2]. In the sustainable policy for climate change mitigation, three technological pillars are considered. Namely; energy efficiency, replacing fossil fuels with renewables energy and carbon capture. Renewable energies are absolutely the best energy sources compared to fossil fuels due to their minimal associated emissions of CO₂ and other pollutants. According to the International Energy Agency, about 1.4 billion people currently lack access to electricity and about 2.7 billion people are using biomass for cooking [6]. Due to Africa's low capacity to adapt to change, its impending water crises, population growth and

overreliance on subsistence agriculture, the United Nations has regarded it as one of the continents with maximum vulnerability to the effects of climate change [7].

The South African economy heavily relies on coal for electricity generation and it is in conflict with sustainable development. In an effort to reduce its carbon footprint of electricity and increase energy efficiency, the South African Renewable Energy Independent Power Producers Procurement Programme was launched in 2011 [8]. The programme was expensive at first but proved successful. With the rising costs of coal and decreasing cost of renewables, the Witbank coal fields that have been exploited mainly are nearing exhaustion and moving to other coal fields requires new infrastructure and investments and rising cost as reported by Richard and Colin [9], for the new coal-based power stations at Medupi and Kusile.

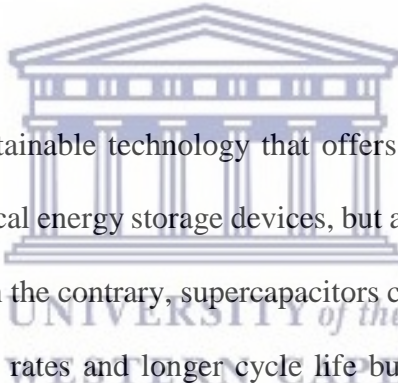
Overall, countries worldwide are looking for new types of clean and sustainable energy which could replace conventional fossil fuels and the development of renewable energy is considered the focus as a new trend of industry promotion and development [10]. The need to mitigate the environmental hazards of fossil fuel usage, the volatility of fuel prices and enhancement of the national energy security necessitates a phenomenal change in the energy supply chain. Although the need for electricity generation and storage will be far greater in future, the problem of ensuring power quality is already upon us, as evidenced by recent power outages.

1.3 Electrical Energy Storage

With the increased awareness for global warming and the high demand for renewable energy sources, electrical energy storage and conversion systems have become very crucial to replace the traditional fossil fuels. The chief renewable energy sources are wind and solar energy.

However, these sources although sustainable, are intermittent due to their dependence on the weather, resulting in output fluctuations, unavailability, and unpredictability. In this regard, electrochemical energy storage devices such as batteries and supercapacitors become more appealing. These devices will therefore, enable electricity to be produced at times of either low demand, low generation cost or from intermittent energy sources to be used at times of high demand, high generation cost or when no generation means is available. Indeed, these devices are a priceless and sustainable technological approach for improving the reliability and the general use of the entire power system (generation, transmission and distribution) [11,12].

1.4 Research Problem and Motivation



Lithium ion batteries are a sustainable technology that offers higher energy densities when compared to other electrochemical energy storage devices, but are confined by their low power densities and poor cycle life. On the contrary, supercapacitors can provide much higher power densities, fast charge-discharge rates and longer cycle life but also suffer from low energy densities. In view of numerous applications of electronic devices and hybrid electric vehicles, there has been great demand for high-performance energy storage devices with both high energy density and power density. To solve this problem, a supercapacitor–battery hybrid energy storage system - supercapattery, has emerged in recent years, composed of a capacitor-type electrode and a battery-type electrode and thus expected to possess the best features of both supercapacitors and batteries [13,14]. However, the key to enhancing the energy output of these energy storage devices for large scale utilization lies in the choice of potential high performance electrodes. Various hybrid systems based on the supercapacitor-battery design have been developed. Although most works have reported fabrication of such devices based on activated carbon as a supercapacitor-type electrode material, and $\text{Li}_4\text{Ti}_5\text{O}_{12}$, LiFePO_4 , graphite

or metal oxides as the battery-type electrode materials [15–18]. The poor conductivity, low capacity or instability of these materials during cycling have limited the electrochemical performance of the devices.

Lithium transition metal orthosilicates (Li_2MSiO_4 , $\text{M} = \text{Mn, Fe, Co}$) have attracted extensive attention as possible next generation cathode materials for lithium-ion batteries due to their overwhelming advantages. These include; high theoretical capacity ($\sim 330 \text{ mA h g}^{-1}$), high thermal stabilities through strong Si-O bonds, environmental friendliness and low cost. Among the orthosilicates, $\text{Li}_2\text{MnSiO}_4$ shows great promise due to the potential extraction of two Li^+ per formula unit, utilizing the $\text{M}^{2+}/\text{M}^{4+}$ redox couples at potential range of current electrolytes. However, like many other polyanionic cathode materials, $\text{Li}_2\text{MnSiO}_4$ suffers low electronic conductivity and structural instability linked with the Jahn-Teller distortion at the Mn site resulting in large capacity fading which limits its practical application [19,20]. Several strategies such as particle size reduction, coating with conductive carbon (CNTs, graphene), metal oxides (ZnO , TiO_2) and partial substitution of manganese cations with Fe^{2+} , Mg^{2+} , Cr^{3+} and Al^{3+} have realized an improvement in the electrochemical performance of $\text{Li}_2\text{MnSiO}_4$ cathode material. Recently, fast ultrasound synthesis of $\text{Li}_2\text{MnSiO}_4$ nanoparticles and chelate induced- formation of $\text{Li}_2\text{MnSiO}_4$ nanorods which delivered high initial discharge capacities ranging from of $260\text{-}275 \text{ mA h g}^{-1}$, corresponding to $\sim 80 \%$ of the theoretical capacity. It is evident from these reports that the synthetic route as well as the doping/conductive coating and the relative purity of the synthesized materials can greatly improve the reversible capacity and overall electrochemical performance of $\text{Li}_2\text{MnSiO}_4$ cathode material [21–23].

Layered and orthorhombic structured V_2O_5 has been extensively investigated as a promising cathode material for lithium-ion batteries due to unique intercalation structure, low cost and its capability of reversibly accepting multiple Li^+ ions yielding a high capacity $\sim 294 \text{ mA h g}^{-1}$ in

a voltage range of 1.5-4.0 V. Unfortunately, poor electrical conductivity and low Li^+ ion diffusion coefficient hinders its practical application [24,25].

Graphol (hydroxylated graphene) is a new member of the graphene family with a distinct structure, defined band gap and the availability of groups for high density functionalization of the carbon backbone. Graphol has shown high electro-catalytic properties towards biomarkers and possesses great potential for multifunctional applications [26,27].

1.5 Research aim and objectives

This research is aimed at developing multifaceted nanoarchitectures based on hydroxylated graphene, vanadia networks and Zn-doped $\text{Li}_2\text{MnSiO}_4$ nanomaterials. Supercapacitor/supercapattery assemblies of the nanoarchitectonic platforms are well investigated in aqueous electrolytes for advanced energy storage applications. The objectives of the study are outlined below.

- ❖ Preparation of graphol, V_2O_5 , $\text{Li}_2\text{MnSiO}_4$, V_2O_5 -CNT-graphol, $\text{Li}_2\text{Mn}_{1-x}\text{Zn}_x\text{SiO}_4$ and nanoarchitectonic $(\text{V}_2\text{O}_5\text{-CNT-graphol})\text{-Li}_2\text{Mn}_{1-x}\text{Zn}_x\text{SiO}_4$ electrode materials. Optimization of parameters to obtain the desired products.
- ❖ Investigation of the nature and relative quantities of graphol and MWCNTs present in the synthesised materials by Raman spectroscopy.
- ❖ Surface, elemental and particle size analysis of the prepared materials by High Resolution Transmission Electron Microscopy (HRTEM), High Resolution Scanning

Electron Microscopy (HRSEM), Energy Dispersive X-ray Spectroscopy (EDS), Small angle X-ray Scattering (SAXS) and X-ray photoelectron spectroscopy (XPS).

- ❖ Crystallographic and functional group analysis of the pristine and Zn-doped materials by X-ray Diffraction (XRD), Fourier Transform Infra-Red Spectroscopy (FTIR) and Solid-State Nuclear Magnetic Resonance Spectroscopy (SS-NMR).
- ❖ Electrochemical characterization of electrode materials to verify material dynamics at the electrode surface using Cyclic Voltammetry (CV) and Electrochemical Impedance Spectroscopy (EIS).
- ❖ Galvanostatic charge/discharge studies of assembled supercapacitor/supercapattery devices and stability test over extended cycling.

1.6 Thesis outline



The thesis is divided into seven chapters as follows

- ❖ **Chapter 1:** Chapter one presents the introduction and background to the research, the problem statement and motivation, research aims and objectives
- ❖ **Chapter 2:** Presents a comprehensive review on the development trends and performance metrics of supercapatteries. Recent advances in materials, device performance and future prospects are also discussed
- ❖ **Chapter 3:** Discusses the preparation, characterisation and application of hydroxylated graphene nanomaterials as supercapacitor electrodes
- ❖ **Chapter 4:** Discusses the preparation, characterisation and application of V_2O_5 -based nanomaterials as supercapacitor electrodes

-
- ❖ **Chapter 5:** Discusses the preparation, characterisation and application of $\text{Li}_2\text{MnSiO}_4$ -based nanomaterials as supercapattery electrodes
 - ❖ **Chapter 6:** Discusses the preparation, characterisation and application of nanoarchitected electrode materials as supercapattery electrodes
 - ❖ **Chapter 7:** Presents a summary of the research findings and recommendations for future work

References

- [1] M. Aneke, M. Wang, Energy storage technologies and real life applications – A state of the art review, *Appl. Energy*. 179 (2016) 350–377. doi:10.1016/j.apenergy.2016.06.097.
- [2] C. Zou, Q. Zhao, G. Zhang, B. Xiong, Energy revolution: From a fossil energy era to a new energy era, *Nat. Gas Ind.* 36 (2016) 1–10. doi:10.3787/j.issn.1000-0976.2016.01.001.
- [3] K.R. Khalilpour, *Moving Forward to the Past , With Adaptation and Flexibility: The Special Role of Resource Storage*, Elsevier Inc., n.d. doi:10.1016/B978-0-12-813306-4.00001-X.
- [4] S. Hong, C.J.A. Bradshaw, B.W. Brook, Global zero-carbon energy pathways using viable mixes of nuclear and renewables, *Appl. Energy*. 143 (2015) 451–459. doi:10.1016/j.apenergy.2015.01.006.
- [5] D. Gielen, F. Boshell, D. Saygin, M.D. Bazilian, N. Wagner, R. Gorini, The role of renewable energy in the global energy transformation, *Energy Strateg. Rev.* 24 (2019) 38–50. doi:10.1016/j.esr.2019.01.006.

-
- [6] G. Mao, N. Huang, L. Chen, H. Wang, Research on biomass energy and environment from the past to the future : A bibliometric analysis, *Sci. Total Environ.* 635 (2018) 1081–1090. doi:10.1016/j.scitotenv.2018.04.173.
- [7] A.K. Aliyu, B. Modu, C.W. Tan, A review of renewable energy development in Africa : A focus in South, *Renew. Sustain. Energy Rev.* 81 (2018) 2502–2518. doi:10.1016/j.rser.2017.06.055.
- [8] G. Schwerhoff, M. Sy, Developing Africa’s energy mix, 3062 (2019). doi:10.1080/14693062.2018.1459293.
- [9] D. Richard, A. Colin, Renewable energy gathers steam in South Africa, *Renew. Sustain. Energy Rev.* 41 (2015) 390–401. doi:10.1016/j.rser.2014.08.049.
- [10] G. Li, W. Sun, G.H. Huang, Y. Lv, Planning of integrated energy-environment systems under dual interval uncertainties, *Electr. Power Energy Syst.* 100 (2018) 287–298. doi:10.1016/j.ijepes.2018.02.033.
- [11] K. Chen, D. Xue, Materials chemistry toward electrochemical energy storage, *J. Mater. Chem. A.* 4 (2016) 7522–7537. doi:10.1039/C6TA01527A.
- [12] F. Wang, X. Wu, X. Yuan, Z. Liu, Y. Zhang, L. Fu, Y. Zhu, Q. Zhou, Y. Wu, W. Huang, Latest advances in supercapacitors: From new electrode materials to novel device designs, *Chem. Soc. Rev.* 46 (2017) 6816–6854. doi:10.1039/c7cs00205j.
- [13] G.Z. Chen, G.Z. Chen, Supercapacitor and supercapattery as emerging electrochemical energy stores Supercapacitor and supercapattery as emerging electrochemical energy stores, *Int. Mater. Rev.* 0 (2016) 1–30. doi:10.1080/09506608.2016.1240914.
- [14] M.M. Ndipingwi, C.O. Ikpo, N.W. Hlongwa, Z. Myalo, Orthorhombic Nanostructured

-
- Li₂MnSiO₄/Al₂O₃ Supercapattery Electrode with Efficient Lithium-Ion Migratory Pathway, (2018) 223–235. doi:10.1002/batt.201800045.
- [15] F. Zhang, T. Zhang, X. Yang, L. Zhang, K. Leng, Y. Huang, Y. Chen, A high-performance supercapacitor-battery hybrid energy storage device based on graphene-enhanced electrode materials with ultrahigh energy density, *Energy Environ. Sci.* 6 (2013) 1623–1632. doi:10.1039/c3ee40509e.
- [16] H. Zou, B. Wang, F. Wen, L. Chen, Hydrothermal synthesis of pure LiMn₂O₄ from nanostructured MnO₂ precursors for aqueous hybrid supercapacitors, *Ionics (Kiel)*. 23 (2017) 1083–1090. doi:10.1007/s11581-016-1927-3.
- [17] S.H. Lee, I.H. Im, Excellent performance hybrid supercapacitors based on LiNi_{1/3}Mn_{1/3}Co_{1/3}O₂/activated carbon electrode, *Mater. Lett.* 231 (2018) 38–42. doi:10.1016/j.matlet.2018.07.115.
- [18] W. Zuo, R. Li, C. Zhou, Y. Li, J. Xia, J. Liu, Battery-Supercapacitor Hybrid Devices : Recent Progress and Future Prospects, *Adv. Sci. News.* (2017) 1600539. doi:10.1002/advs.201600539.
- [19] Q. Cheng, W. He, X. Zhang, M. Li, L. Wang, Modification of Li₂MnSiO₄ cathode materials for lithium-ion batteries: a review, *J. Mater. Chem. A.* 5 (2017) 10772–10797. doi:10.1039/C7TA00034K.
- [20] R.J. Gummow, Y. He, Recent progress in the development of Li₂MnSiO₄ cathode materials, *J. Power Sources.* 253 (2014) 315–331. doi:10.1016/j.jpowsour.2013.11.082.
- [21] X. Kong, T. Mei, Z. Xing, N. Li, Z. Yuan, Y. Zhu, Y. Qian, Size controlled synthesis of uniform Li₂MnSiO₄ nanospheres and their electrochemical behaviors in lithium-ion batteries, *Int. J. Electrochem. Sci.* 7 (2012) 5565–5573.


-
- [22] S.-S. Liu, L.-J. Song, B.-J. Yu, C.-Y. Wang, M.-W. Li, Comparative Study of the Cathode and Anode Performance of $\text{Li}_2\text{MnSiO}_4$ for Lithium-Ion Batteries, *Electrochim. Acta.* 188 (2016) 145–152. doi:10.1016/j.electacta.2015.11.144.
- [23] Y. Pei, Q. Chen, C.-Y. Xu, H.-X. Wang, H.-T. Fang, C. Zhou, L. Zhen, G. Cao, Chelate-induced formation of $\text{Li}_2\text{MnSiO}_4$ nanorods as a high capacity cathode material for Li-ion batteries, *J. Mater. Chem. A.* 4 (2016) 9447–9454. doi:10.1039/C6TA01269H.
- [24] X. Liang, G. Gao, Y. Liu, Z. Ge, P. Leng, G. Wu, Carbon nanotubes/vanadium oxide composites as cathode materials for lithium-ion batteries, *J. Sol-Gel Sci. Technol.* 82 (2017) 224–232. doi:10.1007/s10971-016-4293-8.
- [25] Y. Zhang, J. Zheng, Y. Zhao, T. Hu, Z. Gao, C. Meng, Fabrication of V_2O_5 with various morphologies for high-performance electrochemical capacitor, *Appl. Surf. Sci.* 377 (2016) 385–393. doi:10.1016/j.apsusc.2016.03.180.
- [26] A. Ambrosi, C.K. Chua, N.M. Latiff, A.H. Loo, C.H.A. Wong, A.Y.S. Eng, A. Bonanni, M. Pumera, Graphene and its electrochemistry – an update, *Chem. Soc. Rev.* 45 (2016) 2458–2493. doi:10.1039/C6CS00136J.
- [27] H.L. Poh, Z. Sofer, P. imek, I. Tomandl, M. Pumera, Hydroboration of graphene oxide: Towards stoichiometric graphol and hydroxygraphane, *Chem. - A Eur. J.* 21 (2015) 8130–8136. doi:10.1002/chem.201406168.

CHAPTER TWO

LITERATURE REVIEW

Development Trends and Performance Metrics of Supercapatteries. Recent Advances in Materials, Device Performance and Future Prospects

2.1 . Introduction



The global drive and vast investments to harness the unlimited but intermittent renewable energy sources such as solar, wind and tidal into one of the primary sources for electricity production is very critical in facilitating the transition towards decarbonising the currently fossil-fuel dependent energy economy. Key requirements of grid compatible electrical energy storage technologies need to be addressed in order to meet this goal in the nearest future. These include high energy and power densities, long cycle life, fast charge-discharge rates, stable operation and performance, cost-effectiveness and easy scale-up [1,2].

The basis of energy storage involves the conversion of energy from one form to another that can deliver the stored energy when needed in an efficient, cost-effective and reliable manner. In this regard, electrical energy storage devices such as supercapacitors and Li-ion batteries become strategic elements to facilitate these energy evolutions as they are able to store charges in a fast and efficient way, enabling the harvest and conversion of renewable energy to usable forms. Both supercapacitors and Li-ion batteries rely on electrochemical processes but work

based on different distinct charge storage mechanisms. The Li-ion battery is a mature technology characterised by increasing energy densities ($\sim 180 \text{ W h Kg}^{-1}$) meeting industry requirements, low cost and a high margin of safety. However, the battery possesses limited charging ability and low power output as a result of kinetically limited faradaic reactions such as ion diffusion and charge transfer processes which occur in the bulk of the electrode materials [3,4]. On the other hand, supercapacitors which store charge through accumulation of ions at the electrode-electrolyte interface (electrochemical double-layer capacitors-EDLC) or quick redox processes at the electrode surface (pseudocapacitors), have high power densities ($\sim 10 \text{ KW Kg}^{-1}$) and very long cycle stability as compared to batteries. However, their energy densities are much lower compared to Li-ion batteries [5,6], as summarized in Table 2.1.

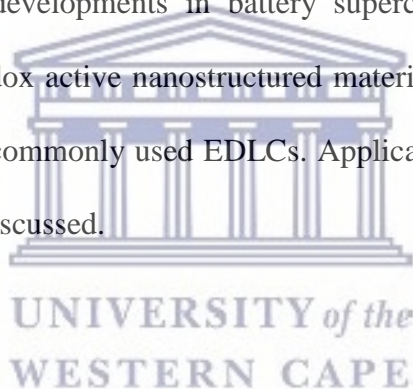


Table 2.1: Comparison between batteries and supercapacitors based on operational Parameters [7].

Comparison Parameter	Battery	Supercapacitor
Energy storage	High (bulk)	Limited (surface area)
Storage mechanism	Chemical	Physical
Power limitation	Reaction kinetics, mass transport	Electrolyte conductivity
Charge rate	Kinetically limited	High charge and discharge
Cycle life limitation	Mechanical stability, chemical reversibility	Side reactions

Many investigators for the past few years have directed their efforts towards improving the power density and cycle life of Li-ions and energy storage capabilities of supercapacitors to meet the increasing requirements of electrical power systems. This has led to the development of new energy storage technologies including hybrids of rechargeable battery and supercapacitors into one device, known as supercapattery or supercabattery as proposed by George Chen [8,9]. A supercapattery exhibits capacitive performance with enhanced energy density, whereas a supercabattery delivers battery-type performance with improved power capability.

This review presents recent developments in battery supercapacitor hybrids particularly supercapatteries, associated redox active nanostructured materials as faradaic electrodes and carbon-based materials as the commonly used EDLCs. Applications of these hybrid systems and future directions are also discussed.



2.2 . Supercapatteries among electrochemical energy storage devices: Ragone Plot

The Ragone plot named by David Vincent Ragone is a very useful chart for directing the development of energy storage devices and their limitations based on how much energy they can store (energy density) and how rapidly the energy can be accessed (power density). Both parameters are very important for determining a particular device's specific function and has been used to compare the performance of energy devices such as fuel cell, internal combustion engine and batteries [10,11]. Supercapatteries which are analogous to the hybrid supercapacitor, seek to achieve comparable performance to capacitors in power capability and cycle life, and to batteries in energy density.

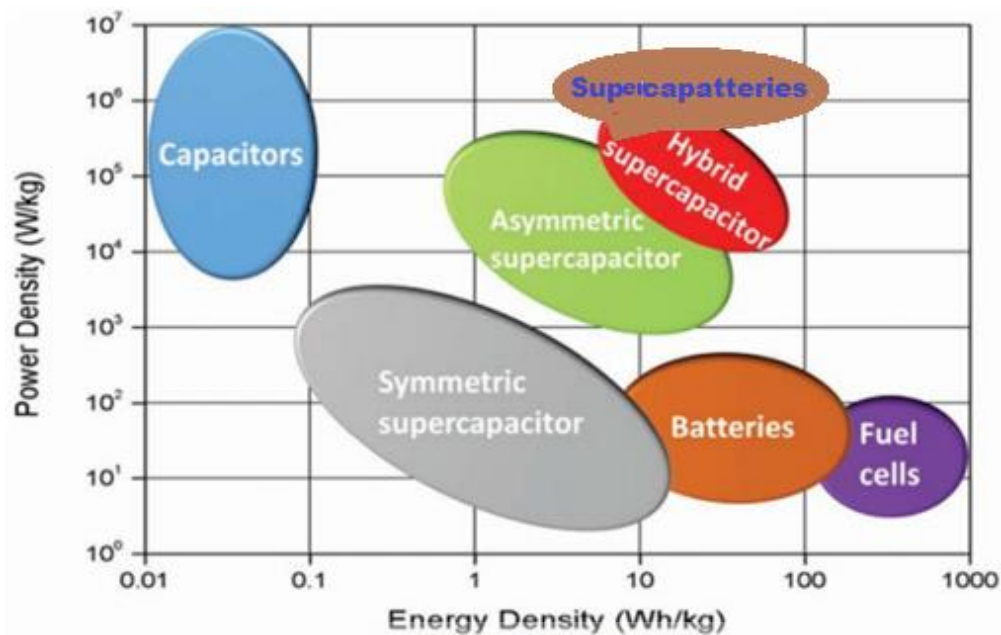


Figure 2.1.: Comparing the energy and power densities of hybrid supercapacitors, batteries and fuel cells [12].

Energy storage devices like batteries, fuel cells and supercapacitors are characterised by electrochemical conversion processes. Compared to fuel cells, batteries and symmetrical supercapacitors, hybrid supercapacitors show higher power density with elevated capacitance and energy storage capabilities as shown on the Ragone plot, Figure 2.1. They have fetched wide attention due to their propensity of combining the properties of EDLCs and pseudocapacitors [7,12,13]. However, they have significant lower power density compared to conventional capacitors. Supercapacitors differ from conventional capacitors in their charge storage mechanism. Capacitors consist of dielectric plates for electrostatic charge storage meanwhile supercapacitors consist of two electrodes kept apart by a separator and submerged in an electrolyte that allows for the diffusion of electrolytic ions. Supercapacitors may be symmetric or asymmetric based on either two different electrodes or same electrodes with differences in charge storage mechanisms.

2.3. Components, design considerations and mechanism of Energy storage in Supercapatteries

The key factors that characterise the cost, operation and application of supercapatteries are classified according to the following domains.

2.3.1. Typical components of electrical energy storage devices

In the likeness of many other energy storage devices, supercapatteries are composed of positive (positrode) and negative (negatrode) electrodes set apart by separators to prevent short circuiting and electrolytes for movement of charged species as shown in Figure 2.2.

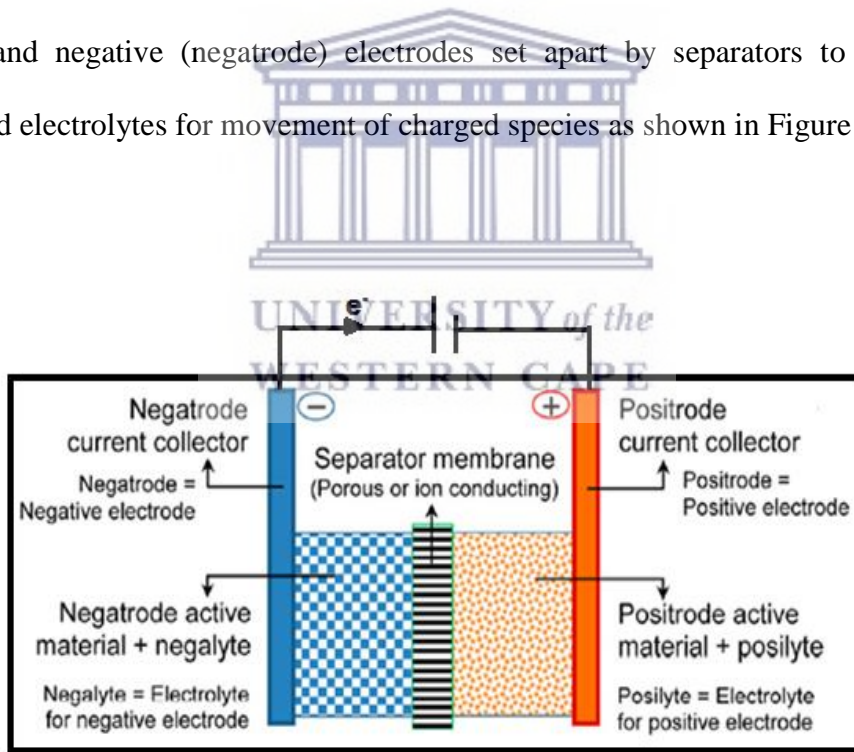


Figure 2.2: Schematic representation of a single cell of a typical electrical energy storage device [8].

The negative and positive electrodes are made of materials that possess high conductivity such as metals, ceramics, carbons and their polymeric composites. These electrodes are usually coated on electronically conducting substrates known as current collectors, which are chemically and electronically inert in the cell environment. Electrical polarities of the electrodes are determined by their potential window. That is, the electrode with the more positive potential is used as the positive electrode and vice versa. Current flows through the external circuit from positive to the negative electrode and electrons in the opposite direction [8].

2.3.2. Design considerations of supercapattery

The supercapattery design as shown in Figure 2.3 includes one battery-type electrode and one capacitive-type electrode which may either be used as a positive or negative electrode depending on its potential window. In general, battery-type materials in the hybrid device are considered to be those charged through faradaic redox reactions including pseudocapacitive metal oxides, conducting polymers, intercalation compounds and electroactive clusters or molecular species. While materials charged through capacitive double layer are regarded as the capacitive-type electrode [14,15]. Mainly high surface area carbons are used as the capacitive-type electrode. Even though the supercapattery (battery-supercapacitor hybrid) is asymmetric in nature, it is different from the conventional asymmetric supercapacitor in which both electrodes are capacitive but with asymmetric capacitive charge storage [16]. Another asymmetric device comparable to the supercapattery is the Li / Na ion capacitor, where the battery-type electrode is a Li / Na -intercalating electrode [17,18], which offers high energy density while the capacitive type electrode provides high power capability in the system.

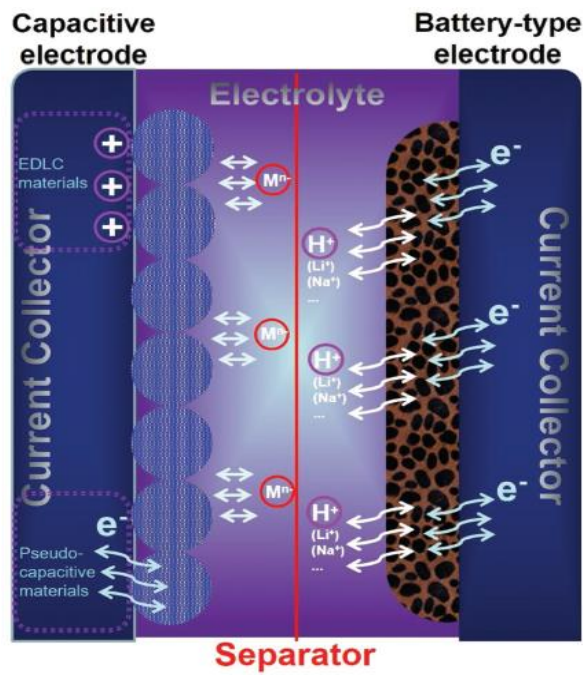


Figure 2.3: General design of a supercapattery.

A general and comprehensive approach to classify hybrids of batteries and supercapacitors involving combinations of electrode materials and combinations of whole battery and supercapacitors devices is illustrated in Figure 2.4, as designed by Dubal *et al.*, [14]. Specific challenges associated with either battery or supercapacitor devices can be addressed by proper design of a hybrid device.

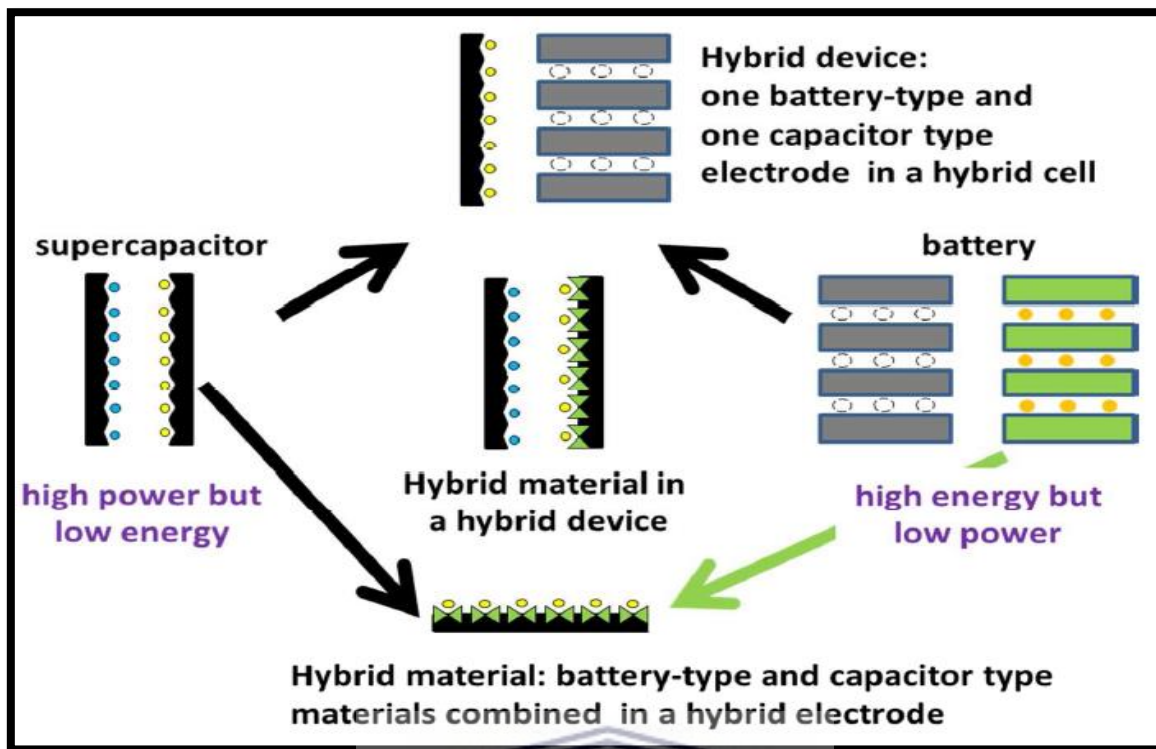


Figure 2.4: Different hybridization approaches between battery and supercapacitor-type electrodes and materials.



2.3.3. Mechanism of energy storage in supercapatteries

The mechanism of charge storage in electrical energy storage systems defines the fundamental basis on which the devices are developed and their resulting applications. In general, electrical charge can be stored depending on three main mechanisms (shown in Figure 2.5) on the surface and/or the bulk of the electrode materials namely, double-layer charging, non-capacitive faradaic charge storage (Nernstian) and capacitive faradaic charge storage (pseudocapacitive) mechanisms [19].

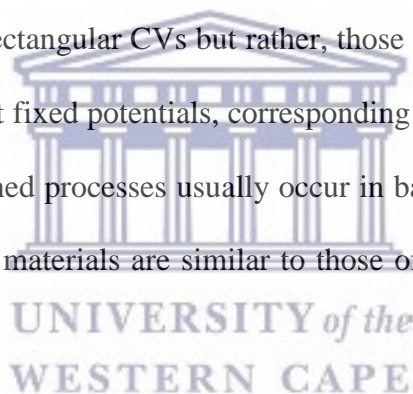
2.3.3a. Non-faradaic capacitive charge storage

Fundamentally, the EDL charge storage results from the accumulation or adsorption of charges at the electrode/electrolyte interface based on electrostatic and non-faradaic processes. Although charge storage in EDLCs is the same as that in traditional electrolytic capacitors, the high surface area and porosity of active electrode materials, for instance, activated carbon, increases the capacitance. However, the high porosity and surface area of activated carbon at some point renders it weaker and less conducting resulting in lower capacitance output $\sim 100 \text{ Fg}^{-1}$, which is the lower limit for the calculated capacitance range ($100 \text{ Fg}^{-1} - 300 \text{ Fg}^{-1}$) for activated carbon. Carbon nanotubes and three-dimensional structures such as graphene with EDLC charge storage with curved surfaces instead of the flat shape of carbon, benefit from the sp^2 carbon hybridization within the framework and electron conduction channels which yield larger adsorption surfaces and higher capacitance values up to 550 Fg^{-1} [20]. Apart for the curved surface of these nanomaterials, the 3D nature of the sp^2 carbon materials also influence the capacitance performance at the microscale, which is the main difference between EDLCs and traditional electrolytic capacitors [20,21].

2.3.3b. Capacitive faradaic charge storage (pseudocapacitive)

In principle, the faradaic process results from the transfer of valence electrons across ions or molecules at the electrode-electrolyte interface known as the Nernstian process, due to its dependence on the Nernstian equation. For charge storage in a faradaic process, huge pseudocapacitance arises from electrosorption of ions accompanied by surface reduction and oxidation processes with the transfer of electrons across the current collector and active

material [19,22]. However, both EDLCs and pseudocapacitors with capacitive charge storage experimentally offer rectangular-shaped cyclic voltammograms (CV) and linear or triangular-shaped galvanostatic charge-discharge (GCD) profiles. As explained by the band theory, the rectangular CVs and triangular GCD in pseudocapacitive materials with capacitive faradaic charge storage develop from the transfer of delocalised valence electrons which spread over a large range of energy levels as well as potentials [22]. This commonly occurs in many semiconductor materials such as transition metal oxides like RuO₂, MnO₂, SnO₂, and electronically conducting polymers such as polyaniline, polypyrrole and poly(3,4-ethylene dioxathiophene). The specific capacitance of such electrodes is usually greater than that obtained from EDLC carbon-based materials. However, the Nernstian equation cannot predict these faradaic processes with rectangular CVs but rather, those occurring through the transfer of localised valence electrons at fixed potentials, corresponding to peak-shaped CVs and non-linear GCDs. The aforementioned processes usually occur in battery electrodes whereby, the valence electrons of the active materials are similar to those of the ions or molecules in the electrolyte [23].



2.3.3c. Non-capacitive faradaic charge storage (Nernstian)

Charge storage in battery electrodes is characterised by non-capacitive faradaic processes due to the transfer of localised valence electrons within fixed energy levels which correspond to a distinctive electrode potential (E°) giving rise to peak-shaped CVs. This faradaic process is described by the Nernst equation (Equation 2.1) in terms of the mole fraction, x , of the reduced sites on the electrode surface [24,25].

$$E = E^{\circ} + \frac{nF}{RT} \ln\left(\frac{1-x}{x}\right) \quad (2.1)$$

If the process occurs under Nernstian conditions with reversible participation of the electrode material in the redox process, the theoretical charge capacity of the electrode can be expressed in terms of the Faraday equation (Equation 2.2).

$$Q_M = \frac{nF}{M} \quad (2.2)$$

Where Q is the Faradaic charge, n is the number of electrons transferred, F the Faraday constant (96485 C g⁻¹) and M the molar mass of the electrode material.

The various charge storage mechanisms as well as the electronic states of the electrode materials are illustrated in Figures 2.5 and 2.6.

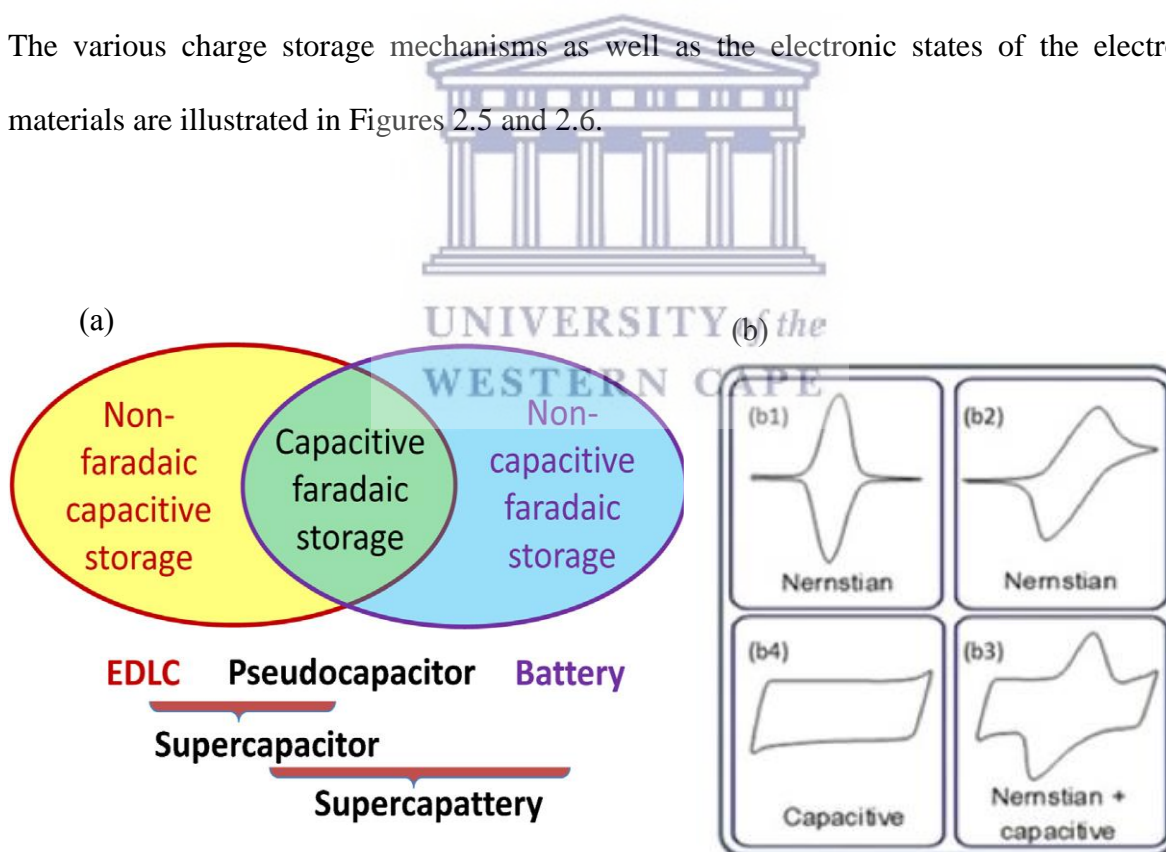


Figure 2.5: Scheme demonstrating similarities between capacitive and faradaic charge storage in EDL capacitor, pseudocapacitor, battery and supercapattery (a) [19], Voltammetric

representation of Nernstian (b1, b2), mixed Nernstian and capacitive (b3) and capacitive (b4) charge storage mechanisms (b).

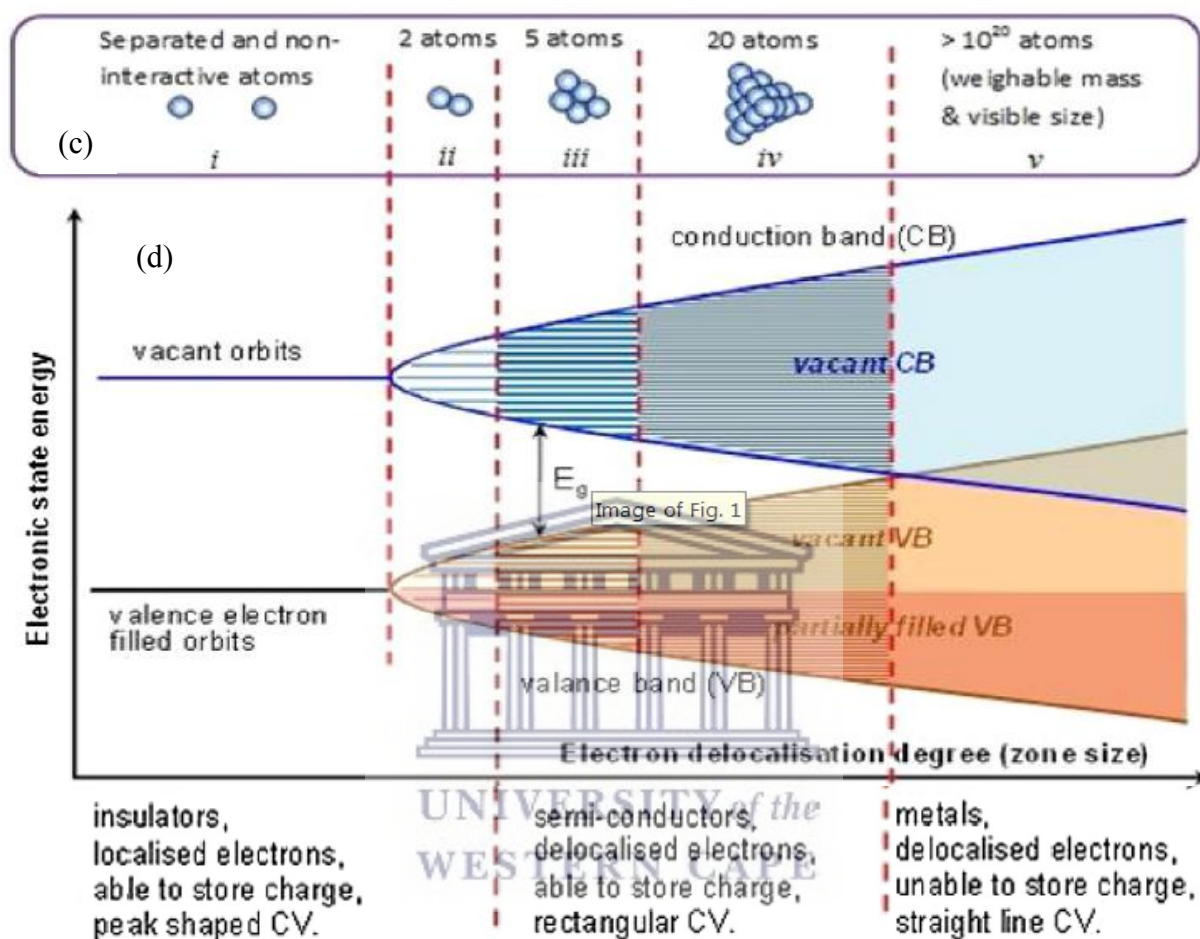


Figure 2.6: Outline of the band model for chemical bonding between metal atoms (c); that are separated and non-interactive (i), and forming clusters of 2 (ii), 5 (iii), 20 (iv) and 10²⁰ atoms (v). Energy levels of the valence electrons as a function of the degree (or zone size) of delocalisation of valence electrons in the respective clusters of metal atoms (d) [22,25].

2.4. Measurement of key performance parameters

The electrochemical performance of electrical energy storage devices are generally evaluated based on three critical parameters: voltage, current and time. These parameters are usually obtained using electrochemical techniques such as cyclic voltammetry (CV), galvanostatic charge-discharge (GCD) or constant current charge-discharge (CCCD) and electrochemical impedance spectroscopy. Other parameters such as operating potential window, cell capacitance/capacity (C), energy and power density and equivalent series resistance (ESR) can be obtained from the three key parameters. Additional tests such as cycling stability, capacitance/capacity retention, coulombic efficiency and time constant also shed more light on the electrochemical performance of the energy storage device [26,27].

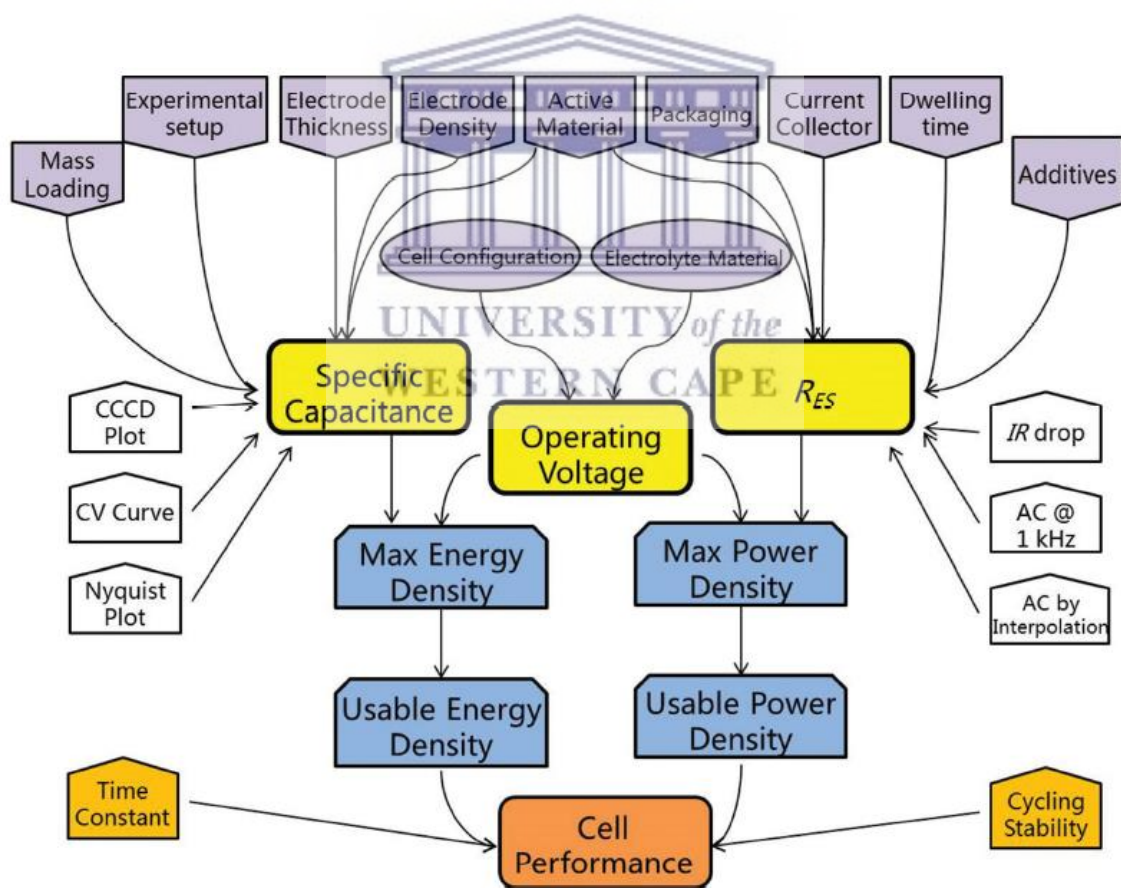


Figure 2.7: Scheme showing key performance parameters, characterisation techniques and factors affecting the evaluation of supercapacitors [27].

2.4.1 Capacitance

The total charge storage capability of a supercapattery device is determined by the total capacitance (C_T) of the cell. C_T is defined as the electrical charge ΔQ stored measured in ampere seconds at a defined voltage change ΔV in volts.

$$C_T = \frac{\Delta Q}{\Delta V} \quad (2.3)$$

The charge storage ability of a supercapattery material is given by a more intrinsic quantity, specific capacitance (C_{sp}), defined as the capacitance per unit mass, volume or area of the active material or the whole device. The ensuing capacitance is either termed as gravimetric ($F g^{-1}$), volumetric ($F cm^{-3}$) or areal ($F cm^{-2}$) capacitance.

$$C_{sp} = \frac{\Delta Q}{\Delta V_x} \quad (2.4)$$



Where x is either the mass, volume or area of the electrode material or device.

C_{sp} is the most informative way to describe the charge storage ability of a material and it's considered the most important parameter to characterise supercapacitor/supercapattery materials.

The cell capacitance can be evaluated from cyclic voltammetry, galvanostatic charge-discharge test and electrochemical impedance spectroscopy according to Equations 2.5, 2.6 and 2.7, respectively [26,27].

$$C_{sp} = \frac{1}{2\nu\Delta V_x} \int_{-v}^{+v} Idv \quad (2.5)$$

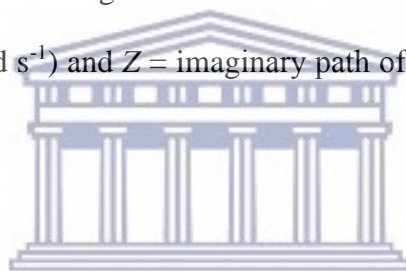
$$C_{sp} = \frac{I \Delta t}{(\Delta V - IR_{drop}) x} \quad (2.6)$$

$$C_T = \frac{-1}{\omega Z^n} \quad (2.7)$$

Where, x = the mass, volume or surface area of the material or device, v = scan rate ($V s^{-1}$),

$\int_{-v}^{+v} Idv$ = absolute area under the cyclic voltammogram (ΔV), I = constant current (A), Δt =

charge/discharge time (s), IR_{drop} = voltage variation at the initial stage of the discharging curve (V), ω = angular frequency ($rad s^{-1}$) and Z = imaginary path of impedance (Ω) obtained from the Nyquist plot.



UNIVERSITY of the
WESTERN CAPE

2.4.2 Energy and Power

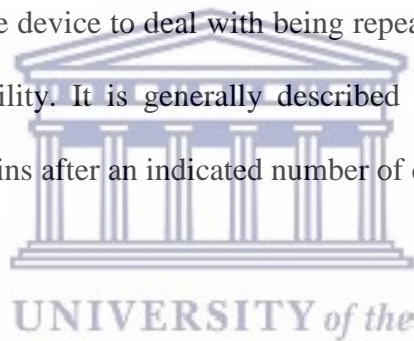
Energy and power stored/delivered are important aspects used to evaluate the performance of various energy storage and conversion devices. The Ragone plot illustrated in Figure 2.2 is used to express the relationship between these quantities. They are either measured gravimetrically in the case of specific energy ($W h kg^{-1}$) and specific power ($W kg^{-1}$), or volumetrically/area based for energy density ($W h L^{-1} / W h cm^{-2}$) and power density ($W L^{-1} / W cm^{-2}$). The specific energy or energy density is the amount of energy stored per unit mass or volume/area of the active electrode material or device, evaluated using Equation 2.8. Specific power or power density refers to the amount of power a device can deliver per unit mass or volume/area of the electrode active material or whole device as described by Equation 2.9.

$$E = \frac{1}{2} C_{sp} \times \Delta V^2 \times \frac{1}{3.6} \quad (2.8)$$

$$P = \frac{E}{\Delta t} \times 3600 \quad (2.9)$$

2.4.3 Cycle Stability and capacitance retention

The ability of an energy storage device to deal with being repeatedly charged and discharged is described by its cycle stability. It is generally described as a percentile of the initial capacitance that the device retains after an indicated number of cycles.



2.5. Recent advances in materials and performance of supercapattery electrodes

With increasing pursuits of high energy hybrid supercapacitors without compromising their high power and long cycle life, recent research efforts have been devoted to advancing electrode materials by combining battery and supercapacitor chemistries, creating new reaction mechanisms with faster charge-discharge and high rate performance. Supercapatteries are hybrid systems which range from ion capacitors (Li/Na) to asymmetric supercapacitors. Different capacitive (with non-faradaic and faradaic charge storage) and battery-type electrode combinations have been employed, with ion adsorbing/desorbing on one electrode surface and charge transfer reactions with Li^+/Na^+ intercalation/deintercalation in the bulk of the other.

The capacitive-type electrode materials with non-faradaic charge storage (EDLCs) commonly used in hybrid systems are carbonaceous materials (activated carbon, carbon nanotubes and graphene). Among these materials, activated carbon is the most widely used due to its simpler production methods, high surface area and satisfactory electrical conductivity. Graphene is also widely investigated due to its high conductivity, high electron mobility and strong chemical stability with large surface area. However, graphene suffers from a degree of irreversible agglomeration of the thin sheets due to high π - π stacking and van der Waals interactions which lead to a decrease in its surface area, thus limiting its high rate applications [28].

Transition metal oxides (TMOs) are actively studied as redox and intercalation pseudocapacitive electrodes employing faradaic charge storage mechanisms. Examples of TMOs include RuO_2 , Co_3O_4 , MnO_2 , NiO , V_2O_5 and mixed transition metal spinels like Fe_3O_4 , MnFe_2O_4 , NiCo_2O_4 and CuCo_2O_4 . These materials have been extensively reviewed by Augustyn's [29] and Yan's [30] groups. The TMOs exhibit the widest range of materials with pseudocapacitance due to their ability to undergo multiple oxidation/reduction reactions with change in oxidation states of the metal ion. By carefully selecting the TMOs with proper architectures and investigating their electrochemical performance, such materials are expected to become the basis for high rate electrochemical energy storage devices. Even though the pseudocapacitor materials show superior electrochemical performance, the high cost of some of these materials, for example, Ru in ruthenium oxide supercapacitor systems, substantially limits their commercial usage and cost-effective materials with high energy densities and better rate capability become the point of focus. Lately, V_2O_5 [31] has been explored as a suitable pseudocapacitor material for supercapacitors among others metal oxides like NiO [32], Fe_2O_3 [33] and metal phosphates such as $\text{Co}_3(\text{PO}_4)_2$ [34,35] due to the low cost, comparable charge storage capacity and its good catalytic activity.

Battery-type electrodes consist of Li^+/Na^+ intercalation materials usually used as positive electrodes in batteries and conversion-type materials studied as negative electrodes in batteries. Conversion-type electrode materials such as transition metal fluorides (FeF_3 , NiF_2), oxides (Fe_2O_3 , MnO) and phosphides (NiP_2), rely on multi-electron reversible redox reactions by continuous lithium/sodium intercalation and phase transformation reactions. The intercalation-types involve the electrochemical redox reactions of Li^+/Na^+ and electrolyte ions such as H^+ , OH^- , ClO_4^- , NO_3^- and SO_4^{2-} . The Li^+/Na^+ intercalation electrodes include layered oxides (LiCoO_2), spinels (LiMn_2O_4), metal phosphates (LiFePO_4 , LiMnPO_4) and metal silicates ($\text{Li}_2\text{MnSiO}_4$, $\text{Na}_2\text{MnSiO}_4$, LiFeSiO_4). In these materials, the charge transfer kinetics are controlled by ion diffusion processes occurring in the bulk of the materials resulting in slower kinetics and unsatisfactory rate performance. A recent review by Tie *et al.*, [36] reports on the extrinsic pseudocapacitance behaviour of battery-type electrodes, indicating that the rate performance of these materials can be modified by structural regulations. That is, battery-type materials exhibit varying degrees of capacitance characteristics when the material size is down to the nanoscale or with specific nanostructures. Many researchers have reported the fabrication of supercapacitor-battery hybrid devices using battery materials as either the positive or negative electrode. The battery-type electrodes mostly used include LiMn_2O_4 [37], Li_xMnO_2 [18], LiMnPO_4 [17], $\text{LiNi}_{1/3}\text{Mn}_{1/3}\text{Co}_{1/3}\text{O}_2$ [38], LiFePO_4 [39], $\text{Na}_4\text{Mn}_9\text{O}_{18}$ [40], $\text{Li}_2\text{FeSiO}_4$ [41] and $\text{Li}_2\text{MnSiO}_4$ [42,43]. Among them, the silicate-based electrode materials (Li_2MSiO_4 , $\text{M} = \text{Mn, Fe}$) offer more prospects due to their intrinsic stability, natural abundance and the possibility of the extraction of more than one Li^+ ion per formula unit which results in high electrochemical performance.

2.5.1. Activated carbon (AC)

Activated carbon is produced generally through physical or chemical activation of various types of carbonaceous materials like wood, coal or nutshells. Physical activation involves treatment of carbon precursors at high temperatures (700-1200 °C) in the presence of oxidizing gases like steam, CO₂ and air. Whereas, chemical activation is performed at lower temperatures (400-700 °C) and activating agents such as potassium hydroxide, sodium hydroxide, zinc chloride as well as phosphoric acid are used [44,45]. By careful selection of the activating agent and the carbonaceous precursor, AC with different morphologies such as powders, monoliths and fibres have been obtain with specific surface areas of up to 3000 m²/g. A number of reviews are available on the electrochemical performance of AC, where AC is reported to deliver higher specific capacitance in aqueous electrolytes (ranging from 100 to 300 F g⁻¹) over organic electrolytes (<150 F g⁻¹) [45,46].

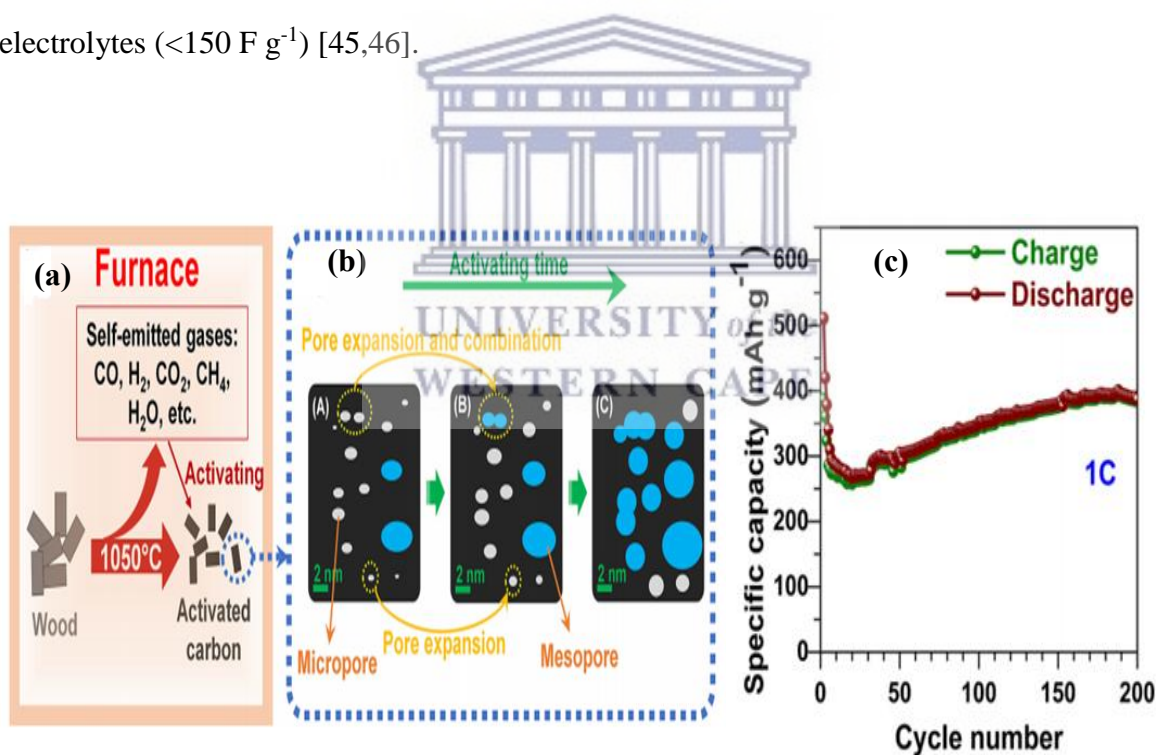


Figure 2.8: physical activation of AC from wood (a), changes in pore size with activation time and electrochemical performance of AC negative electrode (b) [47].

2.5.2. Doped Graphenes (Hydroxylated graphene- Graphol)

Graphene, a zero-gap semiconductor with a two-dimensional layer of sp² hybridized carbon atoms arranged in a hexagonal crystalline structure, has attracted wide research attention in recent years. The interest in graphene stems from its excellent physicochemical properties such as astounding surface area, high mechanical strength, high electrochemical stability and exceptional electrical conductivity. These appealing properties enable its applications in various technological domains ranging from lightweight to flexible energy storage systems, Photovoltaics, biomedical and environmental applications [48,49], as shown in Figure 2.9.



Figure 2.9: Recent developments and applications of graphene and graphene-based composites [48].

Graphene exhibits attractive capacitive performance. For instance, the intrinsic capacitance of single-layer graphene can amount to 550 F g⁻¹, which sets an upper limit for carbon-based

materials. However, graphene is hydrophobic and thus insoluble in water and polar solvents, which can cause it to restack irreversibly back to graphite [50,51]. This logically hinders its production, storage and further restricts improvement of most of its applications. To address this, researchers have developed strategies to manipulate the structure of graphene by either chemical functionalization or cutting graphene into nanoribbons or quantum dots. Chemical functionalization stands out from others due to the profound theoretical support from chemistry and several reaction routes [50,52,53]. Chemical functionalization of graphene by doping with elements such as P-block elements (nitrogen, boron, sulphur, hydrogen, oxygen and fluorine) rearranges its planar structure by introducing other elements that alter its electronic properties. In spite of this, the modifications have subsequently widened the applications of graphene and its derivatives in various technological systems [54].

Gong *et al.*, prepared hydroxyl functionalized graphene (graphol) by a systematic substitution of fluorine atoms with hydroxyl groups through an oxofluorinated graphene (OFG) intermediate according to Figure 2.10 [53]. Fluorinated graphene (FG) was obtained from liquid exfoliation of commercially available fluorinated graphite in N-methyl-2-pyrrolidone. The mechanism of formation of graphol (G-ol) from FG is shown by Equation 2.10, Where R_3C represents graphene subunits.

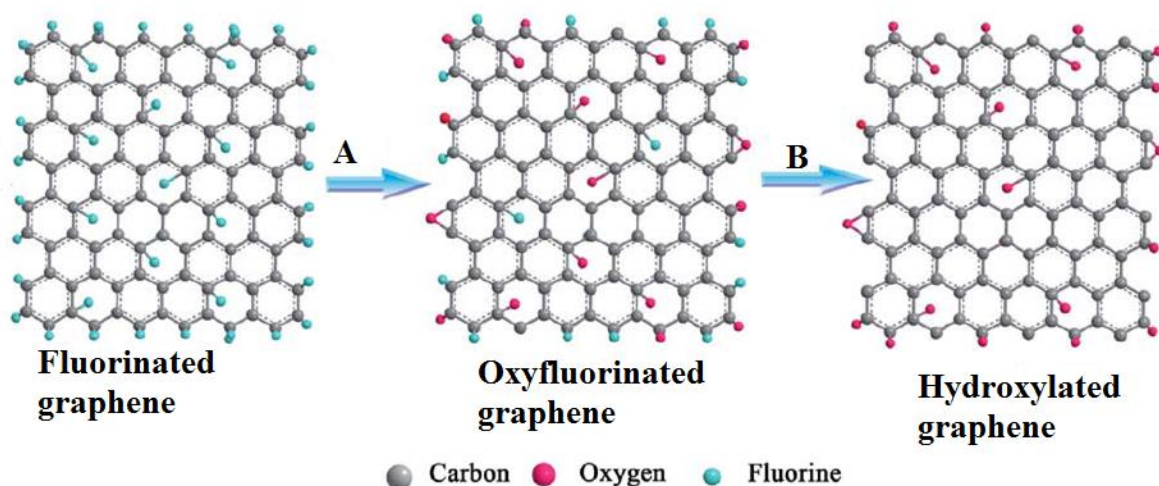


Figure 2.10: Synthesis route of hydroxylated graphene; A- Formation of oxyfluorinated graphene via hydroxyl substitution of fluorine atoms, B-Further substitution to graphol [53].



The formation of graphol via substitution of hydrophobic fluorine atoms with hydrophilic hydroxyl groups not only initiates new grounds for the application of graphene and FG, but enhances the fluorescent potentials of the materials by opening the band gap and modifying the dispersivity.

Poh *et al.*, reported on chemical functionalization of graphene with hydroxyl groups with the formation of stoichiometric graphol composition as shown in Figure 2.11 [55]. This was achieved through hydroboration of graphene oxide to an alkyl borane and subsequent oxidation in peroxide and sodium hydroxide to stoichiometric graphol ($\text{C}_1\text{O}_{0.78}\text{H}_{0.75}$)_n. Graphol in this study was tested for the electrochemical detection of biomarkers and hydrogen evolution reaction. Graphol demonstrated high catalytic properties towards hydrogen evolution reaction.

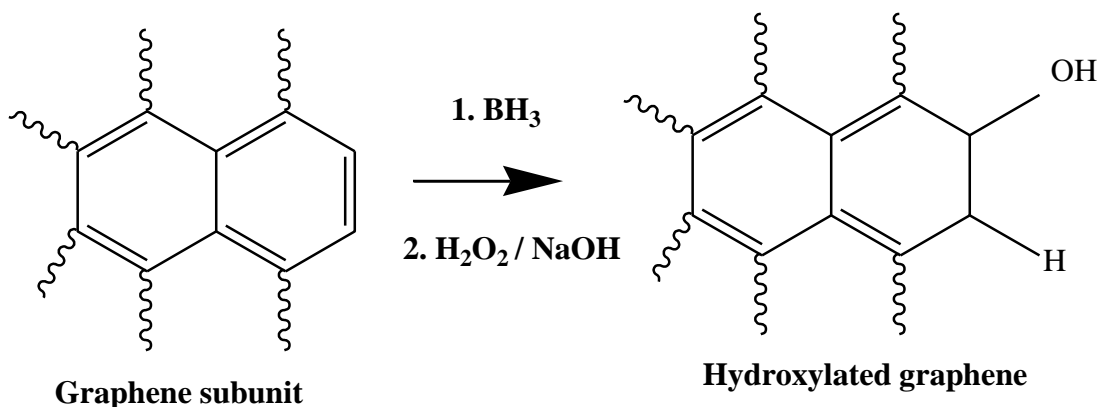


Figure 2.11: Formation of hydroxylated graphene (graphol) through hydroboration [55].

Manthiram and Zu prepared hydroxylated graphene-sulphur nanocomposites with a sponge-like morphology through a combination of ultrasonication and hydrothermal synthesis [52]. The nanocomposite exhibited high rate performance as cathode materials for lithium-sulfur batteries. The sponge-like morphology enabled good electrolyte penetration and feasibly absorbed volume changes induced by cycling.

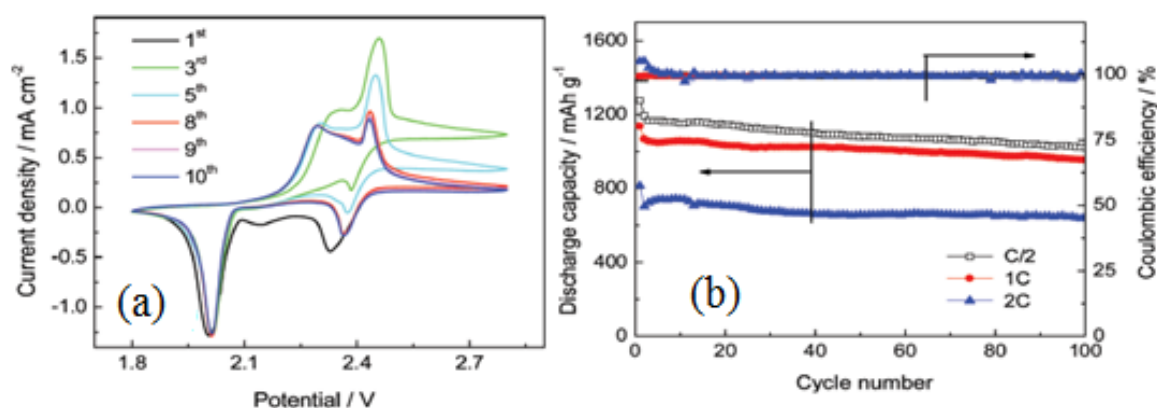


Figure 2.12: Electrochemical characterisation of hydroxylated graphene-sulfur nanocomposites: cyclic voltammograms of the Li-S cell with nanocomposite as cathode (a), cyclic performance of the Li-S cell (c) [52].

Recently, Ding *et al.*, reported on surface hydroxylated graphene sheets prepared by molten hydroxide-assisted exfoliation of natural graphite [56]. This method yielded highly flexible hydroxylated graphene sheets with high thermal and electrical conductivity. The hydroxylated graphene sheets exhibited super flexibility with up to 3000 bending and folding cycles.

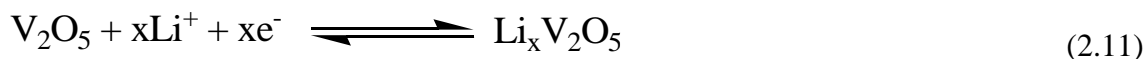
2.5.3. Carbon nanotubes (CNTs)

Carbon nanotubes have been extensively studied since their discovery in the early 1990s due to their distinctive structure and outstanding electronic properties. CNTs can be described as nanoscale concentric cylinders of graphene with closed ends. Structures consisting of one cylinder are known as single-walled carbon nanotubes (SWCNTs), while those with two or more concentric cylinders are considered as multi-walled carbon nanotubes (MWCNTs). SWCNTs depending on how the graphene sheets are rolled up can have either the zigzag, armchair or chiral crystallographic configuration, and thus exhibits metallic or semiconducting behaviour based on the configuration. MWCNTs show metallic properties where electrical conductivity is through the outermost shell. Catalytic chemical vapour deposition is widely used by researchers to produce CNTs with various configurations [57,58]. Even though CNTs are 10^5 times thinner than human air, they exhibit extraordinary aspect ratios (can grow to several centimetres long) with high flexibility and mechanical strength (tensile strength up to 100 GPa) [59]. Both SWCNTs and MWCNTS are investigated as electrode materials in energy storage devices such as Li-ion batteries and supercapacitors. The specific capacitance of CNTs is affected by the purity and morphology. Purified CNTs are reported to deliver specific capacitance in the range of 15 to 80 F g⁻¹ with surface areas between 120 to 400 m² g⁻¹ [60]. The capacitance and energy density of CNT based materials is limited by the density of CNTs.

Thus, research efforts are focused on developing CNT composite materials to enhance their electrochemical performance.

2.5.4. Vanadium pentoxide (V₂O₅)

V₂O₅ is a typical intercalation compound, explored as a promising electrode material for Li-ion batteries and supercapacitors due to its wide availability, ease of preparation and rich structural chemistry. Besides, the variable electrochemically accessible oxidation states of vanadium offer the possibility of storing more than one Li⁺ ion per formula unit leading to high capacity. V₂O₅ has a layered structure and orthorhombic unit cell made up of bilayers of VO₅ square pyramids which share corners and edges to form zigzag chains as shown in Figure 2.11 [61]. The layers are bonded by weak van der Waals forces between vanadium and oxygen of the neighbouring pyramid [62]. The open-layered structure of V₂O₅ makes it a good host for reversible intercalation/ de-intercalation of Li⁺ ions into the interlayer space, offering the potential for it to store more Li⁺ ions than other intercalation compounds. The mechanism of charge storage in V₂O₅ (intercalation reaction) is based on the reversible insertion/ de-insertion of Li⁺ ion into the host structure, depicted by Equation 2.11.



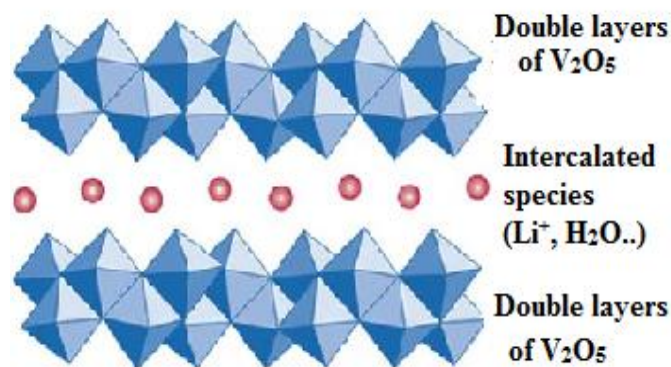


Figure 2.13: Crystal structure of V_2O_5

The amount of Li^+ inserted determines the phase of $Li_xV_2O_5$ formed. For the formation of the α -phase of $Li_xV_2O_5$ ($x < 0.01$), ϵ -phase ($0.35 < x < 0.7$), δ -phase ($0.7 < x < 1$) and γ -phase ($1 < x < 2$) [63]. A rock salt-type structure and irreversible ω -phase is formed when further lithiation ($2 < x < 3$) occurs after formation of the γ -phase [63,64]. The calculated theoretical capacity of V_2O_5 is at 147 mA h g^{-1} when one mole of Li^+ ion is intercalated/ de-intercalated, 294 mA h g^{-1} for two moles and as high as 442 mA h g^{-1} when three moles of Li^+ ions are inserted/extracted [61,65]. However, the practical application of V_2O_5 is restricted by low electronic conductivity and Li^+ ion diffusion coefficient, which lower the kinetics of Li^+ ion and electron transport, resulting in low rate performance. Hence, values of the specific capacity /capacitance obtained experimental vary considerably with V_2O_5 particle size and morphology. Nanotechnology has open limitless opportunities in material science including based V_2O_5 -electrode materials. It is reported that employing nano-morphologies significantly improves the electrochemical performance due to shorter ion and electron transport distances as well as high packing density and high active-area exposure to electrolyte. Various V_2O_5 nanostructures such as nanoparticles [66], nanorods [67], nanowires [68], nanobelts [69] and nanocomposites with carbon-based materials such as conducting polymers, carbon black, graphene and carbon

nanotubes [70–72] have been prepared to boost the electrochemical performance. A range of synthetic protocols have also been employed to prepare thin films of V₂O₅, which are reported in literature. These include: Hydrothermal, sol-gel, solvothermal, electrospinning, electrochemical deposition and electron beam evaporation. It is well understood that the method of synthesis influences the architecture of nanomaterials produced as well as their performance in various applications [64,73]. Zhang *et al.*, prepared three dissimilar morphologies of V₂O₅ including nanobelts, nanoparticles and microspheres through hydrothermal synthesis and the nanostructures were investigated as electrodes for supercapacitors [73]. The electrodes delivered good electrochemical performance with the microspheres offering maximum specific capacitance of 238 F g⁻¹, over nanoparticles with 208 F g⁻¹ and nanobelts with 129 F g⁻¹. Zheng *et al.*, reported on mesoporous V₂O₅ flakes with average pore sizes of 28.66 nm prepared by crystallization of aqueous ammonium metavanadate (NH₄VO₃) and subsequent calcination in air according to Equation 2.12 [74].



The material delivered high specific capacitance of 510 F g⁻¹ at a current density of 0.2 A g⁻¹ when investigated as a battery-type electrode for supercapacitors. A capacitance retention of 110 % was obtained after 1000 cycles in [74]. More recently, Bai and co-workers prepared 3D hierarchical porous structure of V₂O₅/holey graphene hybrid electrode by hydrothermal synthesis using holey graphene oxide (HRGO) nanosheets, acetic acid and NH₄VO₃, forming an interconnected and stable 3D porous network. The hybrid electrode exhibited high specific capacitance of 264 F g⁻¹ at a current density of 0.25 A g⁻¹ in 0.5 M K₂SO₄ aqueous electrolyte with a capacitance retention of 85 % after 1000 cycles. The high specific capacitance delivered was reported to be due to electronic conduction channels provided by HRGO nanosheets, the

3D hierarchical porous structure which shortened the diffusion length of electrolyte ions as well as V_2O_5 nanobelts which provided large interstitial spaces for free transport of electrolyte ions and numerous active sites for electrochemical reaction [75].

Table 2.2 displays the comparison of the electrochemical performance of V_2O_5 -based electrode materials with respect to the method of synthesis, particle morphology and size, electrolyte, potential window, capacitance and cyclic stability reported in literature.

Table 2.2: Synthesis methods, morphology, size of particle and electrochemical properties of V_2O_5 - based electrodes reported in literature.

Method	Morphology, size	Electrolyte	Potential window / V	Specific Capacitance / Current density	Capacitance retention	Ref
Sol-gel	V_2O_5 -N- CNFs Core/shell	1 M Na_2SO_4	-1.0 – 1.0	595.1 $F g^{-1}$ @ 0.5 $A g^{-1}$	97 % @ 12000 cycles	[76]
Hydrothermal	V_2O_5 -Ni hollow spheres (300 – 500 nm)	1 M $LiClO_4$ in propylene carbonate	-0.4 – 1.0	135 $F g^{-1}$ @ 0.5 mA g^{-1}	51 % @ 5000 cycles	[77]
	V_2O_5 -W nanobelts	1 M $LiNO_3$	-0.5 – 0.6	407 $F g^{-1}$ @ 0.5 $A g^{-1}$	-	[78]
	2D V_2O_5 /CNTs -SAC	2 M $NaNO_3$	0 – 0.8	357.5 $F g^{-1}$ @ 10 $A g^{-1}$	99.5 % @ 1000 cycles	[71]
	V_2O_5 /N- mesoporous C- spheres			0 – 1.0	487 $F g^{-1}$ @ 0.5 $A g^{-1}$	84 % @ 2000 cycles

	V ₂ O ₅ nanorods-G-popyrole	1 M KCl	0 – 0.8	787 F g ⁻¹ @ 1 A g ⁻¹	78.7 % @ 5000 cycles	[80]
	V ₂ O ₅ nanowires (50 nm)	1 M LiNO ₃	-0.4 – 0.8	351 F g ⁻¹ @ 2 A g ⁻¹	15 % @ 50 cycles	[81]
	3D V ₂ O ₅ /G aerogel	1 M LiClO ₄ in propylene carbonate	-0.8 – 0.8	384 F g ⁻¹ @ 0.1 A g ⁻¹	82.2 % @ 10000 cycles	[82]
Chemical bath decomposition	V ₂ O ₅ intermixed flakes	2 M LiClO ₄	0 – 1.0	222 F g ⁻¹ @ 1 A g ⁻¹	88 % @ 1000 cycles	[83]
Wet spinning	V ₂ O ₅ /SWCNT fiber	PVA-H ₃ PO ₄ gel	0 - 0.8	6.3 F cm ⁻³ @ 10 mA cm ⁻³	90 % @ 3000 cycles	[84]
	V ₂ O ₅ hollow spheres	5 M LiNO ₃	-0.2 – 0.8	559 F g ⁻¹ @ 3 A g ⁻¹	70 % @ 100 cycles	[85]
Solvothermal	3D V ₂ O ₅ nanocorals (50 – 150 nm)	1 M NaNO ₃	0 – 1.0	414 F g ⁻¹ @ 0.3 A g ⁻¹	70 % @ 3000 cycles	[86]

These studies revealed that optimization of a variety of factors such as electrode morphology and size, temperature of annealing of the V₂O₅ particles along with electrolyte characteristics considerably affect the electrochemical behaviour of the electrode.

2.5.5. Lithium manganese silicate (Li₂MnSiO₄)

Lithium transition metal orthosilicates (Li_2MSiO_4 , $\text{M} = \text{Mn, Fe, Co, Ni}$) were proposed in 2002 as alternative and competitive electrode materials for next generation lithium ion batteries, alongside other polyanionic compounds such as phosphates to replace lithium transition metal oxide electrodes. This was motivated by the relative availability and environmental friendliness of metals such as Fe, Mn, and the strong covalent bonds between oxygen and metal ions resulting in high chemical stability towards the electrolyte [87,88]. Remarkably, Li_2MSiO_4 electrodes are more attractive due to the possibility to extract more than one lithium ion per transition metal, resulting in high theoretical capacities of about 333 mA h g^{-1} . Conversely, LiFePO_4 is limited due to the fact that only one lithium ion is extracted from the host with a theoretical capacity up to 170 mA h g^{-1} [89,90].

The electrochemical potential of lithium insertion and extraction in electrodes is calculated based a two electron process and illustrated by Equations 2.13 and 2.14.



The electrochemical potential in Equation 2.13 and 2.14 vary with the transition metal ion. Among the orthosilicate family of electrode materials, $\text{Li}_2\text{MnSiO}_4$ drawn more attention since both lithium ions in each formula unit could potentially be extracted at moderate voltages, resulting in a high theoretical capacity of 333 mA h g^{-1} . This process possibly employs both the $\text{Mn}^{2+}/^{3+}$ and $\text{Mn}^{3+}/^{4+}$ redox couples for the extraction/insertion of the first and second lithium ions respectively. Even though it is also theoretically possible for the Fe and Co counterparts, in the case of Fe and Co, the $\text{Fe}^{3+}/^{4+}$ and $\text{Co}^{3+}/^{4+}$ couples are predicted to be outside the voltage stability window of common electrolytes [90,91] as shown by Figure 2.14.

Even though $\text{Li}_2\text{MnSiO}_4$ demonstrates huge potential as a high capacity cathode material for lithium-ion batteries, drawbacks such as co-existence of impure phases, low electronic conductivity, and poor cycle performance, hinder its extensive applications in electric vehicles (EVs) and hybrid electric vehicles (HEVs).

$\text{Li}_2\text{MnSiO}_4$, as well as the Fe and Co analogues, are iso-structural with tetrahedral lithiophosphate (Li_3PO_4) exhibiting wide polymorphism. Its crystal structure consists of distorted hexagonal close-packed oxygen ions with half tetrahedral sites occupied by Li, M and Si cations.

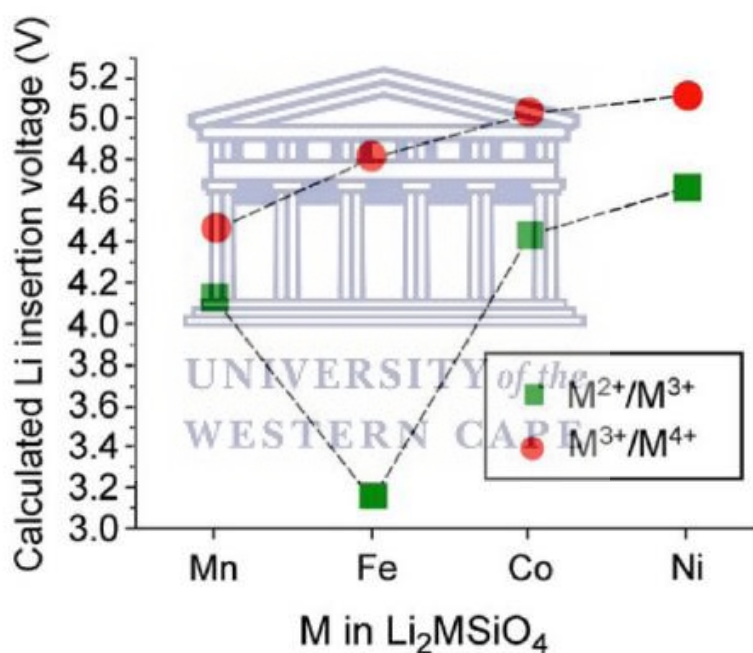


Figure 2.14: Comparison of Li insertion voltage of $\text{M}^{2+}/\text{M}^{3+}$ and $\text{M}^{3+}/\text{M}^{4+}$ redox couples in Li_2MSiO_4 [91].

$\text{Li}_2\text{MnSiO}_4$ exhibits four different structural forms which differ in the arrangement of the tetrahedra. Namely the low-temperature orthorhombic $\text{Pmn}2_1$ and Pmnb forms and the high-

temperature monoclinic $P2_1/n$ and Pn forms. The orthorhombic forms ($Pmn2_1$ and $Pmnb$) have two-dimensional pathways for Li-ion diffusion while the monoclinic forms ($P2_1/n$ and Pn) are framework structures with Li-ion positions interconnected in three dimensions with Si cations. Figure 2.15 displays the crystal structure of the orthorhombic and monoclinic forms of Li_2MnSiO_4 . Mn tetrahedra are denoted by purple, Li sites by green, Si tetrahedra by blue while the red spheres represent oxygen atoms [92,93].

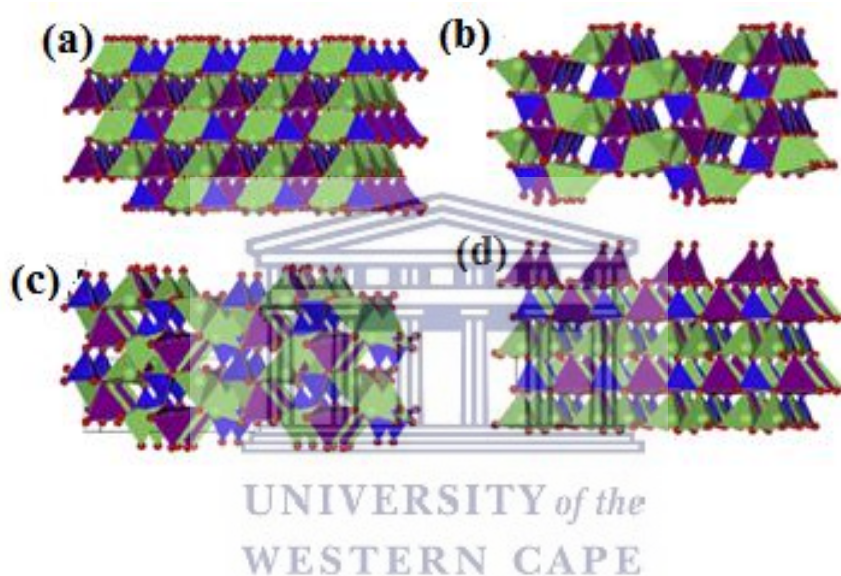


Figure 2.15: Crystal structures of the four orthorhombic and monoclinic polymorphs of Li_2MnSiO_4 : (a) $Pmn2_1$, (b) $Pmnb$, (c) $P2_1/n$ and (d) Pn space groups [92].

Literature studies have demonstrated that due to the variety of pathways of lithium-ion diffusion and the different interconnections of the Mn and Si tetrahedra within the crystal lattice of Li_2MnSiO_4 , the different polymorphs of Li_2MnSiO_4 deliver varying electrochemical performance [94–96].

Different methods of synthesis, structural modifications and use of conductive additives have been employed by researchers to circumvent the drawbacks of Li_2MnSiO_4 electrode material

and to optimise the physical and electrochemical performances. Strategies such as particle size reduction to achieve nanostructures, carbon coating (carbon films and graphene), doping with other metal ions (Mg, Ni, Ti, V, Al, Cr, Ca and La) have been reviewed by a number of researchers [92,97–99]. Carbon coating and nanosizing can improve the electronic conductivity, influence the Li⁺ ion diffusion coefficient and enable high contact area between electrode material particles and electrolyte. Doping with other metal ions can also modify the electrical properties of Li₂MnSiO₄ and further enhance its structural stability.

Table 2.3: Method of synthesis, physical and electrochemical properties of Li₂MnSiO₄- based electrodes reported in literature

Method	Morphology / size	Crystal system / Space group	Capacity / capacitance	Retention / %	Ref
Hydrothermal	Li ₂ MnSiO ₄ /c nanorods / 40–60 nm	Orthorhombic / Pmn2 ₁	275 mA h g ⁻¹ @ 8 mA g ⁻¹	76 @ 50 cycles	[100]
	Li ₂ MnSiO ₄ /Al ₂ O ₃ nanoparticles / 70 ± 3 nm	Orthorhombic / Pmn2 ₁	141.5 F g ⁻¹ @ 0.5 A g ⁻¹	93.6 % @ 100 cycles	[43]
	Li ₂ MnSiO ₄ nanoparticles / 25 nm	Orthorhombic / Pmn2 ₁	52.5 mA h g ⁻¹ @ 1.2 Ag ⁻¹	94 % @ 3300 cycles	[101]
	Li ₂ Mn _{0.85} Ti _{0.15} Si O ₄ nanoparticles / 40 nm	Orthorhombic / Pmn2 ₁	214 mA h g ⁻¹ @ 0.05C	72 % @ 30 cycles	[102]
Sonochemistry	Li _{2-x} Mn _{1-x} V _x SiO ₄ Nanoparticles	Orthorhombic / Pmn2 ₁	261 mA h g ⁻¹ 1	31.8 % @ 50 cycles	[103]

	Li ₂ MnSiO ₄ /C nanoparticles / 22.5 nm	Orthorhombic / Pmn2 ₁	260 mA h g ⁻¹ @ 16.5 mA g ⁻¹	32.5 % @ 50 cycles	[104]
Solvothermal	Li ₂ MnSiO ₄ Prism-shaped nanoplates	Orthorhombic / Pmn2 ₁	326.7 mA h g ⁻¹ @ 0.05 C	50.45 % @ 100 cycles	[95]
	Li _{2+x} MnSi _{1-x} Al _x O ₄ /C Nanoparticles / 7-11 nm	Orthorhombic / Pmn2 ₁	308 mA h g ⁻¹ @ 0.05 C	39 % @ 50 cycles	[105]
	Li ₂ MnSiO ₄ /RGO	Orthorhombic / Pmn2 ₁	210 mA h g ⁻¹	87 % @ 100 cycles	[106]
Ion exchange	Li ₂ MnSiO ₄ nanoparticles / 10 μm	Monoclinic / Pn	120 mA h g ⁻¹	51.6 % @ 50 cycles	[107]
Sol-gel	CNT/Li ₂ MnSiO ₄ /C core-shell nanotubes (70-100 nm,)	Orthorhombic / Pmn2 ₁	227 @ 0.2 C	69.6 @ 50 cycles	[108]
	Li ₂ MnSiO ₄ nanopartilces (40 ± 3 nm)	Monoclinic P2 ₁ /n	100 mA h g ⁻¹	65 % @ 10 cycles	[109]
	Cu-Li ₂ MnSiO ₄ -PANI nano hybrids (30-60 nm)	Orthorhombic / Pmn2 ₁	192 mA h g ⁻¹	63% @ 50 cycles	[110]

	C/Li ₂ MnSiO ₄ nanoparticles (14- 22 nm)	Orthorhombic / Pmn2 ₁	275 mA h g ⁻¹	-	[111]
Solid state	Li ₂ MnSiO ₄ /C core-shell nanoboxes	Orthorhombic / Pmn2 ₁	335 mA h g ⁻¹	65.7 % @ 50 cycles	[112]
	Li ₂ MnSiO ₄ agglomerated nanoparticles (50 μm)	Orthorhombic / Pmnb	230 mA h g ⁻¹	- 1 @20 mA g ⁻¹	[103]
	Li ₂ MnSiO ₄ nanoparticles	Orthorhombic / Pmn2 ₁	92 mA h g ⁻¹	69.2 % @ 10 cycles	[109]
Water in oil emulsion	Li ₂ Mn _{0.87(3)} SiO ₄ nanoparticles	Orthorhombic / Pmn2 ₁	170 mA h g ⁻¹	- 1 @20 mA g ⁻¹	[113]
In-situ template and polymer pyrolysis	Li ₂ MnSiO ₄ /C /15 nm	Orthorhombic / Pmn2 ₁	230 mA h g ⁻¹	81 % @ 100 cycles	[114]

It is clear from these studies that preparation of Li₂MnSiO₄ particles with the orthorhombic Pmn2₁ crystallographic phase has an advantage over obtaining other structural forms since it results in better electrochemical performance over polymorphs. The synthetic method and other physical conditions during material preparation also influence the morphology, size and

electrochemical performance of the electrode material. These studies will serve as important tools to facilitate the choice of methodologies employed in this study to design an electrode system with optimum performance.

2.5.6 Electrochemical Performance of reported Hybrid Energy Storage Devices (HESD)

In recent years, researcher's efforts to meet the high energy and power density requirements of high power electrical systems have led to the integration of batteries and supercapacitors chemistries to produce HESD known as supercapatteries, supercabatteries and Li-ion capacitors with one shadowing the limitation of the other. Battery electrodes contribute to the energy storage capability while the supercapacitor electrodes contributes to the power density advantage. In general, the energy density of HESD can exceed that of conventional supercapacitors due to the fast electrochemical kinetics of battery-type electrodes. The presence of the capacitive electrode and the advanced design of battery-type electrode could overcome the power density limitation of battery electrode. However, the huge capacity asymmetry may cause significantly depressed charge/discharge ability of the battery-type electrode, thereby limiting the energy density of the HESD [14,115].

The potential/voltage window and electrochemical performance of electrodes and HESD devices vary greatly among different electrolytes due to different electrochemical reactions and ion diffusion rates. The selection of proper electrolytes and electrodes working in separate potential windows to utilize the full capacitance of the capacitive electrode could enhance the cell capacitance and overall energy density of the device [3,15].

Table 2.4: Summary of the performance of different hybrid energy storage devices

Device design (negative//positive)	Type	Electrolyte / voltage window	Capacitance (F g ⁻¹) / Current density (A g ⁻¹)	Cycling stability (%) @ cycles	Max. Energy (W h kg ⁻¹) @ Power (W kg ⁻¹)	Ref
Li₄Ti₅O₁₂//LiFePO₄/AC	BSH	LiTf/EC: PC + PVdF-HFP / 0 - 3 V	36 mA h g ⁻¹ / 0.05 A g ⁻¹	~80 @ 100	27.4 @ 75.7	[39]
AC// Li₂Ni₂(MoO₄)₃	HSC	2 M LiOH/ 0 - 1.7 V	1173 F g ⁻¹ / 1 A g ⁻¹	68 @ 10,000	36.5 @ 420	[116]
V₂O₅-NW-G// V₂O₅- NW-G	NIC	1 M Na ₂ SO ₄ /- 1.5 -1.5 V	1002 F g ⁻¹	83.9 @ 5,000	116 @ 1520.2	[68]
AC// Li₂MnSiO₄/Al₂O₃	SCP	1 M LiNO ₃ / 0 - 1.6 V	117.5 / 1 A g ⁻¹	93.6 @ 100	10.4 @ 864.3	[43]
AC// Li₂MnSiO₄/C	LIC	1 M LiPF ₆ /EC: DMC / 0 - 3 V	43 Fg-1 @ 1 mA cm ⁻²	99 @ 1,000	54 @ 150	[42]
AC//CO₃(PO₄)₂/NF	SCP	3 M KOH /0 - 1.7 V	1990 F g ⁻¹ @ 5 mA g ⁻¹	84 @ 20,000	43.2 @ 20.6	[35]
AC// Na₄Mn₉O₁₈	NIC	1 M Na ₂ SO ₄ / 0 - 1.7 V	119.2 F g ⁻¹ @ 100 mA g ⁻¹	84 @ 4,000	34.8 @ 62.1	[40]
AC// LiMn₂O₄/Super P	LIHS	1 M Li ₂ SO ₄ / 0 - 1.2 V	306 F g ⁻¹ @ 1 A g ⁻¹	85 @ 4,500	13 @ 5200	[37]
RGO//LiMnPO₄/RGO	LIHS	1 M LiOH / 0 - 1.5 V	50.3 C g ⁻¹ @ 0.5 A g ⁻¹	91 @ 10,000	16.46 @ 0.38	[17]
Fe₃O₄/3DGr//V₂O₅/3D Gr	ASC	1 M Na ₂ SO ₄ / 0 - 1.8 V	612 F g ⁻¹ @ 1 A g ⁻¹	89.9 @ 10,000	54.9 @ 898	[28]
AC//Li₂Ni₂(MoO₄)₃	ASC	2 M LiOH / 0 - 1.8 V	1137 F g-1 @ 1 A g-1	68 @ 10,000	36.5 @ 420	[116]
Mesoporous C//PANi/MnO₂	ASC	6 M KOH / 0 - 1.6 V	133.7 F g ⁻¹	43 @ 5000	26.6 @ 400	[117]
Li₂FeSiO₄//AC	AHS	1 M LiPF ₆ - EC/DMC / 0 -3 V	49 F g ⁻¹ @ 1 mA cm ⁻²	43 @ 200	43 @ 200	[41]
AC//Li_xMnO₂	LIHS	1 M Li ₂ SO ₄	144.6 F g-1 @	95.2 @ 10,000	88.56 @ 151.8	[18]

For clarity, BSH = battery supercapacitor hybrid, HSC = hybrid supercapacitor, NIC = Na-ion capacitor, SCP = supercapatteries, LIHS = lithium-ion hybrid supercapacitor, ASC = asymmetric supercapacitor, AHS = asymmetric hybrid supercapacitor.

2.6 Conclusion and Future Prospects

Supercapatteries are a new type of hybrid energy storage devices which seek to target both the advantages of high power density supercapacitors and high energy density secondary batteries. These devices are currently under the spotlight due to the likelihood that they can become the ultimate source of power for multi-function electronic equipment and electric/hybrid vehicles in the future. Due to the different energy storage mechanisms occurring in supercapatteries, they are capable of delivering higher energy densities without sacrificing their high power density. Different battery-type and capacitive-type material combinations have been design for supercapattery applications. Although great efforts have been devoted to the fabrication of advanced electrodes and improving both power and energy densities, much work still remains to be done. Pseudocapacitive materials such as metal oxides demonstrate relatively high capacities but low electrical conductivity limits their rate performance and cycle stability. Battery-type materials show considerably high energy densities but are also limited by low conductivity, large volume expansion and slow diffusion of ions within the electrode materials during repeated cycling. The asymmetry in performance of both capacitive and battery type electrodes may lead to reduced charge/discharge ability and energy density of the supercapattery device.

Therefore, further improvement of supercapatteries and other hybrid devices depends on the development of advanced electrode materials and the in-depth understanding of the massive and kinetically matching principles. In the case of designing new and advanced electrodes, computational analysis and other techniques such as spectroelectrochemistry could provide more insights about the charge storage mechanism of the electrode materials. On the other hand, the optimized matching between positive and negative electrodes is critically important to the overall performance of the hybrid device. Careful selection of suitable positive and negative electrodes and proper adjustment of their mass ratios to maximise capacity/capacitance as well as energy/power density of the device is indeed critical for practical application of supercapatteries.

References



- [1] T.M. Gür, Review of electrical energy storage technologies, materials and systems: Challenges and prospects for large-scale grid storage, *Energy Environ. Sci.* 11 (2018) 2696–2767. doi:10.1039/c8ee01419a.
- [2] C. Zou, Q. Zhao, G. Zhang, B. Xiong, Energy revolution: From a fossil energy era to a new energy era, *Nat. Gas Ind.* 36 (2016) 1–10. doi:10.3787/j.issn.1000-0976.2016.01.001.
- [3] A. Vlad, N. Singh, J. Rolland, S. Melinte, P.M. Ajayan, J.F. Gohy, Hybrid supercapacitor-battery materials for fast electrochemical charge storage, *Sci. Rep.* 4 (2014) 1–7. doi:10.1038/srep04315.
- [4] X. Feng, S. Zheng, D. Ren, X. He, L. Wang, X. Liu, M. Li, M. Ouyang, Key

-
- Characteristics for Thermal Runaway of Li-ion Batteries, *Energy Procedia*. 158 (2019) 4684–4689. doi:10.1016/j.egypro.2019.01.736.
- [5] H. Wei, D. Cui, J. Ma, L. Chu, X. Zhao, H. Song, H. Liu, T. Liu, N. Wang, Z. Guo, Energy conversion technologies towards self-powered electrochemical energy storage systems: the state of the art and perspectives, *J. Mater. Chem. A*. 5 (2017) 1873–1894. doi:10.1039/C6TA09726J.
- [6] J. Lee, S. Choudhury, D. Weingarth, D. Kim, V. Presser, High Performance Hybrid Energy Storage with Potassium Ferricyanide Redox Electrolyte, *ACS Appl. Mater. Interfaces*. 8 (2016) 23676–23687. doi:10.1021/acsami.6b06264.
- [7] W. Raza, F. Ali, N. Raza, Y. Luo, K. Kim, J. Yang, Recent advancements in supercapacitor technology, *Nano Energy*. 52 (2018) 441–473. doi:10.1016/j.nanoen.2018.08.013.
- [8] G.Z. Chen, G.Z. Chen, Supercapacitor and supercapattery as emerging electrochemical energy stores, *Int. Mater. Rev.* 0 (2016) 1–30. doi:10.1080/09506608.2016.1240914.
- [9] L. Yu, G.Z. Chen, Ionic Liquid-Based Electrolytes for Supercapacitor and Supercapattery, 7 (2019) 1–15. doi:10.3389/fchem.2019.00272.
- [10] S.C. Lee, W. Young, Analogical understanding of the Ragone plot and a new categorization of energy devices, *Energy Procedia*. 88 (2016) 526–530. doi:10.1016/j.egypro.2016.06.073.
- [11] J. Collins, G. Gourdin, M. Foster, D. Qu, Carbon surface functionalities and SEI formation during Li intercalation, *Carbon N. Y.* 92 (2015) 193–244. doi:10.1016/j.carbon.2015.04.007.
- [12] N. Choudhary, C. Li, J. Moore, N. Nagaiah, L. Zhai, Y. Jung, J. Thomas, Asymmetric

-
- Supercapacitor Electrodes and Devices, *Adv. Mater.* 29 (2017). doi:10.1002/adma.201605336.
- [13] A. González, E. Goikolea, J.A. Barrena, R. Mysyk, Review on supercapacitors: Technologies and materials, *Renew. Sustain. Energy Rev.* 58 (2016) 1189–1206. doi:10.1016/j.rser.2015.12.249.
- [14] D.P. Dubal, O. Ayyad, V. Ruiz, P. Gomez-Romero, Hybrid Energy Storage: The Merging of Battery and Supercapacitor Chemistries, *ChemInform.* 46 (2015) no-no. doi:10.1002/chin.201522308.
- [15] Poonam, K. Sharma, A. Arora, S.K. Tripathi, Review of supercapacitors: Materials and devices, *J. Energy Storage.* 21 (2019) 801–825. doi:10.1016/j.est.2019.01.010.
- [16] D. Kim, K. Lee, M. Kim, Y. Kim, H. Lee, Carbon-based asymmetric capacitor for high-performance energy storage devices, *Electrochim. Acta.* 300 (2019) 461–469. doi:10.1016/j.electacta.2019.01.141.
- [17] L. Xu, S. Wang, X. Zhang, T. He, F. Lu, H. Li, J. Ye, A facile method of preparing LiMnPO₄/reduced graphene oxide aerogel as cathodic material for aqueous lithium-ion hybrid supercapacitors, *Appl. Surf. Sci.* 428 (2018) 977–985. doi:10.1016/j.apsusc.2017.09.247.
- [18] L. Chen, L. Chen, W. Zhai, D. Li, Y. Lin, S. Guo, J. Feng, L. Zhang, L. Song, P. Si, L. Ci, Tunable synthesis of Li_xMnO₂ nanowires for aqueous Li-ion hybrid supercapacitor with high rate capability and ultra-long cycle life, *J. Power Sources.* 413 (2019) 302–309. doi:10.1016/j.jpowsour.2018.12.026.
- [19] L. Guan, L. Yu, G.Z. Chen, Capacitive and non-capacitive faradaic charge storage, *Electrochim. Acta.* 206 (2016) 464–478. doi:10.1016/j.electacta.2016.01.213.

-
- [20] Z. Yang, J. Tian, Z. Yin, C. Cui, W. Qian, F. Wei, Carbon nanotube- and graphene-based nanomaterials and applications in high-voltage supercapacitor : A review, *Carbon* N. Y. 141 (2019) 467–480. doi:10.1016/j.carbon.2018.10.010.
- [21] L. Wang, X. Ye, P. Zhao, H. Jiang, Y. Zhu, Z. Wan, Toward high capacitance and rate capability supercapacitor : Three dimensional graphene network fabricated by electricfield-assisted assembly method, *Appl. Surf. Sci.* 467–468 (2019) 949–953. doi:10.1016/j.apsusc.2018.10.169.
- [22] B. Akinwolemiwa, G.Z. Chen, Fundamental consideration for electrochemical engineering of supercapattery, *J. Braz. Chem. Soc.* 29 (2018) 960–972. doi:10.21577/0103-5053.20180010.
- [23] B. Akinwolemiwa, C. Peng, G.Z. Chen, Redox electrolytes in supercapacitors, 162 (2015) 5054–5059. doi:10.1149/2.0111505jes.
- [24] H. Girard, H. Wang, A.L. Entremont, L. Pilon, Enhancing Faradaic Charge Storage Contribution in Hybrid Pseudocapacitors, *Electrochim. Acta.* 182 (2015) 639–651. doi:10.1016/j.electacta.2015.09.070.
- [25] B. Akinwolemiwa, C. Wei, G.Z. Chen, Mechanisms and Designs of Asymmetrical Electrochemical Capacitors, *Electrochim. Acta.* 247 (2017) 344–357. doi:10.1016/j.electacta.2017.06.088.
- [26] A. Noori, M.F. El-kady, M.S. Rahmanifar, R.B. Kaner, M.F. Mousavi, Towards establishing performance metrics for batteries, supercapacitors and beyond, *Chem. Soc. Rev.* (2019). doi:10.1039/c8cs00581h.
- [27] S. Zhang, N. Pan, Supercapacitors Performance Evaluation, (2015) 1–19. doi:10.1002/aenm.201401401.

-
- [28] H.A. Ghaly, A.G. El-deen, E.R. Souaya, N.K. Allam, Asymmetric supercapacitors based on 3D graphene-wrapped V₂O₅ nanospheres and Fe₃O₄@3D graphene electrodes with high power and energy densities, *Electrochim. Acta.* 310 (2019) 58–69. doi:10.1016/j.electacta.2019.04.071.
- [29] V. Augustyn, B. Dunn, Pseudocapacitive oxide materials for high-rate electrochemical energy storage, *Energy Environ. Sci.* 7 (2014) 1597–1614. doi:10.1039/c3ee44164d.
- [30] Y. Yan, B. Li, W. Guo, H. Pang, H. Xue, Vanadium based materials as electrode materials for high performance supercapacitors, *J. Power Sources.* 329 (2016) 148–169. doi:10.1016/j.jpowsour.2016.08.039.
- [31] R. Manikandan, C.J. Raj, M. Rajesh, B. Chul, S. Yeup, B. Cho, K. Hyun, Polycrystalline V₂O₅/Na_{0.33}V₂O₅ electrode material for Li⁺ ion redox supercapacitor, *Electrochim. Acta.* 230 (2017) 492–500. doi:10.1016/j.electacta.2017.02.031.
- [32] C.O. and K.M.R. N. Padmanathan, Han Shao, David McNulty, Hierarchical NiO–In₂O₃ microflower (3D)/ nanorod (1D) hetero-architecture as a supercapattery electrode with excellent cyclic stability, *J. Mater. Chem. A.* 4 (2016) 4820–4830. doi:10.1039/C5TA10407F.
- [33] F. Zhang, T. Zhang, X. Yang, L. Zhang, K. Leng, Y. Huang, Y. Chen, A high-performance supercapacitor-battery hybrid energy storage device based on graphene-enhanced electrode materials with ultrahigh energy density, *Energy Environ. Sci.* 6 (2013) 1623–1632. doi:10.1039/c3ee40509e.
- [34] H. Shao, N. Padmanathan, D. McNulty, Supercapattery Based on Binder-Free Co₃(PO₄)₂·8H₂O Multilayer Nano/Micro flakes on Nickel Foam, *ACS Appl. Mater. Interfaces.* 3 (2016) 4–10. doi:10.1021/acsami.6b08354.

-
- [35] H. Shao, N. Padmanathan, D. McNulty, Cobalt Phosphate-Based Supercapattery as Alternative Power Source for Implantable Medical Devices, *ACS Appl. Energy Mater.* 2 (2019) 569–578. doi:10.1021/acsaem.8b01612.
- [36] D. Tie, S. Huang, J. Wang, J. Ma, J. Zhang, Y. Zhao, Hybrid energy storage devices : Advanced electrode materials and matching principles, *Energy Storage Mater.* (2019) 1–20. doi:10.1016/j.ensm.2018.12.018.
- [37] L. Chen, W. Zhai, L. Chen, D. Li, X. Ma, Q. Ai, X. Xu, G. Hou, L. Zhang, J. Feng, P. Si, L. Ci, Nanostructured LiMn_2O_4 composite as high-rate cathode for high performance aqueous Li-ion hybrid supercapacitors, *J. Power Sources.* 392 (2018) 116–122. doi:10.1016/j.jpowsour.2018.04.103.
- [38] S.H. Lee, I.H. Im, Excellent performance hybrid supercapacitors based on $\text{LiNi}_{1/3}\text{Mn}_{1/3}\text{Co}_{1/3}\text{O}_2$ /activated carbon electrode, *Mater. Lett.* 231 (2018) 38–42. doi:10.1016/j.matlet.2018.07.115.
- [39] M.K. Singh, S.A. Hashmi, Performance of solid-state hybrid supercapacitor with LiFePO_4 /AC composite cathode and $\text{Li}_4\text{Ti}_5\text{O}_{12}$ as anode, *Ionics (Kiel)*. (2017). doi:10.1007/s11581-017-2027-8.
- [40] X. Liu, N. Zhang, J. Ni, L. Gao, Improved electrochemical performance of sol–gel method prepared $\text{Na}_4\text{Mn}_9\text{O}_{18}$ in aqueous hybrid Na-ion supercapacitor, *J Solid State Electrochem.* 17 (2013) 1939–1944. doi:10.1007/s10008-013-2044-0.
- [41] K. Karthikeyan, V. Aravindan, S.B. Lee, I.C. Jang, H.H. Lim, G.J. Park, M. Yoshio, Y.S. Lee, A novel asymmetric hybrid supercapacitor based on $\text{Li}_2\text{FeSiO}_4$ and activated carbon electrodes, *J. Alloys Compd.* 504 (2010) 224–227. doi:10.1016/j.jallcom.2010.05.097.

-
- [42] K. Karthikeyan, V. Aravindan, S.B. Lee, I.C. Jang, H.H. Lim, G.J. Park, M. Yoshio, Y.S. Lee, Electrochemical performance of carbon-coated lithium manganese silicate for asymmetric hybrid supercapacitors, *J. Power Sources*. 195 (2010) 3761–3764. doi:10.1016/j.jpowsour.2009.11.138.
- [43] M.M. Ndipingwi, C. Ikpo, N.W. Hlongwa, N. Ross, M. Masikini, S.V. John, P. Baker, W. Roos, E.I. Iwuoha, Orthorhombic (Pm_n2₁) nanostructured Li₂MnSiO₄/Al₂O₃ supercapattery electrode with efficient Li-ion migratory pathway, *Batter. Supercaps*. (2018) 1–14. doi:10.1002/batt.201800045.
- [44] Z.S. Iro, C. Subramani, S.S. Dash, A Brief Review on Electrode Materials for Supercapacitor, *Int. J. Electrochem. Sci.* 11 (2016) 10628–10643. doi:10.20964/2016.12.50.
- [45] L.L. Zhang, X.S. Zhao, Carbon-based materials as supercapacitor electrodes, *Chem. Soc. Rev.* 38 (2009) 2520–2531. doi:10.1039/b813846j.
- [46] M. Sevilla, R. Mokaya, Energy storage applications of activated carbons: supercapacitors and hydrogen storage, *Energy Environ. Sci.* 7 (2014) 1250–1280. doi:10.1039/c3ee43525c.
- [47] L. Wei, K. Tian, X. Zhang, Y. Jin, T. Shi, X. Guo, 3D Porous Hierarchical Microspheres of Activated Carbon from Nature through Nanotechnology for Electrochemical Double-Layer Capacitors, *Sustain. Chem. Eng.* 4 (2016) 6463–6472. doi:10.1021/acssuschemeng.6b01227.
- [48] and M.E. Perreault François, Andreia Fonseca De Faria, Environmental Applications of Graphene-Based Nanomaterials *Chemical Society Reviews*, *Chem. Soc. Rev.* 44 (2015) 5861–5896.

-
- [49] M. Zhang, C. Hou, A. Halder, Q. Chi, Graphene papers : smart architecture and specific functionalization for biomimetics , electrocatalytic, *Mater. Chem. Front.* 1 (2016) 37–60. doi:10.1039/C6QM00145A.
- [50] J.T. Liu, Jingquan, J.J. Gooding, Strategies for chemical modification of graphene and applications of chemically modified graphene, *J. Mater. Chem.* 22 (2012) 12435–12452. doi:10.1039/c2jm31218b.
- [51] Q. Li, M. Horn, Y. Wang, J. Macleod, N. Motta, J. Liu, A Review of Supercapacitors Based on Graphene and Redox-Active Organic Materials, *Materials (Basel)*. 12 (2019) 703. doi:10.3390/ma12050703.
- [52] C. Zu, A. Manthiram, Hydroxylated graphene-sulfur nanocomposites for high-rate lithium-sulfur batteries, *Adv. Energy Mater.* 3 (2013) 1008–1012. doi:10.1002/aenm.201201080.
- [53] P. Gong, J. Wang, W. Sun, D. Wu, Z. Wang, Z. Fan, H. Wang, S. Yang, Tunable photoluminescence and spectrum split from fluorinated to hydroxylated graphene, *Nanoscale*. 6 (2014) 3316–3324. doi:10.1039/c3nr05725a.
- [54] C.-L.C. and Q.-W.C. Xiang-Kai Kong, Doped graphene for metal-free catalysis, *Chem. Soc. Rev.* 43 (2014) 2841–2857. doi:10.1039/c3cs60401b.
- [55] H.L. Poh, Z. Sofer, P. imek, I. Tomandl, M. Pumera, Hydroboration of graphene oxide: Towards stoichiometric graphol and hydroxygraphane, *Chem. - A Eur. J.* 21 (2015) 8130–8136. doi:10.1002/chem.201406168.
- [56] J. Ding, O. Rahman, H. Zhao, W. Peng, Hydroxylated graphene-based flexible carbon film with ultrahigh electrical and thermal conductivity, *Nanotechnology*. 28 (2017) 39LT01.

-
- [57] K.A. Shah, B.A. Tali, Synthesis of carbon nanotubes by catalytic chemical vapour deposition : A review on carbon sources , catalysts and substrates, *Mater. Sci. Semicond. Process.* 41 (2016) 67–82. doi:10.1016/j.mssp.2015.08.013.
- [58] A. Yahyazadeh, B. Khoshandam, Carbon nanotube synthesis via the catalytic chemical vapor deposition of methane in the presence of iron , molybdenum , and iron – molybdenum alloy thin layer catalysts, *Results Phys.* 7 (2017) 3826–3837. doi:10.1016/j.rinp.2017.10.001.
- [59] M. Kawamoto, P. He, Y. Ito, Green Processing of Carbon Nanomaterials, *Adv. Materials.* 29 (2016) 1–29. doi:10.1002/adma.201602423.
- [60] Q. Zeng, H. Tian, J. Jiang, X. Ji, D. Gao, C. Wang, High-purity helical carbon nanotubes with enhanced electrochemical properties for supercapacitors, *RSC Advances.* 7 (2017) 7375–7381. doi:10.1039/C6RA27459E.
- [61] X.C.P.J. Yining Ma, Aibin Huang, Huaijuan Zhou, Shidong Ji, Shuming Zhang, Rong Li Heliang Yao, Template-free formation of various V₂O₅ hierarchical structures as cathode materials for lithium-ion batteries, *J. Mater. Chem. A.* 5 (2017) 6522–6531. doi:10.1039/C6TA11194G.
- [62] C.F. Armer, M. Lübke, M. V Reddy, J.A. Darr, X. Li, A. Lowe, Phase change effect on the structural and electrochemical behaviour of pure and doped vanadium pentoxide as positive electrodes for lithium ion batteries, *J. Power Sources.* 353 (2017) 40–50. doi:10.1016/j.jpowsour.2017.03.121.
- [63] X. Huang, X. Rui, H.H. Hng, Q. Yan, Vanadium Pentoxide-Based Cathode Materials for Lithium- Ion Batteries : Morphology Control , Carbon Hybridization , and Cation Doping, *Particle & Particle Systems Characterization.* 32 (2015) 276–294.

-
- doi:10.1002/ppsc.201400125.
- [64] M.M. and S.K.B. Dipanwita Majumdar, Review on V_2O_5 and Its' Carbon-Based Nanocomposites for Supercapacitor Applications, *Chemelectrochem.* 6 (2019) 1623–1648. doi:10.1002/celc.201801761.
- [65] D. McNulty, D.N. Buckley, C.O. Dwyer, Synthesis and electrochemical properties of vanadium oxide materials and structures as Li-ion battery positive electrodes, *J. Power Sources.* 267 (2014) 831–873. doi:10.1016/j.jpowsour.2014.05.115.
- [66] G. Salek, B. Bellanger, I. Mjejri, M. Gaudon, A. Rougier, Polyol Synthesis of Ti- V_2O_5 Nanoparticles and Their Use as Electrochromic Films, *Inorg. Chem.* 55 (2016) 9838–9847. doi:10.1021/acs.inorgchem.6b01662.
- [67] A. De Adhikari, R. Oraon, S.K. Tiwari, J.H. Lee, N.H. Kim, G.C. Nayak, A V_2O_5 nanorod decorated graphene/polypyrrole hybrid electrode: a potential candidate for supercapacitors, *New J. Chem.* 41 (2017) 1704–1713. doi:10.1039/C6NJ03580A.
- [68] D.J. Ahirrao, K. Mohanapriya, N. Jha, V_2O_5 nanowires-graphene composite as an outstanding electrode material for high electrochemical performance and long-cycle-life supercapacitor, *Mater. Res. Bull.* 108 (2018) 73–82. doi:10.1016/j.materresbull.2018.08.028.
- [69] R. Narayanan, Single step hydrothermal synthesis of carbon nanodot decorated V_2O_5 nanobelts as hybrid conducting material for supercapacitor application, *J. Solid State Chem.* 253 (2017) 103–112. doi:10.1016/j.jssc.2017.05.035.
- [70] T. Peng, J. Wang, Q. Liu, J. Liu, P. Wang, Mesoporous V_2O_5 /Ketjin black nanocomposites for all-solid-state symmetric supercapacitors, *CrystEngComm.* 17 (2015) 1673–1679. doi:10.1039/c4ce02305f.

-
- [71] Q. Wang, Y. Zou, C. Xiang, H. Chu, H. Zhang, F. Xu, L. Sun, C. Tang, High-performance supercapacitor based on V_2O_5 /carbon nanotubes-super activated carbon ternary composite, *Ceram. Int.* 42 (2016) 12129–12135. doi:10.1016/j.ceramint.2016.04.145.
- [72] K. Palanisamy, J.H. Um, M. Jeong, W. Yoon, Porous V_2O_5 /RGO/CNT hierarchical architecture as a cathode material : Emphasis on the contribution of surface lithium storage, *Nat. Publ. Gr.* (2016) 1–12. doi:10.1038/srep31275.
- [73] Y. Zhang, J. Zheng, Y. Zhao, T. Hu, Z. Gao, C. Meng, Fabrication of V_2O_5 with various morphologies for high-performance electrochemical capacitor, *Appl. Surf. Sci.* 377 (2016) 385–393. doi:10.1016/j.apsusc.2016.03.180.
- [74] J. Zheng, T. Hu, Y. Zhang, T. Lv, F. Tian, C. Meng, Template-free synthesis of porous V_2O_5 flakes as a battery-type electrode material with high capacity for supercapacitors, *Colloids Surfaces A.* 553 (2018) 317–326. doi:10.1016/j.colsurfa.2018.05.090.
- [75] Y. Bai, Z. Yan, L. Kang, Z. Liu, Preparation and capacitance of V_2O_5 /holey graphene hybrid aerogel electrode with high performance, *J. Alloys Compd.* 780 (2019) 792–799. doi:10.1016/j.jallcom.2018.12.006.
- [76] W. Sun, G. Gao, K. Zhang, Y. Liu, G. Wu, Self-assembled 3D N-CNFs/ V_2O_5 aerogels with core/shell nanostructures through vacancies control and seeds growth as an outstanding supercapacitor electrode material, *Carbon N. Y.* 132 (2018) 667–677. doi:10.1016/j.carbon.2018.03.004.
- [77] Y. Zhang, X. Wang, X. Jing, C. Meng, In-situ synthesis of V_2O_5 hollow spheres coated Ni-foam as binder-free electrode for high-performance symmetrical supercapacitor, *Mater. Lett.* 248 (2019) 101–104. doi:10.1016/j.matlet.2019.04.014.

-
- [78] J. Zheng, Y. Zhang, X. Jing, Q. Wang, T. Hu, N. Xing, Improvement of the specific capacitance of V_2O_5 nanobelts as supercapacitor electrode by tungsten doping, *Mater. Chem. Phys.* 186 (2017) 5–10. doi:10.1016/j.matchemphys.2016.11.027.
- [79] B. Saravanakumar, K. Kamaraj, V_2O_5 /nitrogen enriched mesoporous carbon spheres nanocomposite as supercapacitor electrode, *Microporous Mesoporous Mater.* 258 (2018) 83–94. doi:10.1016/j.micromeso.2017.09.010.
- [80] A. De Adhikari, R. Oraon, S.K. Tiwari, J.H. Lee, N.H. Kim, G.C. Nayak, A V_2O_5 nanorod decorated graphene/polypyrrole hybrid electrode: a potential candidate for supercapacitors, *New J. Chem.* 41 (2017) 1704–1713. doi:10.1039/c6nj03580a.
- [81] N. Wang, Y. Zhang, T. Hu, Y. Zhao, C. Meng, Facile hydrothermal synthesis of ultrahigh-aspect-ratio V_2O_5 nanowires for high-performance supercapacitors, *Curr. Appl. Phys.* 15 (2015) 493–498. doi:10.1016/j.cap.2015.01.026.
- [82] Z. Liu, H. Zhang, Q. Yang, Y. Chen, Graphene/ V_2O_5 hybrid electrode for an asymmetric supercapacitor with high energy density in an organic electrolyte, *Electrochim. Acta.* 287 (2018) 149–157. doi:10.1016/j.electacta.2018.04.212.
- [83] B. Pandit, D.P. Dubal, B.R. Sankapal, Large scale flexible solid state symmetric supercapacitor through inexpensive solution processed V_2O_5 complex surface architecture, *Electrochim. Acta.* 242 (2017) 382–389. doi:10.1016/j.electacta.2017.05.010.
- [84] H. Li, J. He, X. Cao, L. Kang, X. He, R. Jiang, Z. Lei, Z. Liu, All solid-state V_2O_5 -based flexible hybrid fiber supercapacitors, *J. Power Sources.* 371 (2017) 18–25. doi:10.1016/j.jpowsour.2017.10.031.
- [85] J. Yang, T. Lan, J. Liu, Y. Song, M. Wei, Supercapacitor electrode of hollow spherical

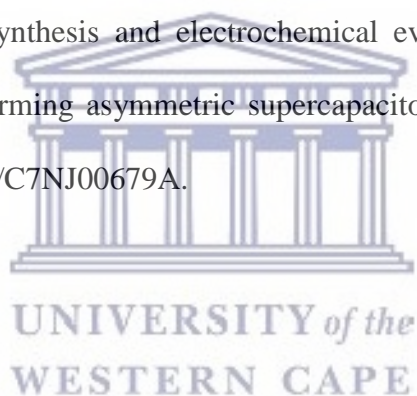
-
- V₂O₅ with a high pseudocapacitance in aqueous solution, *Electrochim. Acta.* 105 (2013) 489–495. doi:10.1016/j.electacta.2013.05.023.
- [86] H. Li, C. Wei, Z. Peng, B. Xie, Novel 3D V₂O₅ nanocorals with continuous size-gradient mesopore channels for high performance supercapacitors, *Mater. Lett.* 220 (2018) 12–15. doi:10.1016/j.matlet.2018.02.092.
- [87] Z. Gong, Y. Yang, Recent advances in the research of polyanion-type cathode materials for Li-ion batteries, *Energy Environ. Sci.* 4 (2011) 3223–3242. doi:10.1039/C0EE00713G.
- [88] R.J. Gummow, Y. He, Recent progress in the development of Li₂MnSiO₄ cathode materials, *J. Power Sources.* 253 (2014) 315–331. doi:10.1016/j.jpowsour.2013.11.082.
- [89] P. Barpanda, L. Lander, S. Nishimura, A. Yamada, Polyanionic Insertion Materials for Sodium-Ion Batteries, *Adv. Energy Mater.* 1703055 (2018) 1703055. doi:10.1002/aenm.201703055.
- [90] A. Gutierrez, N.A. Benedek, A. Manthiram, Crystal-Chemical Guide for Understanding Redox Energy Variations of M^{2+/3+} couples in Polyanion Cathodes for Lithium-Ion Batteries, *Chem. Mater.* 25 (2013) 4010–4016. doi:10.1021/cm401949n.
- [91] H.-N. Girish, G.-Q. Shao, Advances in high-capacity Li₂MSiO₄ (M = Mn, Fe, Co, Ni) cathode materials for lithium-ion batteries, *RSC Adv.* 5 (2015) 98666–98686. doi:10.1039/C5RA18594G.
- [92] R.J. Gummow, Y. He, Recent progress in the development of Li₂MnSiO₄ cathode materials, *J. Power Sources.* 253 (2014) 315–331. doi:10.1016/j.jpowsour.2013.11.082.
- [93] C. Sirisopanaporn, C. Masquelier, P.G. Bruce, A.R. Armstrong, R. Dominko, Dependence of Li₂FeSiO₄ electrochemistry on structure., *J. Am. Chem. Soc.* 133 (2011)

-
- 1263–1265. doi:10.1021/ja109695r.
- [94] S. Fleischmann, M. Mancini, P. Axmann, U. Golla-Schindler, U. Kaiser, M. Wohlfahrt-Mehrens, Insights into the Impact of Impurities and Non-Stoichiometric Effects on the Electrochemical Performance of $\text{Li}_2\text{MnSiO}_4$, *ChemSusChem*. 9 (2016) 2982–2993. doi:10.1002/cssc.201600894.
- [95] Z. Ding, Y. Feng, D. Zhang, R. Ji, L. Chen, D.G. Ivey, W. Wei, Crystallographic Habit Tuning of $\text{Li}_2\text{MnSiO}_4$ Nanoplates for High-Capacity Lithium Battery Cathodes., *ACS Appl. Mater. Interfaces*. 10 (2018) 6309–6316. doi:10.1021/acsami.7b17587.
- [96] M. Arroyo-deDompablo, On the energetic stability and electrochemistry of $\text{Li}_2\text{MnSiO}_4$ polymorphs, *Chem*. 20 (2008) 5574–5584. doi:10.1021/cm801036k.
- [97] H.-N.G. and G.-Q. Shao, Advances in high-capacity Li_2MSiO_4 (M = Mn, Fe, Co, Ni...) cathode material for lithium-ion batteries, *RSC Adv*. 5 (2015) 98666–98686. doi:10.1039/x0xx00000x.
- [98] Q. Cheng, W. He, X. Zhang, M. Li, L. Wang, Modification of $\text{Li}_2\text{MnSiO}_4$ cathode materials for lithium-ion batteries: a review, *J. Mater. Chem. A*. 5 (2017) 10772–10797. doi:10.1039/C7TA00034K.
- [99] K. Huang, B. Li, M. Zhao, J. Qiu, H. Xue, H. Pang, Synthesis of lithium metal silicates for lithium ion batteries, *Chinese Chem. Lett.* 28 (2017) 2195–2206. doi:10.1016/j.ccllet.2017.11.010.
- [100] Y. Pei, Q. Chen, C.-Y. Xu, H.-X. Wang, H.-T. Fang, C. Zhou, L. Zhen, G. Cao, Chelate-induced formation of $\text{Li}_2\text{MnSiO}_4$ nanorods as a high capacity cathode material for Li-ion batteries, *J. Mater. Chem. A*. 4 (2016) 9447–9454. doi:10.1039/C6TA01269H.
- [101] M.M. Ndipingwi, C.O. Ikpo, N.W. Hlongwa, N. Dywili, A.L. Djoumessi Yonkeu, E.I.

-
- Iwuoha, Crystal chemistry and lithium-ion intercalation properties of lithium manganese silicate cathode for aqueous rechargeable Li-ion batteries, *J. Appl. Electrochem.* 49 (2019) 465–474. doi:10.1007/s10800-019-01296-0.
- [102] X. Wu, S. Zhao, L. Wei, E. Zhao, J. Li, C. Nan, Improved Structural Reversibility and Cycling Stability of $\text{Li}_2\text{MnSiO}_4$ Cathode Material by the Pillar Effect of $[\text{TiO}_x]$ Polyanions, *Energy Technol. Environ. Sci.* 3 (2018) 4047–4057. doi:10.1002/slct.201800036.
- [103] R.J. Gummow, N. Sharma, V.K. Peterson, Y. He, Crystal chemistry of the Pmnb polymorph of $\text{Li}_2\text{MnSiO}_4$, *J. Solid State Chem.* 188 (2012) 32–37. doi:10.1016/j.jssc.2012.01.051.
- [104] C. Hwang, T. Kim, Y. Noh, W. Cha, J. Shim, K. Kwak, K.M. Ok, K.K. Lee, Synthesis, characterization, and electrochemical performance of V-doped $\text{Li}_2\text{MnSiO}_4/\text{C}$ composites for Li-ion battery, *Mater. Lett.* 164 (2016) 270–273. doi:10.1016/j.matlet.2015.10.113.
- [105] Q.C. and G.Y. Meng Zhang, Shiju Zhao, $\text{Li}_{2+x}\text{MnSi}_{1-x}\text{Al}_x\text{O}_4/\text{C}$ nanoparticles for high capacity lithium-ion battery cathode applications Meng, *RSC Adv.* 58 (2014) 30876–80.
- [106] F. Milocco, S. Demeshko, F. Meyer, E. Otten, Custom designed nanocrystalline $\text{Li}_2\text{MSiO}_4/\text{reduced graphene oxide}$ (M=Fe, Mn) formulations as high capacity cathodes for rechargeable lithium batteries, *Dalt. Trans.* 47 (2018) 8817–8823. doi:10.1039/C8DT01597J.
- [107] H. Duncan, A. Kondamreddy, P.H.J. Mercier, Y. Le Page, Y. Abu-Lebdeh, M. Couillard, P.S. Whitfield, I.J. Davidson, Novel Pn polymorph for $\text{Li}_2\text{MnSiO}_4$ and its

-
- electrochemical activity as a cathode material in Li-ion batteries, *Chem. Mater.* 23 (2011) 5446–5456. doi:10.1021/cm202793j.
- [108] T. Peng, W. Guo, Q. Zhang, Y. Zhang, M. Chen, Uniform coaxial CNT@Li₂MnSiO₄ @ C as advanced cathode material for lithium-ion battery, *Electrochim. Acta.* 291 (2018) 1–8. doi:10.1016/j.electacta.2018.08.143.
- [109] P. Babbar, B. Tiwari, B. Purohit, A. Ivanishchev, A. Churikov, A. Dixit, Charge/discharge characteristics of Jahn–Teller distorted nanostructured orthorhombic and monoclinic Li₂MnSiO₄ cathode materials, *RSC Adv.* 7 (2017) 22990–22997. doi:10.1039/C7RA02840G.
- [110] S.N. Lee, S. Baek, S. Amaresh, V. Aravindan, K.Y. Chung, B.W. Cho, W.S. Yoon, Y.S. Lee, Cu-Li₂MnSiO₄-polyaniline composite hybrids as high performance cathode for lithium batteries, *J. Alloys Compd.* 630 (2015) 292–298. doi:10.1016/j.jallcom.2015.01.047.
- [111] M. Mancini, E. Bekaert, T. Diemant, M. Marinaro, L. de Biasi, R.J. Behm, M. Wohlfahrt-Mehrens, Study on the stability of Li₂MnSiO₄ cathode material in different electrolyte systems for Li-ion batteries, *Electrochim. Acta.* 176 (2015) 679–688. doi:10.1016/j.electacta.2015.07.015.
- [112] X.F. Yang, J.H. Yang, K. Zaghbi, M.L. Trudeau, J.Y. Ying, Synthesis of phase-pure Li₂MnSiO₄@C porous nanoboxes for high-capacity Li-ion battery cathodes, *Nano Energy.* 12 (2015) 305–313. doi:10.1016/j.nanoen.2014.12.021.
- [113] R.J. Gummow, Y. He, Mesoporous manganese-deficient lithium manganese silicate cathodes for lithium-ion batteries, *RSC Adv.* 4 (2014) 11580–11584. doi:10.1039/c3ra47730d.

-
- [114] S. Qiu, X. Pu, X. Ai, H. Yang, Z. Chen, Y. Cao, Template synthesis of mesoporous $\text{Li}_2\text{MnSiO}_4$ @C composite with improved lithium storage properties, *Electrochim. Acta.* 291 (2018) 124–131. doi:10.1016/j.electacta.2018.08.146.
- [115] W. Zuo, R. Li, C. Zhou, Y. Li, J. Xia, J. Liu, Battery-Supercapacitor Hybrid Devices : Recent Progress and Future Prospects, *Adv. Sci. News.* (2017) 1600539. doi:10.1002/advs.201600539.
- [116] D. Du, R. Lan, K. Xie, S. Tao, Synthesis of $\text{Li}_2\text{Ni}_2(\text{MoO}_4)_3$ as a high-performance positive electrode for asymmetric supercapacitors, *RSC Adv.* 7 (2017) 13304–13311. doi:10.1039/C6RA28580E.
- [117] I.I. Misnon, R. Jose, Synthesis and electrochemical evaluation of the PANI/ MnO_2 electrode for high performing asymmetric supercapacitors, *New J. Chem.* 41 (2017) 6574–6584. doi:10.1039/C7NJ00679A.

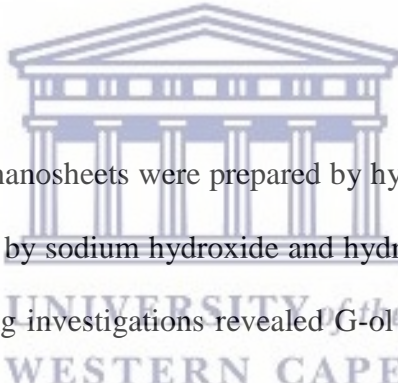


CHAPTER THREE

RESULTS AND DISCUSSION - MANUSCRIPT 1

High Voltage and Freestanding Hydroxylated Graphene Films for Supercapacitors with Aqueous Electrolytes (Prepared for Carbon)

Abstract



Hydroxylated graphene (G-ol) nanosheets were prepared by hydroboration of graphene oxide (GO) and subsequent oxidation by sodium hydroxide and hydrogen peroxide. Morphological and small angle X-ray scattering investigations revealed G-ol nanosheets as single layers of 14- 23 nm thick with average particle sizes of 31.3 nm. X-ray diffraction studies revealed an interlayer spacing of 0.88 nm. Fourier transform infrared spectroscopy showed strong stretching vibrations of sp³ C-H bonds at 2921.6 and 2851.9 cm⁻¹, in addition to stretching and bending vibrations of the OH group at 3409.4 cm⁻¹ in G-ol, indicating covalent functionalization with the hydroxyl groups with GO. Breakage of the stacking order of C-C bonding in GO and increasing degree of oxidation was confirmed by the decrease in the 2D-Raman band of G-ol. Electrochemical studies in 0.5 M LiClO₄ aqueous electrolyte at a potential window of -0.2 – 0.8 V revealed a specific capacitance of 24.0 F g⁻¹ and 73.8 F g⁻¹ for GO and G-ol, respectively at 50 mV s⁻¹ from cyclic voltammetric studies in three electrodes. Electrochemical impedance spectroscopic results showed a lower equivalent circuit resistance

for G-ol ($R_s = 12.43 \Omega$) compared to GO ($R_s = 19.71 \Omega$). The practical application of G-ol in electrochemical capacitors was tested in both symmetric (G-ol//G-ol) and asymmetric (AC//G-ol) devices at a voltage window of 1.6 V. Discharge capacitance values of 137.7 F g^{-1} and 91.73 F g^{-1} were obtained for the symmetric and asymmetric cells, respectively at current load of 0.007 A g^{-1} . The symmetric device was able to deliver a capacitance retention of 83 % and coulombic efficiency of 99.8 % at current load of 0.5 A g^{-1} over 5000 cycles. A specific energy of 47.8 Wh Kg^{-1} and specific power of 377 W kg^{-1} was achieved by the symmetric device at a current load of 0.007 A g^{-1} . The electrochemical performance of these devices highlights the huge potentials of graphol and associated devices in energy storage applications.

Key words: Hydroboration, Hydroxylated graphene, symmetric supercapacitor, high specific energy



3.1 Introduction

The development of sustainable and renewable energy sources has recently become the center of focus for energy research in the scientific and industrial space. However, the intermittent nature of these energy sources requires advanced energy storage devices for back-up and load-leveling during peak production as well as consumption periods. Likewise, the future energy-intensive transportation sector requires electric and hybrid electric vehicles with low CO_2 emissions. To meet the demands of these next-generation applications, a significant improvement in the storage capabilities and cycle life of current energy storage devices is of great importance.

Supercapacitors (SCs), also known as ultracapacitors or electrochemical capacitors, have drawn wide research attention due to their ultrahigh power density, superior rate capability, remarkable safety, and long cycling life. They differ from other energy storage devices such as batteries, which primarily employ chemical oxidation and reduction reactions for charge storage resulting in slow reaction kinetics and low power densities. SCs employ high surface area electrode materials and thin electrolytic dielectrics to achieve higher energy densities than traditional capacitors, greater power density than batteries, ultrafast charge and discharge processes (within several seconds or several minutes). They are considered as highly competitive and promising candidates for next-generation power sources which are able to bridge the gap between conventional capacitors and batteries [1–3]. On the basis of the charge storage mechanism, SCs are classified into electrical double-layer capacitors (EDLCs) and pseudocapacitors. The mechanism of fast adsorption /desorption of electrolyte ions at the electrode surface to store energy is shown by EDLCs, while pseudocapacitors undergo fast and reversible surface or near-surface redox reactions, delivering high power. Yet, to improve the energy density and rate performance of SCs without sacrificing the high power density and cycle life, the development of high-performance advanced electrode materials is crucial. Carbon-based materials, including activated carbon (AC) and carbon nanotubes (CNTs), have been investigated in this regard. Conversely, the microporous nature of the structures limit the active surface area for charge storage [4,5]. Graphene, a two dimensional (2D) material with astounding properties such as high specific surface area, outstanding electrical conductivity, high physicochemical stability, tunable layered structure, and good mechanical flexibility has shown more green light. Coupled with its numerous electrochemical active sites and high theoretical capacitance of 550 F g^{-1} , graphene has attracted considerable attention for its continuous development as novel electrode material for high-performance and new-concept SCs [5–7]. However, graphene-based electrode materials have some intrinsic challenges that

limit their large-scale practical application. These include the loss in hydrophilicity by restacking of graphene sheets during preparation and electrode fabrication, which lead to interplanar pore sizes that block contact with electrolytes. The low packing density of graphene limits its volumetric energy density and overall rate capability [8,9]. The preparation and optimization of graphene materials is therefore key in the performance of graphene in different energy storage systems. Researchers have employed various approaches such as the design of porous 3D graphene structures, graphene composites and doping graphene with heteroatoms, metals or metal oxides, to overcome its downsides.

Cao *et al.* prepared high-quality 3D graphene networks through ethanol assisted chemical vapor deposition. The 3D graphene/metal oxide composites were tested for supercapacitor application in 3 M KOH. The composite with NiO (3D graphene/NiO) delivered a specific capacitance of 816 F g^{-1} at a potential scan rate of 5 mV s^{-1} and no drop in capacitance over 2000 cycles at 80 mV s^{-1} [10]. Miao *et al.* also reported on the hydrothermal synthesis of 3D hierarchical porous graphene-nanosheets on nickel foam as conductive agent and support for high-performance pseudocapacitor applications. The concentration of GO was varied with the addition of KOH to obtain different morphologies of 3D graphene thin films with improved dispersivity of the resultant 3D structure. A hybrid electrode fabricated with Ni-Co-S (NF/G/Ni-Co-S) exhibited high specific capacitance of 2397 F g^{-1} at current densities of 5 A g^{-1} and good cycle stability of 77.0 % after 2000 cycles at a current density of 20 A g^{-1} [11]. Chemical functionalization is a more subtle method of modifying the intrinsic structure and electronic properties of graphene, due to the unfathomable theoretical support from chemistry and variable reaction routes. Moreover, achieving control over its structural and chemical transformation, coupled with the possibility of tuning the concentration of chemical groups on the surface of graphene sheds more light on its structure-property relationship [7,12]. Heteroatoms such as boron, nitrogen, oxygen, sulfur, and phosphorus have been incorporated

into 3D graphene materials. The heteroatomic functional groups are believed to affect the electron-donor characteristics of carbon materials, thus improving the capacitive performance of these materials for Supercapacitors [13,14]. Nankya *et al.* recently investigated a boron-doped mesoporous graphene (BMG) composite prepared by hydrothermal synthesis and a subsequent calcination process to improve its specific surface area. A high specific surface area of $1102 \text{ m}^2 \text{ g}^{-1}$ was achieved with a pore size of 5 nm, leading to enhanced supercapacitor kinetic performance and high electrical conductivity. The BMG composite electrode delivered a specific capacitance of 336 F g^{-1} at a current density of 0.1 A g^{-1} and a capacitance retention of 93.6 % after 5000 cycles at 3 current density A g^{-1} . The good electrochemical performance was attributed to the control of graphene porous structure and the boron configuration [15].

However, many of the methods used in preparing heteroatom doped graphene nanomaterials result in non-stoichiometric composites. Stoichiometric derivatives of graphene (SDG) are of great interest due to their specific and well-defined structures, physical, and chemical properties such as band gap-opening and improved dispersibility. But, SDGs require well-defined synthetic protocols/chemical reactions. Ambrosi *et al.*, reviewed the electrochemistry of graphene and its derivatives with SDGs such as: fluorinated graphene ($\text{C}_1\text{H}_x\text{F}_{1-x}$)_n, hydrogenated graphene (C_1H_1)_n, thiographene [$\text{C}_1(\text{SH})_1$]_n, graphene acid [$\text{C}_1(\text{CO}_2\text{H})_1$]_n, and hydroxylated graphene [$\text{C}_1(\text{OH})_1$]_n [7]. However, only a few studies are available on hydroxylated graphene (Graphol). Gong *et al.*, investigated the preparation of graphol from fluorinated graphene through controlled substitution of fluorine atoms with hydroxyl groups, with resultant exclusive prevalence of hydroxyl groups as oxygen-containing groups in the prepared graphol [12]. The hydrophilicity and good mechanical property of the prepared graphol exhibited favorable activity for cell proliferation with great promise for biomedical applications such as bone, vessel, and skin repair. Hydroxylated graphene–sulfur nanocomposite with sponge-like morphology, prepared by a combination of sonication and

hydrothermal synthesis was reported by Zu and Manthiram [16]. The homogeneously distributed hydroxyl groups on the surface prevented the growth of sulfur into bulk crystalline particles which allowed complete diffusion of electrolyte ions and absorbed the strain-induced volume changes during cycling. The nanocomposite demonstrated promising performance as a cathode material for high rate lithium-sulfur batteries. Furthermore, Poh *et al.* synthesized stoichiometric and highly hydroxylated graphene composite with a stoichiometric ratio of $(C_1O_{0.78}H_{0.75})_n$ through hydroboration of graphene oxide and an ensuing hydroxylation reaction using H_2O_2 [17]. The graphol composite served as a good electrocatalyst for the electrochemical detection of biomarkers and hydrogen evolution reaction. More recently, Singla and Kottantharayil investigated the covalent binding of hydroxyl functionalities on graphene (prepared by chemical vapour deposition) via treatment with H_2O_2 in the presence of UV light [18]. Conductivity is proportional to the movement of charge carriers in the material. Graphol in this study was applied as a channel for field effect transistors, which exhibited p-type character with excellent mobilities.

Herein, with the guidance of classical organic chemical reactions, we report the fabrication of graphol by regioselective hydroboration-oxidation of graphene oxide through an anti-Markovnikov alkyl borane intermediate. Herbert C. Brown of Purdue University received a Noble price in Chemistry (1979) for his work on the addition of diborane over a $-C=C-$ bond which resulted in an alkyl borane with anti-Markovnikov orientation [19]. In essence, hydration of alkenes by hydroboration-oxidation involves the addition of borane (which is usually available as a complex with tetrahydrofuran) to an alkene to form an alkyl borane intermediate. The intermediate is converted to an alcohol by oxidation with aqueous sodium hydroxide and hydrogen peroxide. We successfully performed these reactions and comprehensively characterized graphol using various morphological, spectroscopic and electrochemical techniques. Graphol was further tested as a symmetric and asymmetric electrode material for

supercapacitors. To the best of our knowledge, no extensive studies have been performed on graphol for supercapacitive applications.

3.2 Experimental details

3.2.1 Materials

Microcrystalline graphite (2- 15 μm , 99.99 %) was purchased from Alfar Aesar. Other reagent grade chemicals purchased from Sigma-Aldrich and used without further purification include: potassium permanganate ($\geq 99.0\%$, ACS reagent), hydrogen peroxide solution (30 wt. % in water, ACS reagent), sodium hydroxide (98 – 100.5 %), tetrahydrofuran ($> 99.8\%$), ethanol (absolute, $\geq 99.8\%$). Concentrated sulfuric acid (99.999 %), borane in tetrahydrofuran complex (1 M), lithium perchlorate (99.99 %), chloroform and anhydrous N-methyl-2-pyrrolidone (99.5 %), polytetrafluoroethylene (mean particle size 20 μm), activated charcoal (Norit $\text{\textcircled{R}}$ pellets) and carbon black (4 μm mesoporous carbon matrix, $\geq 99.95\%$ metal basis). Concentrated hydrochloric acid (reagent grade and assay 36.5 – 38.0 %) was obtained from Kimix chemicals and nickel foam (1.6 mm thick, 0.25 μm pore diameter) purchased from MTI Corporation.

3.2.2a. Synthesis of Graphene oxide (GO)

Graphene oxide was prepared by chemical exfoliation of graphite according to a modified Hummers method [20]. Typically, 50 mL of concentrated H_2SO_4 was added into a 250 mL flask containing 2 g of graphite at room temperature and vigorously stirred to avoid agglomeration of the graphite powder. The flask was cooled to 0 $^\circ\text{C}$ in an ice bath, followed by slow addition of 7 g of KMnO_4 with a resultant dark green coloration. The flask was removed from the ice bath and temperature was allowed to rise to 35 $^\circ\text{C}$. The mixture was

stirred for 2 h, cooled down again in an ice bath with subsequent addition of 120 mL of distilled water to give a light pink color. Thereafter, 30 mL of H₂O₂ was added dropwise until gas evolution ceased. The resultant suspension was washed copiously with water and centrifuged to remove the unexfoliated graphite. GO was finally obtained by vacuum drying the product overnight at 65 °C.

3.2.2b. Synthesis of hydroxylated graphene (graphol /G-ol) nanosheets

Graphol was prepared by hydroboration of graphene oxide as illustrated in Figure 3.1. Firstly, 200 mg of graphene oxide obtained in section 3.2.2a above was ultrasonicated in 200 mL of anhydrous tetrahydrofuran (THF) for 1 h followed by addition of 20 mL of borane in THF complex. The mixture was heated at 50 °C with reflux under argon atmosphere for 24 h. A mixture of 3 M aqueous NaOH and 30 % H₂O₂ was slowly added and the reaction was further kept at 50 °C for 3 h under reflux. Hydroxylated graphene nanosheets were obtained by suction filtration and washed several times with THF and water. The nanosheets were dried in a vacuum oven at 50 °C for 48 h.

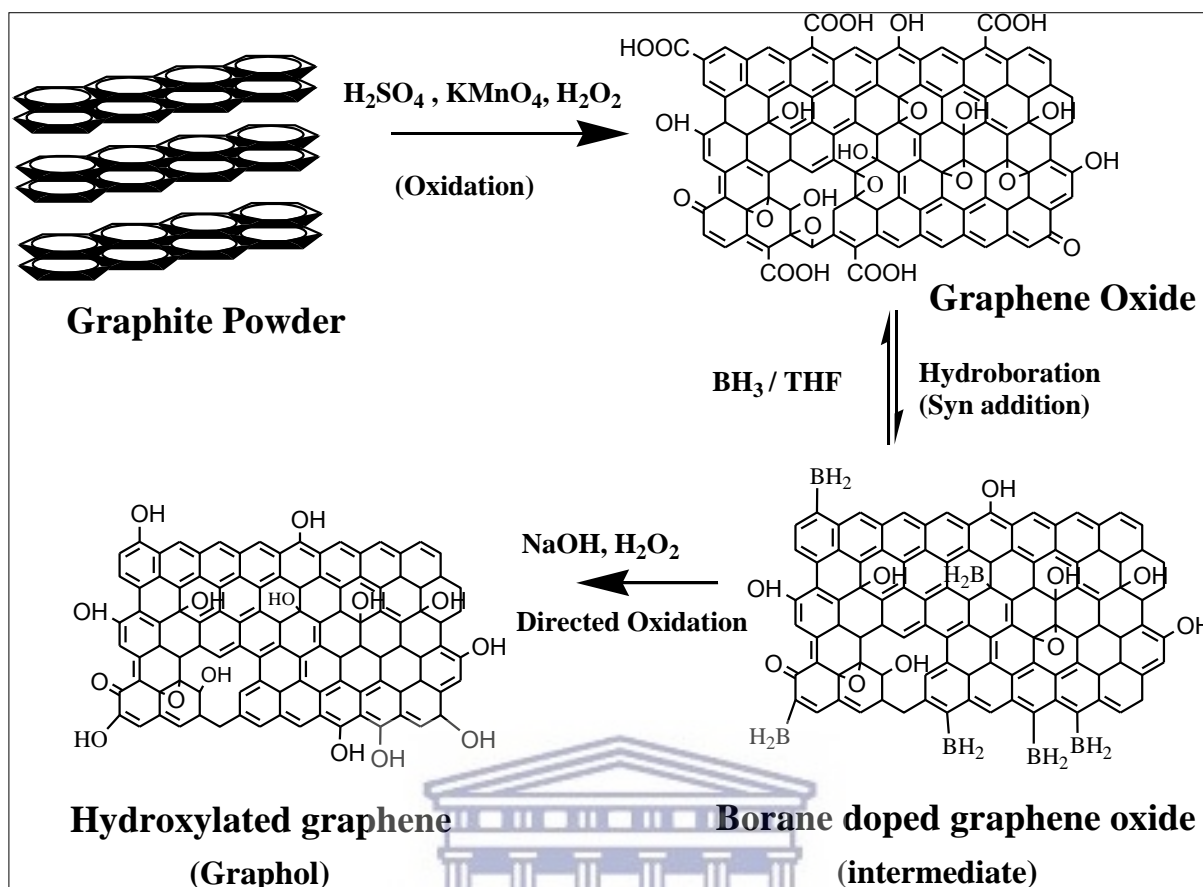


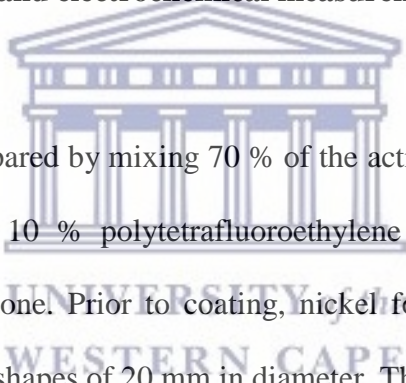
Figure 3.1: Schematic illustration of the synthesis pathway of graphol

3.2.3.1 Material Characterization

The morphology and elemental composition of the nanosheets were obtained using ZEISS ULTRA scanning electron microscope equipped with an energy dispersive spectrometer and a Tecnai G² F₂O X-Twin MAT 200 kV field emission transmission electron microscope from FEI. The analyses were performed on a nickel-copper grid. The particle size distribution of the nanomaterials was obtained by small-angle X-ray scattering experiments performed on an Anton Paar SAXSpace system. Copper K α radiation (0,154 nm) was used and the instrument is equipped with a 1 D mythen 2 position sensitive detector and a beamstop alignment. X-ray

powder diffraction patterns of the carbon-rich nanomaterials were obtained using a D8 advance diffractometer (BRUKER-AXS) using copper $K\alpha_1$ radiation ($\lambda \sim 0.154$ nm) operating at 40 kV and 40 mA. A Perkin Elmer Spectrum 100 series Attenuated Total Reflection (ATR) Fourier Transform Infrared spectrometer with a resolution of 4 cm^{-1} was used to obtain the functional groups present in the materials. A HORIBA scientific Xplora Raman microscope integrated with a 532 nm laser and Labspec spectral software with a resolution of $1\ \mu\text{m}$ was used to obtain the vibrational modes present in the materials. Electrochemical studies were performed using both three and two-electrode cells on a VMP-300 potentiostat from Bio-Logic instruments.

3.2.3.2 Electrode preparation and electrochemical measurements



The working electrode was prepared by mixing 70 % of the active material with 20 % carbon black (conducting agent) and 10 % polytetrafluoroethylene (binder) in a few drops of anhydrous N-methyl-2-pyrrolidone. Prior to coating, nickel foam was cut into rectangular shapes of $0.5 \times 1\text{ cm}^2$ and coin-shapes of 20 mm in diameter. The different sizes were cleaned and etched to remove surface oxide layer using 1 M HCl solution in an ultrasonic bath for 15 mins, then cleaned in absolute ethanol and deionized water for 15 min in sequence by ultrasonication and finally dried at $90\text{ }^\circ\text{C}$ for 12 h. A homogenous paste was obtained using a mortar and pestle and coated on nickel foam with a diameter of 0.5 cm^2 using a spatula and dried at $80\text{ }^\circ\text{C}$ for 12 h. Ag/AgCl and Pt wire were used as the reference and counter electrodes, respectively for studies in three-electrode system. For two-electrode cell analysis, the homogenous paste was coated on coin-shaped nickel foam with a diameter of 20 mm and assembled in a Swagelok using graphol nanosheets as the positive electrodes and activated carbon as the negative electrode. Cyclic voltammograms were recorded in a potential window

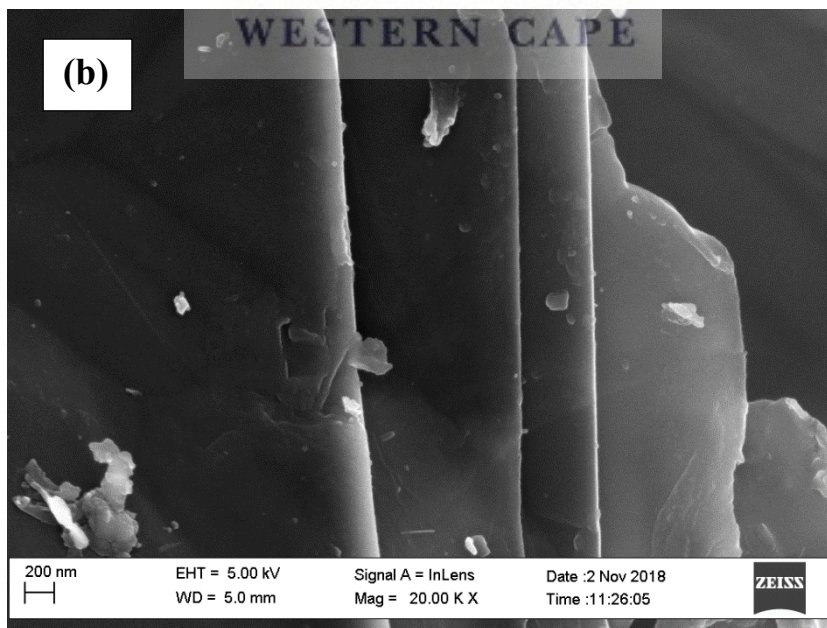
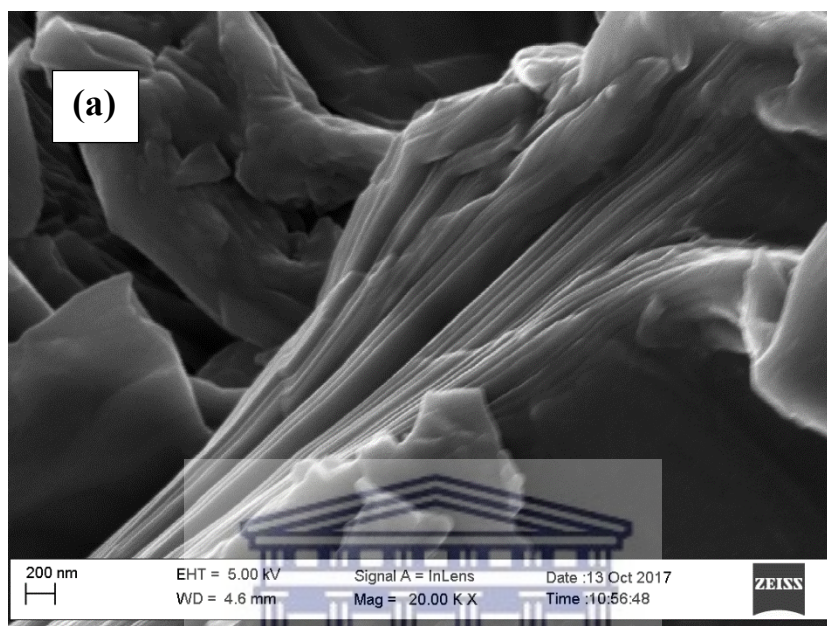
of -0.2 to 0,8 V at different scan rates and electrochemical impedance measurements were obtained at a frequency range of 0.1 MHz –100 kHz with 10 points per decade. CV curves, galvanostatic charge-discharge profiles and the cycling performance of the supercapacitor cells were obtained in aqueous 0.5 M LiClO₄ electrolyte at a voltage of 1.6 V.

3.3 Results and Discussion

3.3.1 High-resolution Scanning and Transmission Electron Microscopic Analysis

Morphological features, elemental composition and the nanostructure of the carbon-based materials were investigated by high-resolution scanning and transmission electron microscopies (HRSEM and HRTEM). SEM high magnification images of graphene oxide and graphol nanosheets are shown in Figure 3.2.1 (a) and (b), respectively. The exfoliated graphene oxide nanosheets are observed to be layers of 11 – 45 nm thick, found in stacks of 20 -25 layers. Whereas, the graphol (G-ol) nanosheets are observed as single layers with a thickness of 14- 23 nm, which is attributed to the disruption of the planar sp² carbon sheets of graphene oxide by the introduction of sp³-hybridized carbon upon oxidation [21]. Figure 3.2.1 (c) and (d) display the HRTEM images of GO and G-ol nanosheets, with their selected area diffraction (SAED) images, (e) and (f) as insets, respectively. The HRTEM images also reveal stacked sheets for GO and G-ol single layers as seen in SEM observations. SAED images reveal that the materials are crystalline, with graphol showing better and clear concentric circles, indicating a more ordered pattern and a reduction in the number of graphene layers [22]. Elemental analysis by energy dispersive spectroscopy (EDS) coupled to TEM is shown in

Figure 3.2.2. G-ol is observed to have a higher oxygen content than graphite and GO as expected.



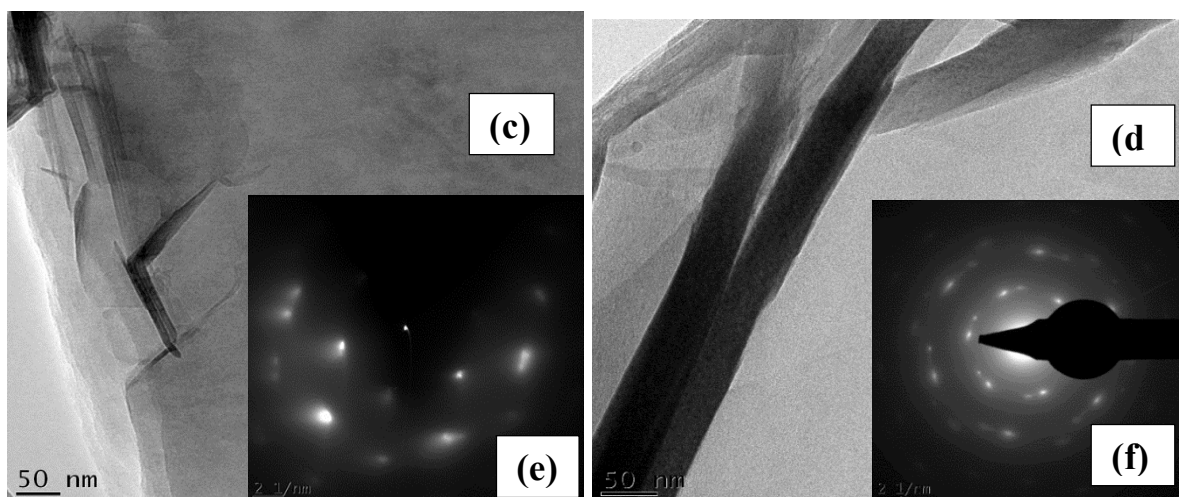


Figure 3.2.1: SEM image of GO (a), G-ol (b), HRTEM image of GO (c), G-ol (d), SAED image of GO (e), G-ol (f)

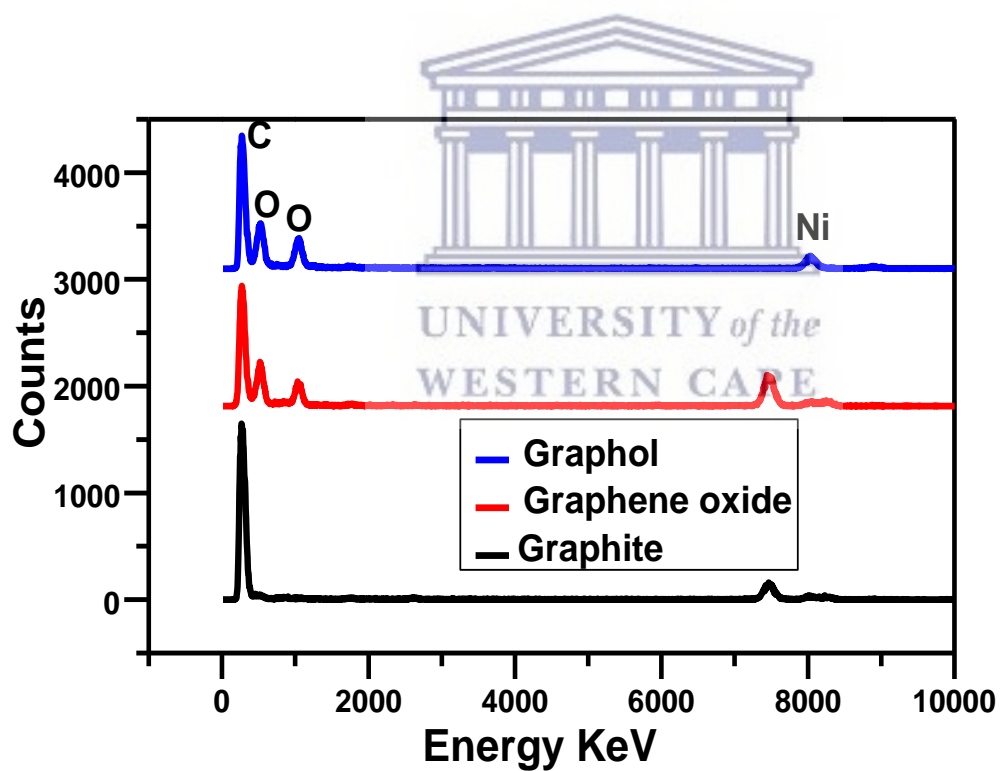


Figure 3.2.2: EDS spectra of Graphite, GO and G-ol

3.3.2 X-ray diffraction Studies

Powder X-ray diffraction was used to study the crystal structure, phase purity and interplanar spacing between the graphitic planes of the nanomaterials. Figure 3.3 shows the XRD spectra of graphite, GO and G-ol at 2 theta range of 5 – 70 °. The spectrum of graphite shows two prominent peaks at 2 theta values of 24.9 and 42.9 °, which belong to the reflections of 002 and 004 planes, respectively. GO and G-ol show much broader peaks for the 002 reflection due to the reduction in the crystallite sizes, with an additional peak developing around 2 θ values of 10 – 11.5 °. This distinct peak is attributed to the 001 plane, induced by functionalization (oxidation) of graphite. These patterns are similar to those reported by previous studies [23,24].

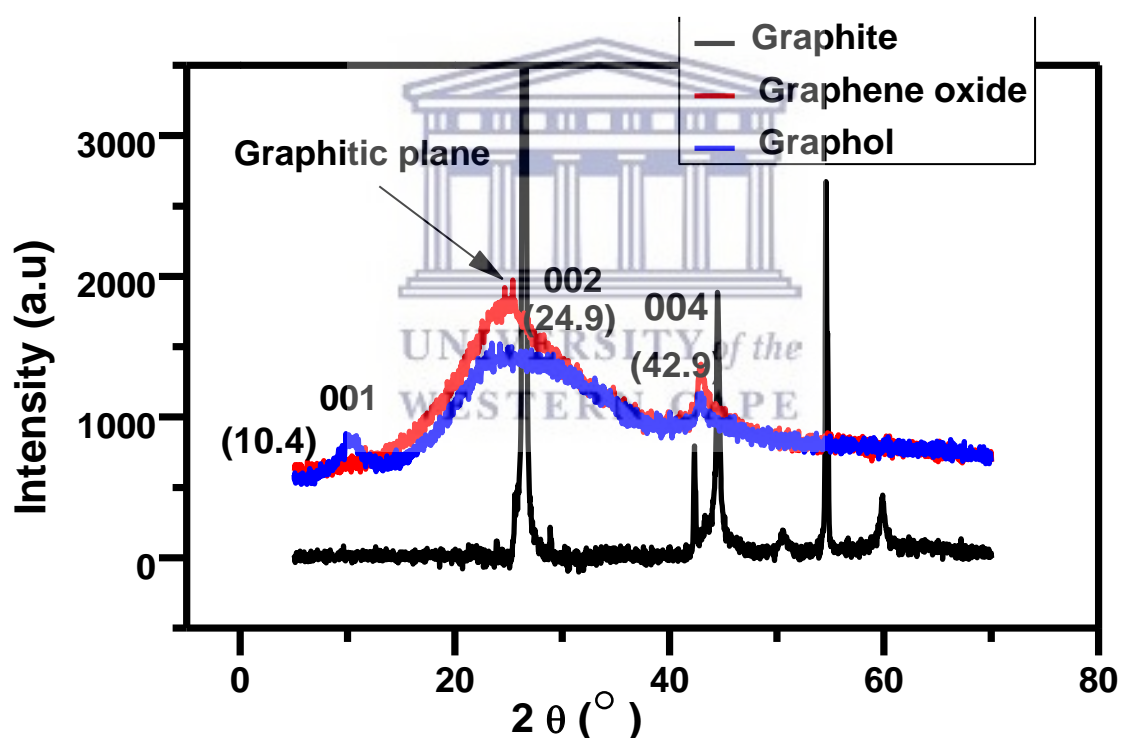


Figure 3.3: XRD pattern of graphite, GO and G-ol.

The interplanar (d) spacing for the carbon-based materials was calculated using Bragg's law, Equation 3.1.

$$n\lambda = 2d\sin\theta \quad (3.1)$$

Where, n is the first order of diffraction ($n = 1$), λ ; the wavelength of the X-ray beam (0.154 nm), d ; the distance between the graphitic sheets or layers (d-spacing) and θ is the diffraction angle. The d-spacing obtained from the 002 plane of graphite at 12.5 degrees was 0.34 nm, while GO and G-ol showed d-spacings of 0.80 nm and 0.88 nm, respectively. These values were calculated from the 001 reflection of GO and G-ol. The interlayer spacing increased from graphite to GO and G-ol due to the intercalated oxygen, hydroxyl, epoxy, and carbonyl functional groups at the basal planes of the graphitic sheets. Weak van der Waals forces between epoxy and carbonyl groups are also said to influence the d-spacing of GO and other functionalized graphitic materials. The increasing values of the d-spacing from graphite to GO and G-ol is considered as good evidence for exfoliation and absence of restacking in the graphitic sheets. These results are in good agreement with literature reports by Zaaba and Emiru *et al.* [25,26].

The average crystallite sizes of graphite, GO and G-ol were calculated using Scherrer's formula, Equation 3.2.

$$D = \frac{K\lambda}{\beta\cos\theta} \quad (3.2)$$

Where: D is the mean crystallite size, K is the shape factor constant (0.89), λ is the wavelength of the X-rays, β is the full width at half maximum (FWHM) of the (210) Bragg peak, and θ is

the angle of reflection of the crystalline plane. The calculated grain sizes were at 59.0 nm for graphite, 34.5 nm for GO and 23.3 nm for G-ol, as shown in Table 3.1.

Table 3.1: Structural properties of graphite, GO and G-ol nanosheets.

Material	Interlayer spacing / nm	Average crystallite size / nm
Graphite	0.34	59.0
GO	0.80	34.5
G-ol	0.88	23.3

Simulation studies were further performed on the crystallographic patterns of the carbon-based materials to determine the atomic positions and the effect of functionalization on the crystalline domains using crystallographic information files (CIF) obtained from phase identification and structure solution (Match and Endeavour) softwares. Prism-shaped crystallite clusters of graphite were observed with interlayer spacing of 0.34 nm and a few oxygen atoms probably emanating from moisture adsorbed during XRD measurements. Oxidation of graphite to GO resulted in the formation of new C-O bonds and spherical clusters of carbon and oxygen atoms sandwiched in between. From the model structure of G-ol, it is evident that graphitic sheets were completely exfoliated with the formation of many new bonds such as C-O, C-OH, and C-O-C. These studies corroborate results obtained from morphological and powder X-ray diffraction studies.

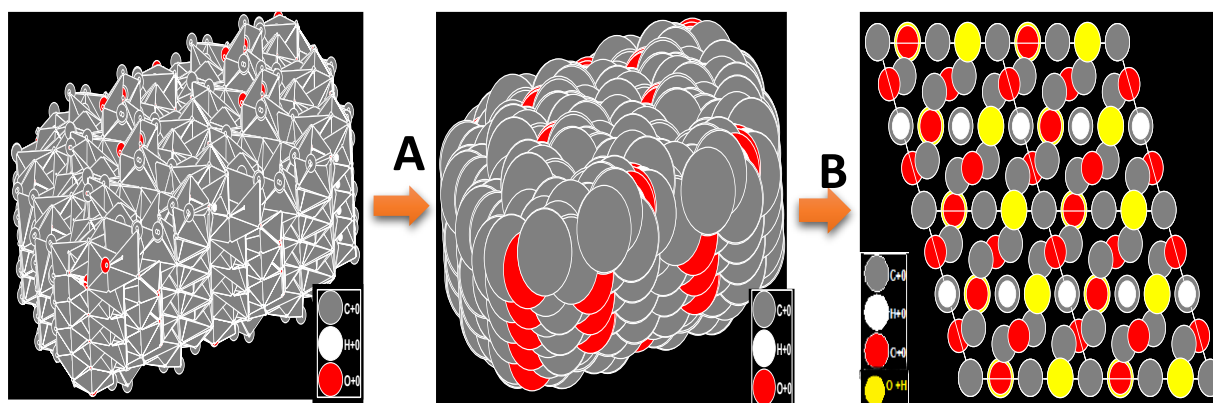


Figure 3.4: Model structures of graphite, GO and G-ol showing the position of all atoms obtained simulated using Match and Endeavour softwares. A = oxidation, B = hydroboration/oxidation.

3.3.3 Small-angle X-ray scattering experiments

The size of the graphitic primary sheets, their aggregates and the size distribution of the nanosheets with oxidation was investigated using SAXS analysis. Figure 3.5 (a) and (b) represent the particle size distribution based on the intensity of the scattered nanosheets and the particle size distribution based on the physical volume of the scattered nanosheets, respectively. The intensity particle size distribution of graphite is characterized by a left-skewed distribution/curve indicating a variation in the sizes of the stacked graphitic sheets. The intensity particle size distribution of GO and G-ol reveal almost a normal distribution or bell-shaped curves displaying a multi-peak arrangement. Small peaks at 17.7 nm and 9.6 nm reveal very small nanosheets of GO and G-ol, respectively. The center peaks at 30.8 nm and 31.3 nm indicate the primary particle sizes for GO and G-ol, respectively with aggregates of the primary particles at 66.7 nm for GO and 45.5 nm for G-ol. These particle size distributions agree well with the average crystallite sizes obtained from XRD measurements. The volume particle size

distribution follows a bell-shaped distribution curve for all materials with a mixture of primary-particles, intermediates, and aggregates of primary particles. The nanosheets display reduced particle sizes due to the fact that at low volume fractions, nucleation behavior is favored with a decrease in size while at high volume fractions, smaller particles outnumber fewer larger particles leading to a decrease in the average diameter of the graphitic sheets [27].

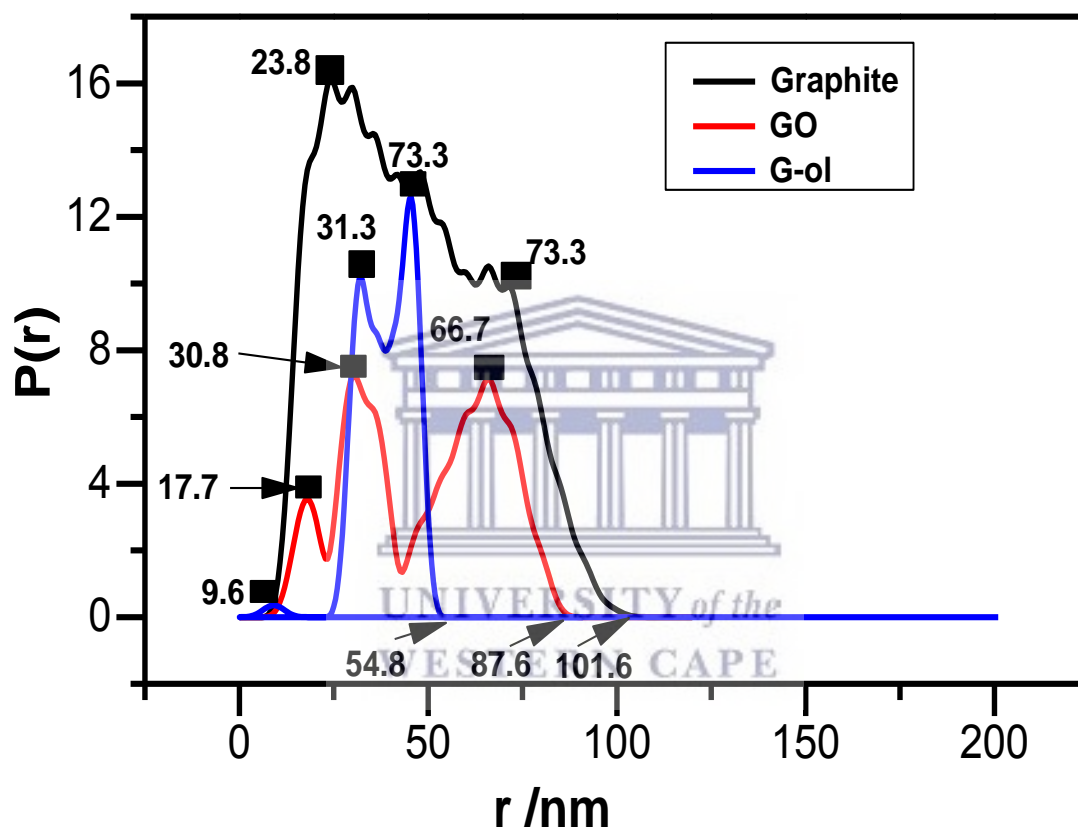


Figure 3.5 (a): Intensity particle size distribution of Graphite, GO and G-ol nanosheets

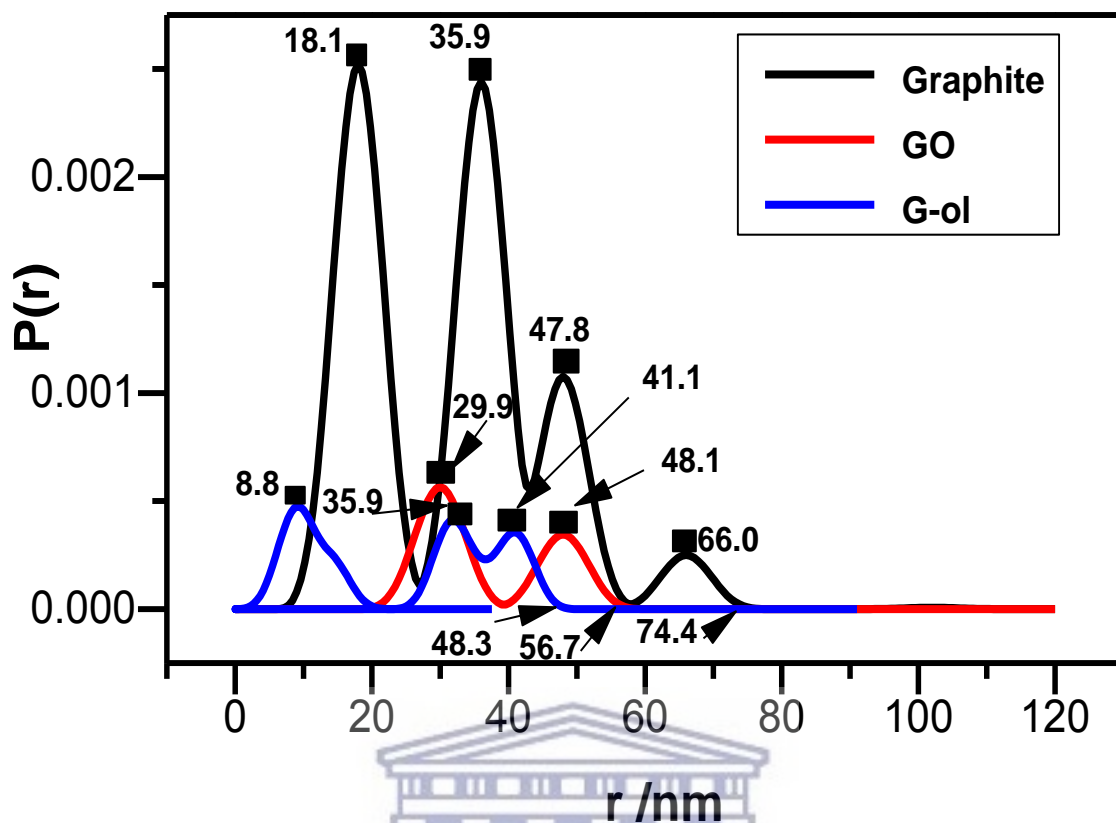


Figure 3.5 (b): Volume particle size distribution of Graphite, GO and G-ol nanosheets

3.3.4 Fourier transform Infrared (FTIR) Spectroscopic Analysis

FTIR spectroscopy was used to investigate the nature of functional groups present and new bonds formed upon oxidation of graphite to GO and subsequent hydroboration/oxidation to G-ol. The FTIR spectra of graphite, GO and G-ol are presented in Figure 3.6 (a), with the enlarged spectrum of GO shown in Figure 3.6 (b). Spectra are presented in the range of $4000 - 400 \text{ cm}^{-1}$ with very little bond vibration observed for graphite. The FTIR spectra of GO and G-ol exhibit characteristic stretching and bending vibrations of the OH group at 3229.8 cm^{-1} for GO with an intense band at 3409.4 cm^{-1} for G-ol, indicating covalent functionalization of carbon backbone with hydroxyl groups. Also, G-ol shows two strong stretching vibrations of sp^3 C-H bonds at 2921.6 and 2851.9 cm^{-1} in addition to the symmetric band at 788.1 cm^{-1} . While GO

exhibits a C-H characteristic band at 2815.1 cm^{-1} . This is due to the presence of sp^2/sp^3 carbon centers in GO and G-ol induced by oxidation [28,29]. The peak at 1720.3 cm^{-1} in G-ol and 1715.6 cm^{-1} in GO is assigned to carbonyl C=O groups. Furthermore, GO exhibits a strong band at 1561.8 cm^{-1} which is characteristic of graphitic domains (C=C), which is blue-shifted in G-ol and appears at 1588.9 cm^{-1} due to the difference in the chemical environment. The peaks at ~ 1254.2 and 1075.6 cm^{-1} in G-ol and 1029.9 cm^{-1} in GO are due to the presence of epoxy and alkoxy functional groups in these materials [30,31]. These analyses are further confirmed by Raman spectroscopic studies.

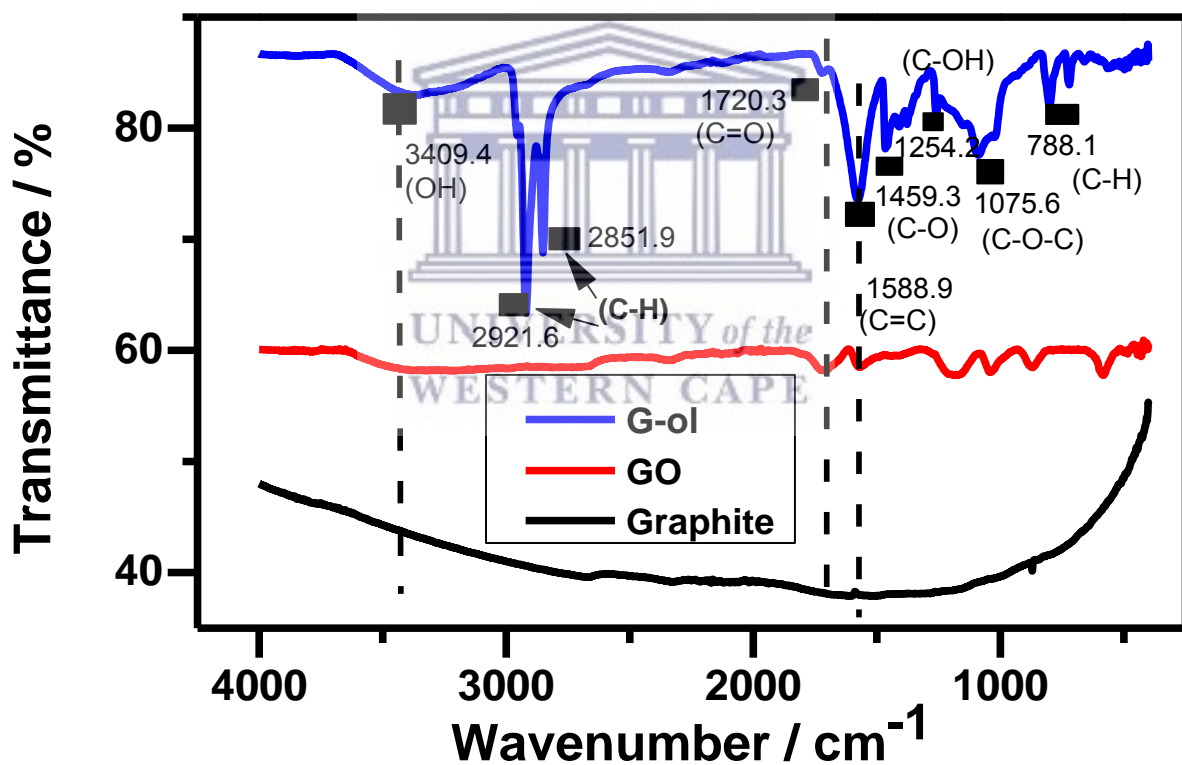


Figure 3.6 (a): FTIR spectra of graphite, GO and G-ol nanosheets

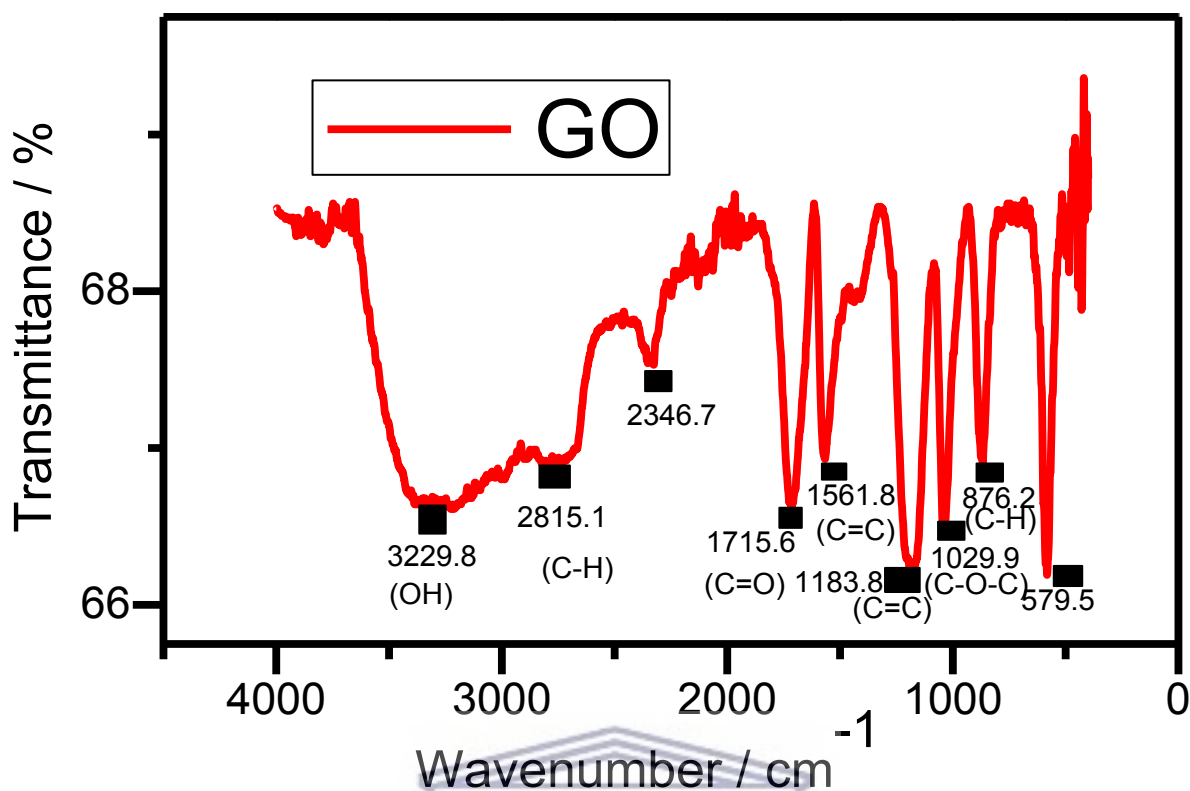


Figure 3.6 (b): FTIR spectrum of GO nanosheets (enlarged)

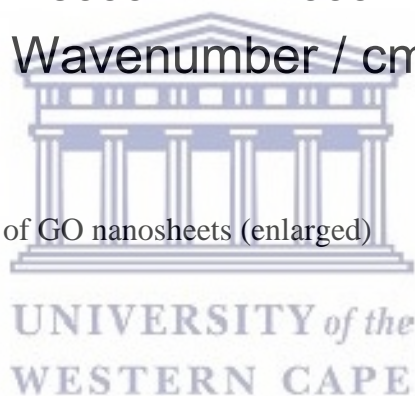


Table 3.2: Functional groups/ bonds present in graphite, GO and G-ol.

Functional groups / bond	Material / Wavenumber		
	Graphite / cm^{-1}	GO / cm^{-1}	G-ol / cm^{-1}
OH	-	3229.8	3409.4
C-H	881.8	2815.1, 876.2	2921.6, 2851.9, 788.1
C=O	-	1715.6	1720.3
C=C	1622.5	1561.8, 1183.8	1588.9, 1145.3

C-O-C	-	1029.9	1075.6
C-OH	-	--	1254.2
C-O	-	-	1459.3

3.3.5 Raman Spectroscopic Studies

Raman spectroscopy was used to investigate the vibrational modes and quality of oxidized GO and G-ol nanosheets. The Raman spectra of Graphite, GO and G-ol are shown in Figure 3.7. The spectra of these graphitic materials are characterized by the D and G modes, whereby, the D mode denotes dispersive vibrations induced by disorder intrinsic to sp² hybridized carbon systems and the G mode which describes the vibration of sp² bound carbon atoms [23,32]. The Raman spectra of graphite, GO and G-ol were collected in the range of 600 to 3500 cm⁻¹. The most prominent peaks are assigned to the D-band, G-band, 2D-band (double overtone of the D-band) and the D+G- band (band indicating the presence of edge-like defects in the basal planes of the graphitic materials). Values obtained for the different Raman modes are recorded in Table 3.3. The D-band was observed at 1460.3 cm⁻¹ for graphite with a slight blue shift for GO (1342 cm⁻¹) and G-ol (1358.2 cm⁻¹). The variation to lower Raman shift values in GO and G-ol is attributed to the disruption of the sp² hybridized carbon network in graphite with the introduction of some sp³ carbon centers in GO and G-ol [29]. The Raman active G-band for sp² hybridized carbon-centers in the materials was observed at 1565.3 – 1573.3 cm⁻¹ and the double overtone 2D-band was obtained at 2436.3 ± 0.6 cm⁻¹ for all three materials. The decrease in the intensity of the 2D-band in G-ol is attributed to the breakage of the stacking order of C-C bonding in GO and increasing degree of oxidation. The D+G combination band

was observed at Raman shift values of 2947 – 2972 cm^{-1} with weak intensities for graphite and GO. G-ol, on the other hand, showed much higher intensities with a shoulder band at 2971.5 cm^{-1} indicating various edge-like defects formed on the basal planes of GO sheets during functionalization [33]. The ratio of the intensity of the D-band to the G-band (I_D/I_G) provides more insights on the nature of defects present in the graphitic layers and the different sp^2 and sp^3 carbon atoms [22,34]. I_D/I_G values calculated from the peak integration showed reducing values from graphite to graphol. This is due to the breakage of graphitic linkages (structural distortions) with more sp^3 character induced by the presence of hydroxyl, carboxyl and epoxide groups on the carbon basal planes as evidenced by XRD and FTIR studies.

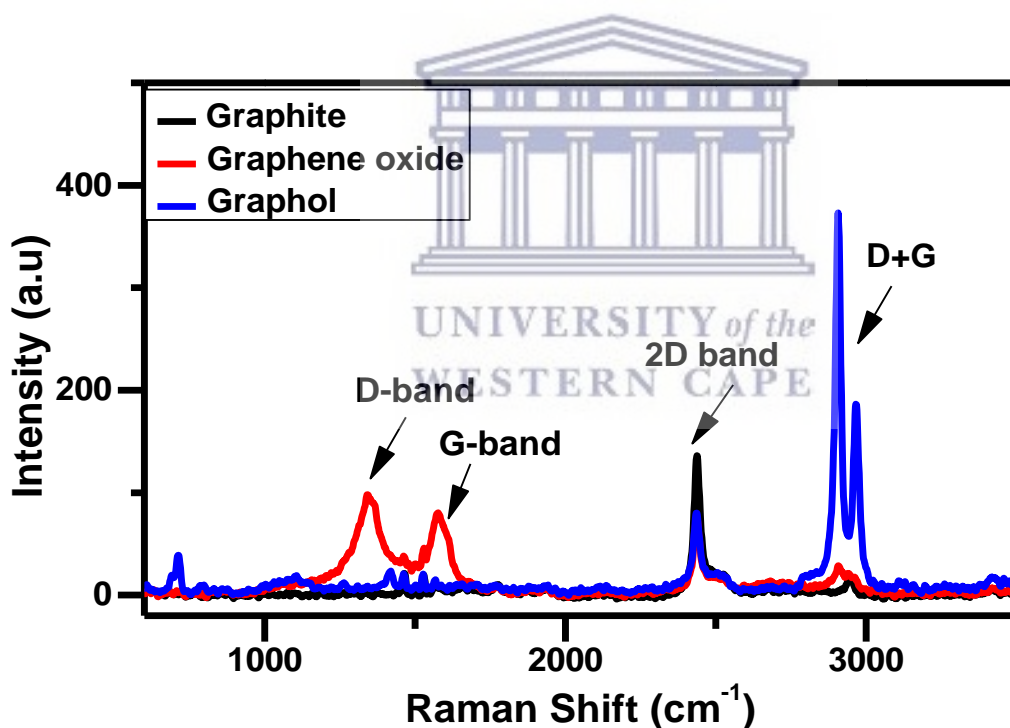


Figure 3.7: Raman spectra of graphite, GO and G-ol nanosheets excited by 514.9 nm laser.

Table 3.3: Raman active modes of graphite, GO and G-ol

Material	D-band (cm^{-1})	G- band (cm^{-1})	2D- band (cm^{-1})	D+G	I_D/I_G
Graphite	1460.3	1565.3	2436.9	2947.89	2.03
Graphene oxide	1342.0	1573.3	2436.3	2908.2	1.23
Graphol	1358.2	1566.6	2436.9	2903.6, 2971.5	0.67

3.3.6 Solid state ^{13}C Magic Angle Spinning Nuclear Magnetic Resonance

Spectroscopic Studies (SS- ^{13}C -MAS NMR)

SS- ^{13}C -MAS NMR was further employed for confirmation of the change in chemical structure and composition with functionalization. Figure 3.8 displays the ^{13}C MAS SS-NMR spectra of graphite, GO and G-ol. Spectra are dominated by resonances from graphitic sp² carbon atoms (-C=C-) occurring at ~110.9 ppm for G-ol and 111.3 for GO and graphite, with spinning sidebands at ~191 ppm for all three materials. The graphitic sp² carbon signal in GO is broadened with a shoulder band at ~128 ppm. This is attributed to the changes in the chemical environment of the hybrid carbon atoms present in GO. These results are consistent with other reports by Si and Wang *et al.* [29,35].

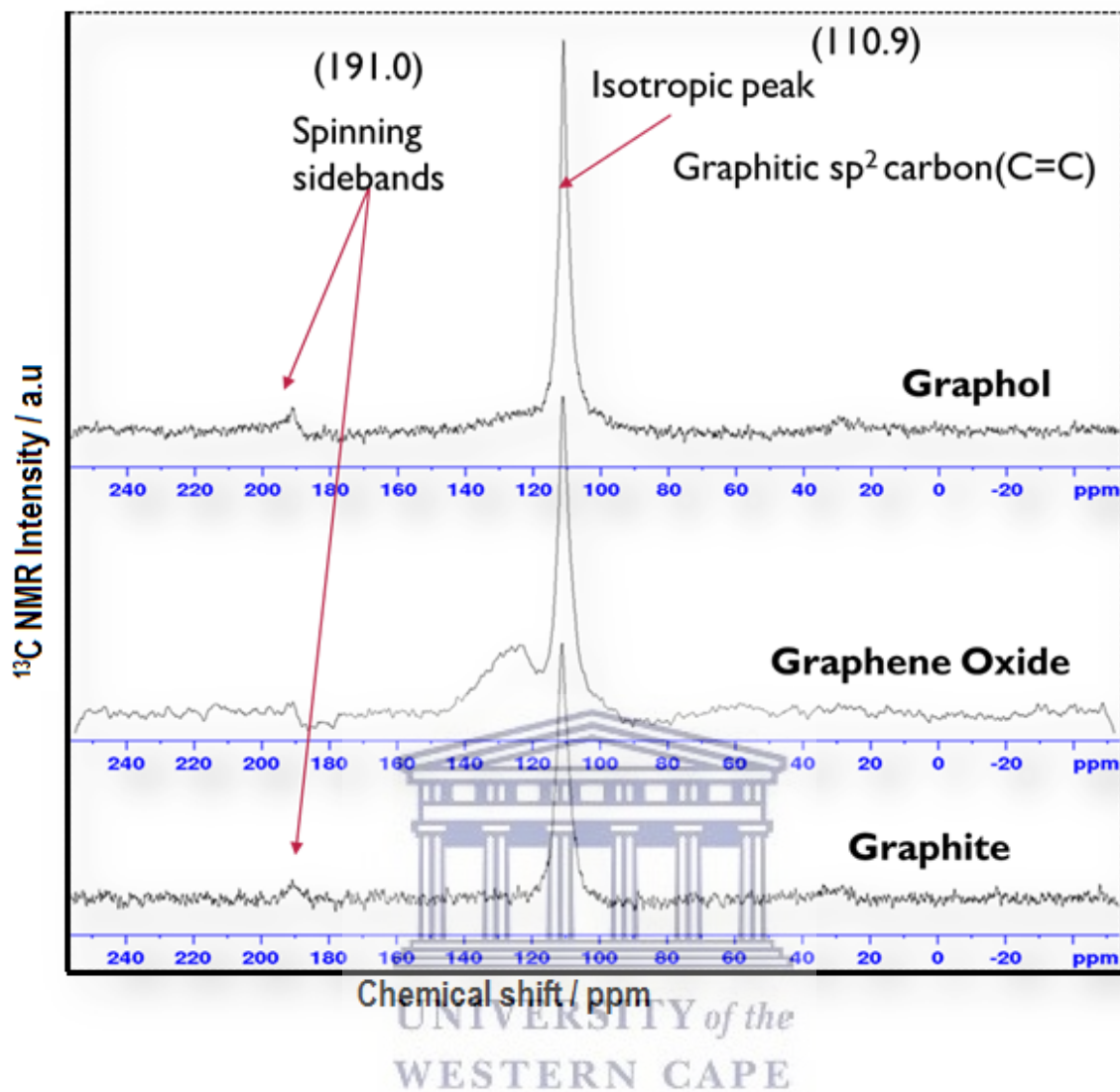


Figure 3.8: ^{13}C MAS SS-NMR spectra of graphite, GO and G-ol nanosheets.

3.3.7 Electrochemical Performance of graphite, GO and G-ol

The electrochemical performance of the carbon-based materials was characterized using cyclic voltammetry (CV), electrochemical impedance spectroscopy (EIS) and galvanostatic charge-discharge studies (GCD) in 0.5 M LiClO_4 -aqueous electrolyte.

i) **Cyclic Voltammetric (CV) studies**

CV curves were obtained at scan rates of 10 – 50 mV s⁻¹ at a potential window of -0.2 – 0.8 V. Figure 3.9 (a) presents a comparative plot of the CV profile of graphite, GO and G-ol at a scan rate of 40 mV s⁻¹. The CV profile of G-ol at different scan rates is shown in Figure 3.9 (b). Graphite showed a very little current response whereas, GO and G-ol showed rectangular-shaped voltammograms exhibiting an increase in current response with increasing scan rate, indicating capacitive charge storage with a high degree of electrochemical reversibility. No redox peaks were observed in the rectangular-shaped CV curves for all scan rates, which is typical of electrical double-layer capacitors [4]. Therefore, no pseudocapacitance contribution was shown by the oxygen and hydroxyl functionalization on the basal planes of the graphitic materials. The specific capacitance of graphite, GO and G-ol were calculated from the cyclic voltammograms using Equation 3.3.


$$C_{sp} = \frac{1}{2m\nu\Delta V} \int_{-V}^{+V} I dv \quad (3.3)$$

Where m denotes the active mass of the electrode, ν is the scan rate, ΔV is the potential window

and $\int_{-V}^{+V} I dv$ is the absolute area under the CV curve. The specific capacitance values are plotted

against potential sweep rates as shown in Figure 3.9 (c). The values vary from 1.68 F g⁻¹ at 10 mV s⁻¹ to 0.71 F g⁻¹ at 50 mV s⁻¹ for graphite, while GO delivered a specific capacitance of 24.0 F g⁻¹ at 10 mV s⁻¹ and 10.5 F g⁻¹ at 50 mV s⁻¹. G-ol demonstrated better electrochemical

performance with a high specific capacitance 73.8 F g^{-1} at 10 mV s^{-1} and up to 43.2 F g^{-1} at 50 mV s^{-1} .

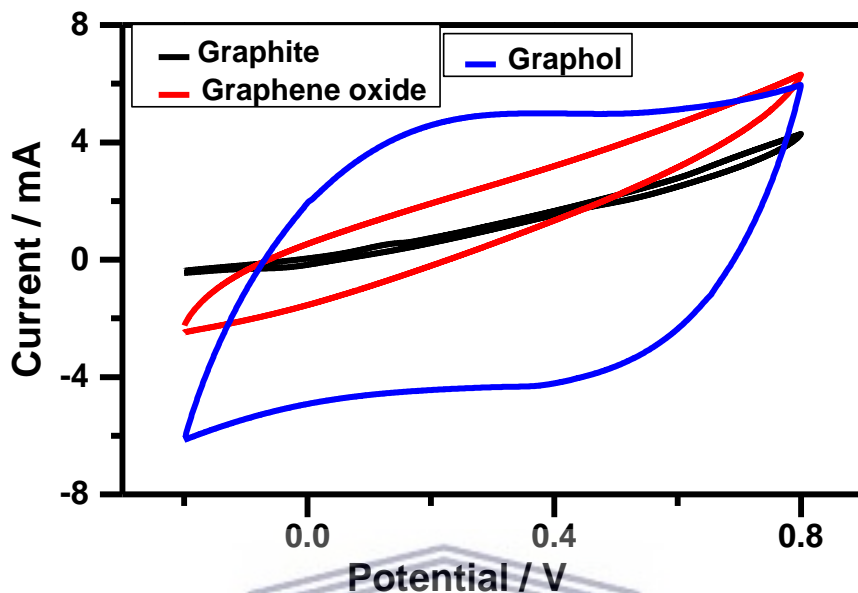


Figure 3.9 (a): CV curves of graphite, GO and G-ol at a scan rate of 40 mV s^{-1} in 0.5 M LiClO_4 -aqueous electrolyte at a potential window of $-0.2 - 0.8 \text{ V}$

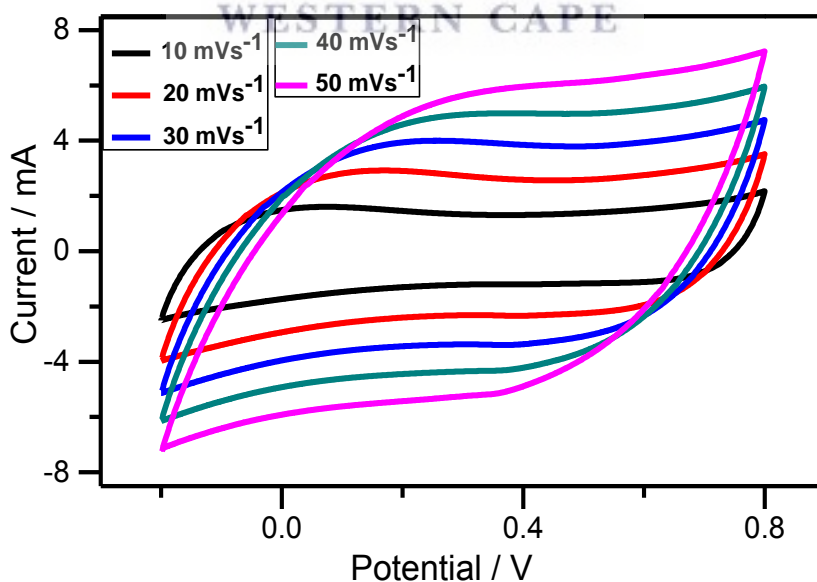


Figure 3.9 (b): CV curves of G-ol at scan rates of $10 - 50 \text{ mV s}^{-1}$ in 0.5 M LiClO_4 -aqueous electrolyte

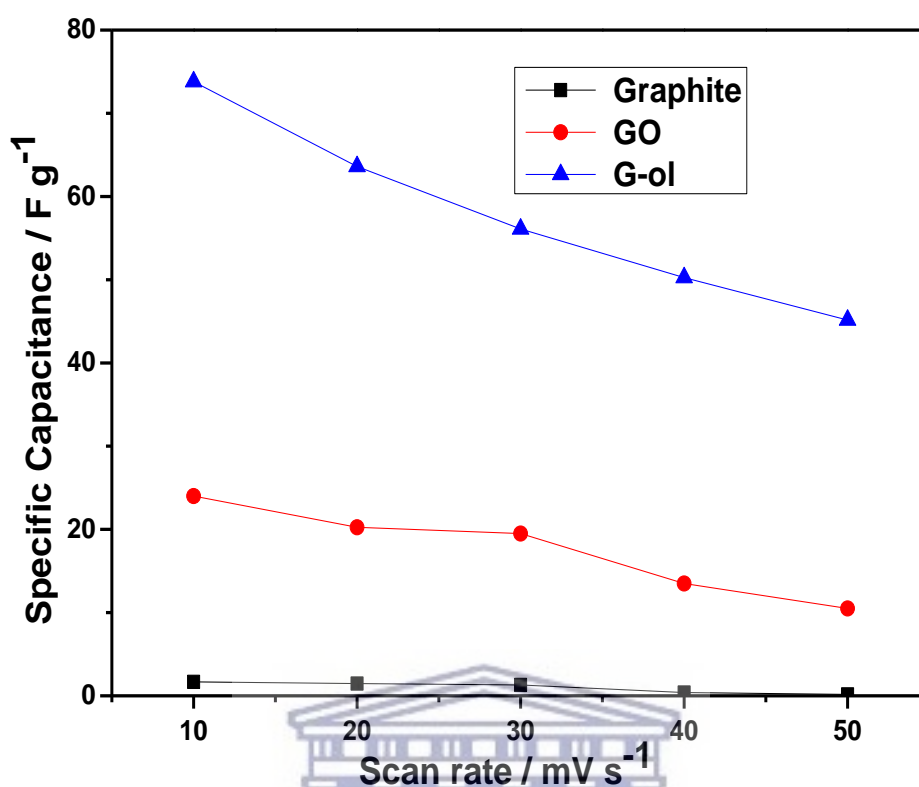


Figure 3.9 (c): Variation of specific capacitance with scan rate for graphite, GO and G-ol

ii) Galvanostatic charge-discharge (GCD) studies

GCD curves of G-ol at current loads of $0.5 - 2.0 \text{ A g}^{-1}$ are presented in Figure 3.10 (a) at a potential window of $-0.2 - 0.8 \text{ V}$. Typical triangular curves are observed, which further confirm the electric double layer capacitive charge storage mechanism occurring at the electrode-electrolyte interface [36]. The charge-discharge curves are almost symmetrical with a small voltage drop arising from the equivalent series resistance (*ESR*). The charging and discharging times are almost the same, signifying a high coulombic efficiency and electrochemical reversibility. The specific charge and discharge capacitances were obtained from the GCD plots using Equation 3.4.

$$C_{sp} = \frac{I \times t}{m(V - IR_{drop})} \quad (3.4)$$

Where, m represents the active mass of the electrode (g), V is the potential window (V), IR_{drop} is the voltage drop / equivalent series resistance (V), I is the applied current (A) and t is the charge/discharge time (s). G-ol delivered specific charge and discharge capacitances of 135.5 F g^{-1} and 77.5 Fg^{-1} , respectively at a current load of 0.5 A g^{-1} . Even at a higher current load of 2.0 A g^{-1} , the G-ol electrode delivered good specific charge and discharge capacitances of 59.3 F g^{-1} and 56.1 Fg^{-1} , respectively at a coulombic efficiency of 94.5 %. The specific charge and discharge capacitance values decreased with increasing current load as presented in Figure 3.10 b. These capacitance values are in good agreement with the CV results.

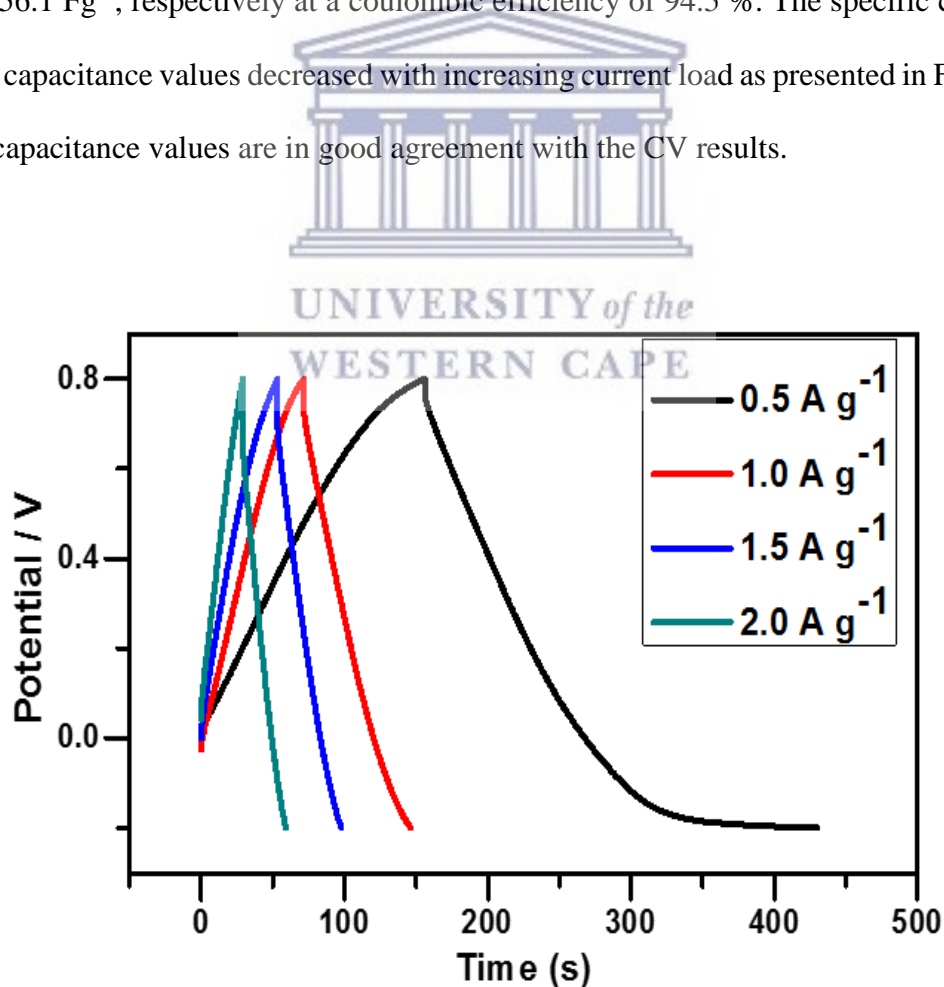


Figure 3.10 (a): GCD profiles of G-ol at different current loads

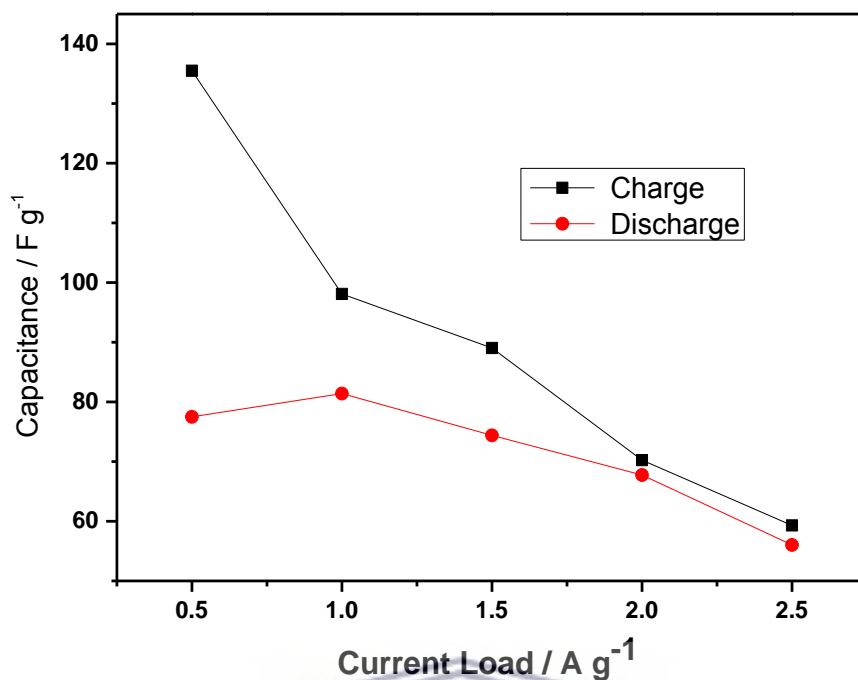
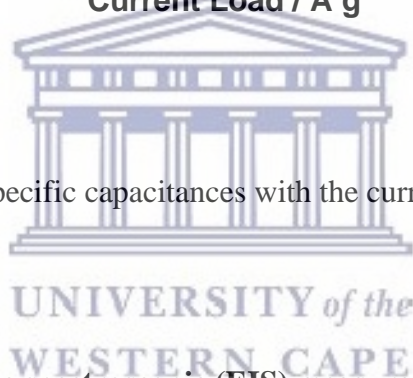


Figure 3.10 (b): Variation of specific capacitances with the current load of G-ol



iii) Electrochemical impedance spectroscopic (EIS) measurements

EIS was used to study the electron transfer processes between the interfacial electrode surface and the electrolyte. EIS measurements were recorded at open-circuit voltage (OCV) in the frequency range of 0.1 MHz to 100 kHz at an amplitude of 5 mV. As shown in Figure 3.11 (a), the Nyquist plots consist of a semicircle at the high-frequency domain, which is related to the charge transfer resistance (R_{ct}). The bulk electrolyte resistance and inter/intra-particle electrical resistances originating from the porous nature of the electrode materials is shown by the intercept of the semicircle to the Z_{real} axis, known as the equivalent circuit resistance (ESR) denoted by R_s in the circuit diagrams as illustrated in Figure 3.11 (b). An inclined line in the

middle to low-frequency region of the curve represents Warburg diffusion (W_o) within the host of the materials. The constant phase element (CPE) which describes the double layer capacitance between the electrodes –electrolyte interface as a function of electrode potential was also observed. Values of the R_{ct} , R_s , W_o , and CPE are tabulated in Table 3.4, obtained by curve fitting the EIS plots in Z view according to the circuit models in Figure 3.11 (b).

As seen on the high-frequency enlarged area of the Nyquist plots of graphite, GO and G-ol (the inset), it is eminent that graphite does not exhibit a distinct semicircle, indicating lack of a faradaic contribution associated with redox species at the electrode surface. G-ol shows a slightly higher R_{ct} value than GO due to the presence of excessive oxygenated and hydroxyl species (observed in FTIR and Raman spectroscopies) which arouse some insulating characteristics and slightly hinder its electrochemical properties [37]. This is further explained in a report by Abouelamaiem and co-workers, where it is ascertained that polar sides on the basal planes of graphitic materials absorb water molecules and hinder the movement of electrolyte ions [38]. On the other hand, G-ol shows a lower impedance at the end of the semicircle (21.03Ω) as opposed to GO (24.64Ω), implying that GO holds a higher polarization resistance than G-ol when further extrapolated to the Z_{real} axis. Moreover, G-ol exhibited a lower equivalent circuit resistance ($R_s = 12.43 \Omega$) compared to GO ($R_s = 19.71 \Omega$), which is attributed to the increased total pore volume and lower internal resistance of G-ol. The increase in the oxygen content in the carbon-based materials optimizes the material wettability thereby enhancing its admittance [39].

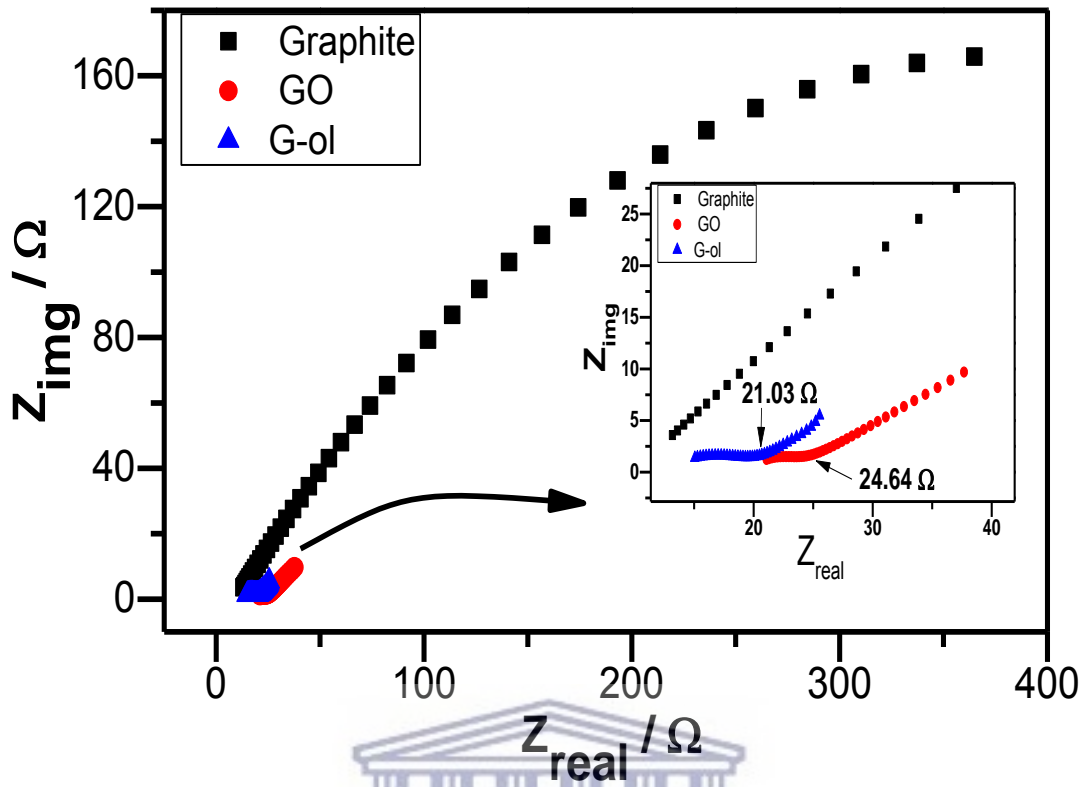


Figure 3.11 (a): Nyquist plot of Graphite, GO and G-ol

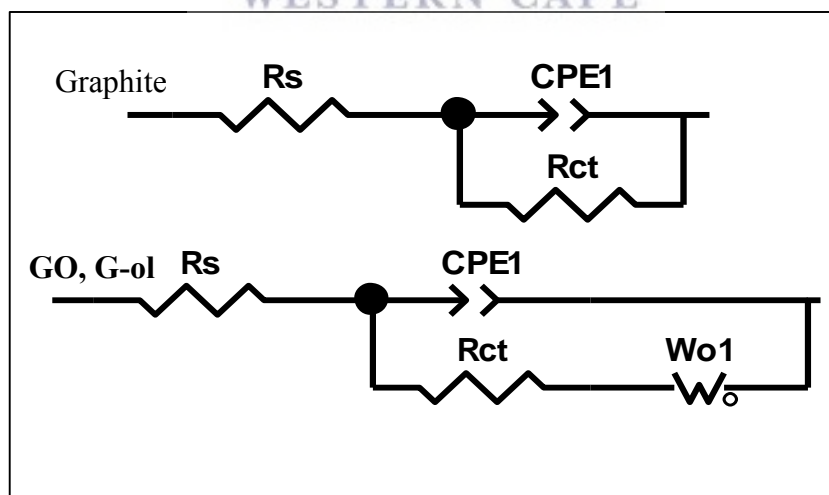
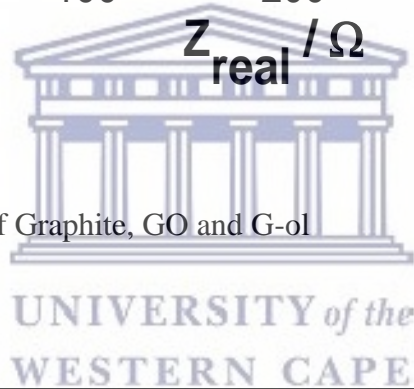


Figure 3.11 (b): Circuit models used to fit EIS data

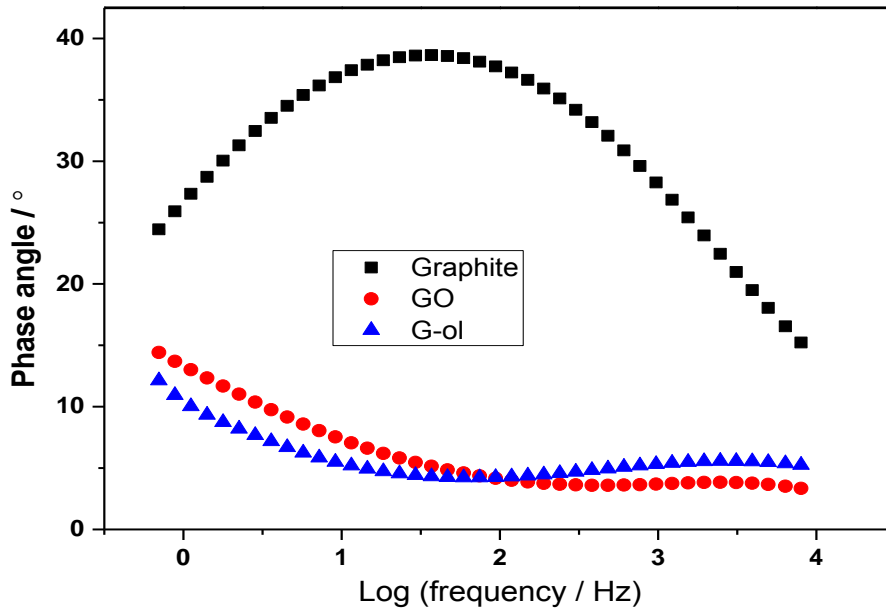


Figure 3.11 (c): Phase angle Bode plots of Graphite, GO and G-ol

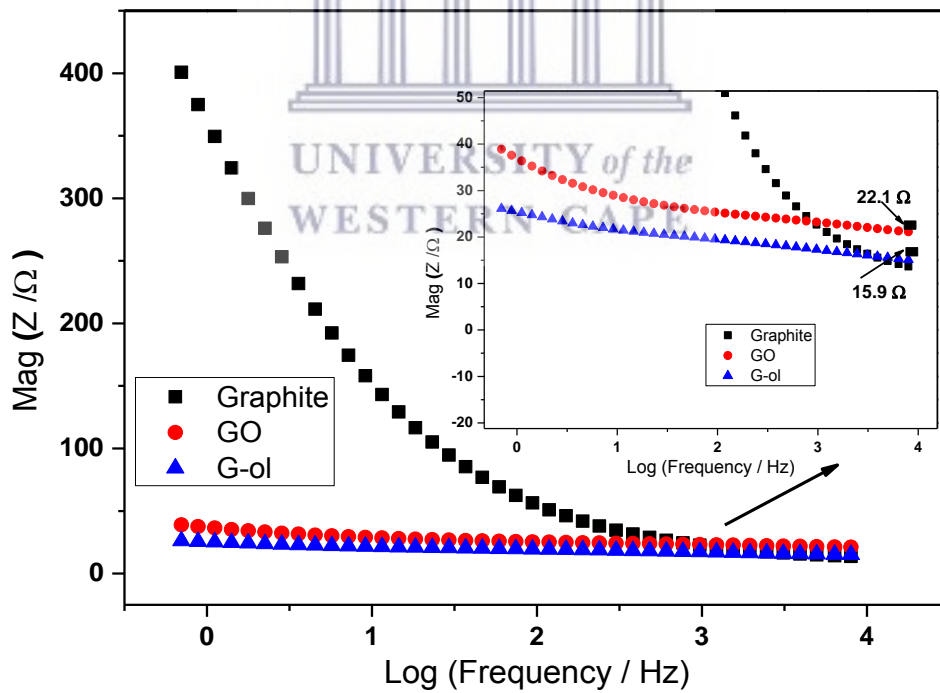


Figure 3.11 (d): Total impedance Bode plots of Graphite, GO and G-ol

The phase angle and total impedance Bode plots of Graphite, GO and G-ol are shown in Figure 3.11 (c) and (d) respectively. All three carbon-based materials show a phase angle less than 45° demonstrating a slow transition from resistive to capacitive behavior. From low to high frequencies, the magnitude of the total impedance decreased from GO (22.1Ω at max frequency) to G-ol (15.9Ω at max frequency) as the samples are oxidized and morphology of the graphitic sheets changes from stacked sheets to less stacked or single sheets in G-ol. The apparent resistive to capacitive behaviour of the materials may be attributed to the variation in pore sizes created by functionalization of the graphitic sheets leading to a mixture of macro, meso, and micro-pores. Therefore, the capacitive character of the electrodes will only dominate once the pores are adjusted such that the electrolyte ions can diffuse through the smallest pore sizes [38,40].

Table 3.4: EIS curve fitting data of graphite, GO and G-ol

Electrode material	R_s / Ω	CPE/ μF	R_{ct} / Ω	$W_o / \Omega s^{-1/2}$	Z at f_{max} / Ω
Graphite	9.86	0.53	755.61	-	14.41
GO	19.71	0.71	3.92	0.38	22.12
G-ol	12.43	0.46	8.12	0.46	15.92

3.3.8 Fabrication and Electrochemical Performance of flexible supercapacitor devices

To explore the potential application of G-ol in electrochemical capacitors considering its good electrochemical properties, G-ol was used as both positive and negative electrode to assemble a flexible Swagelok-type supercapacitor device (symmetric design) which is denoted as G-

ol//G-ol as shown in Figure 3.12 and as a positive electrode with activated carbon as the negative electrode (asymmetric design) denoted as AC//G-ol, in 0.5 M LiClO₄ aqueous electrolyte at a voltage window of 1.6 V. Activated carbon is a widely used active carbon-based material in electrochemical double-layer capacitors, asymmetric and hybrid supercapacitors [41]. The rate performance of the devices was also characterized by cyclic voltammetry, extended charge-discharge tests and electrochemical impedance spectroscopic measurements before and after cycling.

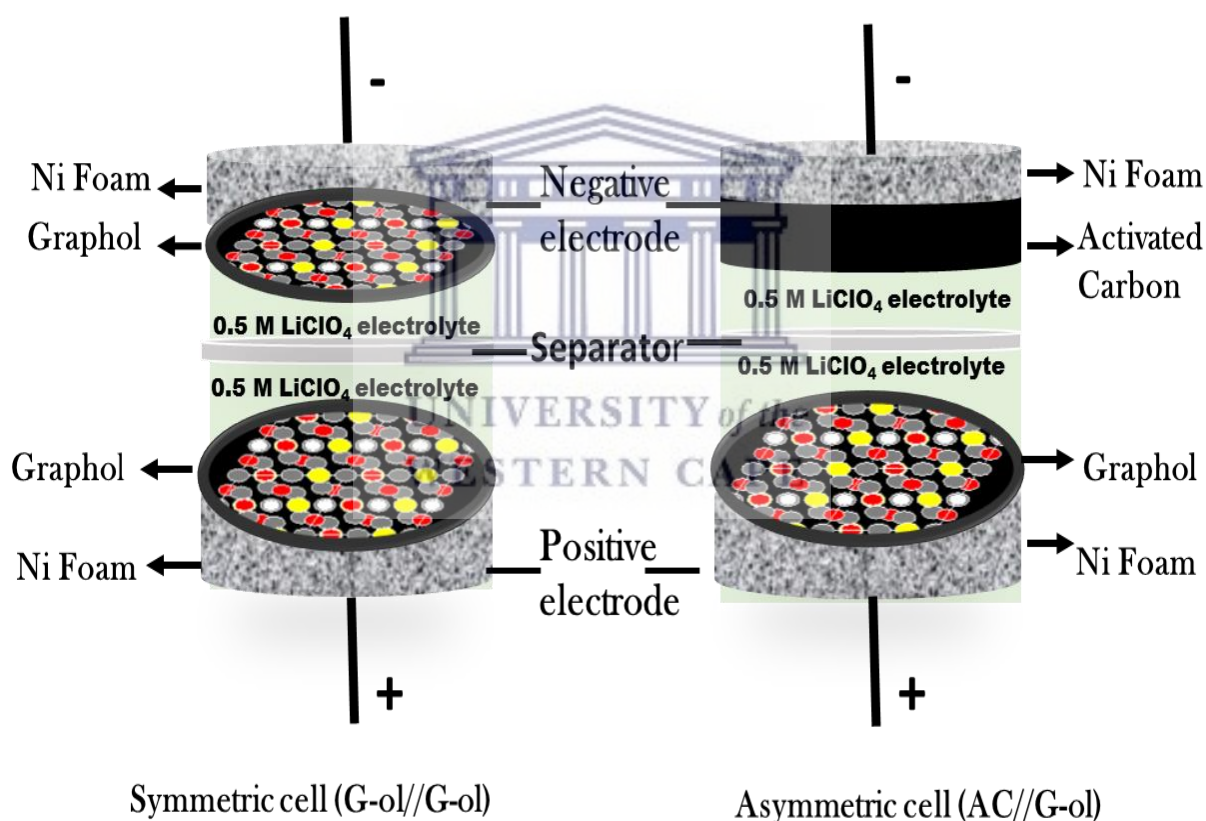


Figure 3.12: Symmetric and asymmetric supercapacitor designs.

i) **Voltage window determination via Cyclic Voltammetric Studies**

Figure 3.13 (a) displays the CV curves of the symmetric-G-ol//G-ol and asymmetric -AC//G-ol supercapacitor devices at a scan rate of 80 mV s^{-1} . Both CV curves display a rectangular shape indicating the double layer capacitance nature of the devices with that of G-ol//G-ol demonstrating an increased current response over AC//G-ol. This is indicative of the better symmetry and no polarity between G-ol//G-ol electrodes with superior supercapacitive performance. To further confirm the optimum or stable voltage window of the device to maximize its specific energy in 0.5 M LiClO_4 aqueous electrolyte, the device was investigated at different voltages ranges from $1 - 1.8 \text{ V}$ at a scan rate of 80 mV s^{-1} as shown in Figure 3.13 (b). It is observed that the CV curves retain a rectangular shape up to 1.8 V , with no increase in anodic current, indicating no electrolyte decomposition or unwanted side reactions [42]. Thus further confirming the good capacitive behavior and high electrochemical reversibility of the symmetric supercapacitor.

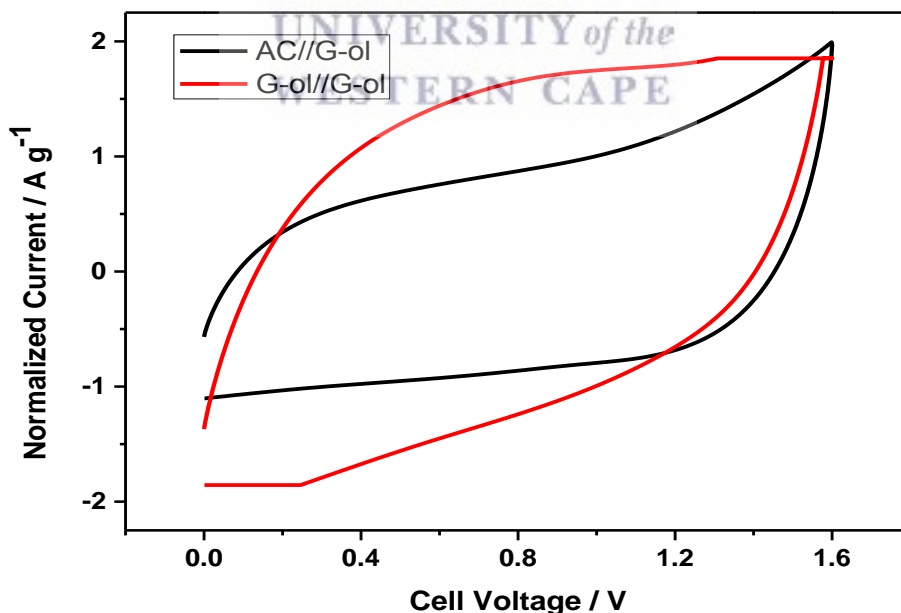


Figure 3.13 (a): CV curves of G-ol//G-ol and AC//G-ol devices at a scan rate of 80 mV s^{-1} in 0.5 M LiClO_4 aqueous electrolyte at a voltage window of 1.6 V .

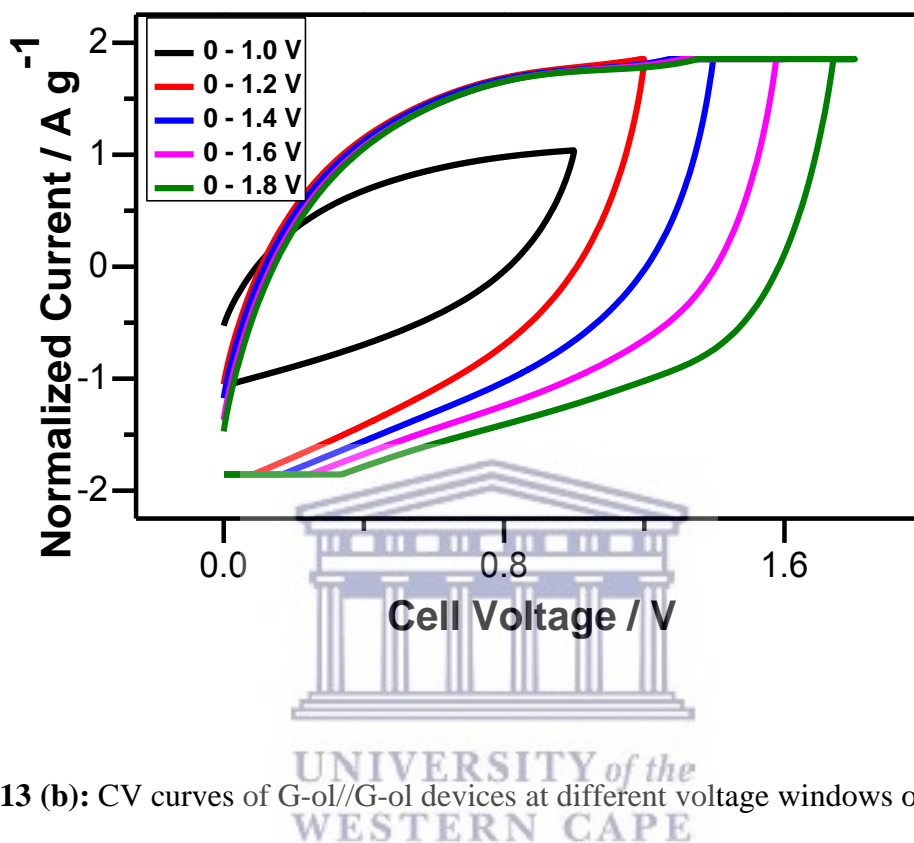


Figure 3.13 (b): CV curves of G-ol//G-ol devices at different voltage windows of $1.0 - 1.8 \text{ V}$ in 0.5 M LiClO_4 aqueous electrolyte

ii) Galvanostatic charge-discharge studies

The capacitive performance of the devices was further obtained by galvanostatic tests at different current loads. Figures 3.14 (a) and (b) show the charge-discharge profiles of G-ol//G-ol and AC//G-ol devices at current loads of $0.07 - 1.5 \text{ A g}^{-1}$, respectively at a voltage window of 1.6 V while Figure 3.14 (c) is a comparative plot of the GCD curves of G-ol//G-ol and AC//G-ol at a current load of 0.07 A g^{-1} . The GCD profiles represent almost symmetric and near-linear shaped curves with low IR_{drop} (0.11 V at 1.5 A g^{-1}), further confirming the

reversible charge-discharge performance and small internal resistance of the supercapacitor devices [43]. The capacitive performance of the two-electrode systems is said to be strongly controlled by the total active masses of the positive and negative electrodes more specifically in the asymmetric design. The mass loading of the positive and negative electrodes was adjusted according to the charge-balance equation as shown by Equation 3.5 [44].

$$\frac{M^+}{M^-} = \left(\frac{C_{sp}^-}{C_{sp}^+} \right) \left(\frac{\Delta V^-}{\Delta V^+} \right) \quad (3.5)$$

Where, M , C_{sp} and ΔV denote the active mass, specific capacitance and the potential window obtained from the individual half-cells, respectively. The mass loading of G-ol//G-ol symmetric device was at 5.43 mg while that of AC//G-ol asymmetric device was adjusted to 9.45 mg. The specific capacitance of the symmetric and asymmetric devices were calculated according to Equation 3.6.

$$C_{sp} = \frac{4I}{m \Delta V / \Delta t} \quad (3.6)$$

Where I is the applied current (A), m is the total mass of positive and negative electrodes (g), $\Delta V/\Delta t$ is the slope obtained by fitting a straight line to the discharge curve ($V s^{-1}$) and V is the maximum voltage [44,45]. The variation of discharge capacitance with current load is displayed in Figure 3.14 (e). The supercapacitor devices exhibit good electrochemical performance due to their high mass loadings with the G-ol//G-ol device revealing better discharge capacitance of $137.7 F g^{-1}$ at a current load of $0.07 A g^{-1}$ and up to $72.4 F g^{-1}$ at a current Load of $1.5 A g^{-1}$. On the other hand, the AC//G-ol delivered a discharge capacitance

of 91.73 F g^{-1} at a current load of 0.07 A g^{-1} and maintained a discharge capacitance of 41.83 F g^{-1} at a current density of 1.5 A g^{-1} . The high specific capacitance of G-ol//G-ol can be ascribed to the greater porosity and conjugation structure of G-ol which improves fast ion movements during the charging-discharging process. The specific capacitance is also observed to decrease with increasing current load. This is can be attributed to rapid potential changes and the low penetration likelihood of ions into the inner region of pores. These results are in good agreement with the CV performance of the devices and also consistent with literature reports [4,46].

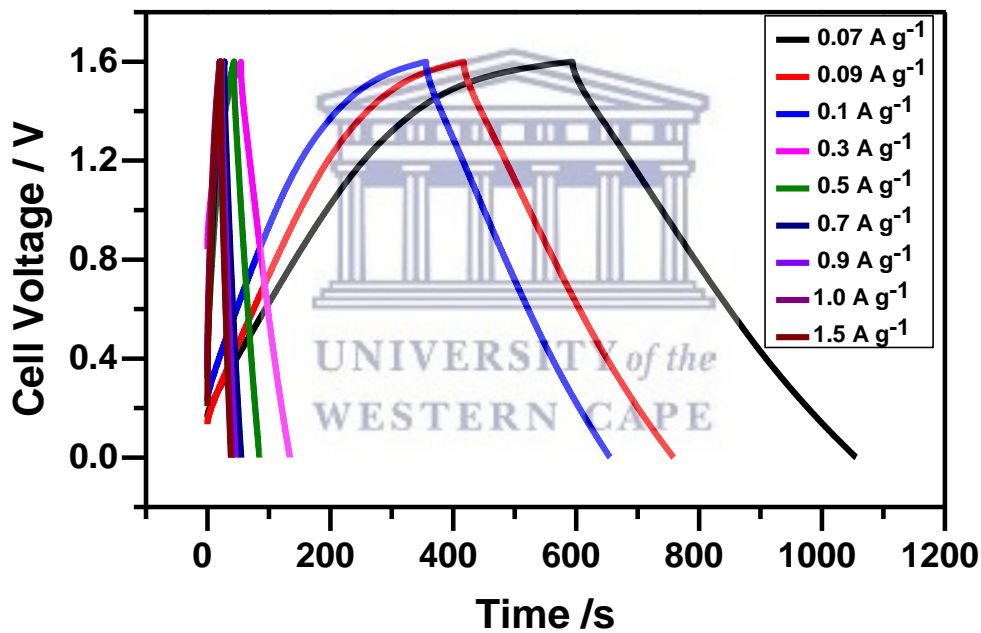


Figure 3.14 (a): GCD profiles of symmetric device - G-ol//G-ol at current loads of 0.07 A g^{-1} - 1.5 A g^{-1}

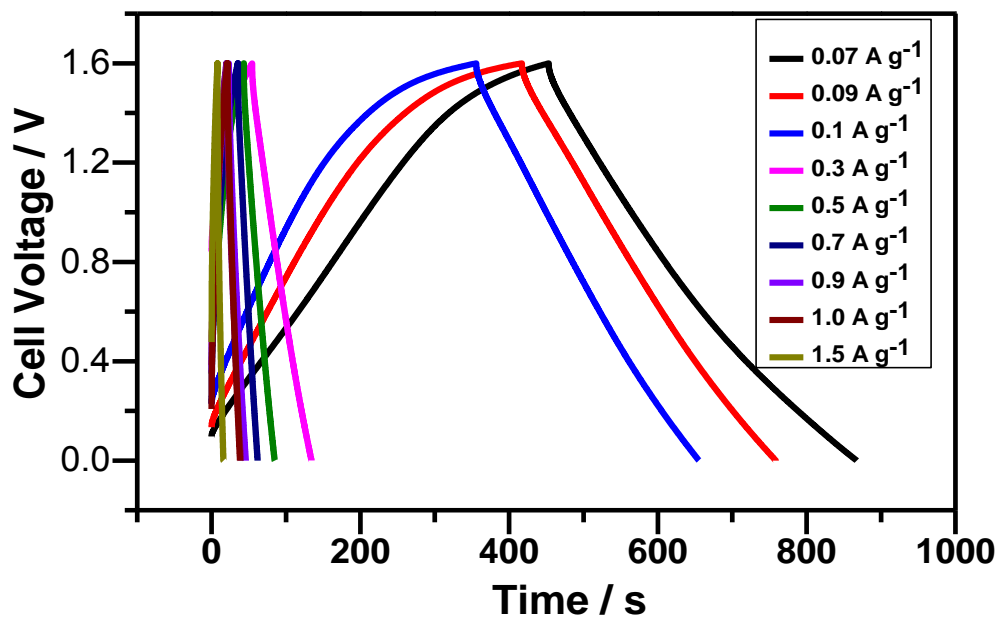


Figure 3.14 (b): GCD profiles of asymmetric device - AC//G-ol at current loads of 0.07 A g⁻¹-1.5 A g⁻¹

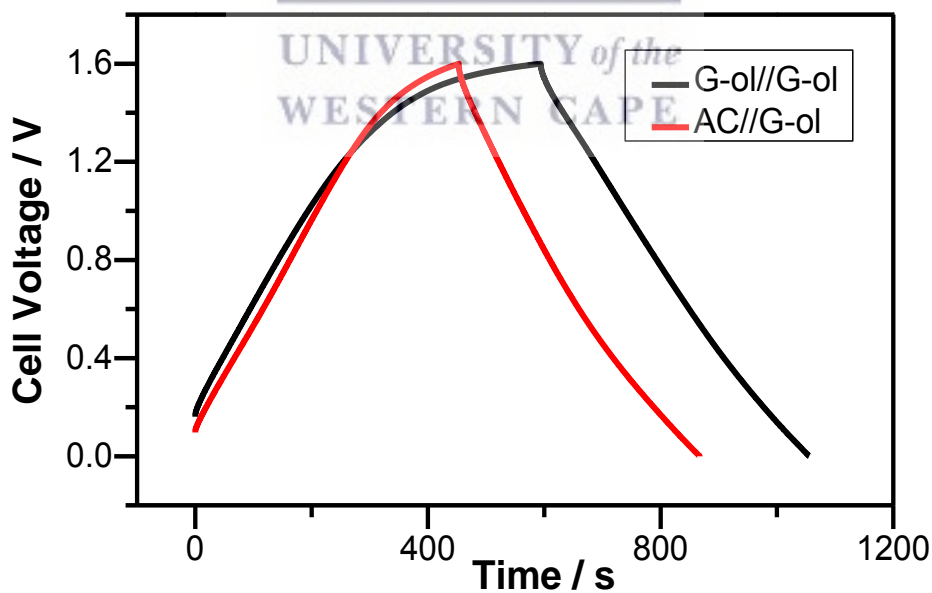


Figure 3.14 (c): Comparative plot of G-ol//G-ol and AC//G-ol at a current load of 0.07 A g⁻¹

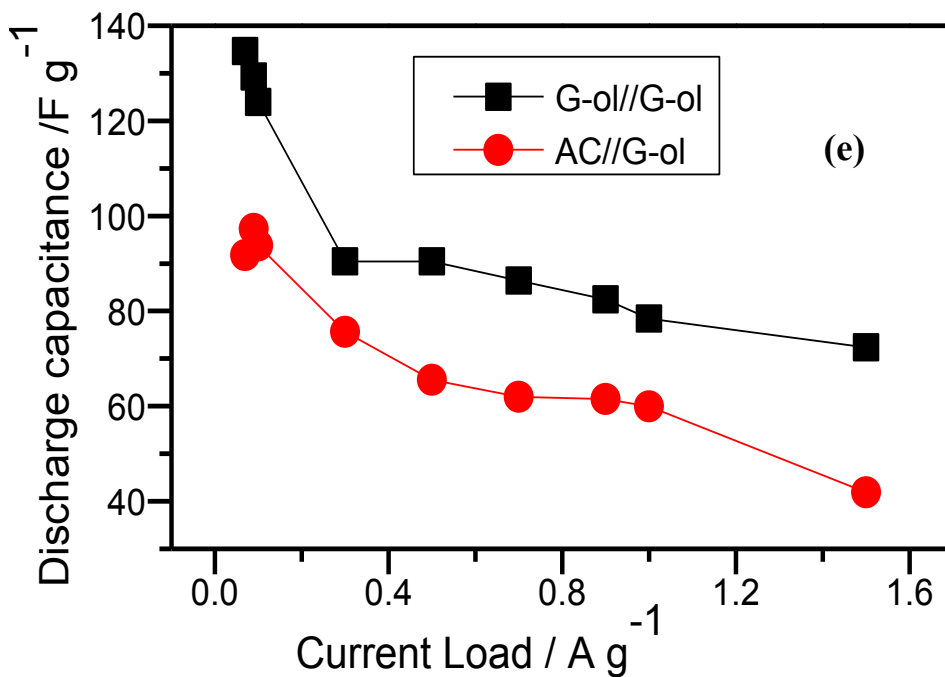


Figure 3.14 (e): Variation of discharge capacitance with current load for G-ol//G-ol and AC//G-ol.



iii) Electrochemical cycling/stability studies

Another key parameter used to demonstrate the practical application of supercapacitors is the cycling stability. Extended charge-discharge tests were performed on the G-ol//G-ol and AC//G-ol devices at a current load of 0.5 A g^{-1} . As shown in Figure 3.15, both devices maintain more than 83 % of the initial capacitance after 5000 cycles with an excellent coulombic efficiency of 99.8 % per cycle. Notably, this demonstrates appreciable electrochemical stability and cycle reversibility.

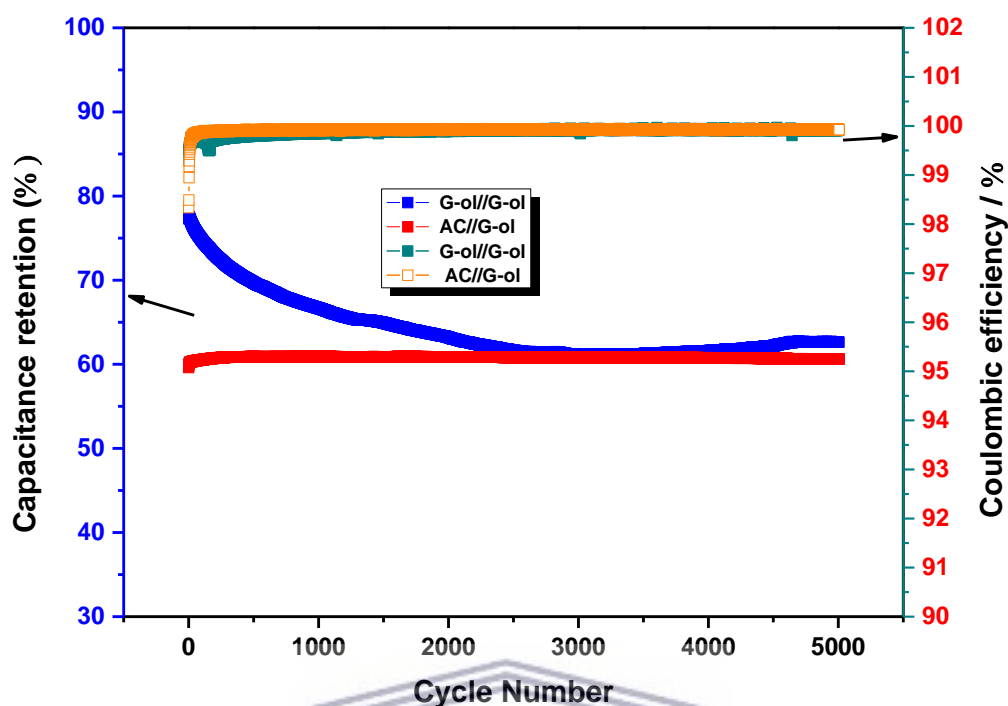


Figure 3.15: Cycling stability of G-ol//G-ol and AC//G-ol supercapacitors over 5000 cycles.

iv) **Electrochemical Impedance studies before and after cycling**

EIS measurements were further performed before and after extended cycling. Figures 3.16 (a), (b) and (c) represent the Nyquist plots, Phase angle Bode plots and the total impedance Bode plots of G-ol//G-ol and AC//G-ol, respectively before and after cycling. EIS data fitted using circuit models in Figure 3.16 (d) and (e) is shown in Table 3.5. It is observed that R_s and R_{ct} values obtained from curve fitting the Nyquist plots at the low to medium frequency region, increases from before to after 5000 cycles in the symmetric device. Conversely, the asymmetric device shows a decrease in R_s and R_{ct} values from before to after 5000 cycles. The increase in the equivalent circuit and charge transfer resistances in the G-ol//G-ol device can be attributed to a form of cycling degradation caused by the formation of a resistant film with cycling along

the electrode/electrolyte interface. This resistant film may induce higher interfacial resistance which gradually impedes charge transfer. Whereas in the case of the AC//G-ol device, due to the asymmetric nature of the device, an irregular resistant film may be formed, which favors conduction channels for electrolyte ions and thus lowers charge transfer resistance with cycling [47]. However, from analysis of the Bode plots, higher phase angles are achieved in the symmetric device before cycling (35.5°) and after cycling (37.6°) over the asymmetric device before cycling (19.59°) and after cycling (19.7°), indicating better electrical conductivity in the former device than later. The symmetric device, therefore, demonstrates a transmission boundary between resistive to capacitive behavior before and after cycling as observed in previous EIS characterization in three-electrode configuration. At maximum frequency in the total impedance Bode plot, it is also observed that the symmetric device shows a lower total impedance of $1.69\ \Omega$ before cycling and $1.88\ \Omega$ after cycling, compared to $4.64\ \Omega$ before cycling and $6.44\ \Omega$ after cycling in the asymmetric design.

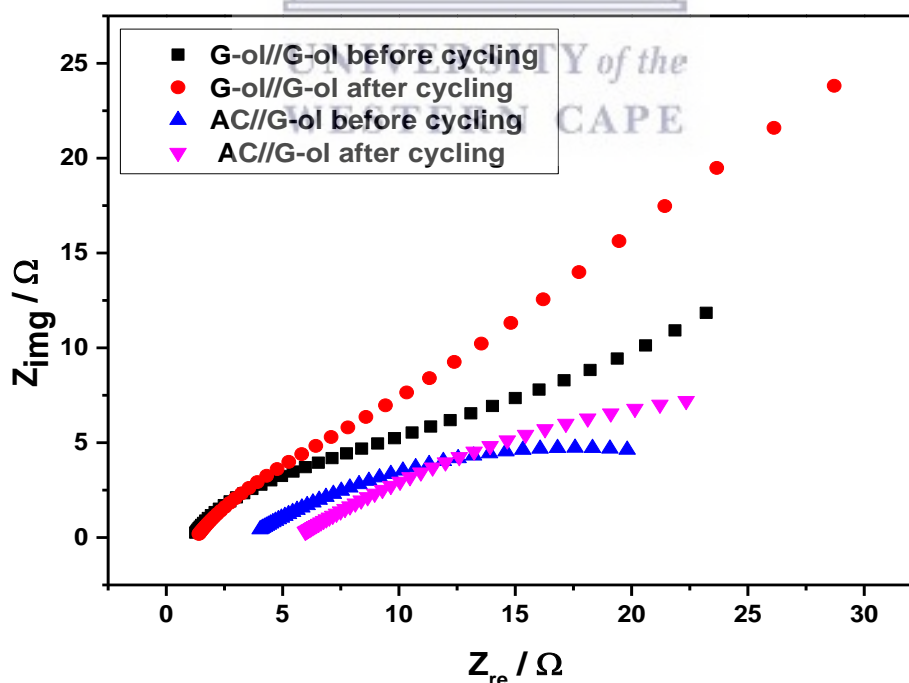


Figure 3.16 (a): Nyquist plots of G-ol//G-ol and AC//G-ol devices before and after cycling at OCV

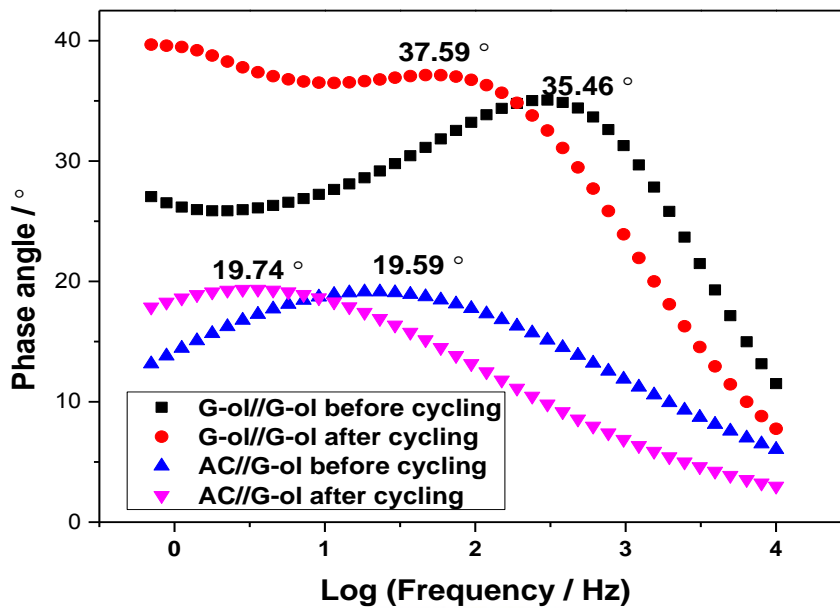


Figure 3.16 (b): Phase angle Bode plots of G-ol//G-ol and AC//G-ol devices before and after cycling at OCV

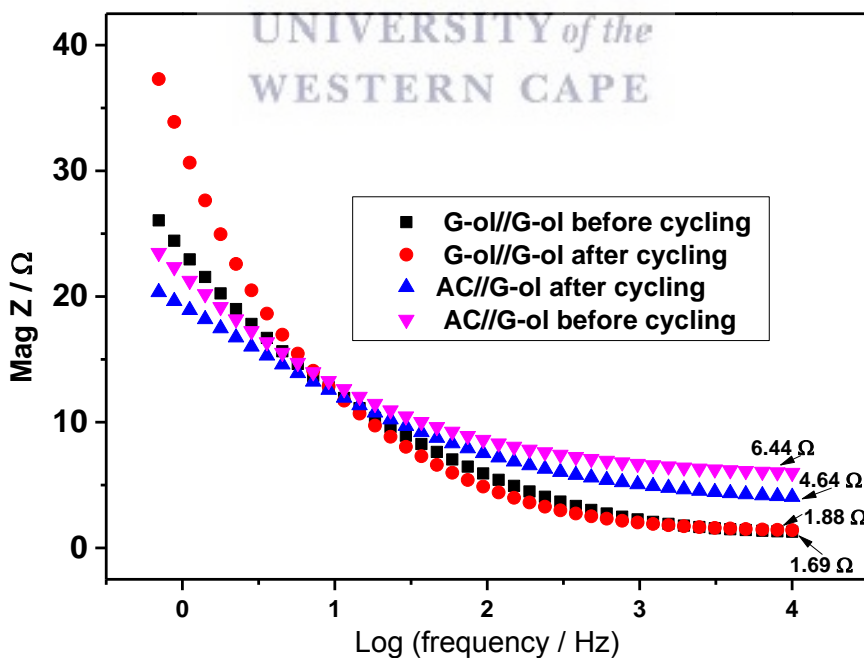


Figure 3.16 (c): Total impedance Bode plots of G-ol//G-ol and AC//G-ol devices before and after cycling at OCV

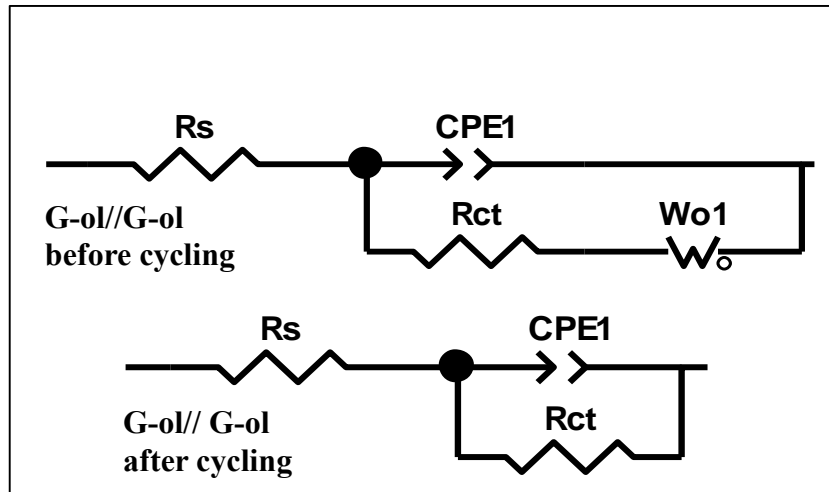


Figure 3.16 (d): EIS data fitting circuit models of G-ol//G-ol device before and after cycling

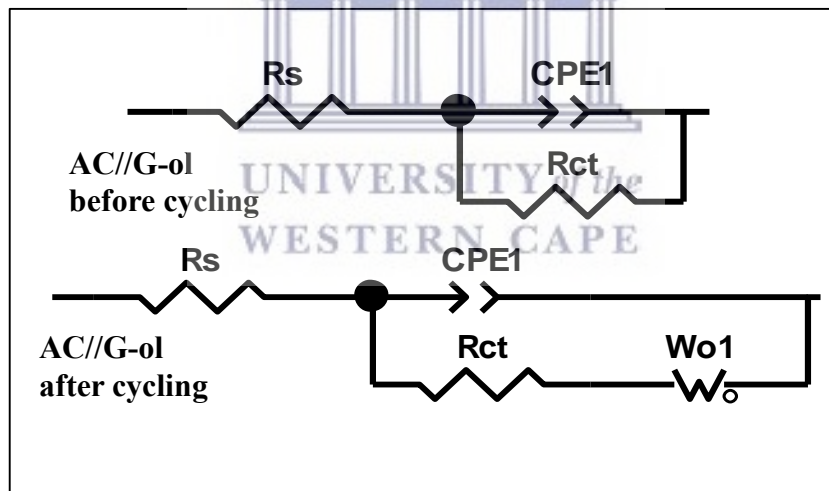


Figure 3.16 (e): EIS data fitting circuit models of AC//G-ol device before and after cycling

Table 3.5: EIS simulation data of G-ol//G-ol and AC//G-ol supercapacitor devices before and after cycling.

Cell Design	R_s / Ω	CPE / μF	R_{ct} / Ω	$W_o / \Omega\text{s}^{-1/2}$	Phase angle / $^\circ$
G-ol//G-ol before cycling	1.14	0.75	3.62	0.31	35.56
G-ol//G-ol after cycling	3.45	0.41	28.32	-	37.59
AC//G-ol before cycling	5.56	0.42	45.11	-	19.59
AC//G-ol after cycling	1.28	0.65	13.84	0.51	19.7

3.3.9 Specific Energy and Specific Power

The specific energy (Wh Kg^{-1}) and specific power (W Kg^{-1}) at different current loads were calculated according to Equation 3.7 and 3.8.

$$E = \frac{1}{2} C_{sp} \times \Delta V^2 \times \frac{1}{3.6} \quad (3.7)$$

$$P = \frac{E}{\Delta t} \times 3600 \quad (3.8)$$

Where C_{sp} represents the specific capacitance of the supercapacitor (F g^{-1}), ΔV is the applied voltage (V) and Δt is the supercapacitor discharge time (s) [48]. The Ragone plot of G-ol//G-ol and AC//G-ol supercapacitors is presented in Figure 3.17. It is clearly observed that the symmetric device delivers high specific energy of 47.8 Wh Kg^{-1} with a corresponding specific power of 377 W kg^{-1} at a current load of 0.007 A g^{-1} . Even at a current load of 1.5 mA g^{-1} , the

symmetric device was able to retain a specific energy of 25.72 Wh Kg⁻¹ and a specific power of 6432 W Kg⁻¹. Whereas, the asymmetric supercapacitor delivered a slightly lower specific energy of 32.61 Wh Kg⁻¹ and a specific power of 286.6 W kg⁻¹. The asymmetric device was also able to retain a specific energy of 14.87 Wh kg⁻¹ and associated specific power of 5130.1 W kg⁻¹ at a current load of 1.5 mA g⁻¹. These results are comparable to those of nitrogen-doped porous carbon symmetric supercapacitor cells [49] and ionic liquid-based capsicum seed-porous carbon symmetric device [50] and even higher than biomass-derived ultra-microporous carbon and porous graphene-like symmetric devices [51,52]. Moreover, the ability of the devices to maintain more than 83 % of the initial capacitance with an excellent coulombic efficiency of 99.8 % after 5 000 cycles further demonstrates their potentials in energy storage applications.

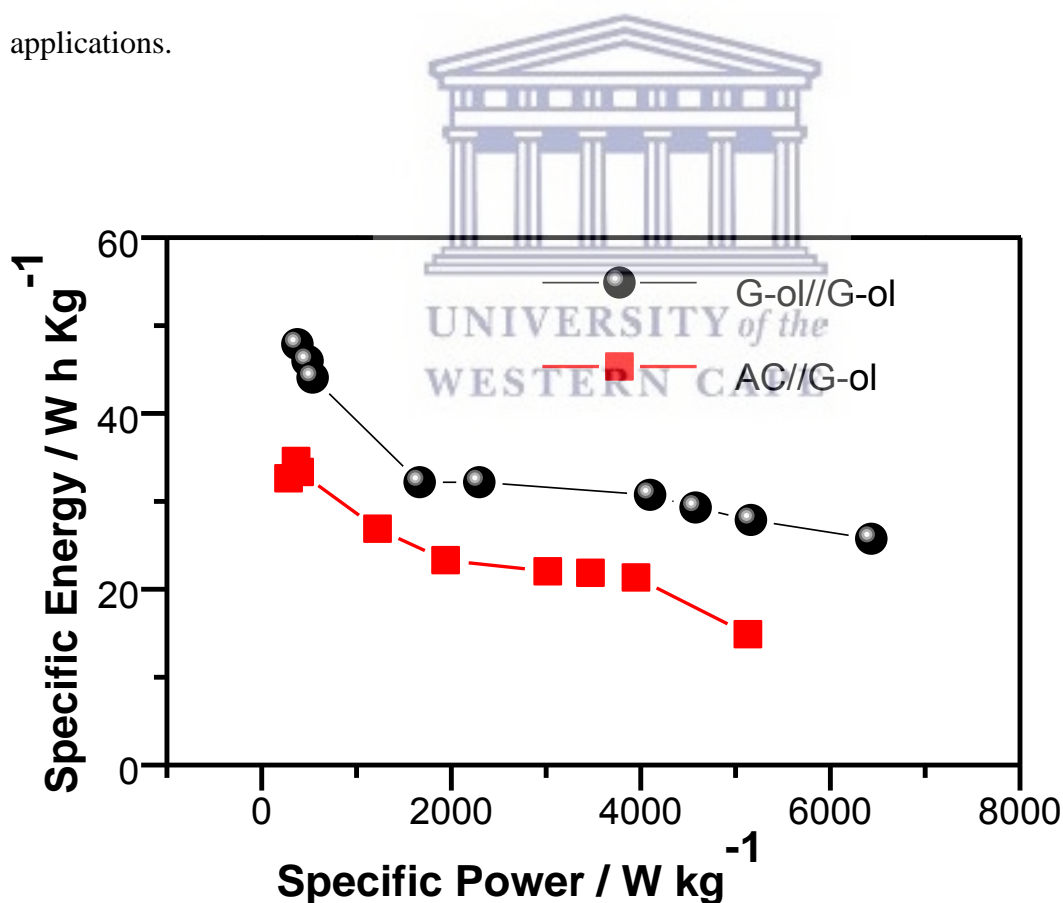
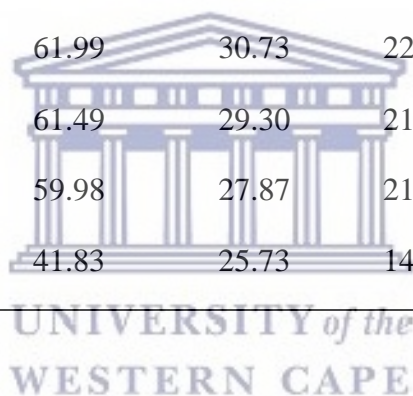


Figure 3.17: Ragone plot of G-ol//G-ol and AC//G-ol supercapacitors at different current loads

Table 3.6: Electrochemical performance data of G-ol//G-ol and AC//G-ol flexible supercapacitors

Current Load / A g⁻¹	Specific capacitance (G-ol//G-ol) / F g⁻¹	Specific capacitance (AC//G-ol) / F g⁻¹	Specific Energy (G-ol//G-ol) / W h Kg⁻¹	Specific Energy (AC//G-ol) / W h Kg⁻¹	Specific Power (G-ol//G-ol) / W Kg⁻¹	Specific Power (AC//G-ol) / W Kg⁻¹
0.007	134.67	91.73	47.88	32.61	377	283.60
0.009	129.31	97.27	45.98	34.59	484.91	362.90
0.1	123.95	93.74	44.07	33.33	537.50	401.58
0.3	90.45	75.61	32.16	26.88	1667.10	1221.80
0.5	90.45	65.52	32.16	23.31	2297.14	1941.33
0.7	86.43	61.99	30.73	22.04	4097.46	3019.40
0.9	82.41	61.49	29.30	21.86	4578.33	3470.20
1	78.39	59.98	27.87	21.33	5161.50	3949.04
1.5	72.36	41.83	25.73	14.87	6432.00	5130.10



3.4 Conclusion

In this work, graphol nanosheets were prepared by hydroboration of GO in anhydrous THF and 1 M borane/THF complex and subsequent oxidation by sodium hydroxide and hydrogen peroxide. The materials were comprehensively characterized by various physical and electrochemical techniques. As observed from microscopic characterizations by SEM and HRTEM, GO sheets exfoliated from graphite were found to be layers of 11 – 45 nm thick, occurring in stacks of 20 -25 layers. While the G-ol nanosheets were observed as single layers of 14- 23 nm thick. XRD studies revealed crystalline nanosheets with interlayer spacing of 0.34 nm for graphite, 0.8 nm for GO and 0.88 nm for G-ol with corresponding average crystallite

sizes of 59.0, 34.5 and 23.3 nm for graphite, GO and G-ol, respectively. XRD and morphological studies were corroborated by simulations performed using phase identification and structure solution softwares such as Match and Endeavour. Meanwhile, SAXS investigations revealed left-skewed intensity particle size distribution for graphite indicating variation in sizes of stacked graphitic sheets. A bell-shaped intensity particle size distribution was obtained for GO and G-ol with center peaks at 30.8 nm and 31.3 nm representing the primary particle sizes for GO and G-ol, respectively with aggregates of the primary particles at 66.7 nm for GO and 45.5 nm for G-ol. Functional group analysis by FTIR of G-ol showed two strong stretching vibrations of sp³ C-H bonds at 2921.6 and 2851.9 cm⁻¹ in addition to the stretching and bending vibrations of the OH group at 3409.4 cm⁻¹, indicating covalent functionalization with hydroxyl groups. Breakage of the stacking order of C-C bonding in GO and increasing degree of oxidation was confirmed by the decrease in the 2D-Raman band of G-ol in Raman spectroscopic analysis, while ¹³C-NMR spectroscopy showed resonances of the graphitic sp² carbon atoms (-C=C-) at ~110.9 ppm and 111.3 ppm for G-ol and GO, respectively. Electrochemical studies in 0.5 M LiClO₄ aqueous electrolyte at a potential window of -0.2 – 0.8 V revealed a specific capacitance of 1.68 F g⁻¹, 24.0 F g⁻¹ and 73.8 F g⁻¹ for graphite, GO and G-ol, respectively at 50 mV s⁻¹ from CV studies in three electrodes. EIS results further revealed that G-ol showed a slightly higher *R*_{ct} value than GO due to the presence of excessive oxygenated and hydroxyl species (observed in FTIR and Raman spectroscopies) which arouse some insulating characteristics and slightly hindered its electrochemical properties. However, G-ol showed a lower equivalent circuit resistance (*R*_s = 12.43 Ω) compared to GO (*R*_s = 19.71 Ω). To explore the potential application of G-ol in electrochemical capacitors, both symmetric (G-ol//G-ol) and asymmetric (AC//G-ol) devices were assembled and investigated at a voltage window of 1.6 V. Discharge capacitance values of 137.7 F g⁻¹ and 91.73 F g⁻¹ were obtained for the symmetric and asymmetric cells, respectively at current load

of 0.07 A g⁻¹. The devices were able to retain more than 83 % of the initial capacitance at a current load of 0.5 A g⁻¹ with an excellent coulombic efficiency of 99.8 % over 5000 cycles. The symmetric device delivered a high specific energy of 47.8 Wh Kg⁻¹ with a corresponding specific power of 377 W kg⁻¹ at a current load of 0.007 A g⁻¹. Even at a current load of 1.5 A g⁻¹, the symmetric device was able to retain a specific energy of 25.72 Wh Kg⁻¹ and a specific power of 6432 W Kg⁻¹. The asymmetric cell delivered a slightly lower specific energy of 32.61 Wh Kg⁻¹ and a specific power of 286.6 W kg⁻¹ at 0.007 A g⁻¹ and a specific energy of 14.87 Wh kg⁻¹ and specific power of 5130.1 W kg⁻¹ at current load of 1.5 A g⁻¹. The electrochemical performance of these devices is comparable and even better than some literature reports, indicating the huge potentials of graphol and associated devices in energy storage applications.



References

- [1] Poonam, K. Sharma, A. Arora, S.K. Tripathi, Review of supercapacitors: Materials and devices, *J. Energy Storage*, 21 (2019) 801–825. doi:10.1016/j.est.2019.01.010.
- [2] Y. Yan, T. Wang, X. Li, H. Pang, H. Xue, Noble metal-based materials in high-performance supercapacitors, *Inorg. Chem. Front.* 4 (2017) 33–51. doi:10.1039/c6qi00199h.
- [3] H.M.N. Graphene, Z. Wu, W. Ren, D. Wang, F. Li, B. Liu, H. Cheng, High-Energy MnO₂ Nanowire/Graphene and Graphene Asymmetric Electrochemical Capacitors, *ACS Nano*. 4 (2010) 5835–5842.
- [4] S. Kannappan, H. Yang, K. Kaliyappan, R.K. Manian, A. Samuthira Pandian, Y.S. Lee, J.H. Jang, W. Lu, Thiolated-graphene-based supercapacitors with high energy density and stable cycling performance, *Carbon N. Y.* 134 (2018) 326–333.

-
- doi:10.1016/j.carbon.2018.02.036.
- [5] W.K. Chee, H.N. Lim, Z. Zainal, N.M. Huang, I. Harrison, Y. Andou, Flexible Graphene-Based Supercapacitors : A Review, *J. Phys. Chem. C.* 120 (2016) 4153–4172. doi:10.1021/acs.jpcc.5b10187.
- [6] X. Shi, S. Zheng, Z.S. Wu, X. Bao, Recent advances of graphene-based materials for high-performance and new-concept supercapacitors, *J. Energy Chem.* 27 (2018) 25–42. doi:10.1016/j.jechem.2017.09.034.
- [7] A. Ambrosi, C.K. Chua, N.M. Latiff, A.H. Loo, C.H.A. Wong, A.Y.S. Eng, A. Bonanni, M. Pumera, Graphene and its electrochemistry – an update, *Chem. Soc. Rev.* 45 (2016) 2458–2493. doi:10.1039/C6CS00136J.
- [8] J.T. Liu, Jingquan, J.J. Gooding, Strategies for chemical modification of graphene and applications of chemically modified graphene, *J. Mater. Chem.* 22 (2012) 12435–12452. doi:10.1039/c2jm31218b.
- [9] A. Kaplan, Z. Yuan, J.D. Benck, G. Rajan, Q. Hua, M.S. Strano, Current and future directions in electron transfer chemistry of graphene, *Chem. Soc. Rev.* (2017). doi:10.1039/C7CS00181A.
- [10] X. Cao, Y. Shi, W. Shi, G. Lu, X. Huang, Q. Yan, Preparation of Novel 3D Graphene Networks for Supercapacitor Applications, *Small.* 7 (2011) 3163–3168. doi:10.1002/smll.201100990.
- [11] P. Miao, J. He, Z. Sang, F. Zhang, J. Guo, D. Su, X. Yan, X. Li, H. Ji, Hydrothermal growth of 3D graphene on nickel foam as a substrate of nickel-cobalt-sulfur for high-performance supercapacitors, Elsevier B.V., 2018. doi:10.1016/j.jallcom.2017.10.243.
- [12] P. Gong, J. Wang, W. Sun, D. Wu, Z. Wang, Z. Fan, H. Wang, S. Yang, Tunable

-
- photoluminescence and spectrum split from fluorinated to hydroxylated graphene, *Nanoscale*. 6 (2014) 3316–3324. doi:10.1039/c3nr05725a.
- [13] M.D. Esrafil, Boron and nitrogen co-doped graphene nanosheets for NO and NO₂ gas sensing, *Phys. Lett. Sect. A Gen. At. Solid State Phys.* 383 (2019) 1607–1614. doi:10.1016/j.physleta.2019.02.017.
- [14] W. Yang, W. Yang, L. Kong, A. Song, X. Qin, G. Shao, Phosphorus-doped 3D hierarchical porous carbon for high-performance supercapacitors: A balanced strategy for pore structure and chemical composition, *Carbon N. Y.* 127 (2018) 557–567. doi:10.1016/j.carbon.2017.11.050.
- [15] R. Nankya, J. Lee, D.O. Opar, H. Jung, Electrochemical behavior of boron-doped mesoporous graphene depending on its boron configuration, *Appl. Surf. Sci.* 489 (2019) 552–559. doi:10.1016/j.apsusc.2019.06.015.
- [16] C. Zu, A. Manthiram, Hydroxylated graphene-sulfur nanocomposites for high-rate lithium-sulfur batteries, *Adv. Energy Mater.* 3 (2013) 1008–1012. doi:10.1002/aenm.201201080.
- [17] H.L. Poh, Z. Sofer, P. Simek, I. Tomandl, M. Pumera, Hydroboration of graphene oxide: Towards stoichiometric graphol and hydroxygraphane, *Chem. - A Eur. J.* 21 (2015) 8130–8136. doi:10.1002/chem.201406168.
- [18] R. Singla, A. Kottantharayil, Stable hydroxyl functionalization and p-type doping of graphene by a non-destructive photo-chemical method, *Carbon N. Y.* 152 (2019) 267–273. doi:10.1016/j.carbon.2019.06.021.
- [19] L. Wade, J. Simek, *Organic Chemistry*, 8th Edition, Pearson Education, Inc., 2012.
- [20] M. Fahrul, R. Hanifah, J. Jaafar, M. Aziz, A. Fauzi, M.A. Rahman, M.H. Dzarfan,

-
- Synthesis of Graphene Oxide Nanosheets via Modified Hummers' Method and Its Physicochemical Properties, 1 (2015) 189–192.
- [21] P. Guo, H. Song, X. Chen, Electrochemical performance of graphene nanosheets as anode material for lithium-ion batteries, *Electrochem. Commun.* 11 (2009) 1320–1324. doi:10.1016/j.elecom.2009.04.036.
- [22] C.N.R. Rao, K. Gopalakrishnan, A. Govindaraj, Synthesis, properties and applications of graphene doped with boron, nitrogen and other elements, *Nano Today*. (2014) 1–20. doi:10.1016/j.nantod.2014.04.010.
- [23] J. Guerrero-Contreras, F. Caballero-Briones, Graphene oxide powders with different oxidation degree, prepared by synthesis variations of the Hummers method, *Mater. Chem. Phys.* 153 (2015) 209–220. doi:10.1016/j.matchemphys.2015.01.005.
- [24] Mahima Khandelwal and Anil Kumar, One-step chemically controlled wet synthesis of graphene nanoribbons from graphene oxide for high performance supercapacitor applications, *J. Mater. Chem. A*. 3 (2015) 22975–88. doi:10.1039/x0xx00000x.
- [25] N.I. Zaaba, K.L. Foo, U. Hashim, S.J. Tan, W.W. Liu, C.H. Voon, Synthesis of Graphene Oxide using Modified Hummers Method: Solvent Influence, *Procedia Eng.* 184 (2017) 469–477. doi:10.1016/j.proeng.2017.04.118.
- [26] T.F. Emiru, D.W. Ayele, Controlled synthesis, characterization and reduction of graphene oxide: A convenient method for large scale production, *Egypt. J. Basic Appl. Sci.* 4 (2017) 74–79. doi:10.1016/j.ejbas.2016.11.002.
- [27] H.K. Kammler, G. Beaucage, D.J. Kohls, N. Agashe, J. Ilavsky, Monitoring simultaneously the growth of nanoparticles and aggregates by in situ ultra-small-angle x-ray scattering, *J. Appl. Phys.* 97 (2005). doi:10.1063/1.1855391.

-
- [28] J. Park, Y.S. Kim, S.J. Sung, T. Kim, C.R. Park, Highly dispersible edge-selectively oxidized graphene with improved electrical performance, *Nanoscale*. 9 (2017) 1699–1708. doi:10.1039/c6nr05902c.
- [29] S. Wang, Y. Dong, C. He, Y. Gao, N. Jia, Z. Chen, W. Song, The role of sp²/sp³ hybrid carbon regulation in the nonlinear optical properties of graphene oxide materials, *RSC Adv*. 7 (2017) 53643–53652. doi:10.1039/c7ra10505c.
- [30] A.H.W. and I.W. Kundi, Synthesis of Graphene Nano Sheets by the Rapid Reduction of Electrochemically Exfoliated Graphene Oxide Induced by Microwaves, *J. Chem. Soc. Pakistan*. 38 (2016) 11–15. doi:10.1039/c4cy01074d.
- [31] T. Somanathan, K. Prasad, K.K. Ostrikov, A. Saravanan, V.M. Krishna, Graphene oxide synthesis from agro waste, *Nanomaterials*. 5 (2015) 826–834. doi:10.3390/nano5020826.
- [32] J.L. Gómez-Urbano, J.L. Gómez-Cámer, C. Botas, N. Díez, J.M. López del Amo, L.M. Rodríguez-Martinez, D. Carriazo, T. Rojo, Hydrothermally reduced graphene oxide for the effective wrapping of sulfur particles showing long term stability as electrodes for Li-S batteries, *Carbon N. Y.* 139 (2018) 226–233. doi:10.1016/j.carbon.2018.06.053.
- [33] P. Dash, T. Dash, T.K. Rout, A.K. Sahu, S.K. Biswal, B.K. Mishra, Preparation of graphene oxide by dry planetary ball milling process from natural graphite, *RSC Adv*. 6 (2016) 12657–12668. doi:10.1039/c5ra26491j.
- [34] M.M. Mokhtar, S.A. Abo-El-Enein, M.Y. Hassaan, M.S. Morsy, M.H. Khalil, Mechanical performance, pore structure and micro-structural characteristics of graphene oxide nano platelets reinforced cement, *Constr. Build. Mater.* 138 (2017) 333–339. doi:10.1016/j.conbuildmat.2017.02.021.

-
- [35] Y. Si, E.T. Samulski, Synthesis of water soluble graphene, *Nano Lett.* 8 (2008) 1679–1682. doi:10.1021/nl080604h.
- [36] G.Z. Chen, Understanding supercapacitors based on nano-hybrid materials with interfacial conjugation, *Prog. Nat. Sci. Mater. Int.* 23 (2013) 245–255. doi:10.1016/j.pnsc.2013.04.001.
- [37] J. Yang, S. Gunasekaran, Electrochemically reduced graphene oxide sheets for use in high performance supercapacitors, *Carbon N.Y.* 51 (2013) 36–44. doi:10.1016/j.carbon.2012.08.003.
- [38] D.I. Abouelamaiem, G. He, T.P. Neville, D. Patel, S. Ji, R. Wang, I.P. Parkin, A.B. Jorge, M.M. Titirici, P.R. Shearing, D.J.L. Brett, Correlating electrochemical impedance with hierarchical structure for porous carbon-based supercapacitors using a truncated transmission line model, *Electrochim. Acta.* 284 (2018) 597–608. doi:10.1016/j.electacta.2018.07.190.
- [39] F. Wang, Z. Liu, X. Yuan, J. Mo, C. Li, L. Fu, Y. Zhu, X. Wu, Y. Wu, A quasi-solid-state Li-ion capacitor with high energy density based on Li_3VO_4 /carbon nanofibers and electrochemically-exfoliated graphene sheets, *J. Mater. Chem. A Mater. Energy Sustain.* 0 (2017) 1–8. doi:10.1039/C7TA03920D.
- [40] P. Karthika, N. Rajalakshmi, K.S. Dhathathreyan, Functionalized Exfoliated Graphene Oxide as Supercapacitor Electrodes, *Soft Nanosci. Lett.* 2 (2012) 59–66. doi:10.4236/sn.2012.24011.
- [41] C.F. Liu, Y.C. Liu, T.Y. Yi, C.C. Hu, Carbon materials for high-voltage supercapacitors, *Carbon N. Y.* 145 (2019) 529–548. doi:10.1016/j.carbon.2018.12.009.
- [42] A.S. Rajpurohit, N.S. Punde, C.R. Rawool, A.K. Srivastava, Fabrication of high energy

-
- density symmetric supercapacitor based on cobalt-nickel bimetallic tungstate nanoparticles decorated phosphorus-sulphur co-doped graphene nanosheets with extended voltage, *Chem. Eng. J.* (2019) 679–692. doi:10.1016/j.cej.2019.04.100.
- [43] S. Khalid, C. Cao, L. Wang, Y. Zhu, Microwave Assisted Synthesis of Porous NiCo₂O₄ Microspheres: Application as High Performance Asymmetric and Symmetric Supercapacitors with Large Areal Capacitance, *Sci. Rep.* 6 (2016) 1–13. doi:10.1038/srep22699.
- [44] M.M. Ndipingwi, C. Ikpo, N.W. Hlongwa, N. Ross, M. Masikini, S.V. John, P. Baker, W. Roos, E.I. Iwuoha, Orthorhombic (Pmn2₁) nanostructured Li₂MnSiO₄/Al₂O₃ supercapattery electrode with efficient Li ion migratory pathway, *Batter. Supercaps.* (2018) 1–14. doi:10.1002/batt.201800045.
- [45] A.C. Nwanya, M.M. Ndipingwi, N. Mayedwaa, L.C. Razanamahandry, C.O. Ikpo, T. Waryo, S.K.O. Ntwampe, E. Malenga, E. Fosso-Kankeu, F.I. Ezema, E.I. Iwuoha, M. Maaza, Maize (*Zea mays* L.) fresh husk mediated biosynthesis of Copper Oxides: Potentials for Pseudocapacitive Energy Storage, *Electrochim. Acta.* (2019). doi:10.1016/j.electacta.2019.01.186.
- [46] D. Majumdar, S. Pal, Hydroxy-Functionalized Graphene: A Proficient Energy Storage Material, *Fundam. Renew. Energy Appl.* 6 (2016). doi:10.4172/20904541.1000209.
- [47] O.S. Mendoza-Hernandez, E. Hosono, D. Asakura, H. Matsuda, Y. Sone, M. Umeda, Kinetic analysis of graphitized-carbon reactions in Li-ion cells before and after cycling degradation, *Solid State Ionics.* 321 (2018) 98–105. doi:10.1016/j.ssi.2018.04.012.
- [48] C. Zhao, Y. Huang, C. Zhao, X. Shao, Z. Zhu, Rose-derived 3D carbon nanosheets for high cyclability and extended voltage supercapacitors, *Electrochim. Acta.* 291 (2018)

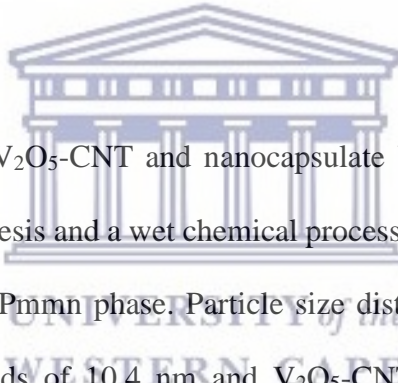
-
- 287–296. doi:10.1016/j.electacta.2018.09.136.
- [49] Y. Ma, M. Chen, X. Zheng, D. Yu, X. Dong, Synergetic effect of swelling and chemical blowing to develop peach gum derived nitrogen-doped porous carbon nanosheets for symmetric supercapacitors, *J. Taiwan Inst. Chem. Eng.* 101 (2019) 24–30. doi:10.1016/j.jtice.2019.04.031.
- [50] D. Momodu, N.F. Sylla, B. Mutuma, A. Bello, T. Masikhwa, S. Lindberg, A. Matic, N. Manyala, Stable ionic-liquid-based symmetric supercapacitors from Capsicum seed-porous carbons, *J. Electroanal. Chem.* 838 (2019) 119–128. doi:10.1016/j.jelechem.2019.02.045.
- [51] C. Long, X. Chen, L. Jiang, L. Zhi, Z. Fan, Porous layer-stacking carbon derived from in-built template in biomass for high volumetric performance supercapacitors, *Nano Energy*. 12 (2015) 141–151. doi:10.1016/j.nanoen.2014.12.014.
- [52] L. Guardia, L. Suárez, N. Querejeta, V. Vretenár, P. Kotrusz, V. Skákalová, T.A. Centeno, Biomass waste-carbon/reduced graphene oxide composite electrodes for enhanced supercapacitors, *Electrochim. Acta.* 298 (2019) 910–917. doi:10.1016/j.electacta.2018.12.160.

CHAPTER FOUR

RESULTS AND DISCUSSION - MANUSCRIPT 2

Vanadia-Hydroxylated Graphene Nanocapsules as Scherbinaite Active Supercapacitor Electrodes (Prepared for ACS Applied Materials & Interfaces)

Abstract



In this work, V_2O_5 nanorods, V_2O_5 -CNT and nanocapsulate V_2O_5 -CNT-G-ol crystals were prepared by hydrothermal synthesis and a wet chemical process. All materials were indexed to the Scherbinaite orthorhombic $Pmmn$ phase. Particle size distribution obtained from SAXS revealed primary V_2O_5 nanorods of 10.4 nm and V_2O_5 -CNT as well as V_2O_5 -CNT-G-ol particles at 26.8 and 22.9 nm, respectively. Stretching and bending vibrations of V=O, V-O-V bonds were observed at 1012.6, 835.8 and 608.6 cm^{-1} in FTIR analysis. These bands were slightly shifted to lower wavenumbers due to the interaction of V_2O_5 with CNTs and G-ol in V_2O_5 -CNT and V_2O_5 -CNT-G-ol electrode materials. The skeletal and bending vibrations of V-O-V and V-bonds were observed at Raman shift values of 283.6 cm^{-1} and 337.1 cm^{-1} , respectively. Electrochemical studies performed in three electrodes in 1 M $LiNO_3$ aqueous electrolyte delivered a specific capacitance of 209.5 $F g^{-1}$, 142.6 $F g^{-1}$, and 88.1 $F g^{-1}$ for V_2O_5 , V_2O_5 -CNT and V_2O_5 -CNT-G-ol electrodes, respectively at a scan rate of 5 $mV s^{-1}$. A lower charge transfer resistance was obtained for the nanocapsulate electrode indicating better faster charge transfer reactions in the nanocomposite. Asymmetric supercapacitors assembled to

V₂O₅-based electrodes and activated carbon delivered a specific capacitance 173.4 F g⁻¹ for AC//V₂O₅-CNT-G-ol at a voltage of 1.6 V. This value was 2.3 times greater than that of the AC//V₂O₅-CNT device (75.4 F g⁻¹) and even 7.1 times greater than the AC//V₂O₅ device. This higher capacitance can be attributed to the synergistic effect G-ol, CNTs and V₂O₅-nanorods, which reduced aggregation of V₂O₅ nanorods and provided a larger surface area for diffusion of Li⁺ ions, leading to enhanced electrochemical performance. A cycling stability of 69 % was obtained for the AC//V₂O₅-CNT-G-ol device over 4,000 cycles at a specific energy of 63.2 Wh kg⁻¹ and specific power of 609.2 W kg⁻¹. These findings highlight the potentials of V₂O₅ and G-ol composite electrode materials as high energy supercapacitor electrodes and may open up new avenues for wide ranging applications.

Keywords: V₂O₅ nanorods, Graphol, Nanocapsules, Activated carbon, Asymmetric supercapacitor, High specific energy



4.1 Introduction

The global drive towards decarbonizing the energy economy and environmental concerns have motivated worldwide pursuits of sustainable energy sources and storage technologies. The research community is therefore, engaging in wide-ranging research in the development of energy storage/conversion devices with high power and energy densities [1]. Rechargeable batteries and supercapacitors owing to their high energy and power densities are considered as the most promising energy storage devices which could enable stable and steady electricity supply from intermittent renewable energy sources in electric, hybrid electric vehicles and large

scale grid energy storage [2,3]. Supercapacitors have the advantages of high power density, long cycling life over rechargeable batteries and can ensure fast energy collection and delivery due to their very fast charge/discharge rates. Supercapacitors are applied in emergency doors, power back up systems and electric vehicles [4]. As for the energy and power density, they can act as a bridge between batteries and conventional batteries. Based on the charge storage mechanism, supercapacitors have two categories, which are: Electric double-layer capacitors (EDLCs), mainly carbon-based materials which store charge electrostatically at the electrode/electrolyte boundary and pseudocapacitors which mostly are transition metal oxides (TMO) and conducting polymers which store charge through reversible faradaic redox reactions [5]. The two mechanisms can all together rely on the nature of the electrode material. Carbonaceous materials such as activated carbon, carbon nanotubes and graphene have been used as electrode materials due to their ease of processability, low cost, tunable surface porosity and good electrocatalytically active sites for various redox reactions. However, their charge storage capability is restricted by agglomeration and lack of faradaic processes which limits the specific capacitance of EDLCs [6,7]. The development of composites electrode materials consisting of EDLCs and pseudocapacitors therefore becomes inevitable.

Among the available pseudocapacitive TMOs, V_2O_5 has been a candidate of many literature studies due to its low cost, layered structure for efficient ion diffusion, high theoretical capacitance of 2120 F g^{-1} , ease of synthesis and multiple oxidation states (+2 - +5) for a wide redox behavior [8,9]. However, poor lithium-ion diffusion, low electrical conductivity and high dissolution in liquid electrolyte lead to undesirable capacity retention and rate capability [10,11]. These problems according to previous reports can be alleviated by preparing porous V_2O_5 nanoparticles with various morphologies for larger surface area and faster diffusion of Li-ions [1,12], nanocomposites with carbonaceous materials such as graphene [9,13], carbon nanotubes [14] as well as doping V_2O_5 with various metals [15], to enhance electrical

conductivity and cycle stability. It is well recognized that electrode materials in nano-dimensions enable increased contact area between the electrode particles and the electrolyte with a corresponding shorter diffusion length of Li-ions within the host material. Carbonaceous materials with high porosity and specific surface area on the other hand, can act as scaffolds to support, stabilize and disperse the active electrode material, yielding more sites for charge storage. In this regard, Ahirrao *et al.*, reported a high surface area V₂O₅ nanowire-reduced graphene oxide composite prepared via hydrothermal synthesis, with improved electrical conductivity and a high gravimetric capacitance of 1002 F g⁻¹ at current load of 1 A g⁻¹ and energy density of 116 Wh Kg⁻¹ [16]. Narayanan prepared a carbon nanodot entrapped V₂O₅ nanobelts by hydrothermal synthesis which demonstrated an enhanced electronic and ion propagation property with a specific capacitance of 270 F g⁻¹ at current load 1 A g⁻¹ and an energy density of 60 Wh Kg⁻¹ [17]. More recently, Bai *et al.*, [18] and Zhang *et al.*, [19] synthesized freeze dried V₂O₅/holey reduced graphene oxide hydrogel and mesoporous carbon hollow spheres/3D-V₂O₅ nanosheets, respectively by hydrothermal synthesis and subsequent freeze drying. The V₂O₅/holey reduced graphene oxide composite showed an interconnected 3D porous network with V₂O₅ nanosheets distributed over the aerogel preventing restacking of the reduced graphene oxide sheets. The electrode exhibited a high specific capacitance of 264 F g⁻¹ at a current load of 0.25 A g⁻¹. Efficient electronic transport was shown by the mesoporous carbon hollow spheres/3D-V₂O₅ hybrid electrode with a high specific capacitance of 313 F g⁻¹ at a current load of 0.25 A g⁻¹. Although considerable improvements on the specific capacitance and overall electrochemical performance of V₂O₅ and composites have been achieved, a few open questions are still to be addressed such as, restacking or self-aggregation of V₂O₅ nanosheets and carbon scaffolds which limits the surface area of electrochemical active sites as well as mass transport. However, the use of nanoporous networks with high degree of pore

connectivity and enhanced mass transport is expected to provide high specific capacitance and commendable electrochemical performance.

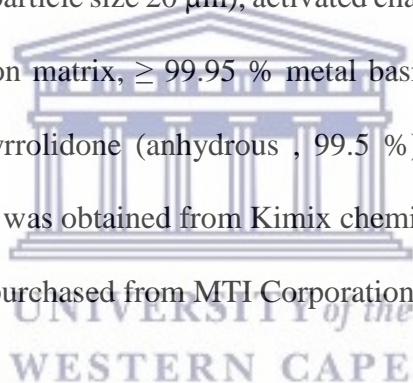
Hydroxylated graphene (Graphol or G-ol) has recently emerged as a flexible and aqueous dispersible form of tuned graphene, with a distinct structure, defined bandgap, high electrical and thermal conductivity and available sites for high density functionalization of the carbon backbone [20,21]. Sun *et al.*, [22] prepared hydroxylated graphene with good mechanical characteristics and promising biomedical applications such as bone, vessel and skin regeneration. Zu and Manthiram [23] reported a hydroxylated graphene-sulfur nanocomposite prepared by chemical deposition method. The nanocomposite delivered high electrochemical performance as a positive electrode for lithium sulfur batteries.

Herein, we report on the synthesis of V_2O_5 nanorods and formation of a nanocapsulate composite with CNTs and G-ol (V_2O_5 -CNT-G-ol) via a combination of hydrothermal synthesis and wet chemistry. Nanocapsulate morphology of the V_2O_5 -CNT-G-ol nanocomposite electrode showed an increased interlayer spacing and reduced aggregation of V_2O_5 nanorods, which allowed faster diffusion of Li^+ ion within the electrode host, with improved electrochemical performance. An asymmetric supercapacitor fabricated using the nanocomposite electrode as positive electrode and activated carbon as the negative electrode delivered high specific energy and power. These findings may promote the use of V_2O_5 and carbon-based nanocomposites for supercapacitive applications.

4.2 Experimental details

4.3 Materials

Microcrystalline graphite (2- 15 μm , 99.99 %) was purchased from Alfar Aesar, while the rest of the chemicals used were supplied by Sigma-Aldrich and were all used without further purification. These include, vanadium (V) oxide (> 98 % reagent grade), oxalic acid dehydrate (≥ 99 % ACS reagent), isopropanol (70 % in water), ethanol (absolute, ≥ 99.8 %), hydrogen peroxide solution (30 wt. % in water, ACS reagent), carbon nanotubes, multiwalled (> 98% carbon basis, 6 - 13 nm x 2.5 - 20 μm), sodium hydroxide (98 – 100.5 %), Tetrahydrofuran (THF, > 99.8 %), Borane in THF complex (1 M), ethanol (absolute, ≥ 99.8 %), polytetrafluoroethylene (mean particle size 20 μm), activated charcoal (Norit $\text{\textcircled{R}}$ pellets), carbon black (4 μm mesoporous carbon matrix, ≥ 99.95 % metal basis), lithium nitrate (99.99 %), chloroform and N-methyl-2-pyrrolidone (anhydrous, 99.5 %). Hydrochloric acid (reagent grade and assay 36.5 – 38.0 %) was obtained from Kimix chemicals and nickel foam (1.6 mm thick, 0.25 μm pore diameter) purchased from MTI Corporation.

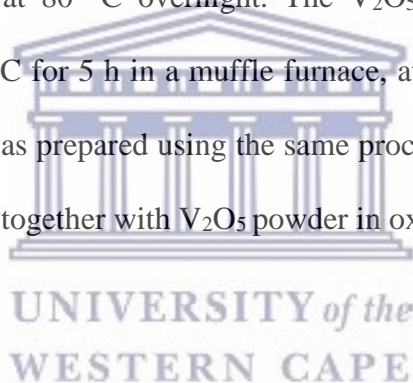


4.3.1 Functionalization of CNTs by acid oxidation

Multiwalled CNTs were purified and further shortened in length by acid oxidation in nitric acid [24]. Customarily, 120 mg of CNTs were dispersed in 10 mL of 3 M nitric acid solution for 24 h. Thereafter, the solid products were collected on a filter paper and washed several times with distilled water until the pH of the filtrate was around neutral (pH ~ 7). The functionalized CNTs were obtained by further drying at 80 $^{\circ}\text{C}$ in a vacuum oven overnight.

4.3.2 Synthesis of V₂O₅ nanorods and V₂O₅-CNT nanonetwork

Nanoporous V₂O₅ electrode material was synthesized by an oxalic acid-assisted hydrothermal synthetic route with subsequent calcination. Typically, V₂O₅ powder was dissolved in 10 mL of 0.5 M oxalic acid solution. The mixture was vigorously stirred at 60 °C for 6 h with the formation of a clear blue colouration. The solution was allowed to cool down slowly to room temperature and a mixture of isopropanol and H₂O₂ in the ratio of 6:1 was slowly added and the resultant mixture further stirred for 30 mins. The mixture was transferred into a Teflon-lined autoclave and heated at 170 °C for 18 h, followed by centrifuging, copious washing with water and ethanol, and dried at 80 °C overnight. The V₂O₅ nanorods were obtained by annealing the particles at 550 °C for 5 h in a muffle furnace, at a heating rate of 5 °C min⁻¹. The V₂O₅-CNT nanonetwork was prepared using the same procedure with the addition of 7.5 mg of purified CNTs dissolved together with V₂O₅ powder in oxalic acid.



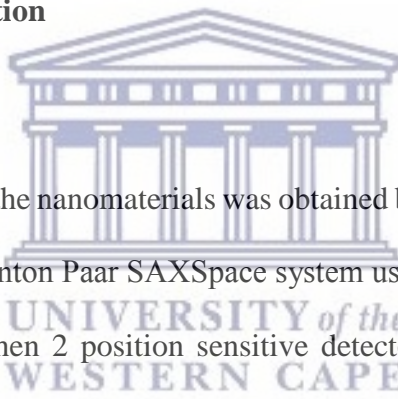
4.3.3 Synthesis of hydroxylated graphene (graphol /G-ol)

Graphol was prepared by hydroboration of graphene oxide proposed by Poh *et al.*, Graphene oxide (200 mg) initially prepared by a modified Hummers method [25] was ultrasonicated in anhydrous THF (200 mL) for 1 h followed by addition of 20 mL of Borane in THF complex. The mixture was heated at 50 °C at reflux under argon atmosphere for 24 h. A mixture of 3 M NaOH / 30 % H₂O₂ was slowly added and the reaction was further kept at 50 °C for 3 h at reflux. Hydroxylated graphene nanosheets were obtained by suction filtration and washed severally with THF and water. The nanosheets were dried in a vacuum oven at 50 °C for 48 h.

4.3.4 Synthesis of V₂O₅-CNT-G-ol nanocapsules

Nanoporous V₂O₅-CNT-G-ol composite was prepared by a wet chemical process whereby, the V₂O₅-CNT nanonetwork and graphol in a ratio of 6:1 were dispersed by ultrasonication in chloroform and evaporated to dryness at room temperature for 36 h. The nanocomposite was further annealed at 350 °C for 2 h in a muffle furnace at a heating rate of 5 °C min⁻¹.

4.3.5 Material Characterization



The particle size distribution of the nanomaterials was obtained by small-angle X-ray scattering experiments performed on an Anton Paar SAXSpace system using copper K α radiation (0,154 nm) equipped with a 1 D mythen 2 position sensitive detector and a beamstop alignment. Morphological studies were done using ZEISS ULTRA scanning electron microscope furnished with an energy dispersive spectrometer and a Tecnai G² F₂O X-Twin MAT 200 kV field emission transmission electron microscope from FEI. The analyses were performed on a carbon grid and nanomaterials were coated with a palladium-gold nanoalloy to improve contrast during analysis. X-ray powder diffraction patterns of V₂O₅, V₂O₅-CNT and V₂O₅-CNT-G-ol were obtained using a D8 advance diffractometer (BRUKER-AXS) using copper K α_1 radiation ($\lambda \sim 0.154$ nm) operating at 40 kV and 40 mA. A Perkin Elmer Spectrum 100 series Attenuated Total Reflection (ATR) Fourier Transform Infrared spectrometer was used to obtain the functional groups present in the synthesized material. A HORIBA scientific Xplora Raman microscope integrated with a 532 nm laser and Labspec spectral software with

a resolution of 1 μm was used to obtain the vibrational modes present in the materials. Electrochemical studies were performed using both three and two electrode cells on a VMP-300 potentiostat from Bio-Logic instruments, with aqueous 1 M LiNO_3 as electrolyte.

4.3.6 Electrode preparation and electrochemical measurements

Prior to electrochemical analysis, nickel foam was cut into rectangular shapes of $0.5 \times 1 \text{ cm}^2$ and coin-shapes of 20 mm in diameter. The different sizes were cleaned and etched to remove surface oxide layer using 1 M HCl solution in an ultrasonic bath for 15 mins, then cleaned in absolute ethanol and deionized water for 15 min in sequence by ultrasonication and finally dried at 90°C for 12 h. The working electrode was prepared by mixing 70 % of the active material with 20 % carbon black (conducting agent) and 10 % polytetrafluoroethylene (binder) in a few drops of anhydrous N-methyl-2-pyrrolidone. A homogenous paste was obtained using a mortar and pestle and coated on nickel foam with a diameter of 0.5 cm^2 using a spatula and dried at 80°C for 12 h. Ag/AgCl and Pt wire were used as the reference and counter electrodes, respectively for studies in three-electrode system. For studies in the two-electrode cell, the homogenous paste was coated on coin-shaped nickel foam with diameter of 20 mm and assembled in a Swagelok using V_2O_5 , $\text{V}_2\text{O}_5\text{-CNT}$ and $\text{V}_2\text{O}_5\text{-CNT-G-ol}$ nanomaterials as the positive electrodes and activated carbon as the negative electrode. Cyclic voltammograms were recorded in a potential window of -0.2 to 0.8 V at different scan rates and electrochemical impedance measurements were obtained at a frequency range of 10 kHz – 100,000 mHz with 10 points per decade. CV curves, galvanostatic charge-discharge profiles and the cycling performance of the hybrid supercapacitor cells were obtained at a voltage window of 1.6 V.

4.4 Results and Discussion

4.4.1 Structure and morphological Analysis by Scanning and Transmission Electron Microscopies (SEM and HRTEM)

The structure and morphology of V_2O_5 , CNTs, V_2O_5 -CNT and V_2O_5 -CNT-G-ol were examined by SEM and HRTEM. Figure 4.1 (a – f) shows the SEM, HRTEM and selected area diffraction (SAED) images of V_2O_5 , CNTs, V_2O_5 -CNT, G-ol and V_2O_5 -CNT-G-ol nanomaterials obtained at high resolution. The SEM micrographs of V_2O_5 as shown in Figure 4.1 (a) reveal V_2O_5 nanorods growing from a centre point in an irregular manner while CNTs display a fibrous and agglomerated morphology as shown by Figure 4.1 (b). The SEM micrographs of V_2O_5 -CNT also reveal aggregated nanorods growing in a vertical orientation. The sizes of V_2O_5 nanorods obtained from ImageJ show rods with thickness ranging from 10.4 – 130.6 nm, average thickness of 73.5 nm and a standard deviation of 31.9 nm. Meanwhile, V_2O_5 -CNT nanorods range from 70.1 – 105.7 nm with an average thickness of 87.6 nm and a standard deviation of 12.7 nm. The SEM image of V_2O_5 -CNT-G-ol as shown in Figure 4.1 (d) displays nanocapsule-like morphology with sizes varying from 61.6 – 141.9 nm in thickness, with average thickness of 110.7 nm and standard deviation of 37.7 nm. G-ol nanosheets shown as the inset in Figure 4.1 (d) consist of nano-layers of 14- 23 nm thick. A darker contrast is obtained for the V_2O_5 nanorods from HRTEM analysis as shown in Figure 4.1 (e) due to the presence of ethanol used as solvent to disperse material prior to analysis and was not properly evaporated. Lattices fringes and SAED images shown as insets in the HRTEM image confirmed the crystallinity of the V_2O_5 nanomaterial. The presence of the fibrous morphology of CNTs in V_2O_5 -CNT nanonetwork and the capsule-like shape of V_2O_5 -CNT-G-ol

nanocapsules are both observed in the HRTEM images as shown in Figure 4.1 (f) and (g), respectively. Their lattice fringes are also shown as insets on the images and the concentric circles in SAED micrographs, all confirm that the materials possess good crystallinity.

The elemental composition of V₂O₅-CNT-G-ol nanocapsules displayed as energy dispersive spectroscopic (EDS) maps, are shown in Figure 4.1 (h). The contrast of each map indicates the percentage composition of the element in the material.



Figure 4.1 (a): SEM image of V₂O₅

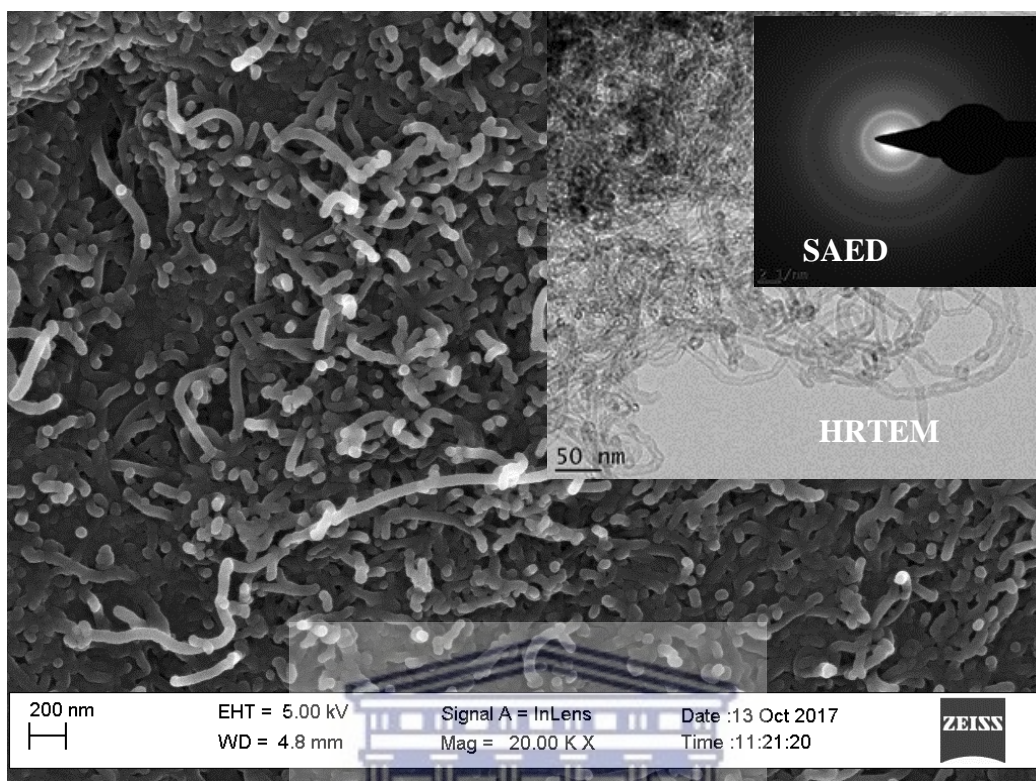
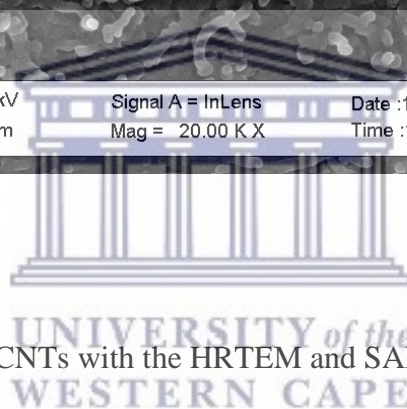


Figure 4.1 (b): SEM image of CNTs with the HRTEM and SAED images as insets



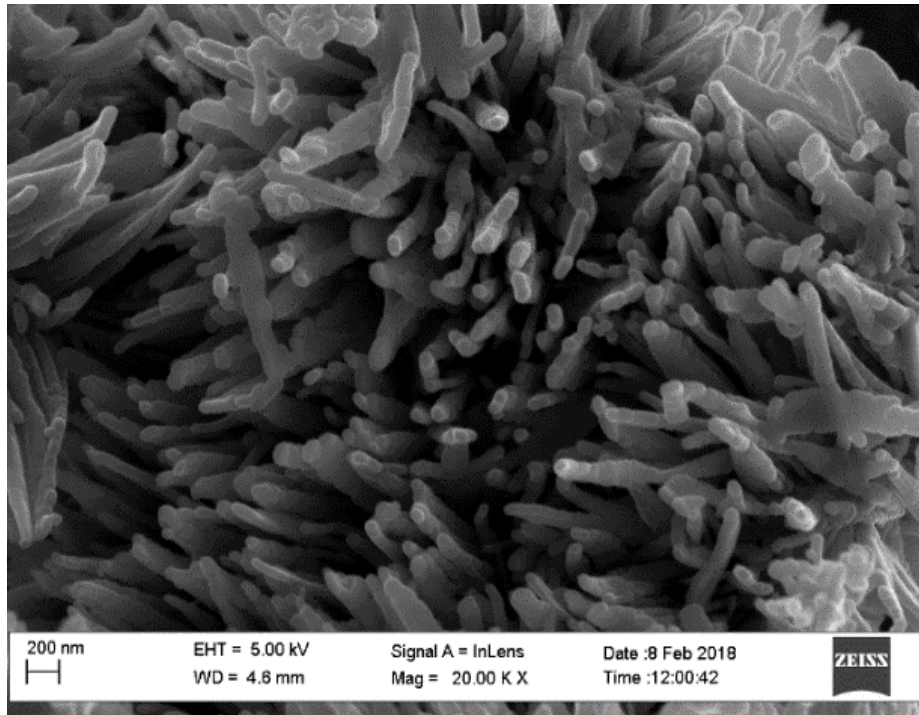


Figure 4.1 (c): SEM image of V_2O_5 -CNT nanonetwork



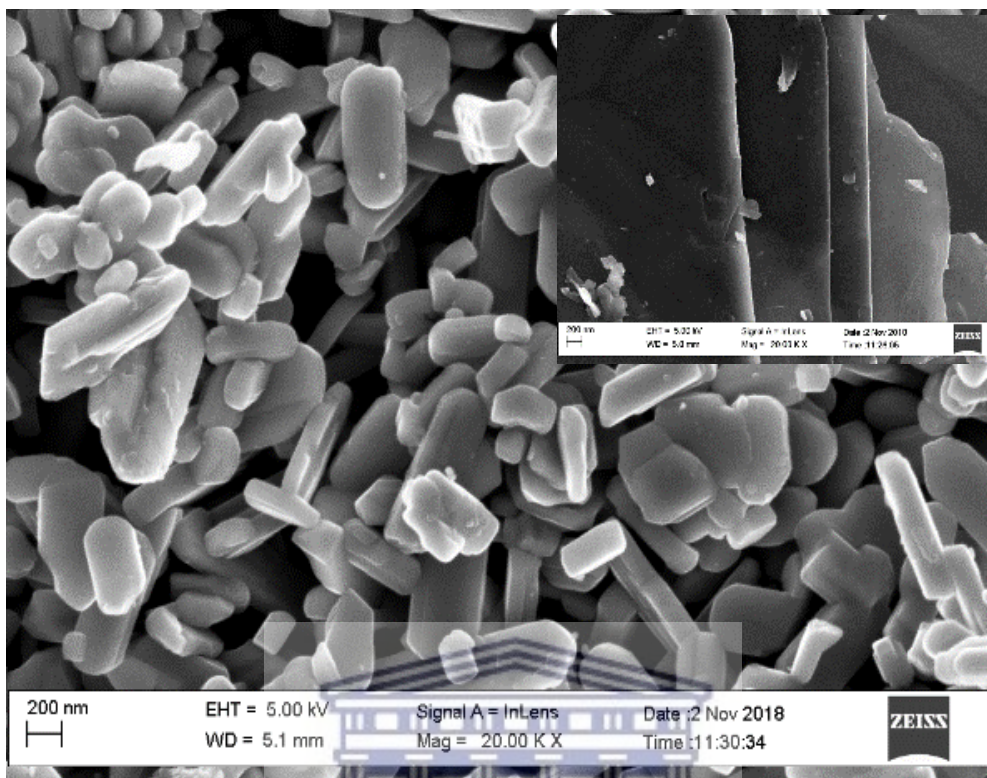
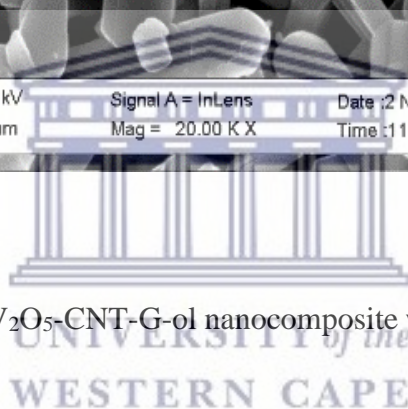


Figure 4.1 (d): SEM image of V_2O_5 -CNT-G-ol nanocomposite with SEM image of G-ol as the inset



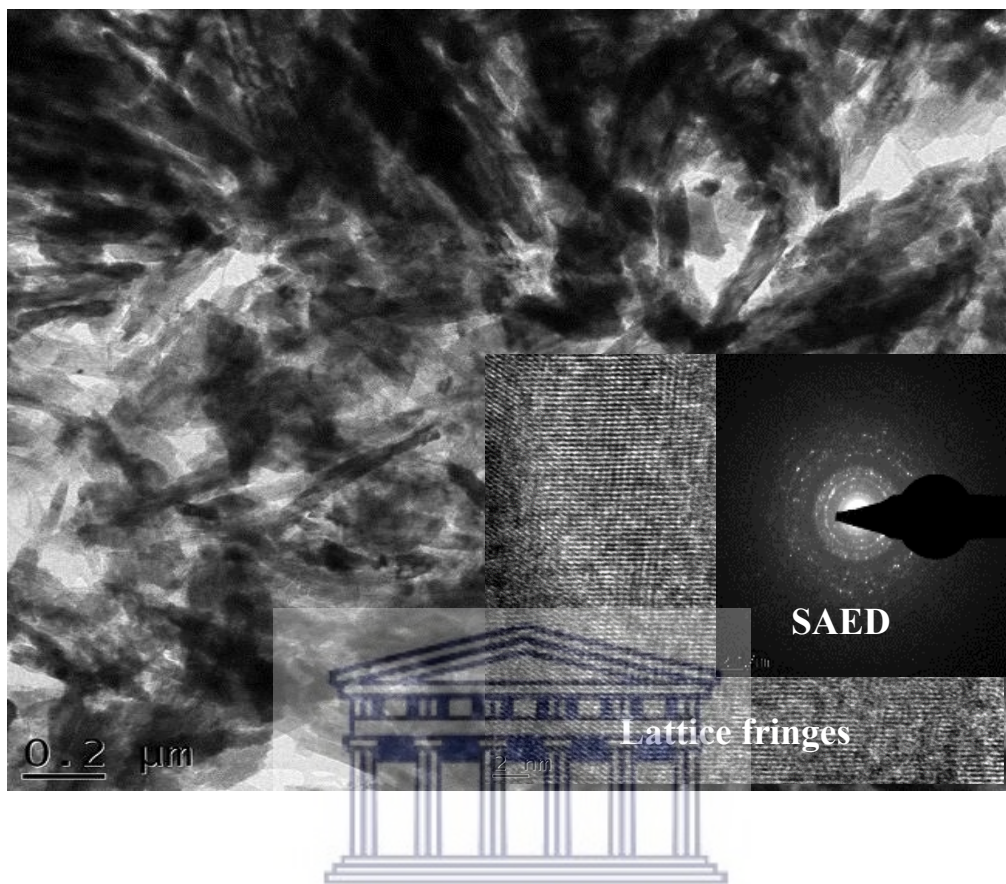


Figure 4 1 (e): HRTEM image of V₂O₅ nanorods with its lattice fringes and SAED image as insets

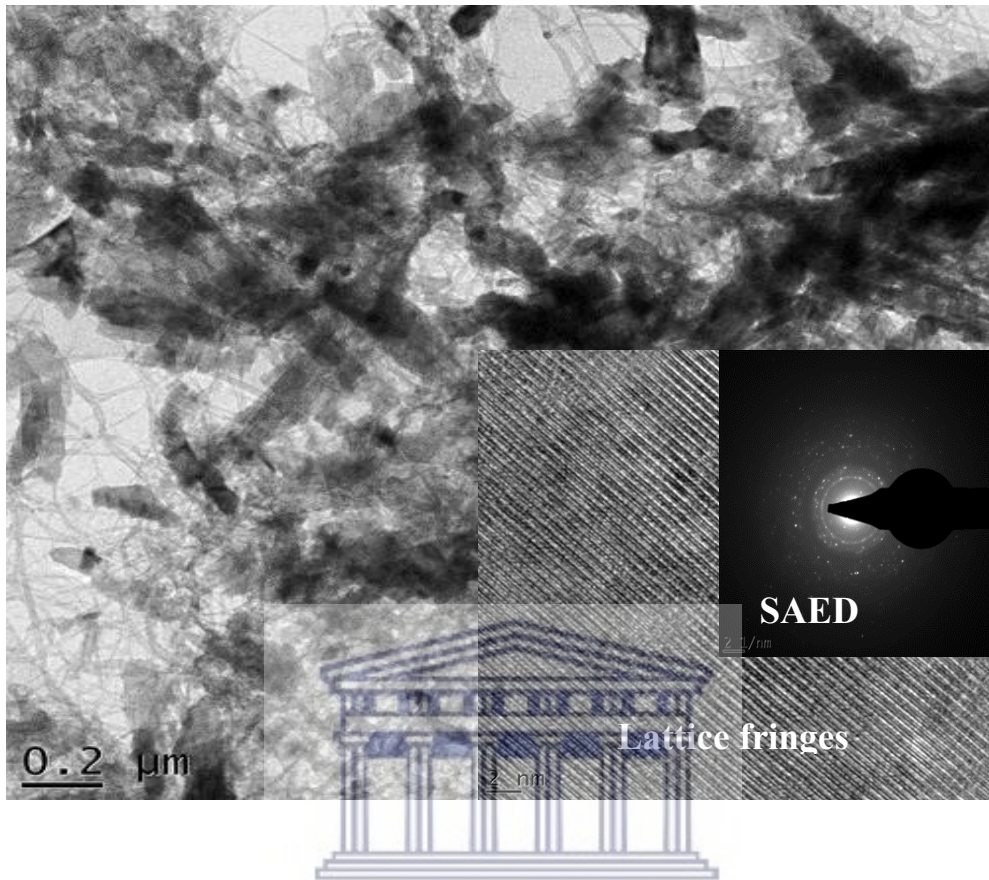


Figure 4 1 (f): HRTEM image of V_2O_5 -CNT nanonetwork with lattice fringes and SAED images as insets

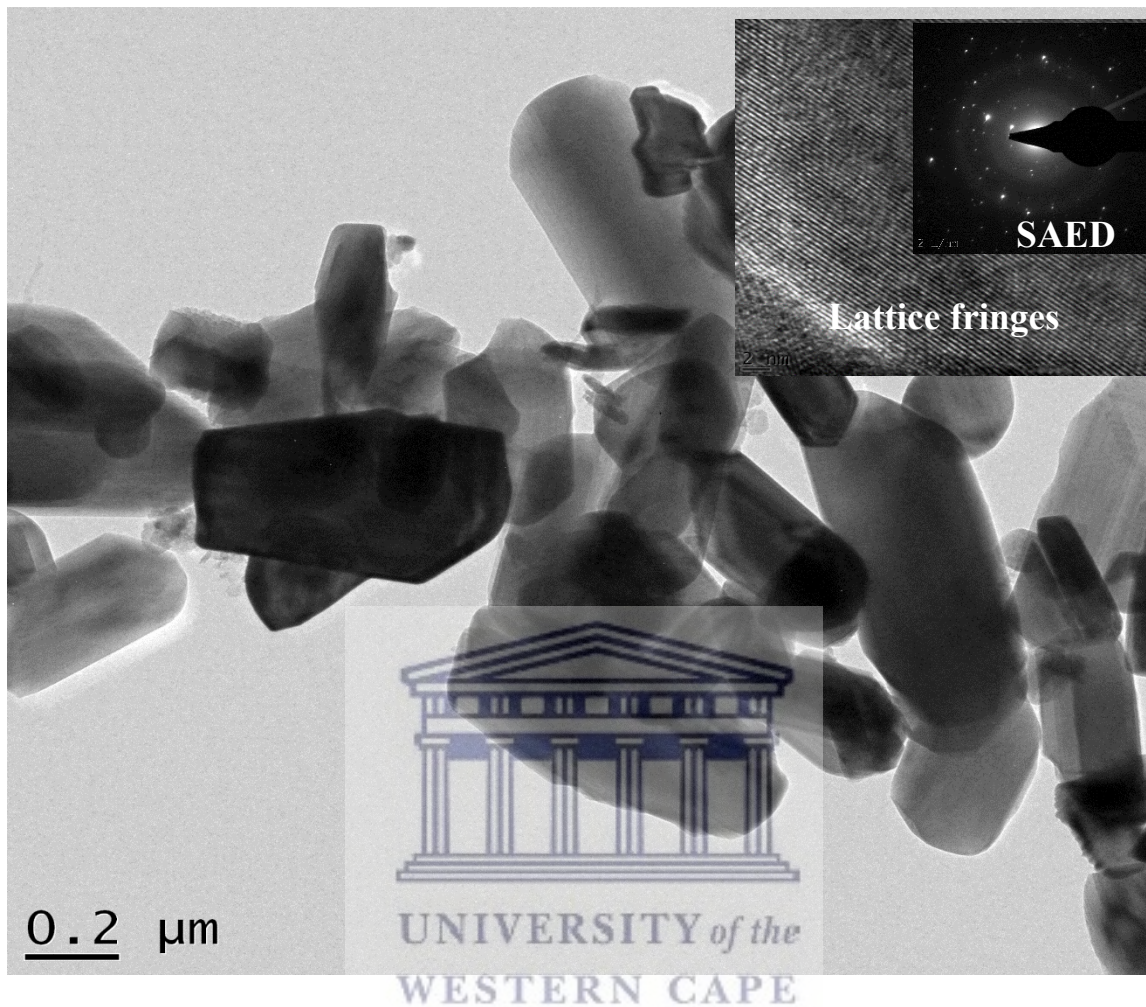


Figure 4.1 (g): HRTEM image of V_2O_5 -CNT-G-ol nanocomposite with lattice fringes and SAED images as insets

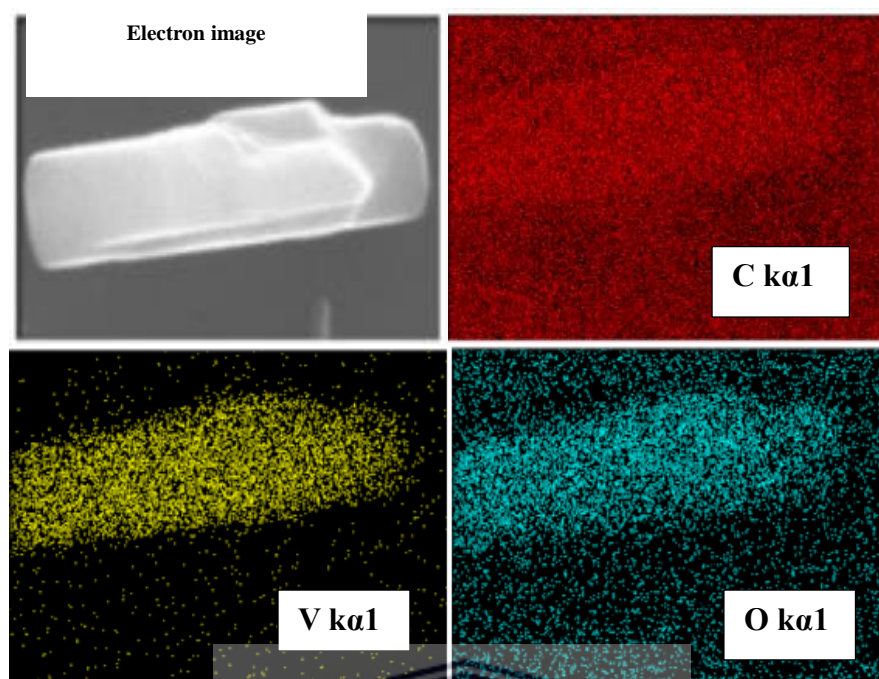


Figure 4.1 (h): EDS maps of V_2O_5 -CNT-G-ol with relative elemental intensities: carbon (red), vanadium (yellow) and oxygen (blue)



4.4.2 Particle size distribution by Small Angle X-ray Scattering (SAXS)

The particle size distribution, primary particle sizes and sizes of aggregates of the primary particles of V_2O_5 , V_2O_5 -CNT, CNTs, G-ol and V_2O_5 -CNT-G-ol nanomaterials were elucidated by SAXS investigations. Figure 4.2 (a) and (b) represents the scattering patterns and pair distance distribution functions $[P(r)]$ according to the physical volume of scattered particles and the number of the scattered particles, respectively. By visual inspection of the pair distance distribution functions in Figure 4.2, the shape of the particles can be deduced. The slightly left skewed nature of the particle size distribution of V_2O_5 nanorods as shown in Figure 4.2 (a) indeed confirms their globular nature and variation in particle sizes of the rods. Moreover, the

shape of V₂O₅-CNT-G-ol as displayed by the number scattering intensities / P(r) in Figure 4.2 (b) with broad maximum particle diameters, indicate some hollow characteristics of the particles [26] and further confirms the nanocapsule morphologies obtained in SEM and HRTEM investigations. The hollow inside may be induced by the presence of CNTs in the material. The particle size distribution by number of CNTs scattered indicates bell-shaped distribution with maxima at 7.9 nm as shown in Figure 4.2 (b). Likewise, the scattering intensities of V₂O₅ nanorods present a left-skewed particle size distribution by volume with the maximum primary particles at 10.4 nm and aggregates of primary particles at 81.9 nm as well as a bell-shaped distribution by number of scattered particles with maximum primary particles at 19.0 nm and aggregates at 89.4 nm. More so, V₂O₅-CNT and V₂O₅-CNT-G-ol show almost a dumbbell-shaped particle size distribution by number of particles scattered with maximum population of primary particles at 26.8 and 22.9 nm, respectively and aggregates or both secondary particles showing a maximum diameter of 131.3 nm. It is worth noting that, the G-ol nanosheets demonstrate the same particle size distribution arrangement as V₂O₅-CNT-G-ol nanocapsules. This is quite informative due to the fact that, on addition of G-ol nanosheets, the morphology of V₂O₅-CNT nanonetwork is transformed from rod-like shape to capsules as revealed by SEM and HRTEM analysis. Therefore, G-ol in V₂O₅-CNT-G-ol acts as a structure/performance directing agent. It is also observed that the center-peak in the particle size distribution by physical volume of particles scattered is lower than that of the number of particles scattered. This can be attributed to an occurrence whereby, at low volume fractions, nucleation of particles is favored with a decrease in size while at high volume fractions, smaller particles outnumber fewer larger particles leading to a decrease in the average diameter of the primary particles [27].

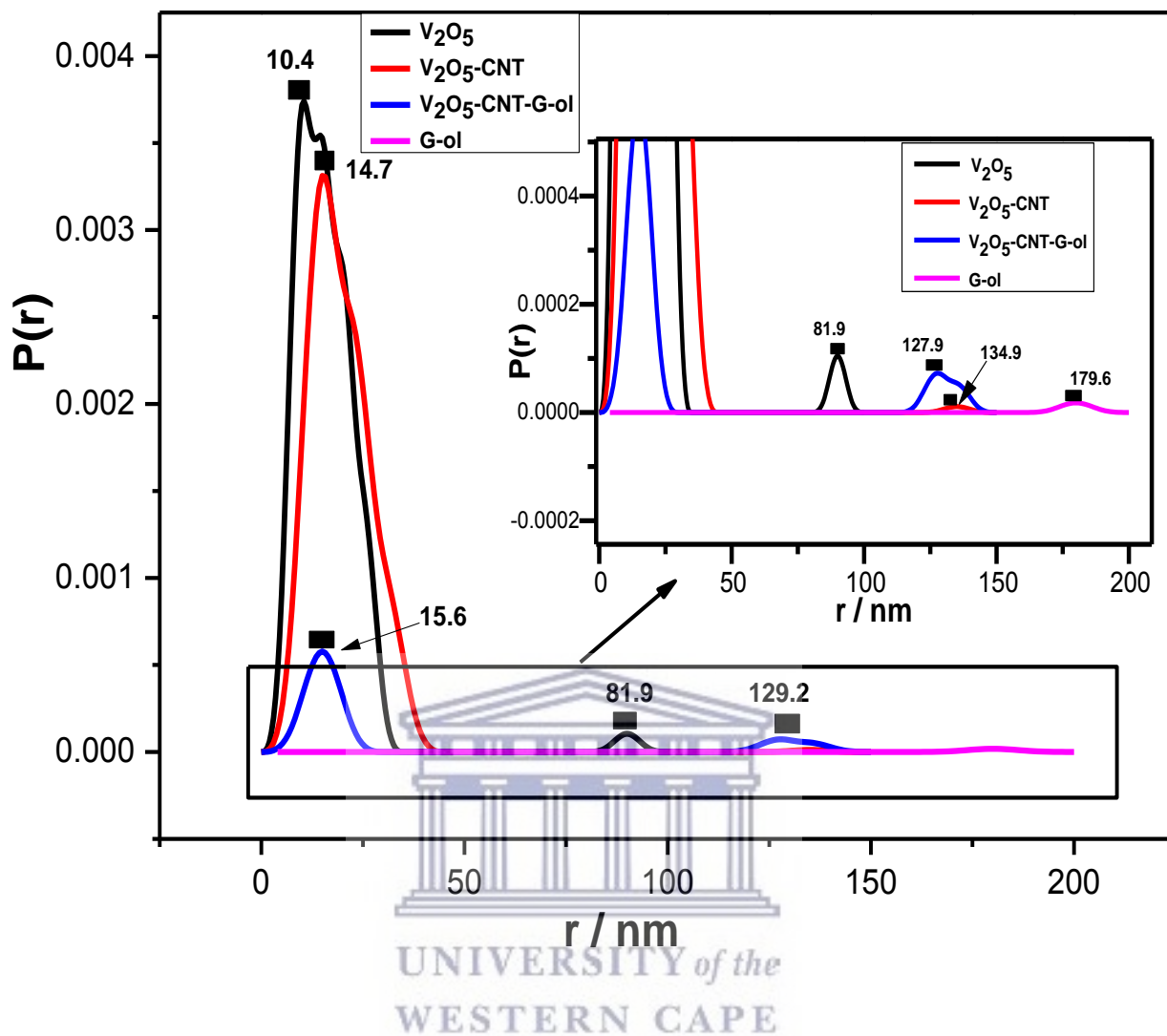


Figure 4.2 (a): SAXS pair distance distribution function by physical volume of scattered particles

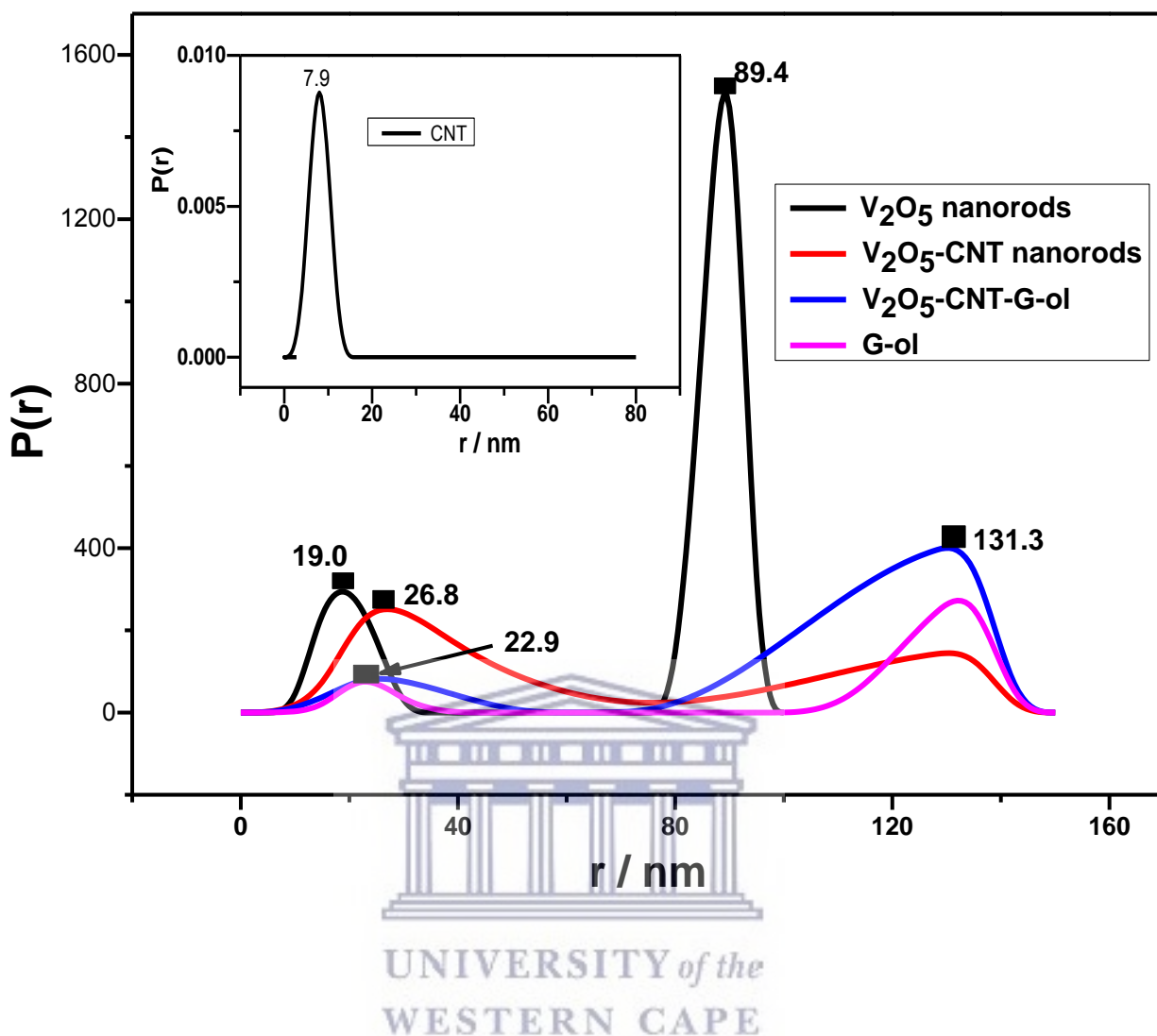


Figure 4.2 (b): SAXS pair distance distribution function by number of particles scattered

4.4.3 Crystallography by X-ray Diffraction Studies (XRD)

4.4.3 (a) Crystal structure and phase identification

The crystal structure, phase purity and average crystallite sizes of V_2O_5 , V_2O_5 -CNT, and V_2O_5 -CNT-G-ol nanomaterials were further examined by XRD analysis. Figure 4.3 (a) shows the XRD pattern of V_2O_5 , V_2O_5 -CNT and V_2O_5 -CNT-G-ol materials obtained at a 2θ range of 8

– 92 °. The XRD patterns obtained for V₂O₅, V₂O₅-CNT and V₂O₅-CNT-G-ol are all crystalline and can be indexed to the Scherbinaite orthorhombic Pmmn (59) standard phase (JCPD file no -41-1426) [16,28]. Typical reflections of 00l peaks of layered vanadium pentoxide structure, which describe the interlayer spacing are well observed with associated lattice parameters of a = 11.51 Å, b = 3.56 Å and c = 4.34 Å [29]. It is fascinating that the conventional crystallographic peak of graphitic sheets, usually located at ~28 ° as displayed by the XRD spectrum of G-ol in Figure 4.3 (b), was not observed in XRD pattern of V₂O₅-CNT-G-ol nanocomposite, possibly resulting from the low content of G-ol in the samples and uniform formation of V₂O₅ nanorods on G-ol sheets [30]. The interlayer spacing (d) was calculated according to Bragg's law, Equation 4.1.

$$n\lambda = 2d\sin\theta \quad (4.1)$$



Where, n denotes the order of diffraction ($n = 1$), λ ; the wavelength of the X-ray beam (0.154 nm), d ; the distance between VO₆ layers (d-spacing) and θ is the diffraction angle. The d-spacing obtained from the 001 reflection of the materials was 0.44 nm for V₂O₅ nanorods, 0.48 nm for V₂O₅-CNT and 0.65 nm for V₂O₅-CNT-G-ol nanocapsules, as shown in Table 4.1.

The Scherer's formula was used to determine the average crystallite sizes of V₂O₅, V₂O₅-CNT and V₂O₅-CNT-G-ol according to Equation 4.2.

$$D = \frac{K\lambda}{\beta\cos\theta} \quad (4.2)$$

Where: D represents the mean crystallite size, K , the shape factor constant (0.89), λ is the wavelength of the X-rays, β is the full width at half maximum (FWHM) of the (001) Bragg peak, and θ is the angle of reflection of the crystalline plane. The calculated crystallite sizes as shown in Table 4.1, were at 45.7 nm for V_2O_5 , 52.6 nm for V_2O_5 -CNT and 72.9 nm for V_2O_5 -CNT-G-ol.

Table 4.1: Structural properties of V_2O_5 , V_2O_5 -CNT, V_2O_5 -CNT-G-ol nanomaterials obtained from XRD studies

Material	Interlayer spacing / nm	Average crystallite size / nm
V_2O_5	0.44	45.7
V_2O_5 -CNT	0.48	52.6
V_2O_5 -CNT-G-ol	0.65	72.9

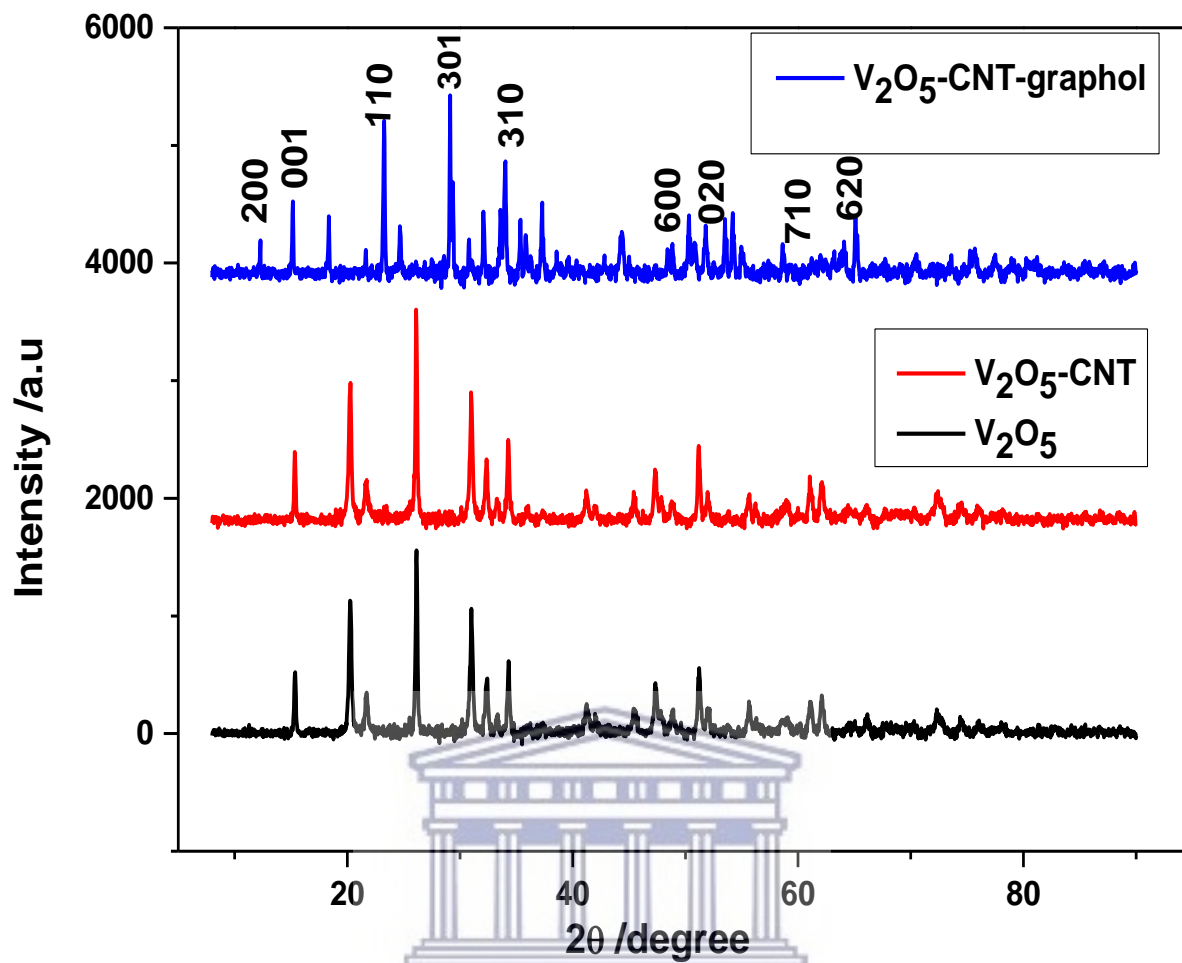


Figure 4.3 (a): XRD pattern of V₂O₅, V₂O₅-CNT and V₂O₅-CNT-G-ol nanomaterials

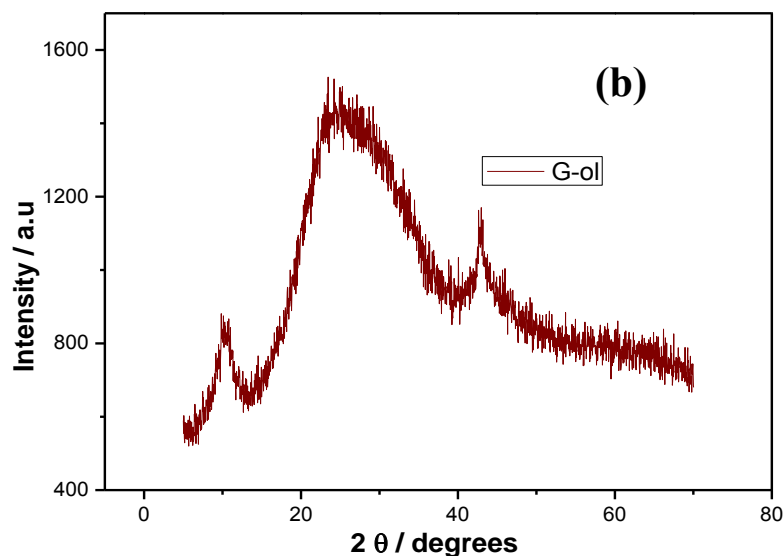
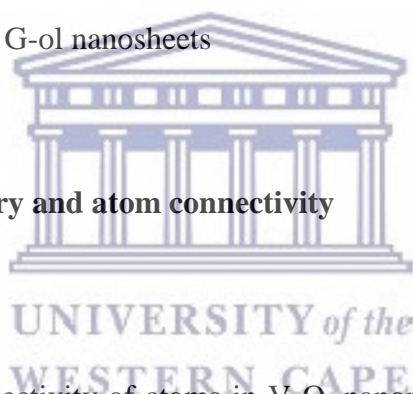


Figure 4.3 (b): XRD pattern of G-ol nanosheets

4.4.3 (b) Crystal geometry and atom connectivity



The crystal geometry and connectivity of atoms in V_2O_5 nanorods, V_2O_5 -CNT nanonetwork and V_2O_5 -CNT-G-ol nanocapsules were revealed by simulation studies using structure solution softwares such as Match and Endeavour. The crystal structure of V_2O_5 nanorods as shown in Figure 4.4 (a), consists of VO_6 octahedra that share corners and edges along one dimension creating a square pyramidal V coordination and a V_2O_9 double octahedral chain when two of such octahedra are linked together through corner sharing [31]. An idealized V_2O_5 structure is reported to be obtained from V_2O_9 double chains first by sharing their edges to form a V_4O_{14} layer, and then by sharing the apical oxygen atoms of adjacent parallel V_4O_{14} layers to form the V_4O_{10} structure [28,31]. However, vanadium atoms are displaced from the center towards corners of the octahedron, with carbon and hydrogen atoms sandwiched between vanadium

and oxygen atoms in the crystal structures of V_2O_5 -CNT and V_2O_5 -CNT-G-ol as shown by Figure 4.4 (b) and (c), respectively. The increased interlayer spacing reported in Table 4.1 is also observed. New bond centers and connections between V-O-C, V-O-H, C-O-H and many others, are depicted by Figure 4.4 (c), which will be further demonstrated by Fourier transform infrared spectroscopy.

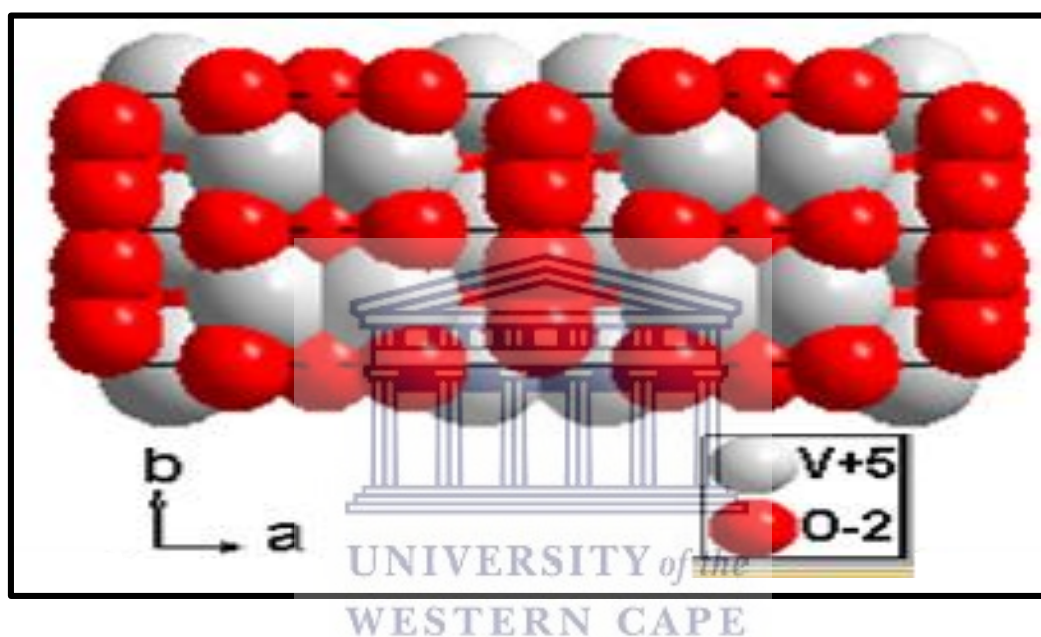


Figure 4.4 (a): Crystal structure models of V_2O_5 nanorods simulated from Match and Endeavour

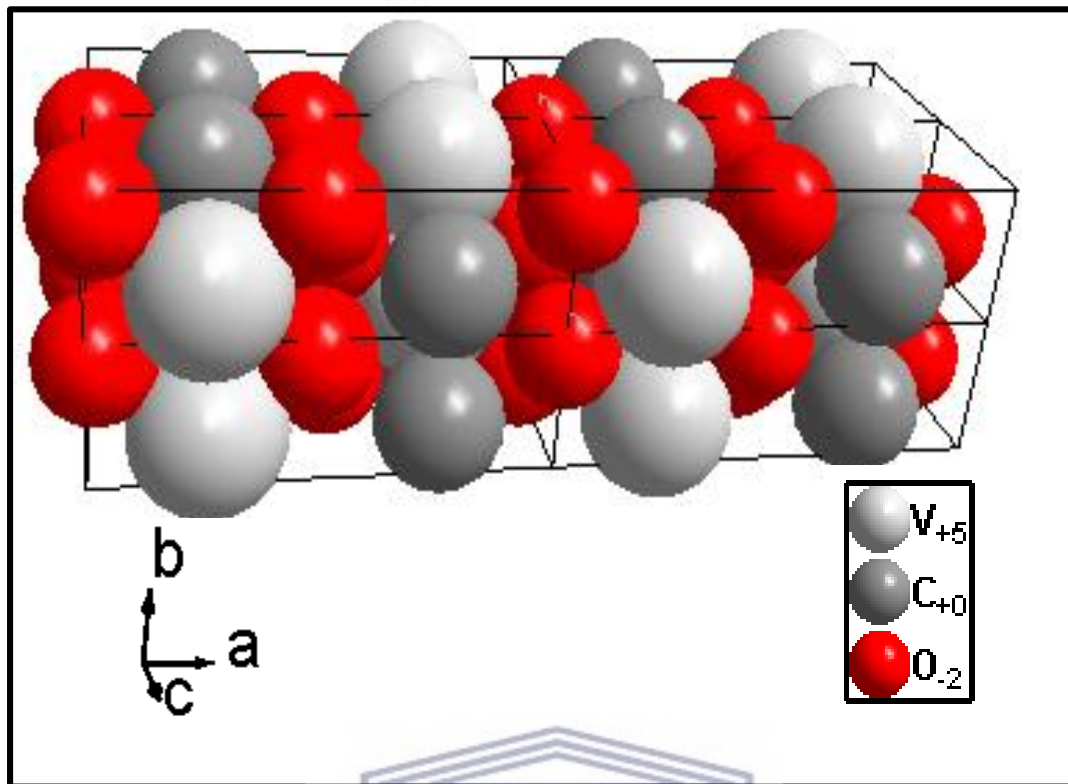


Figure 4.4 (b): Crystal structure models of V_2O_5 -CNT nanonetwork simulated from Match and Endeavour



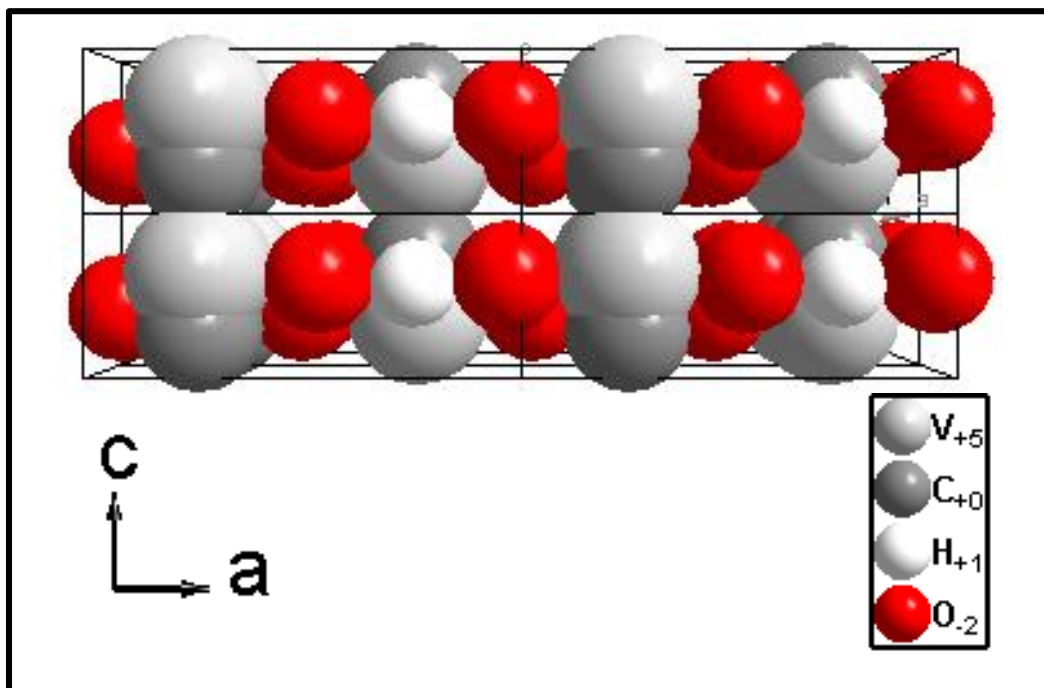


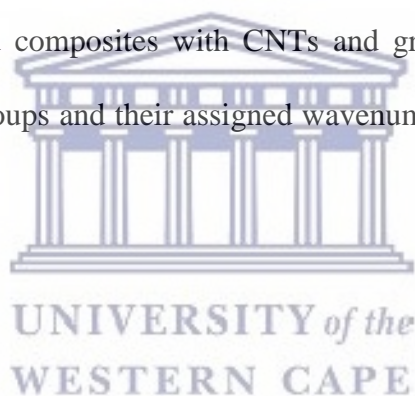
Figure 4.4 (c): Crystal structure models of V_2O_5 -CNT-G-ol nanocapsules simulated from Match and Endeavour



4.4.5 Functional group Analysis by Fourier transform Infrared (FTIR) Spectroscopy

FTIR spectroscopy was used to obtain further details on the chemical bonds and functional groups present in the electrode materials as the V_2O_5 crystal was transformed from vanadium square pyramidal coordination to irregular centers with carbon and hydrogen atoms sandwiched between vanadium and oxygen atoms. Figure 4.5 (a) and (b) represent the overlaid FTIR spectra of V_2O_5 nanorods, V_2O_5 -CNT nanonetwork and V_2O_5 -CNT-G-ol nanocapsules and the FTIR spectra of V_2O_5 -CNT-G-ol nanocapsules showing position of bond vibrations, respectively. The FTIR spectrum of V_2O_5 nanorods is characterized by strong

vibrations at 1012.6, 835.8 and 608.6 cm^{-1} which are attributed to the stretching and bending vibrations of V=O, V-O-V and asymmetric and symmetric vibrations of V-O bonds, respectively. These bands are also observed in the FTIR spectrum of V_2O_5 -CNT nanonetwork and V_2O_5 -CNT-G-ol nanocapsules. However, the position of the bands are slightly shifted to lower wavenumbers due to the interaction of V_2O_5 with CNTs and G-ol. Other significant bands observed in the spectra are at $\sim 1664.4 \text{ cm}^{-1}$ and $\sim 1310.7 \text{ cm}^{-1}$, which are ascribed to the vibration of the new bond linkages (C=C and C-O) observed in simulation studies. Furthermore, the band appearing around $3662.1 - 3104.2 \text{ cm}^{-1}$ in the various spectrum can be ascribed to the vibration of -OH from G-ol or adsorbed water molecules on the surface of the nanomaterials. These results support XRD simulated studies and are in good agreement with literature reports on V_2O_5 and composites with CNTs and graphitic materials [7,16]. The various observed functional groups and their assigned wavenumbers in the nanomaterials are tabulated in Table 4.2.



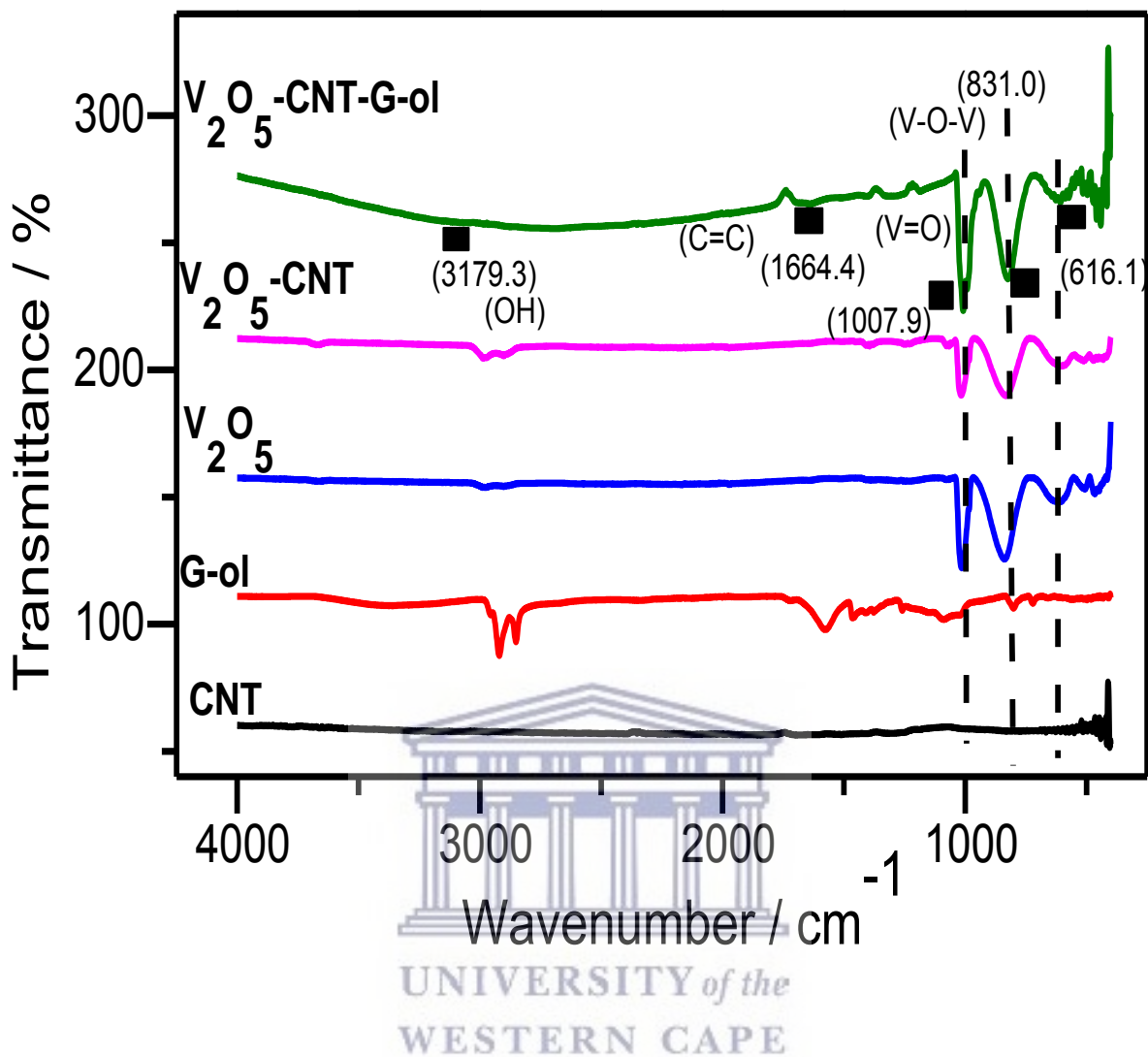


Figure 4.5 (a): FTIR spectrum (overlaid) of V₂O₅ nanorods, V₂O₅-CNT nanonetwork and V₂O₅-CNT-G-ol nanocapsules

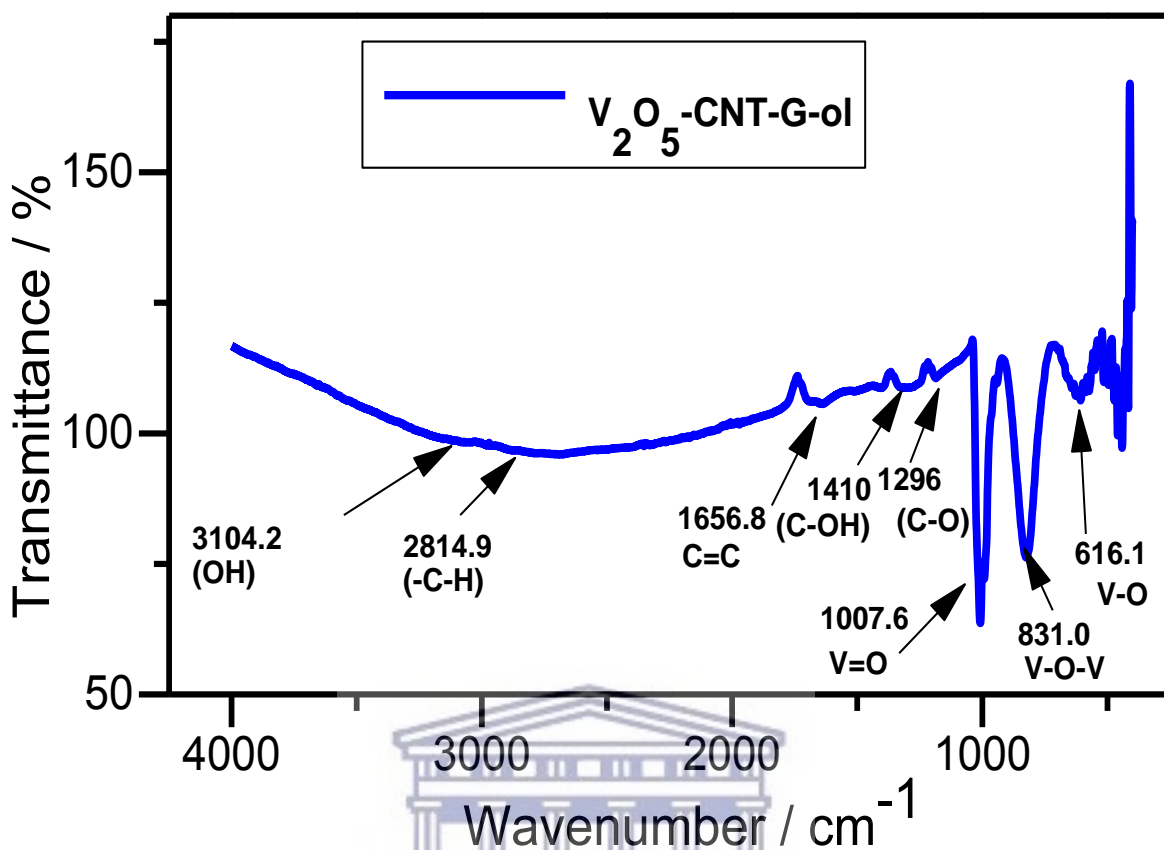


Figure 4.5 (b): FTIR spectrum of V_2O_5 -CNT-G-ol nanocapsules illustrating all bond vibrations

Table 4.2: Functional groups/ bonds vibrations in V_2O_5 nanorods, V_2O_5 -CNT nanonetwork and V_2O_5 -CNT-G-ol nanocapsules.

Functional groups / bond	Material / Wavenumber				
	V_2O_5 / cm^{-1}	$V_2O_5\text{-CNT} / \text{cm}^{-1}$	$V_2O_5\text{-CNT-G-ol} / \text{cm}^{-1}$	G-ol / cm^{-1}	CNT / cm^{-1}
V=O	1012.6	1007.9	1007.9	-	-
V-O-V	835.8	831.8	831.0	-	-

V-O	608.6	607.8	616.1	-	-
OH	-	3667.1	3104.2	3409.4	-
C=C	-	1654.1	1664.4	1588.9, 1145.3	1663.5
C-H	-	2986, 2898	2893.4	2921.6, 2851.9, 788.1	839.5
C-OH	-	--	1184.7	1254.2	
C-O	-	1403.4-	1310.7	1459.3	1313.6

4.4.6 Raman Spectroscopy

Raman spectroscopy was used to obtain supplementary structural information for V₂O₅, V₂O₅-CNT and V₂O₅-CNT-G-ol nanomaterials. Figure 4.6 displays the Raman spectra of V₂O₅ nanorods, V₂O₅-CNT nanonetwork and V₂O₅-CNT-G-ol nanocapsules obtained with an excitation laser of 514.9 nm. The band observed at low wavenumber value of 283.6 cm⁻¹ is attributed to the skeletal bending vibrations of V-O-V bonds, while band at 337.1 cm⁻¹ corresponds to the bending vibrations of V with bridging doubly coordinated O-atoms as observed in XRD crystal geometry and atom connectivity investigations [16]. The peak appearing at ~466.8 cm⁻¹ comes from the silicon background used for Raman analysis [32]. However, the peaks appearing at 686.5 cm⁻¹ and around 1600 – 2000 cm⁻¹ can be due to the interaction between VO and CNTs of G-ol. The presence of CNTs and G-ol in the materials is ascertained by the presence of the D and G-band of graphitic materials at 1461.2 and 1525.4 cm⁻¹ respectively.

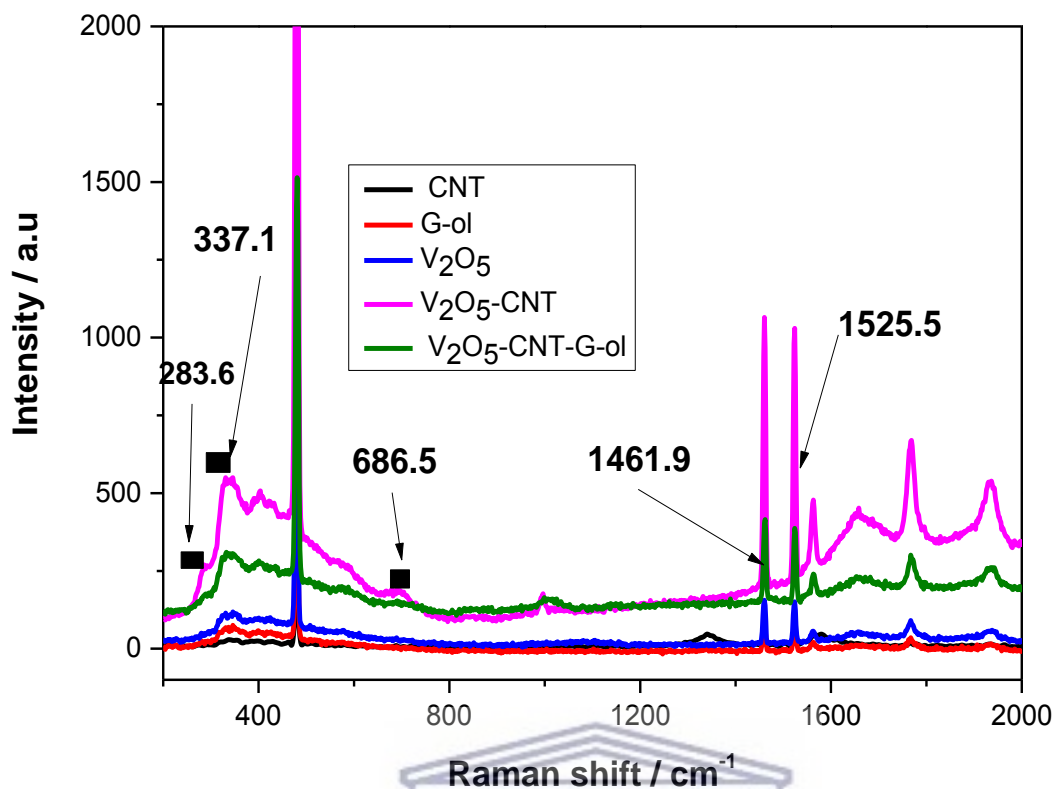
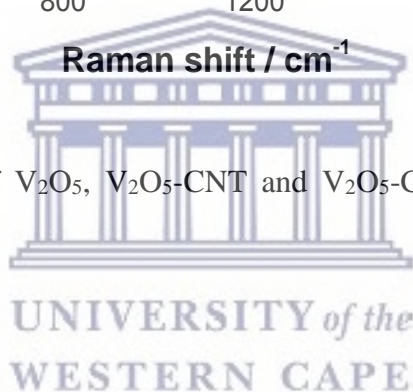


Figure 4.6: Raman spectra of V_2O_5 , V_2O_5 -CNT and V_2O_5 -CNT-G-ol nanomaterials with excitation laser of 514.9 nm.



4.4.7 (a) Electrochemical Performance

The electrochemical properties of V_2O_5 , V_2O_5 -CNT and V_2O_5 -CNT-G-ol nanomaterials and their potentials for supercapacitive applications were evaluated using cyclic voltammetry (CV), electrochemical impedance spectroscopy (EIS) and galvanostatic charge-discharge studies (GCD). V_2O_5 -based nanomaterials have been reported to exhibit better capacitive performance in aqueous nitrate solutions [7]. Electrochemical investigations were therefore performed in 1 M $LiNO_3$ aqueous electrolyte in both three and two electrode configurations.

i) Cyclic Voltammetric (CV) studies

CV curves were obtained at scan rates of 5 – 60 mV s⁻¹ at a potential window of -0.2 – 0.8 V. Figure 4.7 (a) presents a comparative plot of the CV profiles of V₂O₅ nanorods, V₂O₅-CNT nanonetwork and V₂O₅-CNT-G-ol nanocapsules in a three electrode cell, at a scan rate of 10 mV s⁻¹. A set of oxidation and reduction peaks is observed in the CV curves, due to the intercalation and de-intercalation of Li⁺ ions into and out of the V₂O₅ lattice, suggesting a prevailing faradaic charge storage mechanism [9,33]. The Li⁺ ion insertion /extraction reaction of V₂O₅ occurs together with compensating electrons according to Equation 4.3 [34].



Where x represents the number of Li⁺ ions inserted /extracted.

The CV profile of V₂O₅-CNT-G-ol nanocapsules exhibits a higher current response over those of V₂O₅-CNT nanonetwork and V₂O₅ nanorods due to better synergy between the pseudocapacitance of V₂O₅ and the double layer capacitance of G-ol and CNTs. Figure 4.7 (b) shows the CV curves of V₂O₅-CNT-G-ol nanocapsules at different scan rates from 10 – 60 mV s⁻¹. It is observed that the CV curves reveal an increase in current response with increasing scan rate with no significant change in shape, which is indicative of a good capacitive charge storage of the material. The specific capacitance obtained by integrating the area under the CV profiles of the nanomaterials at 5 mV s⁻¹ according to Equation 4.4 [35], was at 209.5 F g⁻¹, 142.6 F g⁻¹, and 88.1 F g⁻¹ for V₂O₅ nanorods, V₂O₅-CNT nanonetwork and V₂O₅-CNT-G-ol

nanocapsules, respectively. Even at a scan rate of 40 mV s⁻¹ the V₂O₅-CNT-G-ol nanocomposite was able to maintain a capacitance of 68.4 F g⁻¹, while V₂O₅-CNT showed a capacitance of 42.7 F g⁻¹, and 28.3 F g⁻¹ was maintained by V₂O₅ nanorods as displayed on Figure 4.7 (c). These results also confirms their good pseudocapacitive performance.

$$C_{sp} = \frac{1}{2m\nu\Delta V} \int_{-V}^{+V} I dv \quad (4.4)$$

Where m denotes the active mass (g) of the electrode, ν is the scan rate (V S⁻¹), ΔV is the

potential window (V) and $\int_{-V}^{+V} I dv$ is the voltammetric charge obtained from the area under the

CV curve (A V).



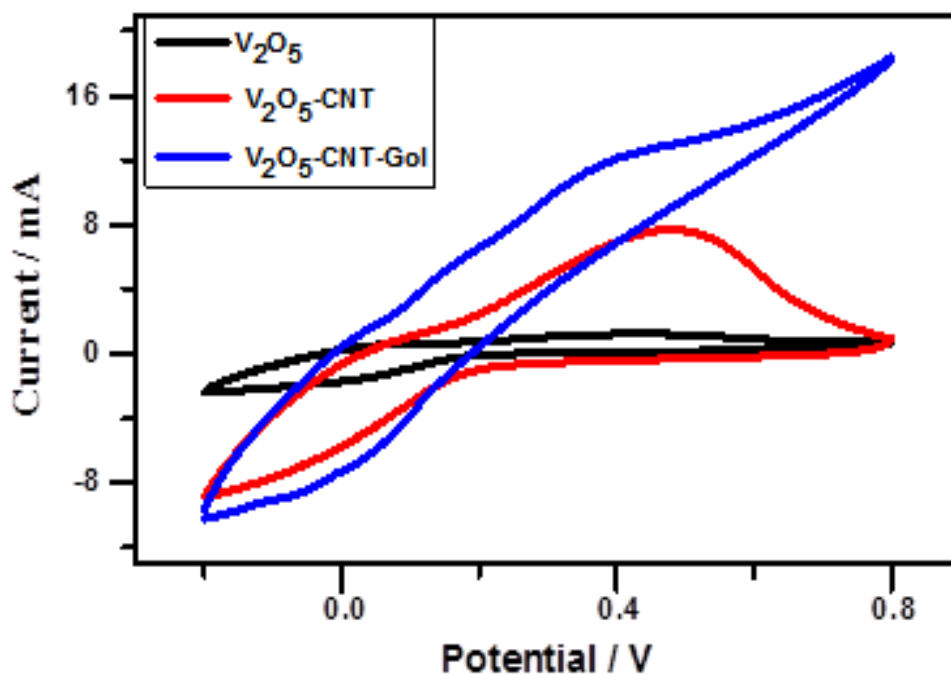


Figure 4.7 (a): CV curves of V_2O_5 nanorods, V_2O_5 -CNT nanonetwork, and V_2O_5 -CNT-G-ol nanocapsules at 10 mV s^{-1} in 1 M LiNO_3 aqueous electrolyte at potential window of $-0.2 - 0.8 \text{ V}$

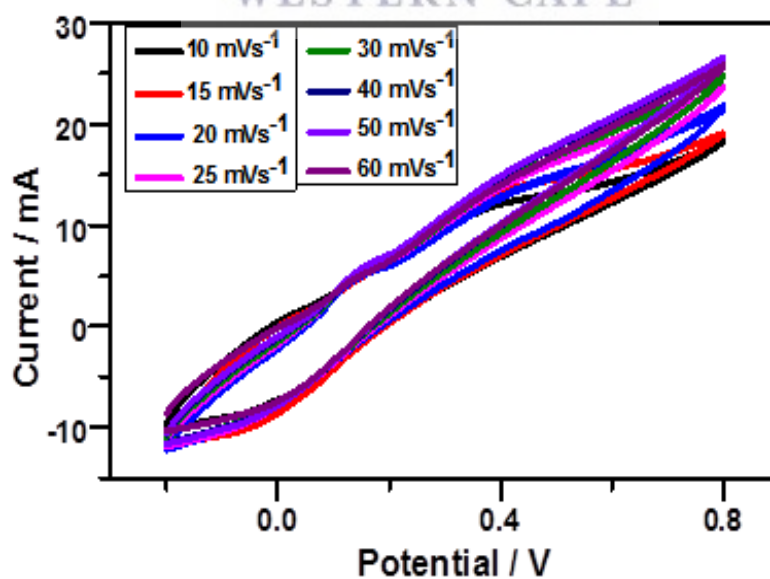


Figure 4.7 (b): CV curves of V_2O_5 -CNT-G-ol at scan rates of $10 - 60 \text{ mVs}^{-1}$ in 1 M LiNO_3 aqueous electrolyte at potential window of $-0.2 - 0.8 \text{ V}$

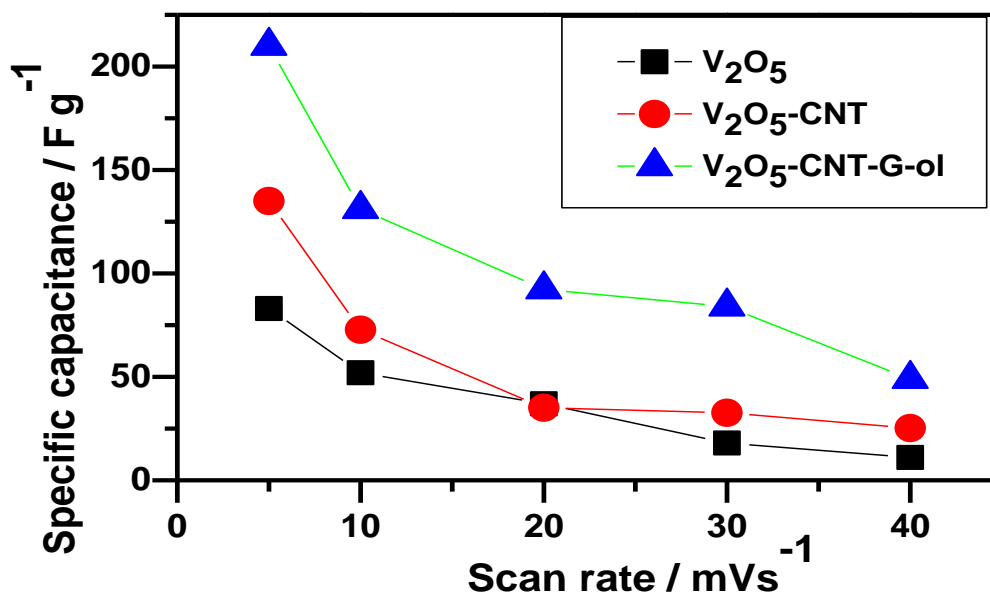


Figure 4.7 (c): Variation of specific capacitance with scan rate for V₂O₅, V₂O₅-CNT and V₂O₅-CNT-G-ol nanomaterials in 1 M LiNO₃ aqueous electrolyte at potential window of -0.2 – 0.8 V

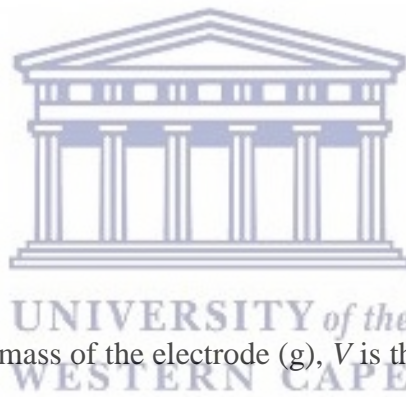


ii) Galvanostatic charge-discharge (GCD) studies

Further capacitive performance investigations were conducted on the V₂O₅-based electrode materials in the three electrode cell using GCD. Figure 4.8 (a) shows the GCD curves of V₂O₅, V₂O₅-CNT and V₂O₅-CNT-G-ol nanomaterials at a current load of 1 A g⁻¹ while the GCD curves of V₂O₅-CNT-G-ol electrode material at different current loads are presented in Figure 4.8 (b). The GCD curves revealed non-linear profiles with plateaus observed during the charging and discharging processes of Li⁺ ions into the V₂O₅ host material. This further confirms the pseudocapacitance behavior of the V₂O₅-based electrode materials. The charge and discharge plateaus of V₂O₅-CNT-G-ol nanocapsules are much more distinguished with a

longer charge and discharge time, as well a reduced IR_{drop} , indicating superior electrochemical performance offered by the synergistic effect of the pseudocapacitance contribution of V_2O_5 and the double layer capacitance delivered by CNTs and G-ol as observed in CV studies. A reduction in the IR_{drop} of V_2O_5 -CNT-G-ol nanocomposite suggest that the carbon based additives significantly reduced the internal resistance of V_2O_5 electrode material. These results are very consistent with literature reports [7,36]. Figure 4.8 (c) shows the variation of capacitance with the current load of V_2O_5 -CNT-G-ol nanocapsules. As expected, the capacitance values decrease with increasing current load. Capacitances values were obtained from the GCD plots using Equation 4.5.

$$C_{\text{sp}} = \frac{I \times t}{m(V - IR_{\text{drop}})} \quad (4.5)$$



Where, m represents the active mass of the electrode (g), V is the potential window (V), IR_{drop} is the voltage drop / equivalent series resistance (V), I is the applied current (A) and t is the charge/discharge time (s).

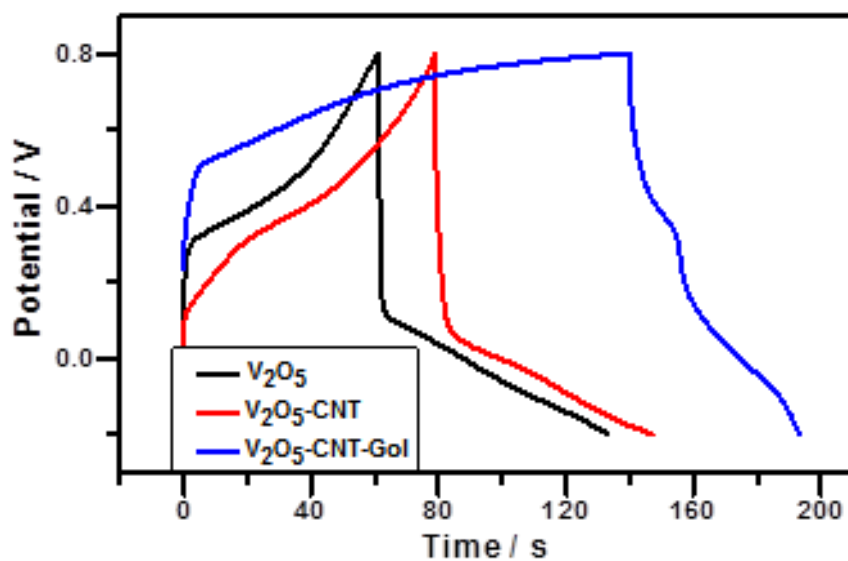


Figure 4.8 (a): GCD profiles of V_2O_5 nanorods, V_2O_5 -CNT nanonetwork and V_2O_5 -CNT-Gol nanocapsules at 1 A g^{-1} in 1 M LiNO_3 aqueous electrolyte at potential window of $-0.2 - 0.8 \text{ V}$

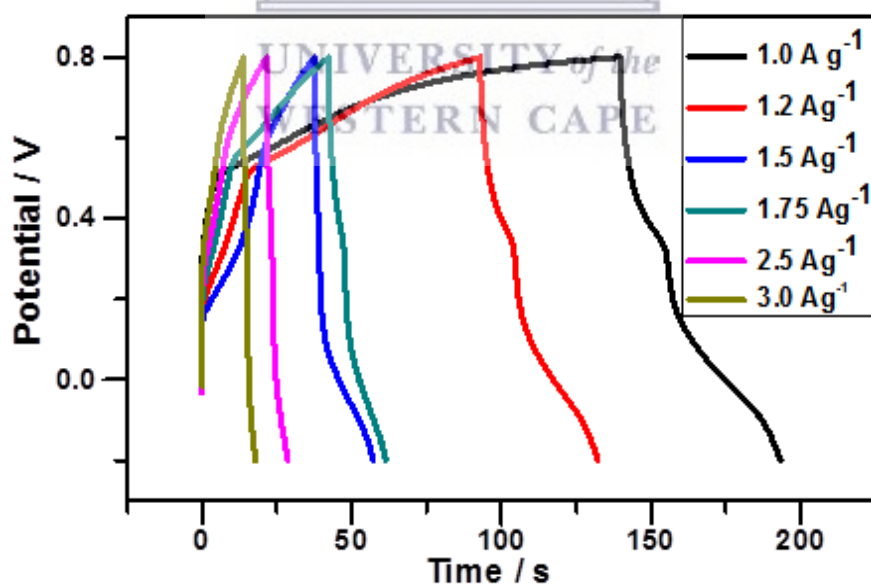


Figure 4.8 (b): GCD curves of V_2O_5 -CNT-Gol at different current loads in 1 M LiNO_3 aqueous electrolyte at potential window of $-0.2 - 0.8 \text{ V}$

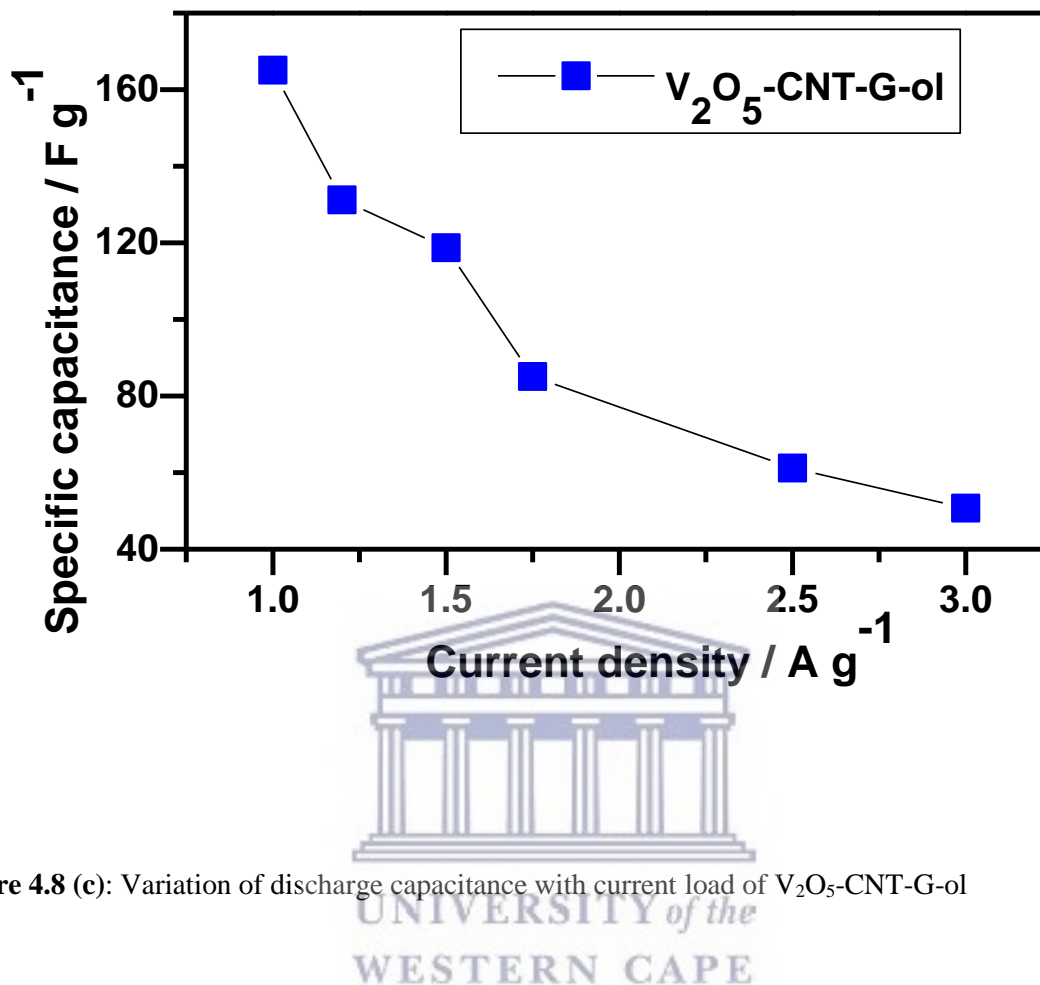


Figure 4.8 (c): Variation of discharge capacitance with current load of V₂O₅-CNT-G-ol

iii) Electrochemical impedance spectroscopic (EIS) measurements

EIS was used to obtain additional electrochemical properties of V₂O₅, V₂O₅-CNT and V₂O₅-CNT-G-ol nanomaterials which described the kinetic processes occurring at electrode/electrolyte interface. EIS measurements were recorded at open circuit voltage (OCV) in the frequency range of 0.1 MHz to 100 KHz at an amplitude of 5 mV. As shown in Figure 4.9 (a), the Nyquist plots reveal three distinct frequency regions. These domains include; a semicircle at the high frequency region, associated to the charge transfer resistance (R_{ct}); the intercept of the semicircle to the Z_{real} axis which describes the internal resistance; and an inclined line in

the middle to low frequency region of the curve representing the frequency dependent Warburg diffusion (W_o) arising from linear diffusion of ions at the outer surface of the electrode material from electrolyte solution [37]. It is observed that V_2O_5 -CNT-G-ol nanocapsules exhibit low impedance due to the synergistic effect of the carbon-based additives as revealed by CV and GCD studies. EIS curves were fitted using the well-known Z-view software according to circuit models displayed in Figure 4.9 (b). The constant phase element (CPE) provides information on the double layer capacitance between the electrodes –electrolyte interface as a function of the electrode potential. Values of the R_{ct} , R_s , W_o and CPE obtained from curve fitting are tabulated in Table 4.3. It is observed that V_2O_5 electrode material demonstrates commendable semiconductive performance as evidenced by the phase angle of 51.3° , followed by V_2O_5 -CNT at 29.2° and V_2O_5 -CNT-G-ol at 10.1° , as shown in the Bode plot, Figure 4.9 (c). However, the V_2O_5 electrode also presents the largest R_{ct} value of 324.6Ω and V_2O_5 -CNT at 29.46Ω . Meanwhile V_2O_5 -CNT-G-ol electrode showed the smallest R_{ct} value of 2.38Ω , suggesting the faster faradaic redox reaction occurring in the electrode material due to the expanded interplanar spacing provided by the presence of CNTs and G-ol as well as the nanocapsule morphology which also provided more pores and reduced aggregation between the nanorods, allowing more electrolyte ions to diffuse within the electrode and electrolyte interface. Moreover, the V_2O_5 -CNT-G-ol electrode also demonstrated a low ion diffusion resistance as indicated by the presence of the vertical line in the low frequency region of the Nyquist plot. All V_2O_5 -based electrode materials showed CPE values with at $0.71 \mu F$ for V_2O_5 , $0.55 \mu F$ for V_2O_5 -CNT and $0.72 \mu F$ for V_2O_5 -CNT-G-ol electrode, suggesting some degree of double layer capacitance contribution to the total capacitance of the materials. Notably, the electrochemical parameters obtained from EIS investigations further reveal the commendable electrochemical performance of the V_2O_5 -based electrode materials and also demonstrate their promising potentials for supercapacitor applications.

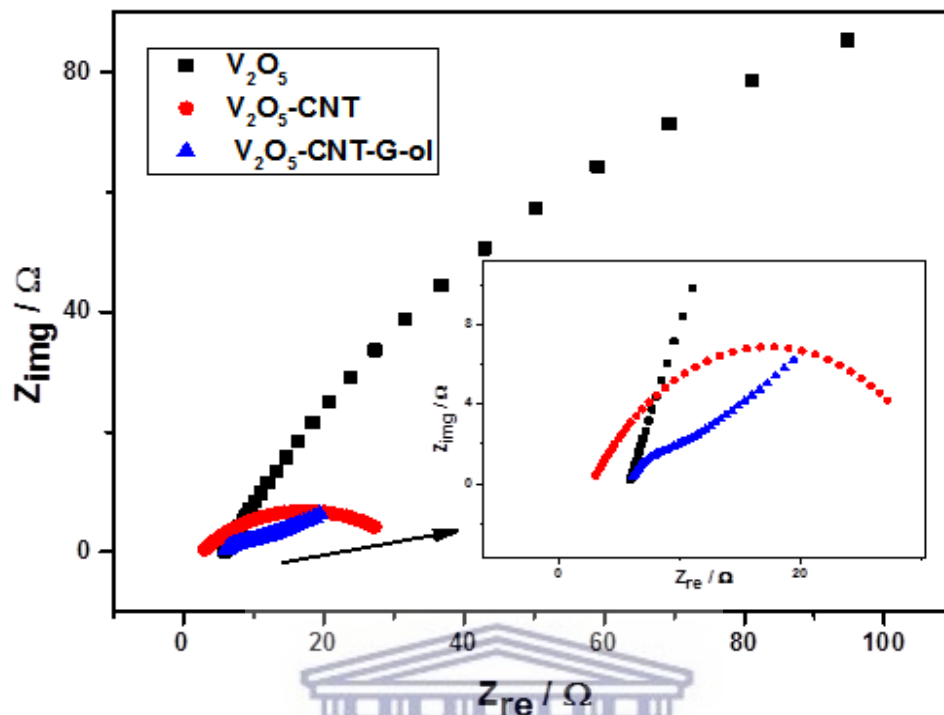


Figure 4.9 (a): Nyquist plots of V_2O_5 , V_2O_5 -CNT and V_2O_5 -CNT-G-ol nanomaterials obtained at OCV

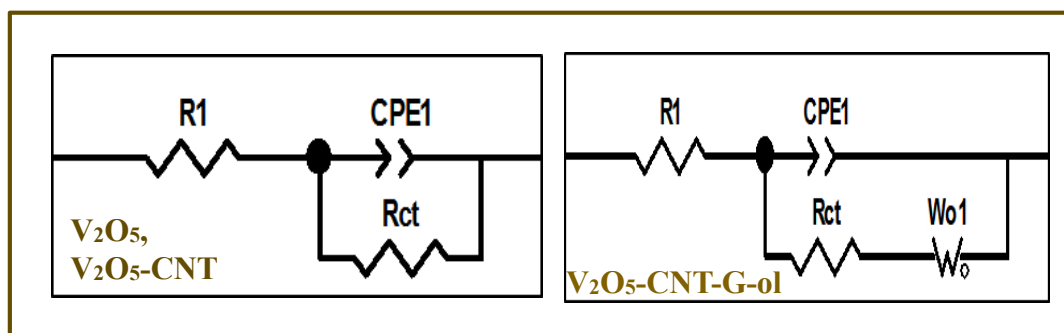


Figure 4.9 (b): Circuit models used to fit EIS data

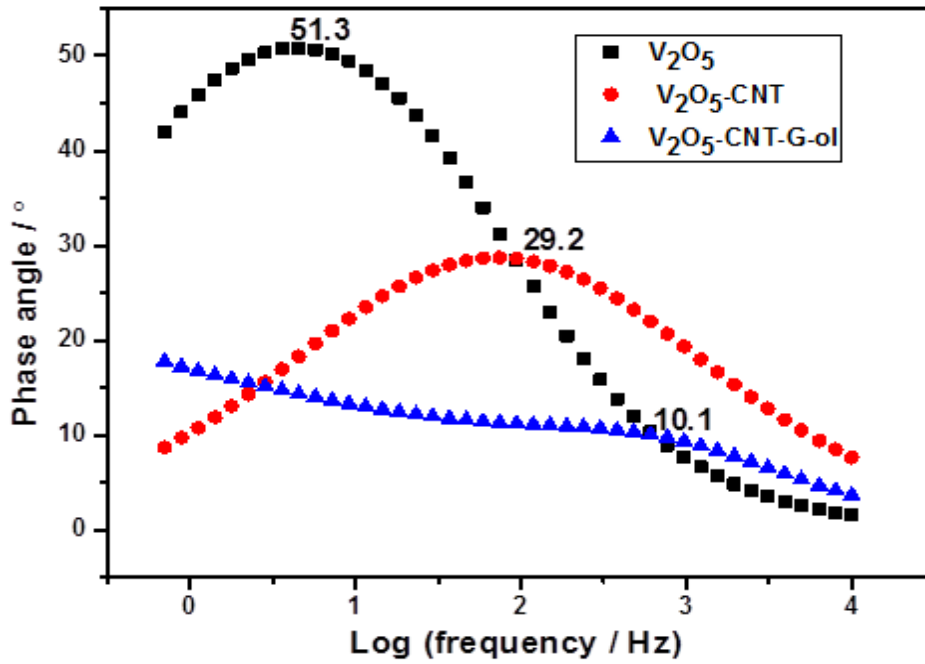


Figure 4.9 (c): Phase angle Bode plots of V_2O_5 , V_2O_5 -CNT and V_2O_5 -CNT-G-ol

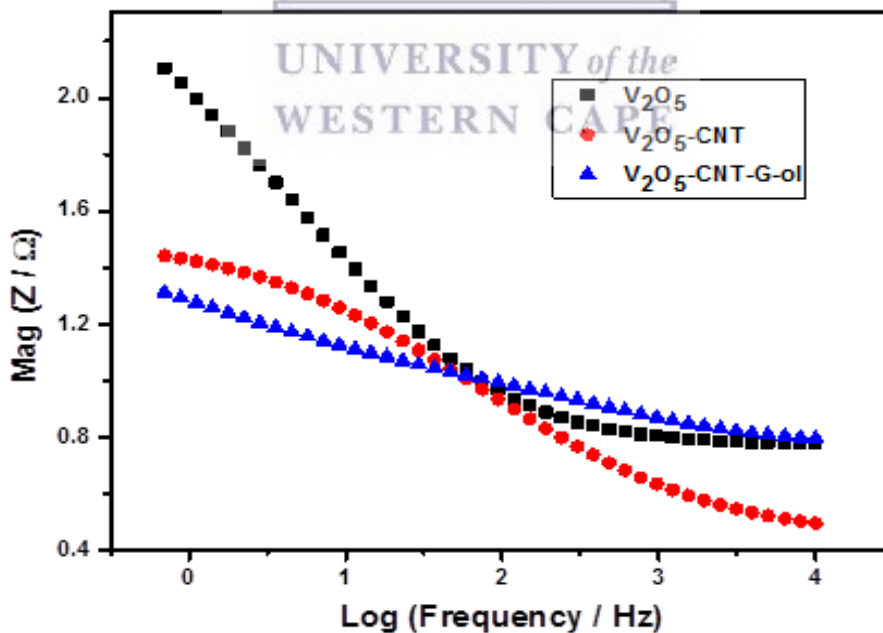


Figure 4.9 (d): Total impedance Bode plots of V_2O_5 , V_2O_5 -CNT and V_2O_5 -CNT-G-ol

Table 4.3: EIS curve fitting data of V₂O₅-based electrode materials

Electrode material	R _s / Ω	CPE/ μF	R _{ct} / Ω	W _o /Ωs ^{-1/2}	Phase angle / °
V ₂ O ₅	5.86	0.71	324.6	-	51.3
V ₂ O ₅ -CNT	2.73	0.55	29.46	-	29.4
V ₂ O ₅ -CNT-G-ol	5.94	0.72	2.38	0.30	11.3

4.4.7 (b) Electrochemical Performance of the fabricated asymmetric supercapacitor devices



Additional evaluation of the potentials for practical application of the V₂O₅-based electrode materials in supercapacitors were done by fabrication of asymmetric supercapacitors, based on the V₂O₅-based electrodes as positive electrodes and activated carbon (AC) as the negative electrode using Ni foam as the current collector. Figure 4.10 (a) displays the CV curves of V₂O₅-CNT-G-ol electrode material and AC electrode material in 1.0 M LiNO₃ aqueous electrolyte at a scan rate of 50 mV s⁻¹, indicating the suitability of using V₂O₅-based materials as positive electrode and AC as negative electrode [38]. As shown in Figure 4.10 (b), the comparative GCD profiles of the asymmetric devices assembled with the V₂O₅-based positive electrodes and AC negative electrode at a current load of 0.25 A g⁻¹ and voltage window of 1.6 V, still maintain the non-linear and plateau characteristics as observed in three electrode

investigations. It is worth noting that the AC//V₂O₅-CNT-G-ol supercapacitor device delivered an impressive specific capacitance 173.4 F g⁻¹ which was 2.3 times greater than that of the AC//V₂O₅-CNT device (75.4 F g⁻¹) and even 7.1 times greater than the AC//V₂O₅ device. This higher capacitance is attributed to the synergy between the carbon-based additives (G-ol and CNTs) and V₂O₅-nanorods, with the unique nanocapsule-like morphology of V₂O₅-CNT-G-ol which reduced aggregation between the nanorods and providing a larger surface area for diffusion of Li⁺ ions, resulting in enhanced electrochemical performance. The GCD profiles of AC//V₂O₅-CNT-G-ol supercapacitor at different current loads as shown in Figure 4.10 (c), exhibit some asymmetry in the discharge curves at low current density (0.125 A g⁻¹ -0.5 A g⁻¹). This can be ascribed to the contribution of the faradaic processes of V₂O₅ electrode material. However, it is also revealed that the capacitance decreases with increasing current load as displayed by Figure 4.10 (d). This is a characteristic behavior observed in energy storage devices, due to the ion transfer limitation of electrolyte ions through the electrode material at higher current loads. As current load increases, electrolyte ions face mass transport limitations within the host material, reducing the accessible electrode volume for the electrochemical reactions. And the inner portion of electrode finds it difficult to sustain the redox transition at higher current loads, leading to reduction in charge storage [16]. The specific charge and discharge capacities of the asymmetric device were calculated based on the total active mass of the two electrodes according to Equation 4.6 [35].

$$C_{sp} = \frac{4I}{m \Delta V / \Delta t} \quad (4.6)$$

Where I is the applied current (A), m is the total mass of positive and negative electrodes (g), $\Delta V/\Delta t$ is the slope obtained by fitting a straight line to the discharge curve ($V s^{-1}$) and V is the voltage window.

As shown in Table 4.4, charge and discharge capacities were found to be $425.2 F g^{-1}$ and $178.1 F g^{-1}$ at a current density of $0.125 A g^{-1}$ as well as $39.7 F g^{-1}$ and $25.8 F g^{-1}$ at a current density of $2 A g^{-1}$, respectively. To optimize the energy storage capabilities of the devices, the mass/charge balance of the different electrodes should be carefully considered since the electrodes operate in different potential windows and deliver varying specific capacitances. The mass loading of the positive and negative electrodes were adjusted according to the charge balance equation, Equation 4.7 [39].

$$\frac{M^+}{M^-} = \left(\frac{C_{sp}^-}{C_{sp}^+} \right) \left(\frac{\Delta V^-}{\Delta V^+} \right) \quad (4.7)$$


The logo of the University of the Western Cape, featuring a classical building with six columns and a pediment, with the text 'UNIVERSITY of the WESTERN CAPE' below it.

Where, M , C_{sp} and ΔV represent the active mass, specific capacitance and the potential window obtained from three electrode investigations of the electrode materials, respectively. The mass loading of AC// V_2O_5 -CNT-G-ol asymmetric device was adjusted to 9.31 mg, while those of AC// V_2O_5 and AC// V_2O_5 -CNT devices were at 10.25mg and 11.13 mg, respectively.

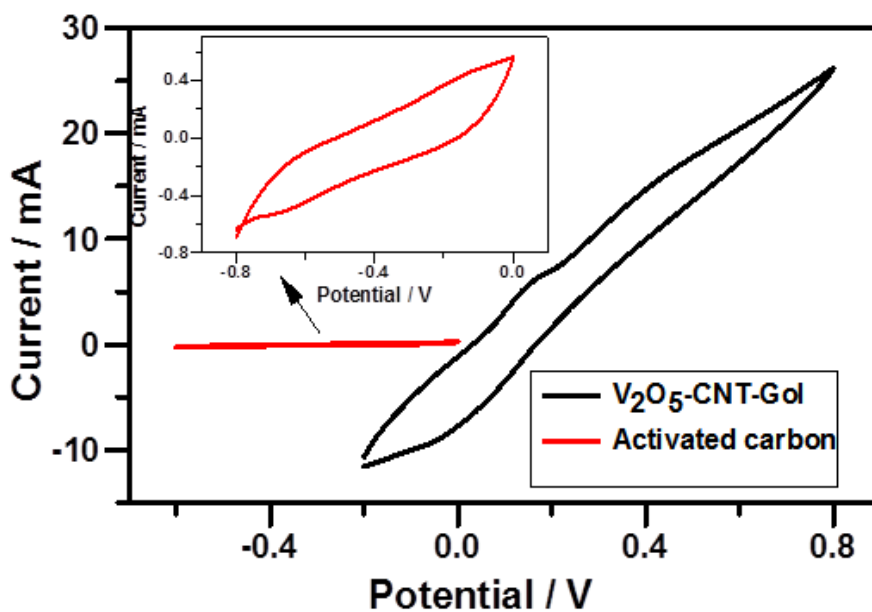


Figure 4.10 (a): comparative CV plots of AC and V_2O_5 -CNT-G-ol electrodes at scan rate of 50 mV s^{-1} in 1.0 M LiNO_3 aqueous electrolyte at different potential windows

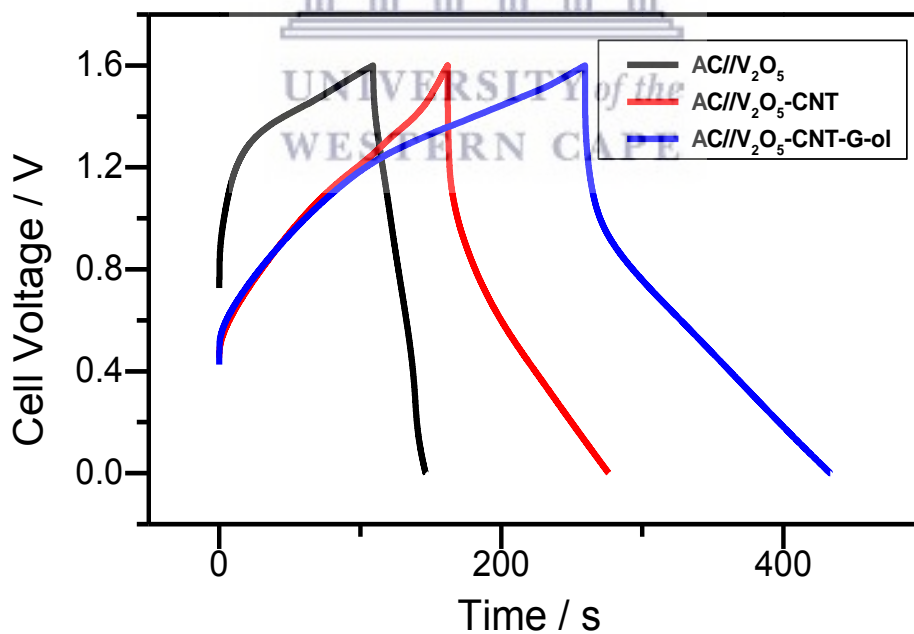


Figure 4.10 (b): Comparative plot of the GCD profiles of AC// V_2O_5 , AC// V_2O_5 -CNT and AC// V_2O_5 -CNT-G-ol asymmetric devices at a current load of 0.25 A g^{-1} in 1.0 M LiNO_3 aqueous electrolyte.

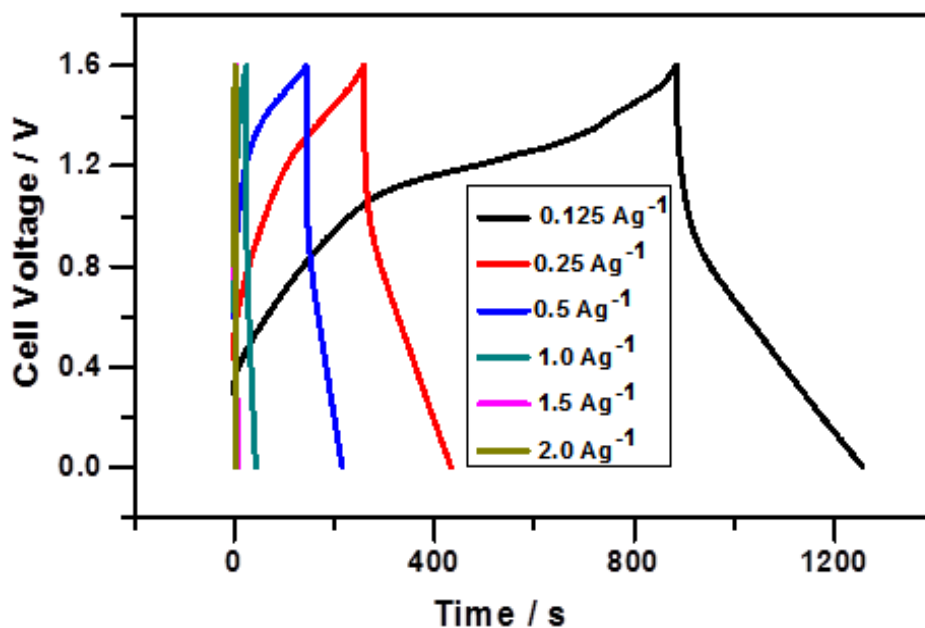


Figure 4.10 (c): GCD profiles of AC//V₂O₅-CNT-G-ol asymmetric device at different current loads in 1.0 M LiNO₃ aqueous electrolyte

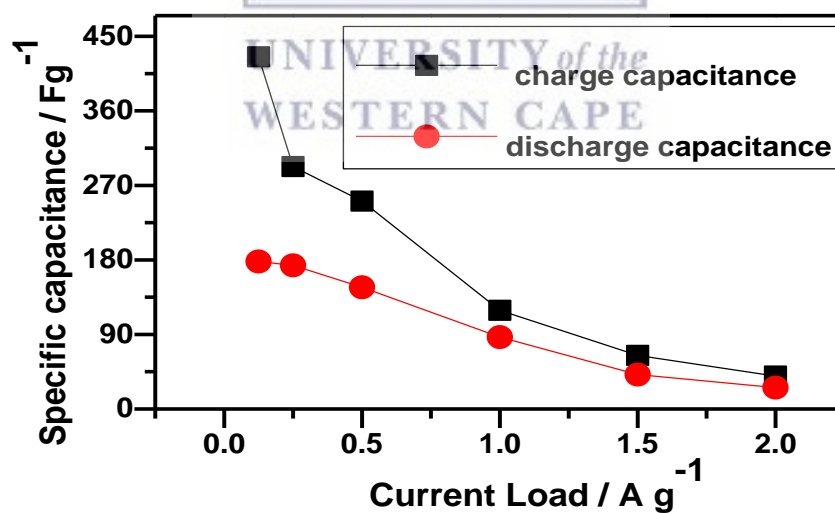


Figure 4.10 (d): Variation of charge and discharge capacitance values with current load of AC//V₂O₅-CNT-G-ol device in 1.0 M LiNO₃ aqueous electrolyte at voltage window of 1.6 V

Table 4.4: Charge and discharge capacities of Asymmetric AC//V₂O₅-CNT-G-ol device

Current Density / A g⁻¹	Specific charge capacity/ F g⁻¹	Specific discharge capacity/ F g⁻¹
0.125	425.2	178.1
0.25	292.7	173.4
0.5	251.0	146.9
1.0	119.2	86.8
1.5	64.6	41.5
2	39.7	25.8

i) Electrochemical cycling / stability studies



The long-term cycle stabilities of the V₂O₅-based supercapacitors were studied up to 4,000 cycles at a current load of 0.5 A g⁻¹. As shown in Figure 4.11 (a), the devices exhibited good cycle stability with a capacitance retention of 69 %, 66.8 % and 110 % over 4,000 cycles for the AC//V₂O₅-CNT-G-ol, AC//V₂O₅-CNT, and AC//V₂O₅ devices, respectively. The coulombic efficiency per cycle is displayed in Figure 4.11 (b). Interestingly, the AC//V₂O₅-CNT-G-ol device delivered an excellent coulombic efficiency of 96.8 % followed by the AC//V₂O₅-CNT device at 94.2 % and AC//V₂O₅ at 93.1 %. It has been reported that combination of transition metal oxide and electrochemically stable graphitic sheets play a significant role in the improvement of electrochemical behavior of supercapacitor electrodes due to the synergy between the pseudocapacitance and EDLC mechanisms [40]. Overall, the very good electrochemical performance as well as the excellent long-term cycle stability of the V₂O₅-based devices can be attributed to the synergistic effect of the pseudocapacitance of V₂O₅

and the double layer capacitance of the carbon based additives. More specifically, G-ol nanosheets and CNTs in the AC//V₂O₅-CNT-G-ol device provided the physical support and reduced the stress due to the larger interlayer spacing during insertion and removal processes of Li-ions which led to the good cyclic stability.

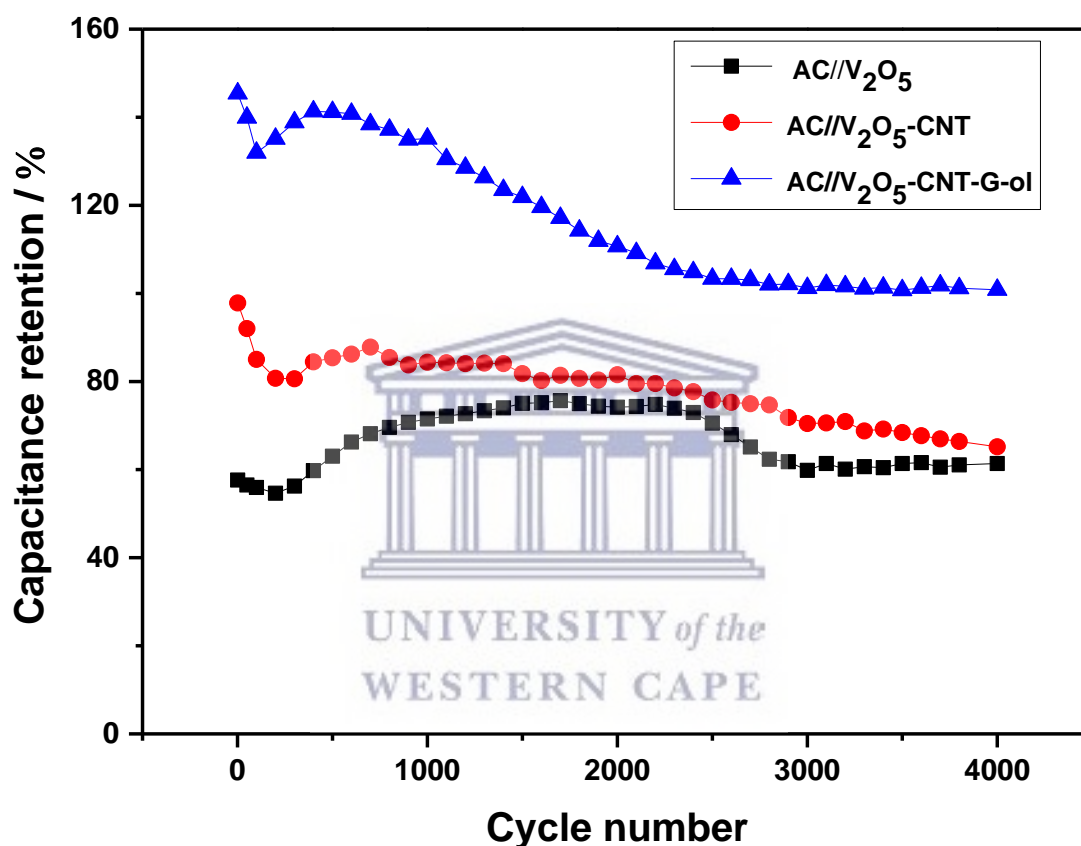


Figure 4.11 (a): Cycling stability of AC//V₂O₅, AC//V₂O₅-CNT, AC//V₂O₅-CNT-G-ol supercapacitor devices over 4000 cycles

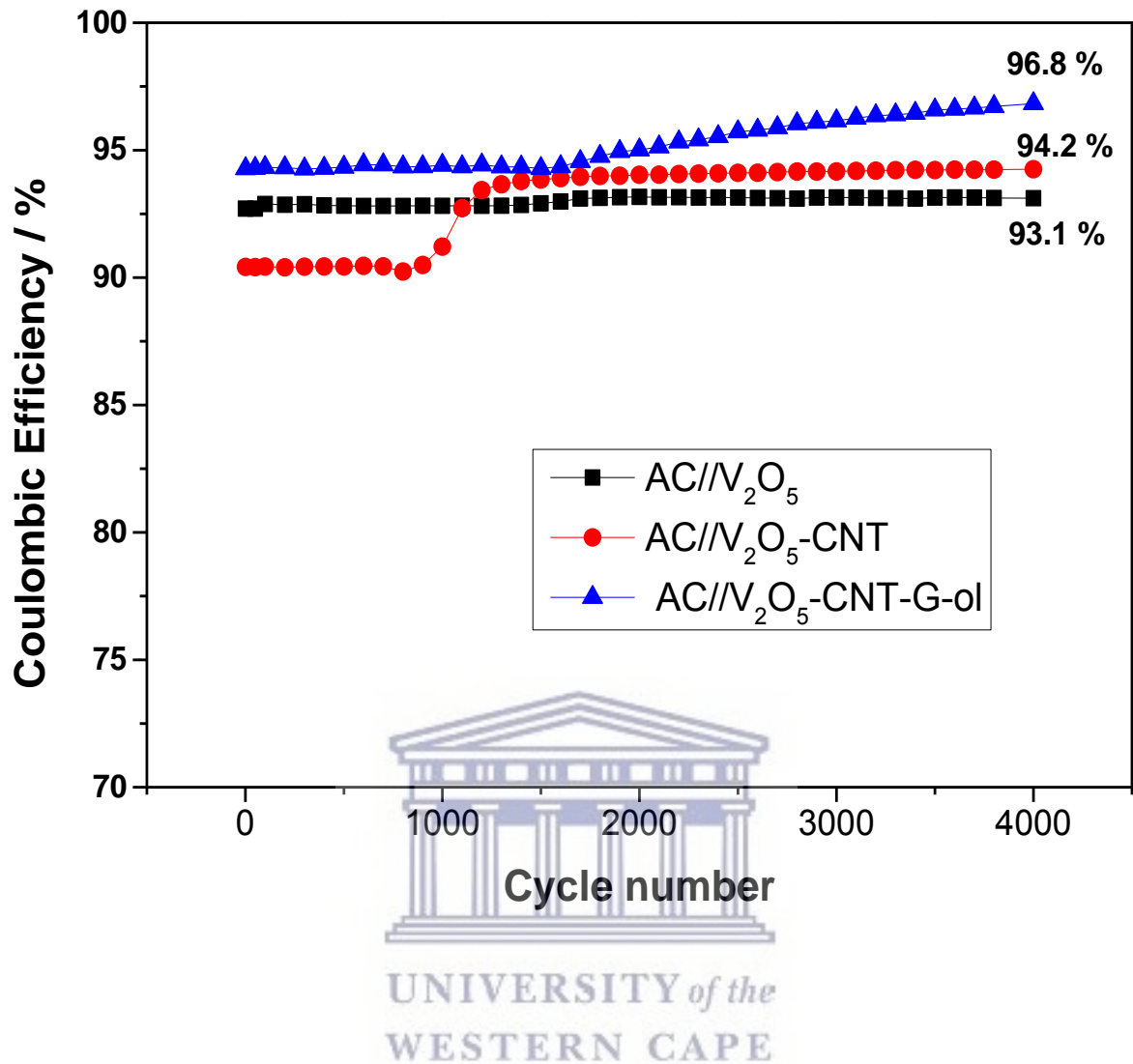


Figure 4.11 (b): Coulombic efficiency of AC/V₂O₅, AC/V₂O₅-CNT, AC/V₂O₅-CNT-G-ol supercapacitor devices over 4000 cycles

4.4.7 (c) Specific Energy and Specific Power

The specific energy (W h Kg⁻¹) and specific power (W Kg⁻¹) are the most important parameters used to evaluate the performance of supercapacitors. The specific energy and power of the asymmetric devices at different current loads were calculated according to Equation 4.8 and 4.9 [41].

$$E = \frac{1}{2} C_{sp} \times \Delta V^2 \times \frac{1}{3.6} \quad (4.8)$$

$$P = \frac{E}{\Delta t} \times 3600 \quad (4.9)$$

Where C_{sp} denotes the specific capacitance of the device ($F g^{-1}$), ΔV is the applied voltage (V) and Δt is the supercapacitor discharge time (s).

The specific energy and power of the devices is displayed in the Ragone plot, Figure 4.12. It was observed that the specific energy of the AC//V₂O₅-CNT-G-ol device could reach 63.2 W h kg⁻¹ at a specific power of 609.2 W kg⁻¹ and still retain a specific energy of 9.2 W h kg⁻¹ when the specific power increased to 34144.3 W kg⁻¹. The AC//V₂O₅-CNT device was able to deliver a specific energy of 43 W h kg⁻¹ at specific power of 487.7 W kg⁻¹. while the AC//V₂O₅ supercapacitor showed a specific energy of 12.3 W h kg⁻¹ at a specific power of 204.2 W kg⁻¹. The obtained results are comparable to literature reports as shown in Table 4.5 and even show better energy storage capabilities over some reports. These results highlight the potentials of V₂O₅ and G-ol composite electrode materials as supercapacitor electrodes and opens up new avenues for wide range applications.

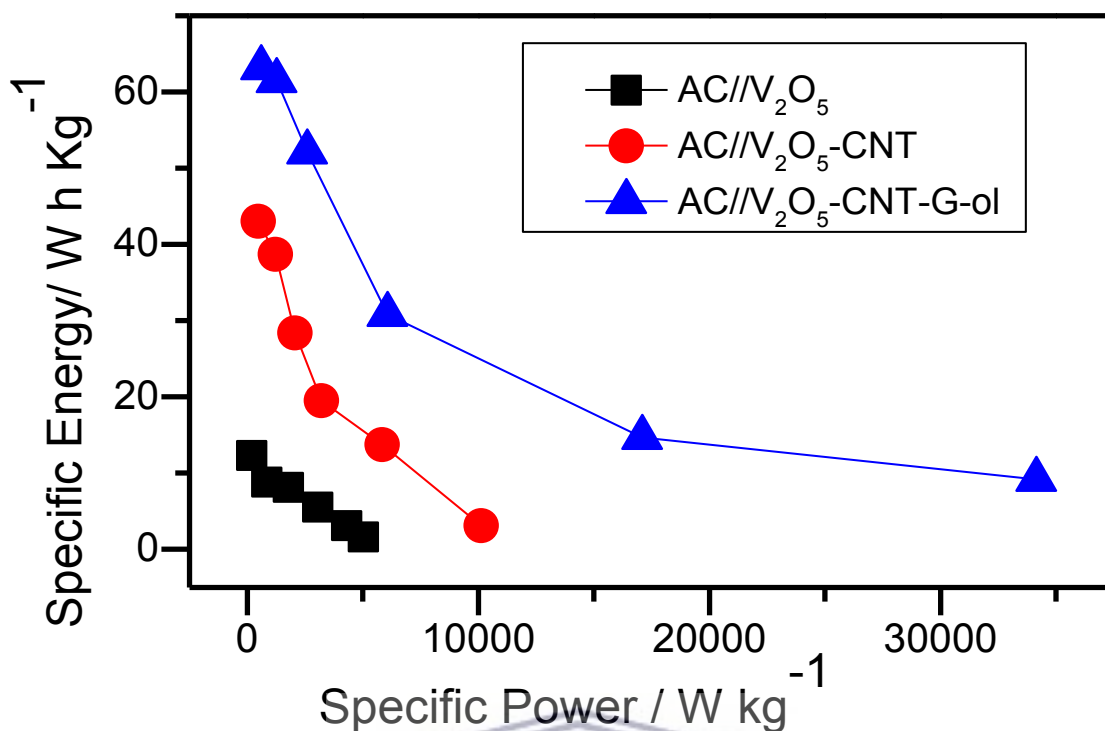


Figure 4.12: Ragone plot of AC/V₂O₅, AC/V₂O₅-CNT, AC/V₂O₅-CNT-G-ol supercapacitor devices at different current loads in 1.0 M LiNO₃ aqueous electrolyte at voltage window of 1.6 V

Table 4.5: Comparison of V₂O₅-CNT-G-ol supercapacitor with other devices assembled with V₂O₅-based electrode materials and composites with different carbon forms.

S. No	Device design (negative//positive)	Electrolyte/ voltage window (V)	Capacitance @ Current density	Cycling stability @ cycles	Max. Energy (Wh kg ⁻¹) @ Power (W kg ⁻¹)	Ref
1	V ₂ O ₅ nanorod/RGO// V ₂ O ₅ nanorod/RGO	5 M LiNO ₃ / 0 – 1.7	83.5 F g ⁻¹ @ 0.5 A g ⁻¹	34.5 % @ 1000	33.5 @ 425.6	[42]

2	RGO/V ₂ O ₅ //AC	0.5 M K ₂ SO ₄ / 0 – 1.0	53 F g ⁻¹ @ 0.5 A g ⁻¹	52 % @ 300	7.4 @ 127	[43]
3	V ₂ O ₅ /CNT//MnO ₂ /C	1 M Na ₂ SO ₄ / 0-1.6	45 F g ⁻¹ @ 0.64 mA cm ⁻²	90 % @ 100	16 @ 75	[44]
4	RGO/C- cloth//V ₂ O ₅ /polyindol e/C-cloth	1 M LiClO ₄ /prop ylene carbonate / 0 – 1.8	275.5 F g ⁻¹ @ 1 A g ⁻¹	91.1 % @ 5000	38.7 @ 900	[45]
5	V ₂ O ₅ nanowire- G//V ₂ O ₅ -nanowire-G	1 M Na ₂ SO ₄ / -1.5 -1.5	1002 F g ⁻¹ @ 1 A g ⁻¹	83.9 % @ 5,000	116 @ 1520.2	[36]
6	Fe ₃ O ₄ /3DG//V ₂ O ₅ /3D G	1 M Na ₂ SO ₄ / 0 – 1.8	612 F g ⁻¹ @ 1 A g ⁻¹	89.9 % @ 10,000	54.9 @ 898	[38]
7	CNT/V ₂ O ₅ nanowire//AC	1 M LiClO ₄ /prop ylene carbonate / 0 – 2.7	-	80 % @ 10,000	40 @ 210	[46]
8	V ₂ O ₅ /Ketjin black// V ₂ O ₅ /Ketjin black	LiCl/polyvi nyl alcohol gel / 0 - 1	4.0 F cm ⁻² @ 5 mA cm ⁻²	90 % @ 8,000	56.8 @ 303	[47]
9	RGO/V ₂ O ₅ //G	1 M LiClO ₄ /prop ylene carbonate / 0 – 2.5	92 F g ⁻¹ @ 0.2 A g ⁻¹	82.2 % @ 10,000	80.4 @ 275	[9]
10	AC//V ₂ O ₅ /N- mesoporous carbon	0.5 M K ₂ SO ₄ / 0 - 1	91 F g ⁻¹ @ 1 A g ⁻¹	84 % @ 500	12.8 @ 317	[48]
11	AC//V ₂ O ₅ -CNT-G-ol	1 M LiNO ₃ / 0 – 1.6	178.1 F g ⁻¹ @ 0.125	69.% @ 4,000	63.2 @ 609.2	This work

4.5 Conclusion

In summary, V₂O₅-based electrode materials and composites with CNTs and G-ol were prepared by a combination of hydrothermal synthesis and wet chemistry. Morphological studies by SEM and HRTEM showed aggregated nanorods of thickness ranging from 10.4 – 130.6 nm for V₂O₅, 70.1 – 105.7 nm for V₂O₅-CNT and nanocapsule-like morphology in range of 61.6 – 141.9 nm for V₂O₅-CNT-G-ol. SAXS results revealed slightly left-skewed particle size distribution of V₂O₅ nanorods indicating the globular shape and variation of nanorod sizes, with maximum primary particles at 10.4 and aggregates of primary particles at 81.9 nm. A dumbbell-shaped particle size distribution by number of particles scattered were obtained for V₂O₅-CNT and V₂O₅-CNT-G-ol electrode materials. Maximum population of primary particles for V₂O₅-CNT and V₂O₅-CNT-G-ol were at 26.8 and 22.9 nm, respectively. XRD studies showed crystalline patterns for all three electrode materials which could be indexed to the Scherbinaite orthorhombic Pmmn (59) standard phase (JCPD file no -41-1426), with an increased interlayer spacing for V₂O₅-CNT-G-ol nanocapsulate electrode. The FTIR spectrum of V₂O₅ nanorods showed strong vibrations at 1012.6, 835.8 and 608.6 cm⁻¹ which were attributed to the stretching and bending vibrations of V=O, V-O-V and asymmetric and symmetric vibrations of V-O bonds, respectively. These bands were slightly shifted to lower wavenumbers due to the interaction of V₂O₅ with CNTs and G-ol in V₂O₅-CNT and V₂O₅-CNT-G-ol electrode materials. The skeletal and bending vibrations of V-O-V and V-bonds were observed at Raman shift values of 283.6 cm⁻¹ and 337.1 cm⁻¹, respectively. The D and G-band of graphitic materials was observed at 1461.2 and 1525.4 cm⁻¹ respectively. Electrochemical studies conducted in three electrodes in 1 M LiNO₃ aqueous electrolyte delivered a specific capacitance of 209.5 F g⁻¹, 142.6 F g⁻¹, and 88.1 F g⁻¹ for V₂O₅, V₂O₅-CNT and V₂O₅-CNT-G-ol electrodes, respectively at a scan rate of 5 mV s⁻¹. EIS studies confirmed

faster faradaic redox reactions occurring in the nanocapsulate electrode with R_{ct} value of 2.38 Ω compared to 29.46 Ω for V_2O_5 -CNT and 324.6 Ω for V_2O_5 . Asymmetric supercapacitors assembled to demonstrate the practical applications of V_2O_5 -based electrode with AC as the negative electrode delivered an impressive specific capacitance 173.4 $F\ g^{-1}$ for AC// V_2O_5 -CNT-G-ol at a voltage of 1.6 V. This value was 2.3 times greater than that of the AC// V_2O_5 -CNT device (75.4 $F\ g^{-1}$) and even 7.1 times greater than the AC// V_2O_5 device. This higher capacitance can be attributed to the synergy between the carbon-based additives (G-ol and CNTs) and V_2O_5 -nanorods, with the unique nanocapsule-like morphology of V_2O_5 -CNT-G-ol which reduced aggregation between the nanorods and provided a larger surface area for diffusion of Li^+ ions, resulting in enhanced electrochemical performance. Long-term cycle stabilities of the V_2O_5 -based supercapacitors studied up to 4,000 cycles at a current load of 0.5 A g^{-1} retained a capacitance of over 65 % for all three devices. The Ragone revealed that the specific energy of the AC// V_2O_5 -CNT-G-ol device could reach 63.2 W h kg^{-1} at a specific power of 609.2 W kg^{-1} and still retain a specific energy of 9.2 W h kg^{-1} when the specific power increased to 34144.3 W kg^{-1} . The AC// V_2O_5 -CNT device was able to deliver a specific energy of 43 W h kg^{-1} at specific power of 487.7 W kg^{-1} , while the AC// V_2O_5 supercapacitor showed a specific energy of 12.3 W h kg^{-1} at a specific power of 204.2 W kg^{-1} . These results are comparable to literature reports and highlight the potentials of V_2O_5 and G-ol composite electrode materials as high energy supercapacitor electrodes and may open up new paths for wide ranging applications.

References

- [1] Y. Zhang, J. Zheng, Y. Zhao, T. Hu, Z. Gao, C. Meng, Fabrication of V_2O_5 with various

-
- morphologies for high-performance electrochemical capacitor, *Appl. Surf. Sci.* 377 (2016) 385–393. doi:10.1016/j.apsusc.2016.03.180.
- [2] X. Zhang, L. Li, E. Fan, Q. Xue, Y. Bian, F. Wu, R. Chen, Toward sustainable and systematic recycling of spent rechargeable batteries, *Chem. Soc. Rev.* 47 (2018) 7239–7302. doi:10.1039/c8cs00297e.
- [3] T.M. Gür, Review of electrical energy storage technologies, materials and systems: Challenges and prospects for large-scale grid storage, *Energy Environ. Sci.* 11 (2018) 2696–2767. doi:10.1039/c8ee01419a.
- [4] X. Guo, T. Wang, T.X. Zheng, C. Xu, J. Zhang, Y.X. Zhang, X.Y. Liu, F. Dong, Quasi-parallel arrays with a 2D-on-2D structure for electrochemical supercapacitors, *J. Mater. Chem. A.* (2018). doi:10.1039/C8TA07869F.
- [5] S.K. Kaverlavani, S.E. Moosavifard, Designing graphene-wrapped nanoporous CuCo_2O_4 hollow spheres electrodes for high-performance asymmetric supercapacitors, *J. Mater. Chem. A Mater. Energy Sustain.* 5 (2017) 14301–14309. doi:10.1039/C7TA03943C.
- [6] A. De Adhikari, R. Oraon, S.K. Tiwari, J.H. Lee, N.H. Kim, G.C. Nayak, A V_2O_5 nanorod decorated graphene/polypyrrole hybrid electrode: a potential candidate for supercapacitors, *New J. Chem.* 41 (2017) 1704–1713. doi:10.1039/c6nj03580a.
- [7] Q. Wang, Y. Zou, C. Xiang, H. Chu, H. Zhang, F. Xu, L. Sun, C. Tang, High-performance supercapacitor based on V_2O_5 /carbon nanotubes-super activated carbon ternary composite, *Ceram. Int.* 42 (2016) 12129–12135. doi:10.1016/j.ceramint.2016.04.145.
- [8] C. Zhu, D. Hu, Z. Liu, Interconnected three-dimensionally hierarchical heterostructures

-
- with homogeneously-dispersed V_2O_5 nanocrystals and carbon for high performance supercapacitor electrodes, *Electrochim. Acta.* 229 (2017) 155–165. doi:10.1016/j.electacta.2017.01.144.
- [9] Z. Liu, H. Zhang, Q. Yang, Y. Chen, Graphene/ V_2O_5 hybrid electrode for an asymmetric supercapacitor with high energy density in an organic electrolyte, *Electrochim. Acta.* 287 (2018) 149–157. doi:10.1016/j.electacta.2018.04.212.
- [10] T. Kim, H. Kim, T. You, J. Kim, Carbon-coated V_2O_5 nanoparticles derived from metal-organic frameworks as a cathode material for rechargeable lithium-ion batteries, *J. Alloys Compd.* 727 (2017) 522–530. doi:10.1016/j.jallcom.2017.08.179.
- [11] A. De Adhikari, R. Oraon, S.K. Tiwari, J.H. Lee, N.H. Kim, G.C. Nayak, A V_2O_5 nanorod decorated graphene/polypyrrole hybrid electrode: a potential candidate for supercapacitors, *New J. Chem.* 41 (2017) 1704–1713. doi:10.1039/C6NJ03580A.
- [12] X. Liu, J. Zeng, H. Yang, K. Zhou, D. Pan, V_2O_5 -Based nanomaterials: Synthesis and their applications, *RSC Adv.* 8 (2018) 4014–4031. doi:10.1039/c7ra12523b.
- [13] G. Zhang, X. Xiao, B. Li, P. Gu, H. Xue, H. Pang, Transition metal oxides with one-dimensional/one-dimensional-analogue nanostructures for advanced supercapacitors, *J. Mater. Chem. A Mater. Energy Sustain.* 5 (2017) 8155–8186. doi:10.1039/C7TA02454A.
- [14] K. Palanisamy, J.H. Um, M. Jeong, W. Yoon, Porous V_2O_5 /RGO/CNT hierarchical architecture as a cathode material: Emphasis on the contribution of surface lithium storage, *Nat. Publ. Gr.* (2016) 1–12. doi:10.1038/srep31275.
- [15] J. Zheng, Y. Zhang, X. Jing, Q. Wang, T. Hu, N. Xing, Improvement of the specific capacitance of V_2O_5 nanobelts as supercapacitor electrode by tungsten doping, *Mater.*

-
- Chem. Phys. 186 (2017) 5–10. doi:10.1016/j.matchemphys.2016.11.027.
- [16] D.J. Ahirrao, K. Mohanapriya, N. Jha, V₂O₅ nanowires-graphene composite as an outstanding electrode material for high electrochemical performance and long-cycle-life supercapacitor, Mater. Res. Bull. 108 (2018) 73–82. doi:10.1016/j.materresbull.2018.08.028.
- [17] R. Narayanan, Single step hydrothermal synthesis of carbon nanodot decorated V₂O₅ nanobelts as hybrid conducting material for supercapacitor application, J. Solid State Chem. 253 (2017) 103–112. doi:10.1016/j.jssc.2017.05.035.
- [18] Y. Bai, Z. Yan, L. Kang, Z.H. Liu, Preparation and capacitance of V₂O₅/holey graphene hybrid aerogel electrode with high performance, J. Alloys Compd. 780 (2019) 792–799. doi:10.1016/j.jallcom.2018.12.006.
- [19] G. Zhang, L. Ren, D. Hu, S. Zhang, H. Gu, Fabrication of mesoporous carbon hollow spheres intercalated three-dimensional network structure V₂O₅ nanosheets with enhanced electrochemical performance, J. Alloys Compd. 781 (2019) 407–414. doi:10.1016/j.jallcom.2018.12.096.
- [20] J. Ding, O. Rahman, H. Zhao, W. Peng, Hydroxylated graphene-based flexible carbon film with ultrahigh electrical and thermal conductivity, Nanotechnology. 28 (2017) 39LT01.
- [21] H.L. Poh, Z. Sofer, P.imek, I. Tomandl, M. Pumera, Hydroboration of graphene oxide: Towards stoichiometric graphol and hydroxygraphane, Chem. - A Eur. J. 21 (2015) 8130–8136. doi:10.1002/chem.201406168.
- [22] J. Sun, Y. Deng, J. Li, G. Wang, P. He, S. Tian, X. Bu, Z. Di, S. Yang, G. Ding, X. Xie, A New Graphene Derivative: Hydroxylated Graphene with Excellent Biocompatibility,

-
- ACS Appl. Mater. Interfaces. 8 (2016) 10226–10233. doi:10.1021/acsami.6b02032.
- [23] C. Zu, A. Manthiram, Hydroxylated graphene-sulfur nanocomposites for high-rate lithium-sulfur batteries, *Adv. Energy Mater.* 3 (2013) 1008–1012. doi:10.1002/aenm.201201080.
- [24] R.C. Carvalho, C. Gouveia-Caridade, C.M.A. Brett, Glassy carbon electrodes modified by multiwalled carbon nanotubes and poly(neutral red): A comparative study of different brands and application to electrocatalytic ascorbate determination, *Anal. Bioanal. Chem.* 398 (2010) 1675–1685. doi:10.1007/s00216-010-3966-3.
- [25] M. Fahrul, R. Hanifah, J. Jaafar, M. Aziz, A. Fauzi, M.A. Rahman, M.H. Dzarfan, Synthesis of Graphene Oxide Nanosheets via Modified Hummers Method and Its Physicochemical Properties, *Jurnal Teknologi.* 1 (2015) 189–192.
- [26] D.I. Svergun, M.H.J. Koch, Small-angle scattering studies of biological macromolecules in solution, *Reports Prog. Phys.* 66 (2003) 1735–1782. doi:10.1088/0034-4885/66/10/R05.
- [27] H.K. Kammler, G. Beaucage, D.J. Kohls, N. Agashe, J. Ilavsky, Monitoring simultaneously the growth of nanoparticles and aggregates by in situ ultra-small-angle x-ray scattering, *J. Appl. Phys.* 97 (2005). doi:10.1063/1.1855391.
- [28] Q. Wei, J. Liu, W. Feng, J. Sheng, X. Tian, L. He, Q. An, L. Mai, Hydrated vanadium pentoxide with superior sodium storage capacity, *J. Mater. Chem. A.* 3 (2015) 8070–8075. doi:10.1039/c5ta00502g.
- [29] F. Coustier, S. Passerini, J. Hill, W.H. Smyrl, Silver-Doped Vanadium Oxides as Host Materials for Lithium Intercalation, *MRS Proc.* 496 (1997) 1355–1360. doi:10.1557/proc-496-353.

-
- [30] M. Li, G. Sun, P. Yin, C. Ruan, K. Ai, Controlling the formation of rodlike V_2O_5 nanocrystals on reduced graphene oxide for high-performance supercapacitors, *ACS Appl. Mater. Interfaces*. 5 (2013) 11462–11470. doi:10.1021/am403739g.
- [31] R.L. Smith, G.S. Rohrer, K.S. Lee, D.K. Seo, M.H. Whangbo, A scanning probe microscopy study of the (001) surfaces of V_2O_5 and V_6O_{13} , *Surf. Sci.* 367 (1996) 87–95. doi:10.1016/S0039-6028(96)00858-8.
- [32] L.T. Kerr, H.J. Byrne, B.M. Hennelly, Optimal choice of sample substrate and laser wavelength for Raman spectroscopic analysis of biological specimen, *Anal. Methods*. 7 (2015) 5041–5052. doi:10.1039/c5ay00327j.
- [33] K. Chen, D. Xue, High Energy Density Hybrid Supercapacitor: In-Situ Functionalization of Vanadium-Based Colloidal Cathode, *ACS Appl. Mater. Interfaces*. 8 (2016) 29522–29528. doi:10.1021/acsami.6b10638.
- [34] D. McNulty, D.N. Buckley, C.O. Dwyer, Synthesis and electrochemical properties of vanadium oxide materials and structures as Li-ion battery positive electrodes, *J. Power Sources*. 267 (2014) 831–873. doi:10.1016/j.jpowsour.2014.05.115.
- [35] A. Noori, M.F. El-kady, M.S. Rahmanifar, R.B. Kaner, M.F. Mousavi, Towards establishing performance metrics for batteries, supercapacitors and beyond, *Chem. Soc. Rev.* (2019). doi:10.1039/c8cs00581h.
- [36] D.J. Ahirrao, K. Mohanapriya, N. Jha, V_2O_5 nanowires-graphene composite as an outstanding electrode material for high electrochemical performance and long-cycle-life supercapacitor, *Mater. Res. Bull.* 108 (2018) 73–82. doi:10.1016/j.materresbull.2018.08.028.
- [37] A. Ray, A. Roy, P. Sadhukhan, S.R. Chowdhury, P. Maji, S.K. Bhattacharya, S. Das,

-
- Electrochemical properties of TiO₂-V₂O₅ nanocomposites as a high performance supercapacitors electrode material, *Appl. Surf. Sci.* 443 (2018) 581–591. doi:10.1016/j.apsusc.2018.02.277.
- [38] H.A. Ghaly, A.G. El-deen, E.R. Souaya, N.K. Allam, Asymmetric supercapacitors based on 3D graphene-wrapped V₂O₅ nanospheres and Fe₃O₄@3D graphene electrodes with high power and energy densities, *Electrochim. Acta.* 310 (2019) 58–69. doi:10.1016/j.electacta.2019.04.071.
- [39] M.M. Ndipingwi, C. Ikpo, N.W. Hlongwa, N. Ross, M. Masikini, S.V. John, P. Baker, W. Roos, E.I. Iwuoha, Orthorhombic (Pmn2₁) nanostructured Li₂MnSiO₄/Al₂O₃ supercapattery electrode with efficient Li ion migratory pathway, *Batter. Supercaps.* (2018) 1–14. doi:10.1002/batt.201800045.
- [40] Y. Yan, B. Li, W. Guo, H. Pang, H. Xue, Vanadium based materials as electrode materials for high performance supercapacitors, *J. Power Sources.* 329 (2016) 148–169. doi:10.1016/j.jpowsour.2016.08.039.
- [41] A.S. Rajpurohit, N.S. Punde, C.R. Rawool, A.K. Srivastava, Fabrication of high energy density symmetric supercapacitor based on cobalt-nickel bimetallic tungstate nanoparticles decorated phosphorus-sulphur co-doped graphene nanosheets with extended voltage, *Chem. Eng. J.* (2019) 679–692. doi:10.1016/j.cej.2019.04.100.
- [42] H. Liu, W. Zhu, D. Long, J. Zhu, G. Pezzotti, Porous V₂O₅ nanorods/reduced graphene oxide composites for high performance symmetric supercapacitors, *Appl. Surf. Sci.* 478 (2019) 383–392. doi:10.1016/j.apsusc.2019.01.273.
- [43] B. Saravanakumar, K. Kamaraj, Fabrication of two-dimensional reduced graphene oxide supported V₂O₅ networks and their application in supercapacitors, *Mater. Chem. Phys.*

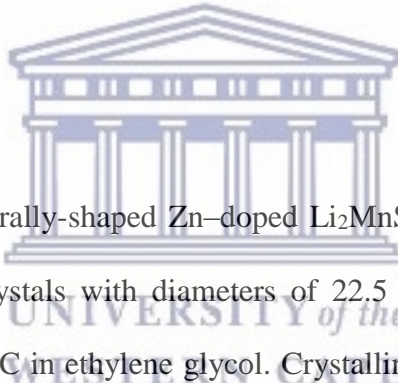
-
- 170 (2016) 266–275. doi:10.1016/j.matchemphys.2015.12.051.
- [44] Z. Chen, Y. Qin, D. Weng, Q. Xiao, Y. Peng, X. Wang, H. Li, F. Wei, Y. Lu, Design and synthesis of hierarchical nanowire composites for electrochemical energy storage, *Adv. Funct. Mater.* 19 (2009) 3420–3426. doi:10.1002/adfm.200900971.
- [45] X. Zhou, Q. Chen, A. Wang, J. Xu, S. Wu, J. Shen, Bamboo-like Composites of V_2O_5 /Polyindole and Activated Carbon Cloth as Electrodes for All-Solid-State Flexible Asymmetric Supercapacitors, *ACS Appl. Mater. Interfaces.* 8 (2016) 3776–3783. doi:10.1021/acsami.5b10196.
- [46] Z. Chen, V. Augustyn, J. Wen, Y. Zhang, M. Shen, B. Dunn, Y. Lu, High-performance supercapacitors based on intertwined CNT/ V_2O_5 nanowire nanocomposites, *Adv. Mater.* 23 (2011) 791–795. doi:10.1002/adma.201003658.
- [47] T. Peng, J. Wang, Q. Liu, J. Liu, P. Wang, Mesoporous V_2O_5 /Ketjin black nanocomposites for all-solid-state symmetric supercapacitors, *CrystEngComm.* 17 (2015) 1673–1679. doi:10.1039/c4ce02305f.
- [48] B. Saravanakumar, K. Kamaraj, V_2O_5 /nitrogen enriched mesoporous carbon spheres nanocomposite as supercapacitor electrode, *Microporous Mesoporous Mater.* 258 (2018) 83–94. doi:10.1016/j.micromeso.2017.09.010.

CHAPTER FIVE

RESULTS AND DISCUSSION - MANUSCRIPT 3

Zinc Doped Lithium Manganese Silicate Mixed Spherical and Rhombohedrally-Shaped Nanocrystals as battery-type Electrodes for Supercapattery Applications (Prepared for ACS Applied Materials & Interfaces)

Abstract

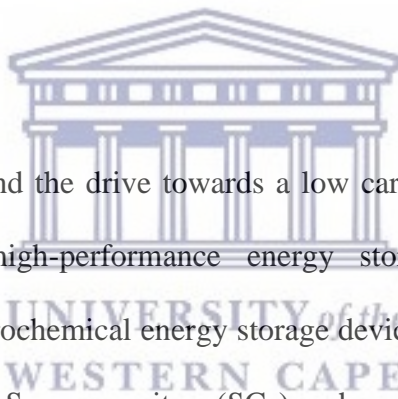


Mixed spherical and rhomboherally-shaped Zn-doped $\text{Li}_2\text{MnSiO}_4$ ($\text{Li}_2\text{Mn}_{1-x}\text{Zn}_x\text{SiO}_4$, $x = 0, 0.02, 0.04, 0.06, 0.08$) nanocrystals with diameters of 22.5 – 30.7 nm were prepared by solvothermal synthesis at 180 °C in ethylene glycol. Crystalline and orthorhombic structural phases of the materials were confirmed by X-ray diffraction. Skewed and bell-shaped particle size distribution of the nanocrystals were revealed by small angle X-ray scattering. Electrochemical studies revealed superior performance of 4 % Zn-doped $\text{Li}_2\text{MnSiO}_4$ ($\text{Li}_2\text{Mn}_{0.96}\text{Zn}_{0.04}\text{SiO}_4$) with a specific capacity of 80.46 C g⁻¹ at a scan rate of 20 mV s⁻¹. The enhanced performance was ascribed to the high nucleation density observed in XRD investigations and majority rhombohedra morphology of the electrode which provided a larger surface area, more available sites for electrolyte penetration and faster diffusion of Li-ions. Supercapattery devices assembled with activated carbon as negative electrode and $\text{Li}_2\text{Mn}_{1-x}\text{Zn}_x\text{SiO}_4$ as the positive electrodes delivered good capacitance retention and coulombic efficiencies over 3000 cycles. The AC// $\text{Li}_2\text{Mn}_{0.96}\text{Zn}_{0.04}\text{SiO}_4$ supercapattery exhibited a specific

energy of 38.4 W h kg^{-1} at a specific power of 516 W kg^{-1} and up to 19.9 W h kg^{-1} was retained at specific power of 14429 W kg^{-1} . The pillar effect of Zn doping as well as the nanocrystallite morphology provided high contact volume of the electrode particles with the electrolyte and enhanced the electrical conductivity of the material leading high rate performance and overall energy storage capability.

Keywords: Nanocrystals, Zn-doping, $\text{Li}_2\text{MnSiO}_4$, supercapattery, high specific energy

5.1 Introduction



Technological advancements and the drive towards a low carbon environment have greatly increased the demand for high-performance energy storage devices. Batteries and supercapacitors are major electrochemical energy storage devices that have been widely used in several practical applications. Supercapacitors (SCs) such as electric double-layer capacitors (EDLCs) and pseudocapacitors have attracted vast attention among several energy storage devices due to their high power density, fast charge-discharge rates, long cycle life and easy device fabrication [1,2]. Lithium-ion batteries which are renowned for their high specific energy, high working voltage, no memory effect, and long cycle life have also been the focus of research in recent times due to their promise of near-term advancements [3]. However, the low specific energy of SCs and low specific power of Li-ion batteries limits their widespread applicability. Therefore, the design of hybrid energy storage devices known as supercapatteries is a promising way of enhancing the energy and power capabilities of these systems. A supercapattery offers improved specific energy without sacrificing its specific power by

combining the high structural and cycling capabilities of EDLC-type materials with the excellent charge-storage properties of redox-type materials. More so, it utilizes carbonaceous EDLC-type materials as a power source and pseudocapacitive/battery-type materials as an energy source [1,4]. Battery-type electrode materials store larger amounts of energy when compared to pseudocapacitive materials due to their diffusion-controlled redox reactions within the bulk of the electrode material and strong dependence on electrode potential whereas pseudocapacitive materials store electrical charge by fast surface-confined redox reactions [5–7]. Hence, battery-type electrode materials with high charge storage capabilities have been widely investigated. Recent developments in Li-ion battery specific energies have been accomplished mainly by modification and optimization of battery cell designs rather than its chemistry [8,9]. To achieve a significant increase in battery capacity, new electrode materials and materials which are able to reversibly intercalate more than one lithium ion per formula unit are crucial. The earliest efforts of this approach have been based on layered oxides like Li_xMO_2 , Li_xVSe_2 , vanadium oxides such as $\text{Li}_x\text{V}_2\text{O}_5$, $\text{Li}_x\text{V}_3\text{O}_8$ and spinels like $\text{Li}_x\text{Mn}_2\text{O}_4$, $\text{Li}_x\text{Ti}_2\text{S}_4$ ($2 < x < 3$) and rhombohedral $\text{Li}_3\text{V}_2(\text{PO}_4)_2$. These technologies were not widely commercialized due to low working potentials, kinetic limitation of the reinsertion of Li-ions and rapid capacity fading of the cells [8,10,11]. In recent years, lithium metal orthosilicates (Li_2MSiO_4 , $\text{M} = \text{Mn, Fe, Ni}$) have been identified as potential cathode materials which can theoretically fulfill the energy requirements of advanced Li-ion batteries. These materials show higher theoretical specific capacities and better safety than the conventional cathodes, with $\text{Li}_2\text{MnSiO}_4$ being the most investigated on account of its high theoretical capacity of 330 mA h g^{-1} , outstanding thermal stability, and natural abundance. However, $\text{Li}_2\text{MnSiO}_4$ electrode material possesses some inherent drawbacks, such as poor electronic conductivity and structural instability caused by Mn coordination change upon oxidation and Jahn-Teller distortion during cycling [12,13]. These drawbacks restrict its wide-ranging applications. To

solve these problems, different strategies have been developed to improve electrochemical kinetics and structural stability of $\text{Li}_2\text{MnSiO}_4$ cathode including; hybridization with carbonaceous materials [14,15], morphology control [16,17] and ion doping [18,19]. Ding *et al.*, prepared hexagonal and prism-shaped $\text{Li}_2\text{MnSiO}_4$ nanoplates using ethylene and diethylene glycol as capping agents/ structure-directing agents. These electrodes delivered a near theoretical discharge capacity of $326.7 \text{ mA h g}^{-1}$ at 0.05 C and good cycling stability [20]. Furthermore, doping of $\text{Li}_2\text{MnSiO}_4$ with aliovalent ions has been reported by many researchers to enlarge its unit cell volume by modifying its crystalline grains, leading to improved electrochemical performance. For instance, Choi *et al.*, prepared $\text{Li}_2\text{MnSiO}_4$ nanoparticles doped with various trivalent ions such as Ga^{3+} , Al^{3+} , and Mg^{2+} by sol-gel chemistry. The cationic ion-doped $\text{Li}_2\text{MnSiO}_4$ electrodes especially Ga^{3+} -doped $\text{Li}_2\text{MnSiO}_4$ demonstrated high initial charge/discharge capacities and good cycling efficiency due to the observed enlarged nucleation density and high surface active sites [21]. Partial substitution of the Mn^{2+} ions in $\text{Li}_2\text{MnSiO}_4$ electrode material with V^{3+} ions has also proven to improve its electrochemical performance by reducing the electrode grain sizes with corresponding higher crystallinity and Li^+ -ion diffusion rates [22]. Don's and Shenouda's groups have also reported the improvement of the electrochemical performance of $\text{Li}_2\text{MnSiO}_4$ electrode material via mild substitution of the Mn-site with La^{3+} [23] and Ni^{2+} [24] ions. These results further confirmed that doping $\text{Li}_2\text{MnSiO}_4$ ions with trivalent or divalent cations can effectively reduce its particle sizes with high nucleation/ packing densities, reduced charge transfer resistance, and enhanced electrochemical performance. High discharge capacities in the range of 150 – 250 mAh g^{-1} were obtained with commendable cycling stabilities. Likewise, the effects of Zn^{2+} doping on the electrochemical performance of several battery and supercapacitor electrode materials including LiFePO_4 , LiMnPO_4 , MnO_2 , Na_2MnO_2 and Fe_2O_3 [25–29] have been investigated. These results demonstrate that a small amount of Zn doping through the pillar effect, can

significantly expand the lattice volume of the unit cell and provide more space for Li-ion intercalation/ de-intercalation. In addition, Zn doping can reduce cell polarization, improve the electrode charge transfer kinetics and the reversibility of lithium intercalation and de-intercalation as a result of shorter diffusion distance of lithium ions. More recently, Mao *et al.*, [30] studied the variation of lattice cell parameters and voltage fading mitigation upon Zn doping in layered $\text{NaNi}_{10.2}\text{Fe}_{0.35}\text{Mn}_{0.45}\text{O}_2$ positive electrode for Na-ion batteries while Zhao *et al.*, [31] investigated the synergistic effect of Zn doping and nanorod morphology on the electrochemical properties of spinel LiMn_2O_4 positive electrode for Li-ion batteries. These studies reveal that a low amount of Zn doping (as low as 2 %) on the Mn-site in combination with the design of nanostructures can effectively stabilize the crystal structure by increasing the lattice volume. A reduction in the Jahn-Teller active Mn^{3+} ions also contributes to the stability of the electrode during repeated intercalation/deintercalation reactions thereby alleviating voltage fading during cycling.

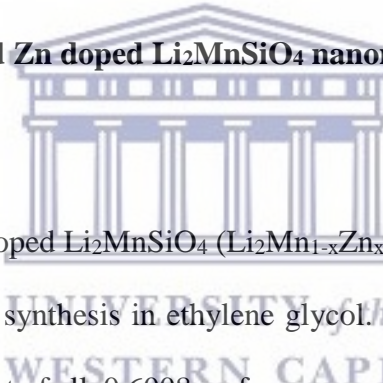
In this work, we report on solvothermal synthesis of $\text{Li}_2\text{MnSiO}_4$ nanomaterials and the effect of Zn doping on its electrochemical performance for the first time. A small amount of Zn doping is observed to enhance the electrochemical performance of undoped $\text{Li}_2\text{MnSiO}_4$ by almost two folds with an optimal ratio of 4 %. The orthosilicate-based electrodes are applied as battery-type electrodes in supercapattery devices assembled with activated carbon as the anode.

5.2 Experimental details

5.2.1 Materials

The following chemicals were purchased from Aldrich and used without further purification. Ethylene glycol (anhydrous, $\geq 99.8\%$), tetraethyl orthosilicate ($\geq 99.0\%$), zinc acetate dihydrate (99.999 % trace metal basis), lithium hydroxide (98 % reagent grade), sodium sulfate ($\geq 99.99\%$ trace metal basis), manganese (II) chloride tetrahydrate (99.99 % trace metal basis), N-methyl-2-pyrrolidone (anhydrous, 99.5 %). ethanol (absolute, $\geq 99.8\%$), polytetrafluoroethylene (mean particle size 20 μm), activated charcoal (Norit® pellets), carbon black (4 μm mesoporous carbon matrix, $\geq 99.95\%$ metal basis). Hydrochloric acid (reagent grade and assay 36.5 – 38.0 %) was obtained from Kimix chemicals and nickel foam (1.6 mm thick, 0.25 μm pore diameter) purchased from MTI Corporation.

5.2.2. Synthesis of pristine and Zn doped $\text{Li}_2\text{MnSiO}_4$ nanomaterials



$\text{Li}_2\text{MnSiO}_4$ and a series of Zn doped $\text{Li}_2\text{MnSiO}_4$ ($\text{Li}_2\text{Mn}_{1-x}\text{Zn}_x\text{SiO}_4$, $x = 0.02, 0.04, 0.06, 0.08$) were prepared by solvothermal synthesis in ethylene glycol. Ethylene glycol acted as both a reducing and capping agent. First of all, 0.6008 g of manganese (II) chloride tetrahydrate (0.01 mols) were dispersed in 20 mL of ethylene glycol until complete dissolution. Afterwards, 2.2329 mL of tetraethyl orthosilicate (0.01 mols) was slowly added to the mixture and vigorously stirred for 30 mins. Then, 0.9580 g of LiOH (0.04 mols) dispersed in distilled water were rapidly added to the mixture. The molar ratio of Li: Mn: Si were kept at 4: 1: 1. The mixture was transferred to a 100 mL Teflon-lined autoclave, stirred for 15 mins and maintained at 180 °C for 15 h. After cooling to room temperature, the obtained products (greyish precipitate) were centrifuged and washed for several times with distilled water and ethanol. The products were preheated at 350 °C for 4 h and calcinated at 700 °C for 18 h. The different ratios of Zn-

doped $\text{Li}_2\text{MnSiO}_4$ were prepared by same procedure but with the addition of different amounts of zinc acetate dihydrate with manganese chloride tetrahydrate.

5.2.3.1 Material Characterization

Structure and morphology of the pristine and Zn doped $\text{Li}_2\text{MnSiO}_4$ nanomaterials were characterized using ZEISS ULTRA scanning electron microscope equipped with an energy dispersive spectrometer and a Tecnai $\text{G}^2\text{F}_2\text{O}$ X-Twin MAT 200 kV field emission transmission electron microscope from FEI. Analyses were performed on a nickel-copper grid. The particle size distribution of the nanomaterials were obtained by small-angle X-ray scattering experiments performed on an Anton Paar SAXSpace system. Copper $\text{K}\alpha$ radiation (0,154 nm) was used and the instrument is equipped with a 1 D mythen 2 position sensitive detector and a beamstop alignment. Powder X-ray diffraction studies were obtained using a D8 advance diffractometer from BRUKER-AXS using copper $\text{K}\alpha_1$ radiation ($\lambda \sim 0.154$ nm) operating at 40 kV and 40 mA. A Perkin Elmer Spectrum 100 series Attenuated Total Reflection (ATR) Fourier Transform Infrared spectrometer with a resolution of 4 cm^{-1} was used to obtain the functional groups present in the materials. Electrochemical studies were performed using both three and two-electrode cells on a VMP-300 potentiostat from Bio-Logic instruments.

5.2.3.2 Electrode preparation and electrochemical measurements

The working electrode was prepared by mixing 70 % of the active material with 20 % carbon black (conducting agent) and 10 % polytetrafluoroethylene (binder) in a few drops of

anhydrous N-methyl-2-pyrrolidone. Prior to coating, nickel foam was cut into rectangular shapes of $0.5 \times 1 \text{ cm}^2$ and coin-shapes of 20 mm in diameter. The different sizes were cleaned and etched to remove surface oxide layer using 1 M HCl solution in an ultrasonic bath for 15 mins, then cleaned in absolute ethanol and deionized water for 15 min in sequence by ultrasonication and finally dried at $90 \text{ }^\circ\text{C}$ for 12 h. A homogenous paste was obtained using a mortar and pestle and coated on nickel foam with a diameter of 0.5 cm^2 using a spatula and dried at $80 \text{ }^\circ\text{C}$ for 12 h. Ag/AgCl and Pt wire were used as the reference and counter electrodes, respectively for studies in three-electrode system. For two-electrode cell analysis, the homogenous paste was coated on coin-shaped nickel foam with a diameter of 20 mm and supercapattery cells were assembled in a Swagelok using pristine and Zn doped $\text{Li}_2\text{MnSiO}_4$ samples as the positive electrodes and activated carbon as the negative electrode. Cyclic voltammograms were recorded in a potential window of 0.1 to 0.8 V at different scan rates and electrochemical impedance measurements were obtained at a frequency range of 0.1 MHz – 100 kHz with 10 points per decade. CV curves, galvanostatic charge-discharge profiles and the cycling performance of the supercapattery cells were obtained in aqueous 1 M Na_2SO_4 electrolyte at a voltage of 1.6 V.

5.3 Results and Discussion

5.3.1 Structure and morphological Analysis by Scanning and Transmission Electron Microscopies (SEM and HRTEM)

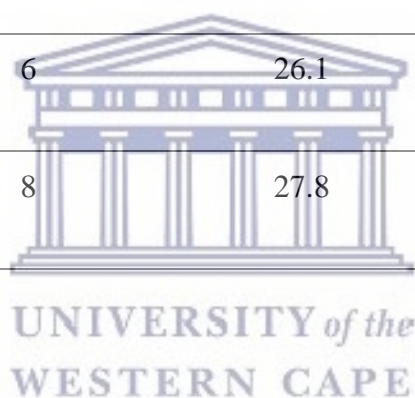
The structure and morphology of $\text{Li}_2\text{MnSiO}_4$ and Zn doped counterparts ($\text{Li}_2\text{Mn}_{0.98}\text{Zn}_{0.02}\text{SiO}_4$, $\text{Li}_2\text{Mn}_{0.96}\text{Zn}_{0.04}\text{SiO}_4$, $\text{Li}_2\text{Mn}_{0.94}\text{Zn}_{0.06}\text{SiO}_4$ and $\text{Li}_2\text{Mn}_{0.92}\text{Zn}_{0.08}\text{SiO}_4$) were examined by SEM and

HRTEM microscopies. Figure 5.1 displays the SEM and HRTEM micrographs of these nanomaterials obtained at low magnification. As shown in Figure 5.1 (a), the SEM image of pristine $\text{Li}_2\text{MnSiO}_4$ shows aggregated and mixed spherical and rhombohedral-shaped nanocrystals. It is observed that Zn doping increases the nucleation density of the nanoparticles and favors the growth of a more rhombohedral morphology of the nanocrystals especially at a zinc doping ratio of 4 % ($\text{Li}_2\text{Mn}_{0.96}\text{Zn}_{0.04}\text{SiO}_4$), as shown in Figure 5.1 (c). HRTEM images present micrographs with a little darker contrast which may be attributed to the presence of ethanol used as solvent to disperse nanocrystals prior to analysis. The rhombohedral shape is more revealed in high resolution micrographs obtained from HRTEM. The lattice fringes and selected area electron diffraction images are displayed as insets in the HRTEM images. The observed concentric circles together with lattice fringes reveal the crystallinity of the materials. Nanocrystal sizes processed using ImageJ are shown in Table 5.1.

Elemental composition of the undoped and Zn-doped $\text{Li}_2\text{MnSiO}_4$ nanocrystals were also verified using energy dispersive X-ray spectroscopy (EDS). Figure 5.1 (f) shows EDS spectra of the nanomaterials and all expected elements are observed. EDS maps of 4 % Zn-doping ratio which showed the desired morphology and particles sizes are shown in Figure 5.1 (g). As observed, the maps portray a homogenous distribution of all expected elements.

Table 5.1: Nanocrystallite sizes of $\text{Li}_2\text{MnSiO}_4$ and $\text{Li}_2\text{Mn}_{0.98}\text{Zn}_{0.02}\text{SiO}_4$, $\text{Li}_2\text{Mn}_{0.96}\text{Zn}_{0.04}\text{SiO}_4$, $\text{Li}_2\text{Mn}_{0.94}\text{Zn}_{0.04}\text{SiO}_4$, and $\text{Li}_2\text{Mn}_{0.92}\text{Zn}_{0.08}\text{SiO}_4$ obtained from HRTEM analysis

Electrode material	Zn content / %	Average diameter / nm	Standard deviation / nm
$\text{Li}_2\text{MnSiO}_4$	0	22.5	± 15.3
$\text{Li}_2\text{Mn}_{0.98}\text{Zn}_{0.02}\text{SiO}_4$	2	30.7	± 16.4
$\text{Li}_2\text{Mn}_{0.94}\text{Zn}_{0.04}\text{SiO}_4$	4	23.5	± 3.2
$\text{Li}_2\text{Mn}_{0.92}\text{Zn}_{0.08}\text{SiO}_4$	6	26.1	± 13.2
$\text{Li}_2\text{Mn}_{0.90}\text{Zn}_{0.1}\text{SiO}_4$	8	27.8	± 18.6



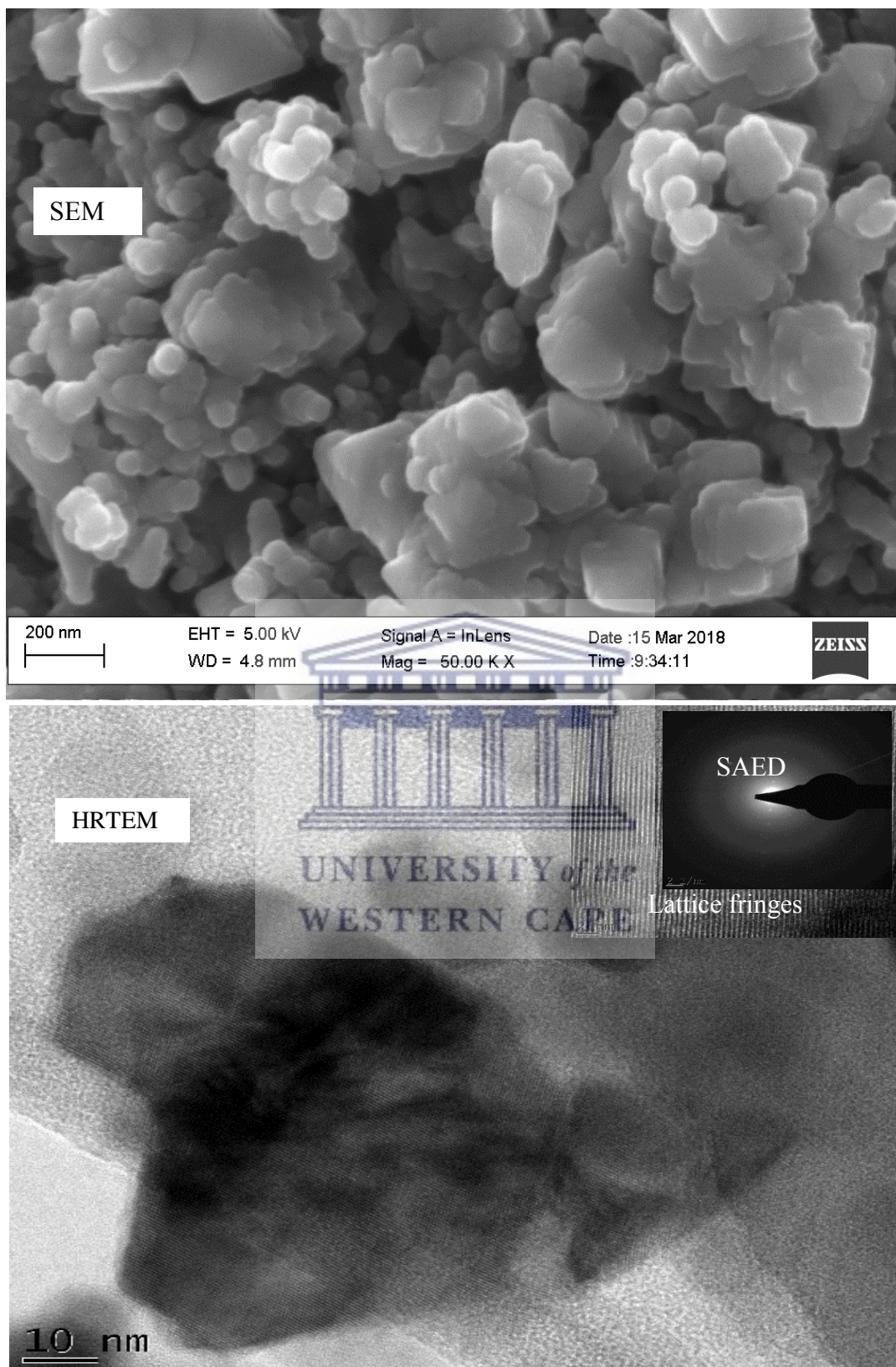


Figure 5.1 (a): SEM and HRTEM micrographs of $\text{Li}_2\text{MnSiO}_4$ with SAED and lattice fringes as insets

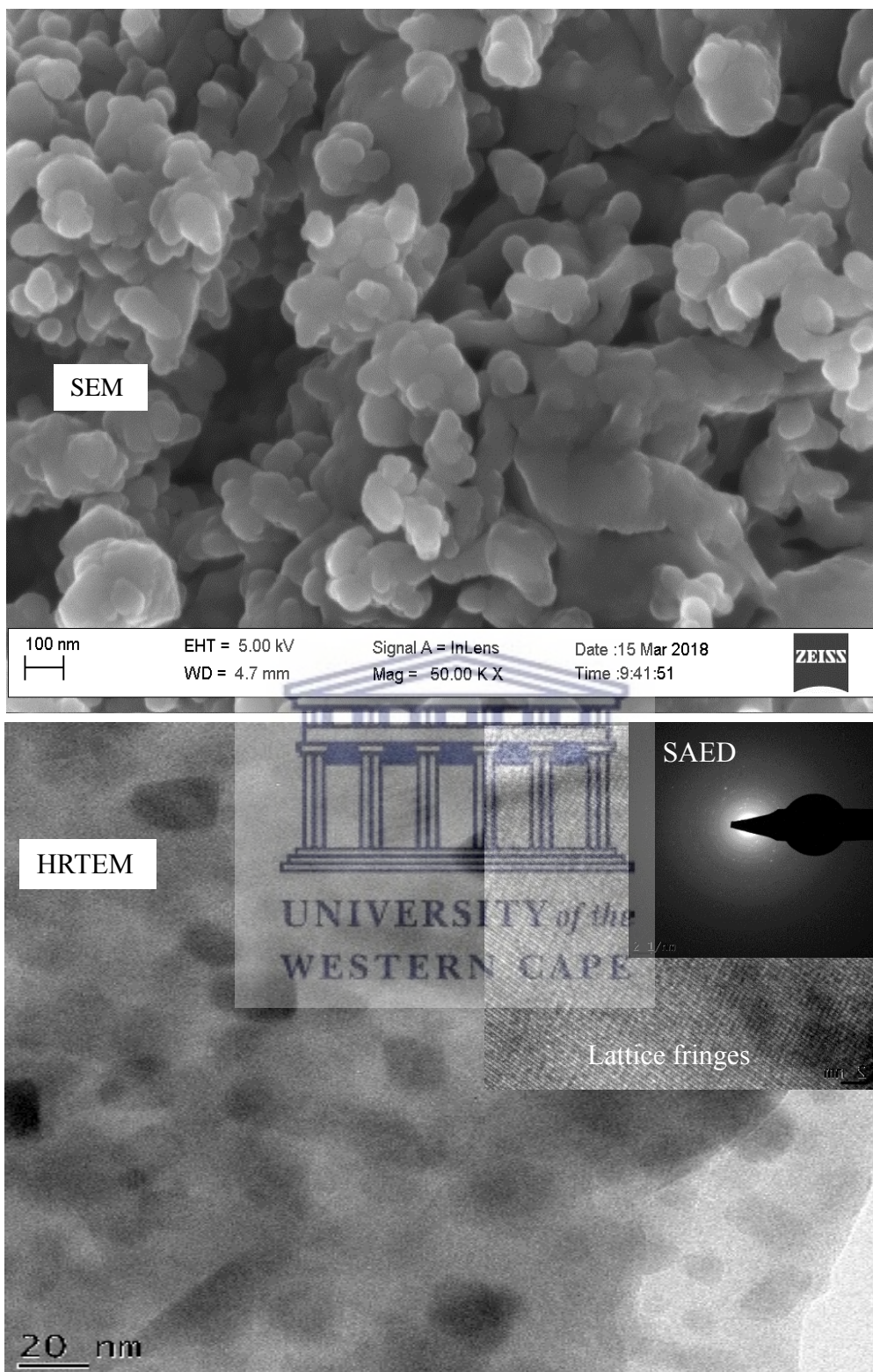


Figure 5.1 (b): SEM and HRTEM micrographs of $\text{Li}_2\text{Mn}_{0.98}\text{Zn}_{0.02}\text{SiO}_4$ with SAED and lattice fringes as insets

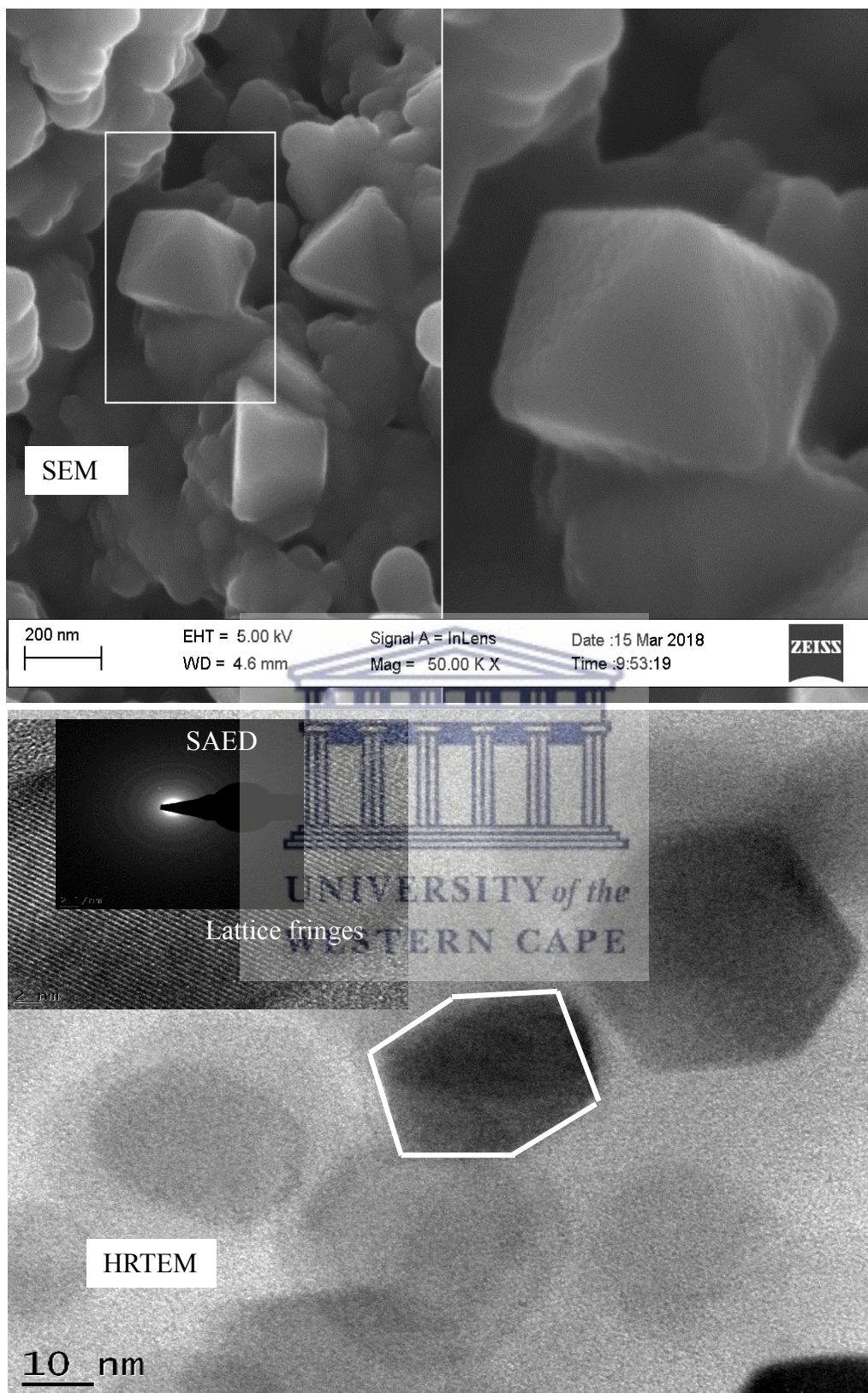


Figure 5.1 (c): SEM and HRTEM micrographs of $\text{Li}_2\text{Mn}_{0.96}\text{Zn}_{0.04}\text{SiO}_4$ with SAED and lattice fringes as insets

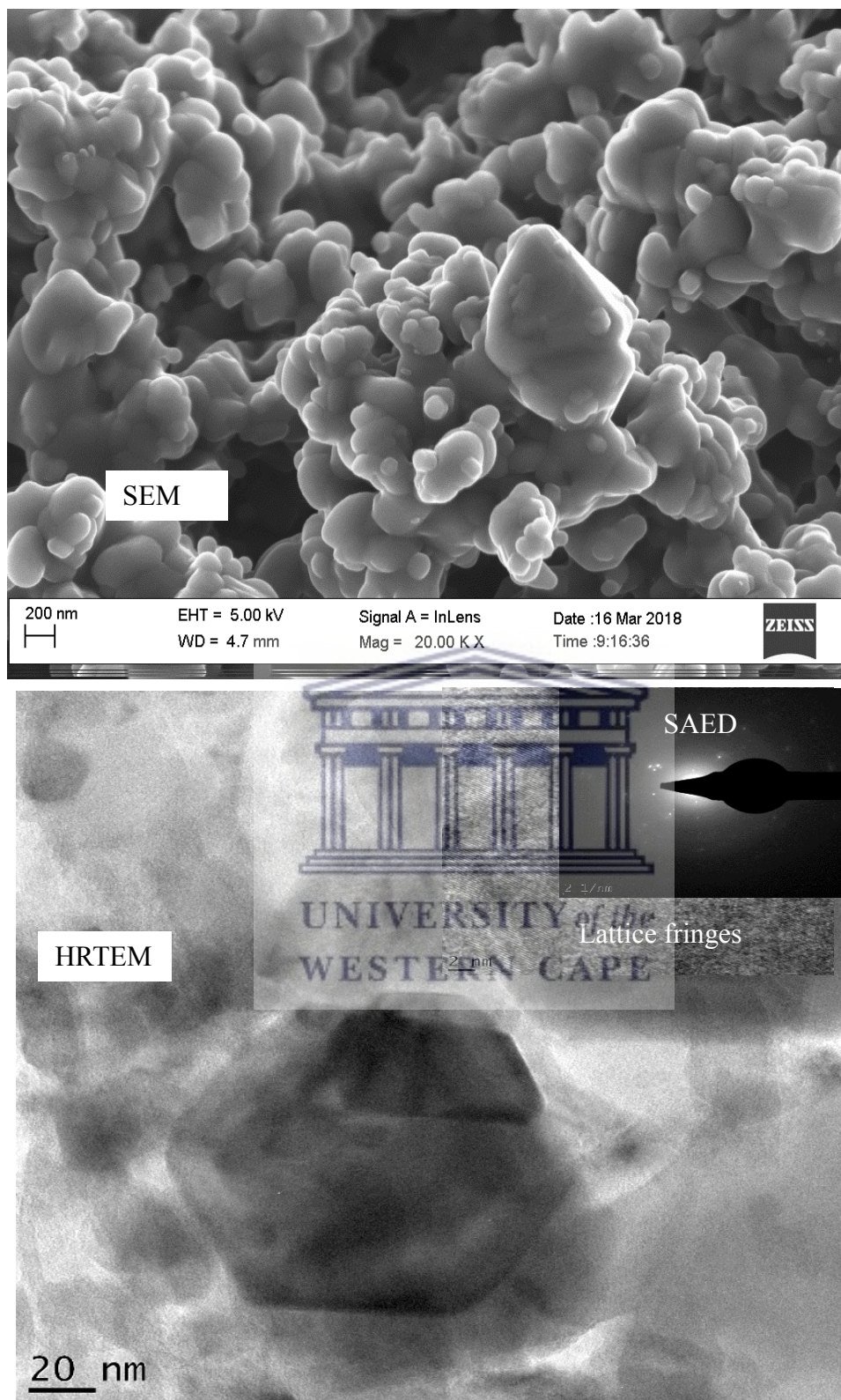


Figure 5.1 (d): SEM and HRTEM micrographs of $\text{Li}_2\text{Mn}_{0.94}\text{Zn}_{0.06}\text{SiO}_4$ with SAED and lattice fringes as insets

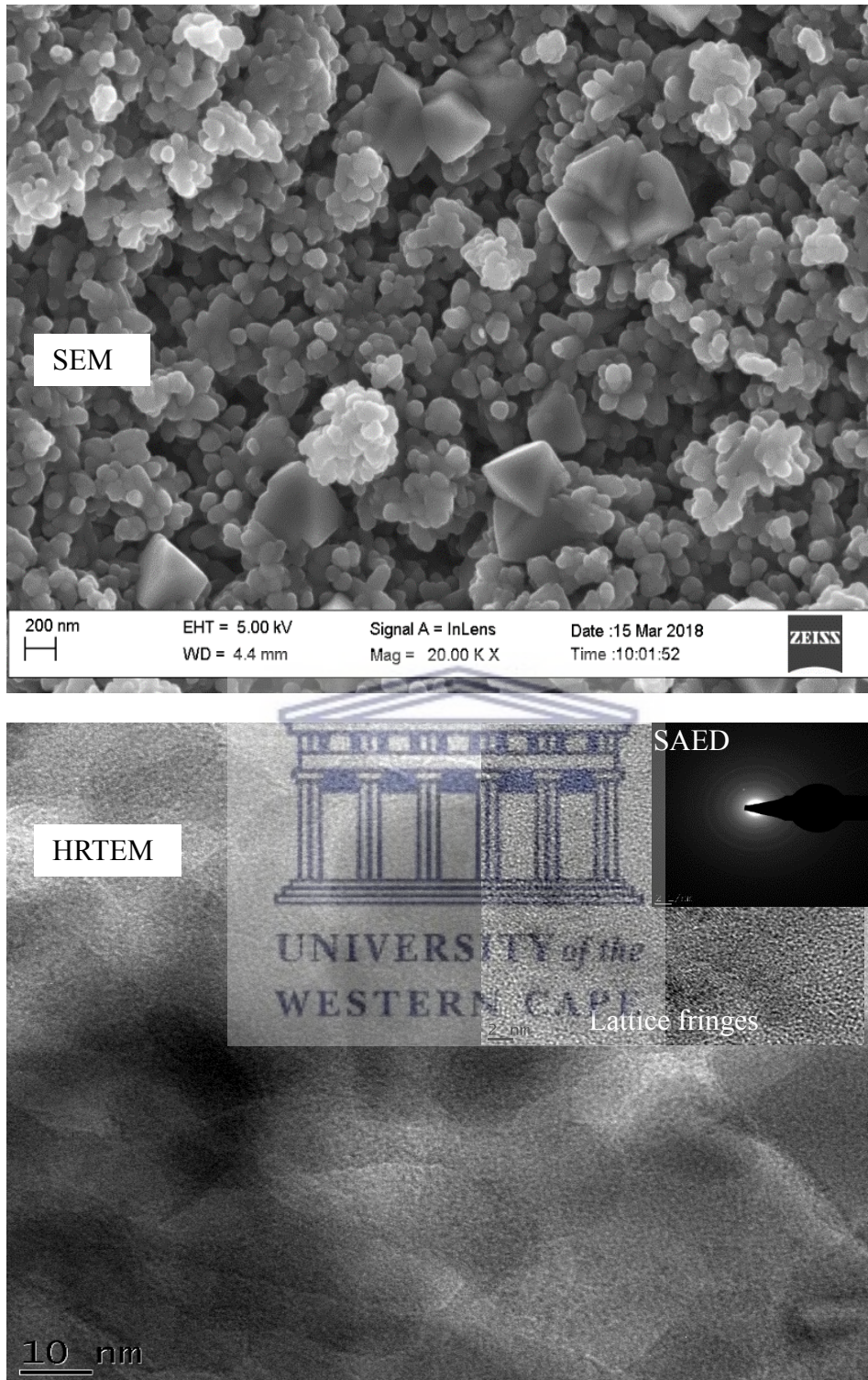


Figure 5.1 (e): SEM and HRTEM micrographs of $\text{Li}_2\text{Mn}_{0.92}\text{Zn}_{0.08}\text{SiO}_4$ with SAED and lattice fringes as insets

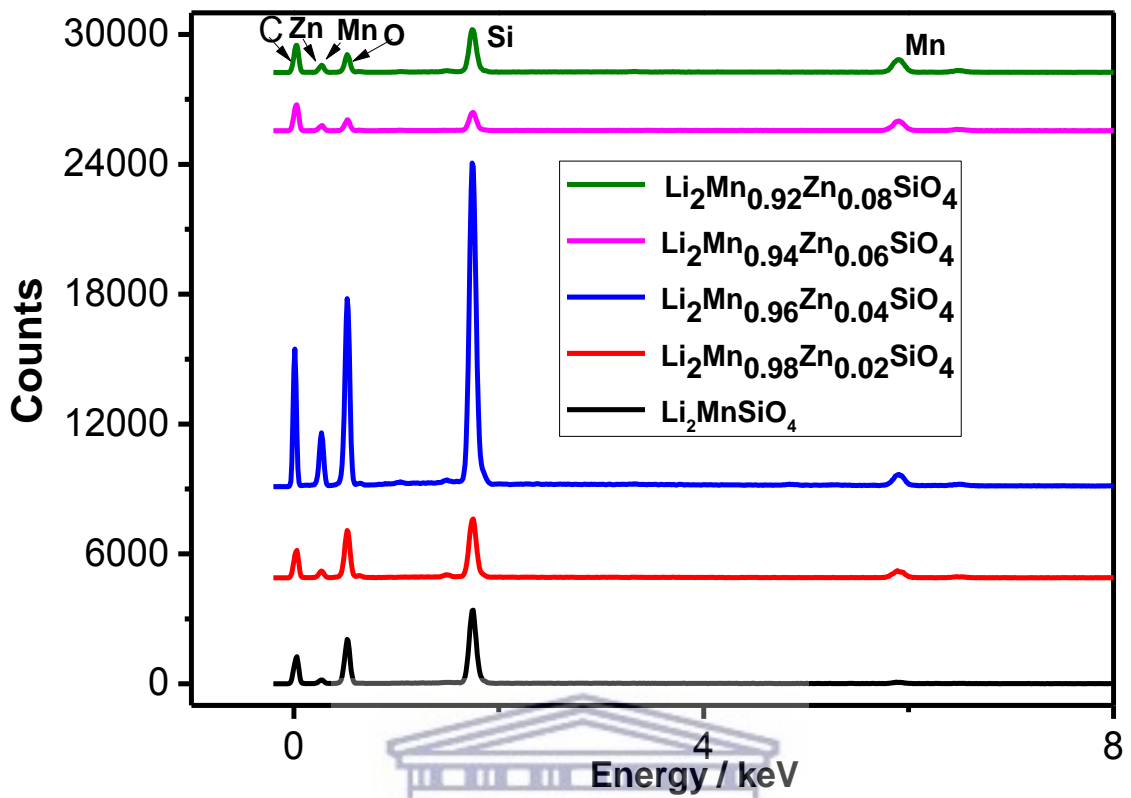
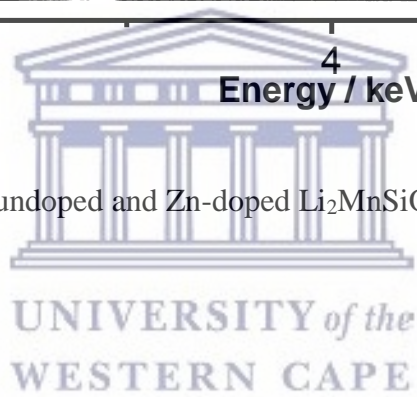


Figure 5.1 (f): EDS spectra of undoped and Zn-doped $\text{Li}_2\text{MnSiO}_4$ nanomaterials



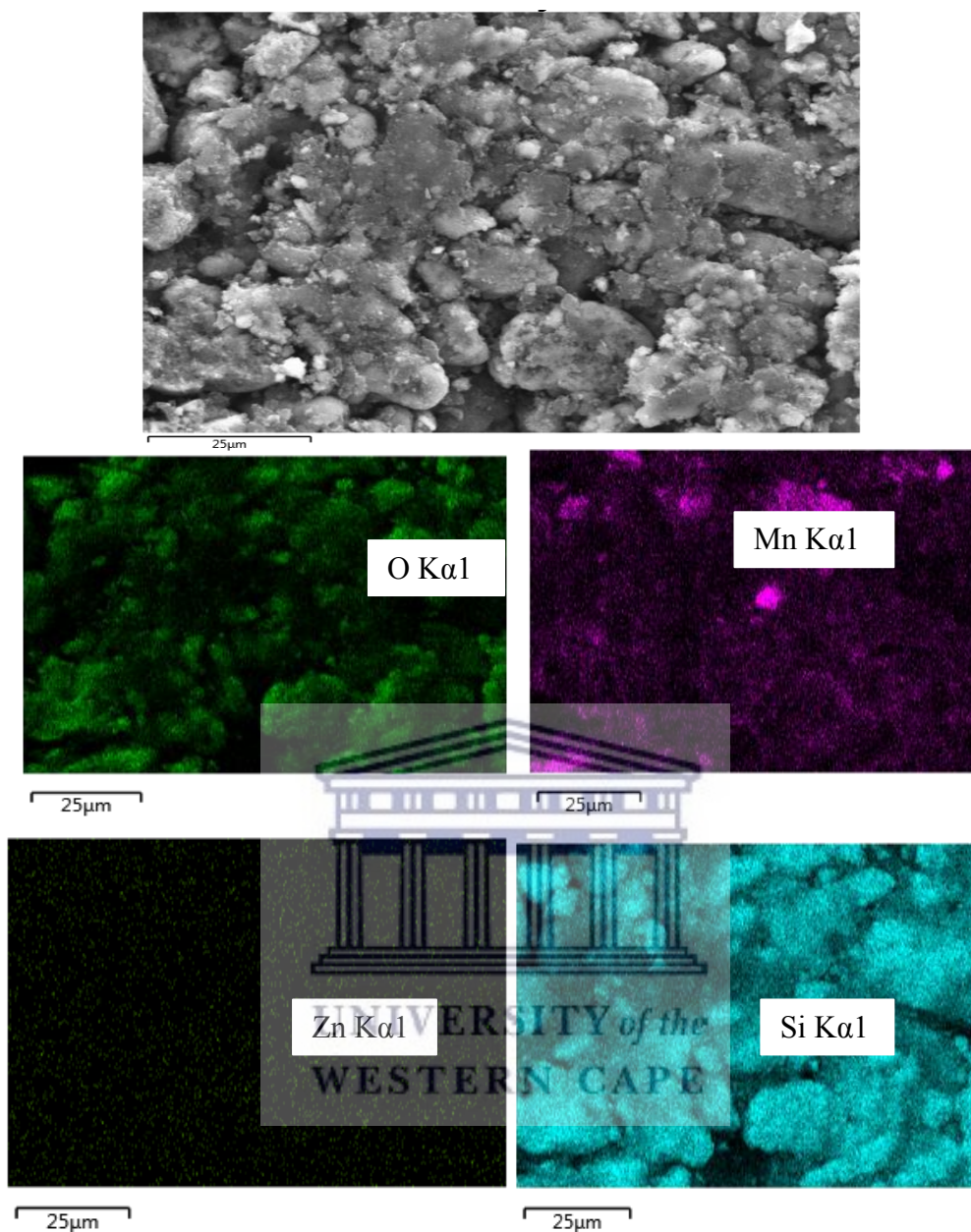


Figure 5.1 (g): EDS maps of $\text{Li}_2\text{Mn}_{0.96}\text{Zn}_{0.04}\text{SiO}_4$ nanocrystals

5.3.2 Particle size distribution by Small Angle X-ray Scattering (SAXS)

SAXS experiments were used to obtain the primary particle sizes, aggregates of the primary particles (secondary particles) and particle size distribution of undoped and Zn-doped

nanomaterials. The scattering curves are presented in the form of pair distance distribution functions with respect to scattering intensities of the particles as shown in Figure 5.2 (a) and the physical volume of the scattered particles as shown in Figure 5.2 (b). The scattering curves of the intensity particle size distribution of pristine $\text{Li}_2\text{MnSiO}_4$ and 2 % Zn dopant ratio ($\text{Li}_2\text{Mn}_{0.98}\text{Zn}_{0.02}\text{SiO}_4$) as shown in Figure 5.2 (a₁), portray bell-shaped distribution of the primary particles diameters with center-peaks at 23 nm and 15 nm, respectively. Aggregates of the primary particles show left-skewed distributions for both electrode materials, indicating a variation in the sizes of the aggregated nanocrystals. An increase in particle nucleation density is highly noticeable in the $\text{Li}_2\text{Mn}_{0.98}\text{Zn}_{0.02}\text{SiO}_4$ electrode material as indicated by the increase in the intensity of the secondary particle diameters with a maximum center-peak at 134.9 nm. The intensity particle size distributions of samples with slightly higher Zn dopant ratios (4 – 8 %) display almost a bell-shaped / normal particle size distribution, indicating almost uniform particle sizes of the nanocrystals as shown in Figure 5.2 (a₁) and (a₂). Primary particles of $\text{Li}_2\text{Mn}_{0.94}\text{Zn}_{0.04}\text{SiO}_4$ electrode materials showed a center peak at 23.1 nm with aggregates at 135.3 nm. Primary particles of $\text{Li}_2\text{Mn}_{0.98}\text{Zn}_{0.02}\text{SiO}_4$ showed diameters with a center peak at 15.8 nm with the absence of the secondary particle sizes. This can be due to an increase in particle nucleation which favored the reduction in the sizes of the nanocrystals.

A cross section of the pair distance distribution function with respect to the volume of the scattered particles is shown in Figure 5.2 (b). Bell-shaped particle size distributions are observed. $\text{Li}_2\text{MnSiO}_4$ showed primary particles diameters with center-peak at 14.7 nm while $\text{Li}_2\text{Mn}_{0.98}\text{Zn}_{0.02}\text{SiO}_4$, $\text{Li}_2\text{Mn}_{0.96}\text{Zn}_{0.04}\text{SiO}_4$, and $\text{Li}_2\text{Mn}_{0.94}\text{Zn}_{0.04}\text{SiO}_4$ showed diameters of 15.6 nm, 16.1 nm and 15.7 nm, respectively for the primary particle sizes.

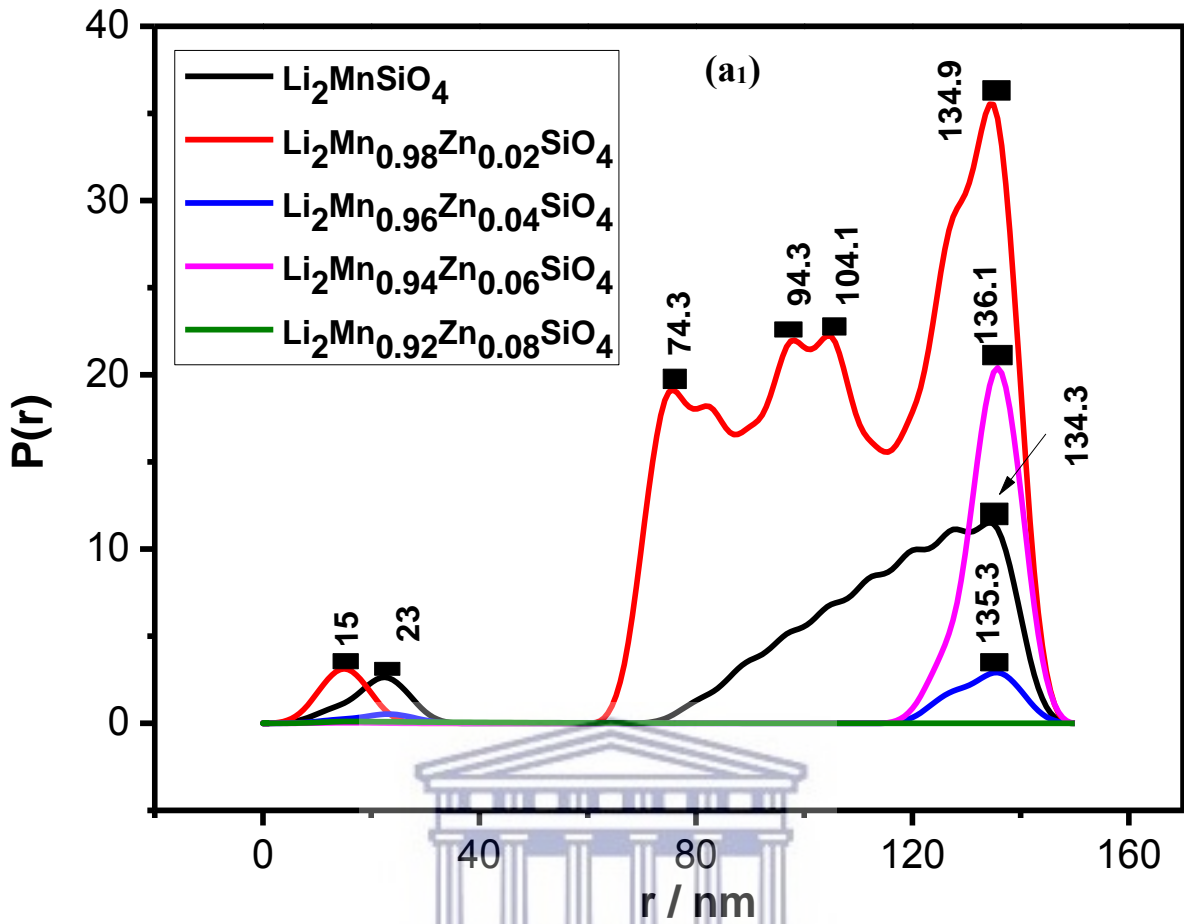


Figure 5.2 (a1): SAXS pair distance distribution functions of undoped and Zn-doped $\text{Li}_2\text{MnSiO}_4$ nanocrystals by intensity of scattered particles

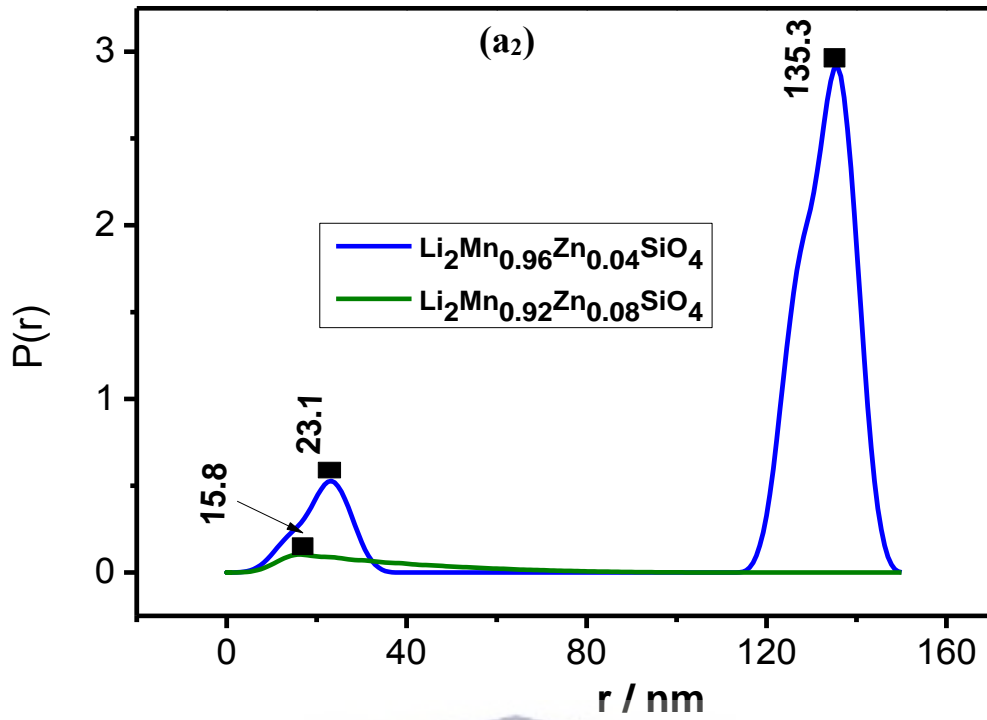


Figure 5.2 (a2): SAXS pair distance distribution functions of undoped and Zn-doped $\text{Li}_2\text{MnSiO}_4$ nanocrystals by intensity of scattered particles (enlarged lower section of a₁)



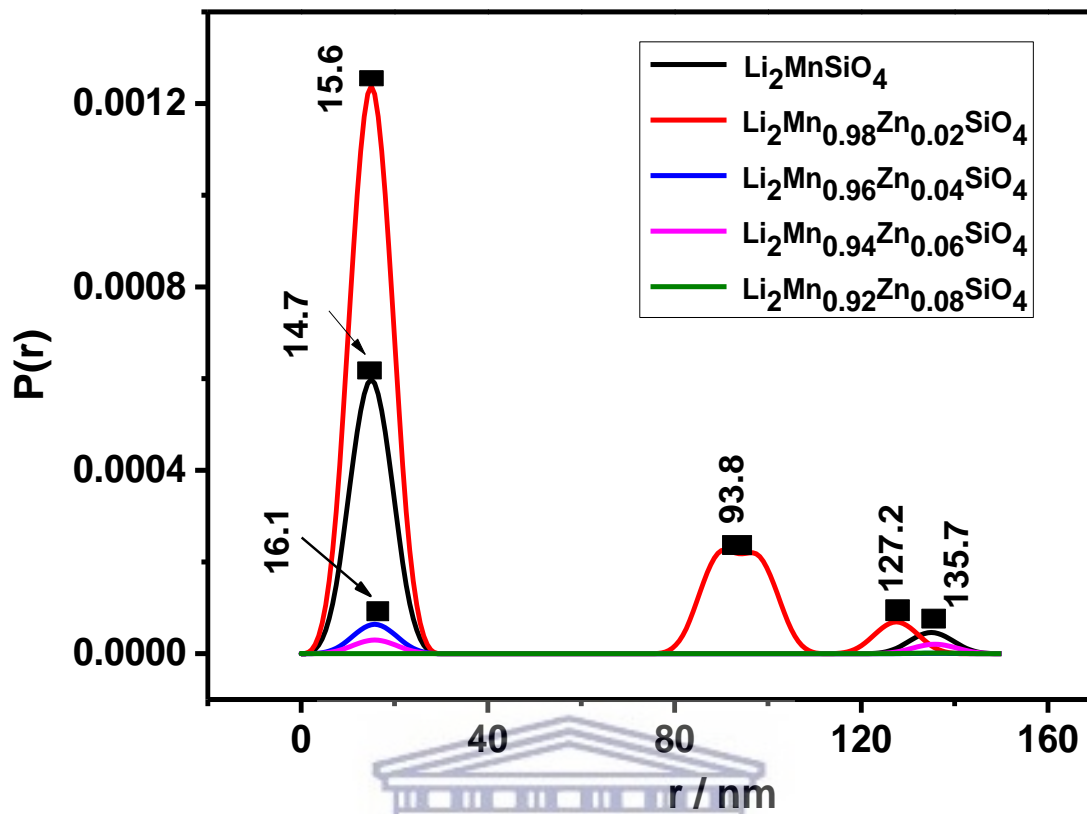


Figure 5.2 (b1): SAXS pair distance distribution functions of undoped and Zn-doped $\text{Li}_2\text{MnSiO}_4$ nanocrystals by physical volume of particles scattered

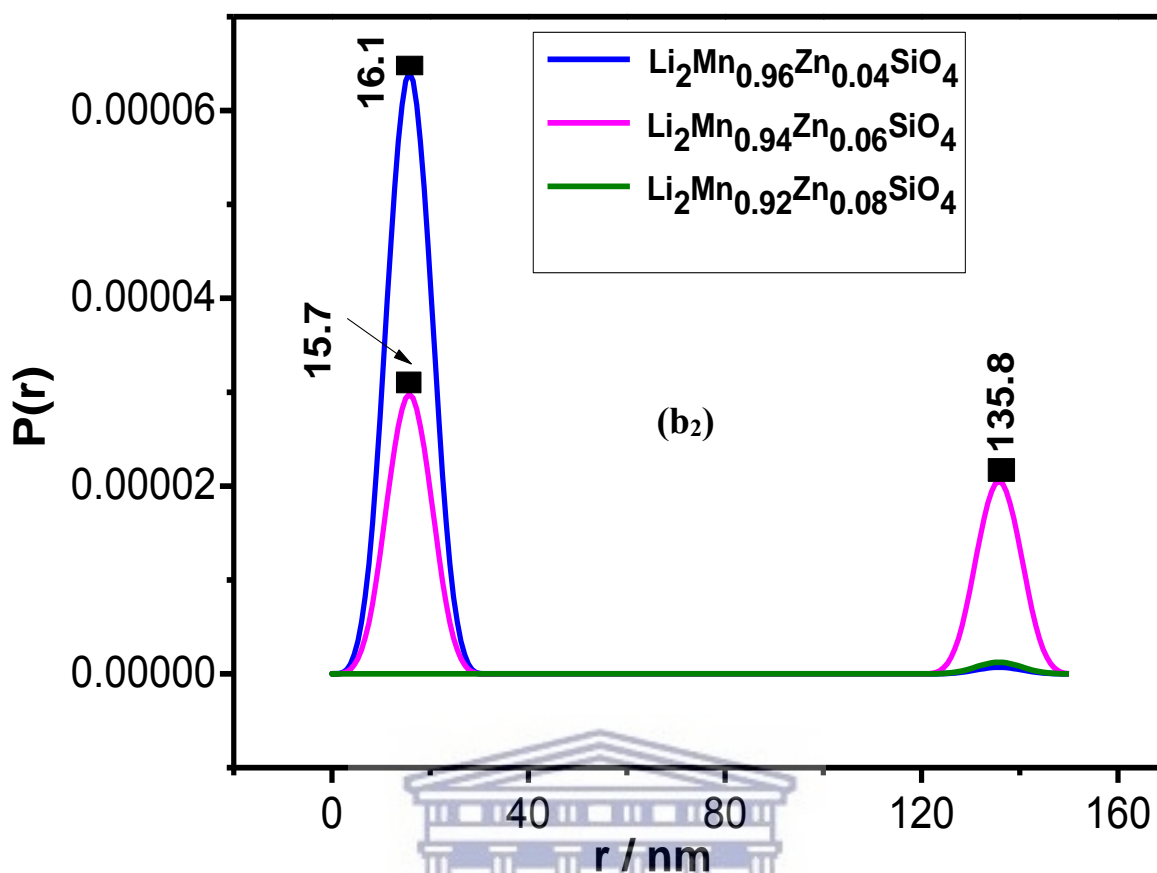


Figure 5.2 (b2): SAXS pair distance distribution functions of undoped and Zn-doped $\text{Li}_2\text{MnSiO}_4$ nanocrystals by physical volume of particles scattered (enlarged lower section of b₁)

5.3.3 Crystallography by X-ray Diffraction Studies (XRD)

5.3.3 (a) Crystal structure and phase identification

XRD was used to study the crystal structure, phase purity and interplanar spacing of undoped and Zn-doped $\text{Li}_2\text{MnSiO}_4$ nanomaterials. Figure 5.3 shows the XRD pattern of the orthosilicate-based nanomaterials at a 2θ range of $8 - 75^\circ$. All the spectra can be indexed to

the orthorhombic Pmn2₁ space group of Li₂MnSiO₄. The sharp peaks indicate the good crystalline nature of the nanomaterials. No major peaks are detected which may be associated with the zinc dopant but a shift in peak positions of the Zn-doped samples is observed. Two minor peaks appearing at 2θ values of 10.70° and 21.95° are attributed to Li₂SiO₃ and MnO impurities, which are reported to co-exist with Li₂MnSiO₄ electrode materials [32]. These results are in good agreement with literature reports by Liu and Rangappa *et al.*[33,34]. The interlayer spacing and average crystallite sizes of the orthosilicate-based materials obtained at 010 reflection are shown in Table 5.2. Crystallite sizes were calculated based on the Scherer's formula as shown in Equation 5.1 while the d-spacings were obtained according to Bragg's law [35], represented by Equation 5.2. It is surprising to note that the crystallite sizes from XRD studies are slightly bigger than those obtained from SAXS studies. This can be attributed to the differences in the scattering methods whereby SAXS uses small-angle beams as opposed to wide-angle beams used in XRD investigations. Data acquisition in SAXS studies is generally spread out over a large number of detector pixels providing a true representation of the sample under investigation. Wide-angle XRD on the other hand maps out crystallographic patterns by a limited number of pixels, thereby providing structural information based on a small sample size [36]. The interlayer spacing is observed to increase with Zn-doping from 0.90 nm for Li₂MnSiO₄ to 0.95 nm at 6 % Zn dopant ratio. This is very vital to provide a dimensional pathway for Li-ion insertion/de-insertion reactions. The electrode material at 8 % Zn-dopant ratio is an exception with a d-spacing of 0.85 nm, which may be attributed to the increase in atomic nucleation in the unit lattice.

$$D = \frac{K\lambda}{\beta \cos \theta} \quad (5.1)$$

Where D is the mean crystallite size, K , the shape factor constant (0.89), λ is the wavelength of the X-rays, β is the full width at half maximum (FWHM) of the (010) Bragg reflection, and θ is the angle of reflection of the crystalline plane.

$$n\lambda = 2d\sin\theta \quad (5.2)$$

Where, n denotes the order of diffraction ($n = 1$), λ ; the wavelength of the X-ray beam (0.154 nm), d ; the distance between MnSiO_4 and LiO_4 layers and θ is the diffraction angle.

Table 5.2: Crystallographic data of $\text{Li}_2\text{MnSiO}_4$, $\text{Li}_2\text{Mn}_{0.98}\text{Zn}_{0.02}\text{SiO}_4$, $\text{Li}_2\text{Mn}_{0.96}\text{Zn}_{0.04}\text{SiO}_4$, $\text{Li}_2\text{Mn}_{0.94}\text{Zn}_{0.06}\text{SiO}_4$, and $\text{Li}_2\text{Mn}_{0.92}\text{Zn}_{0.08}\text{SiO}_4$ electrode materials

Electrode material	Average crystallite size / nm	Interlayer spacing / nm
$\text{Li}_2\text{MnSiO}_4$	37.4	0.90
$\text{Li}_2\text{Mn}_{0.98}\text{Zn}_{0.02}\text{SiO}_4$	52.4	0.97
$\text{Li}_2\text{Mn}_{0.96}\text{Zn}_{0.04}\text{SiO}_4$	42.6	0.95
$\text{Li}_2\text{Mn}_{0.94}\text{Zn}_{0.06}\text{SiO}_4$	44.1	0.95

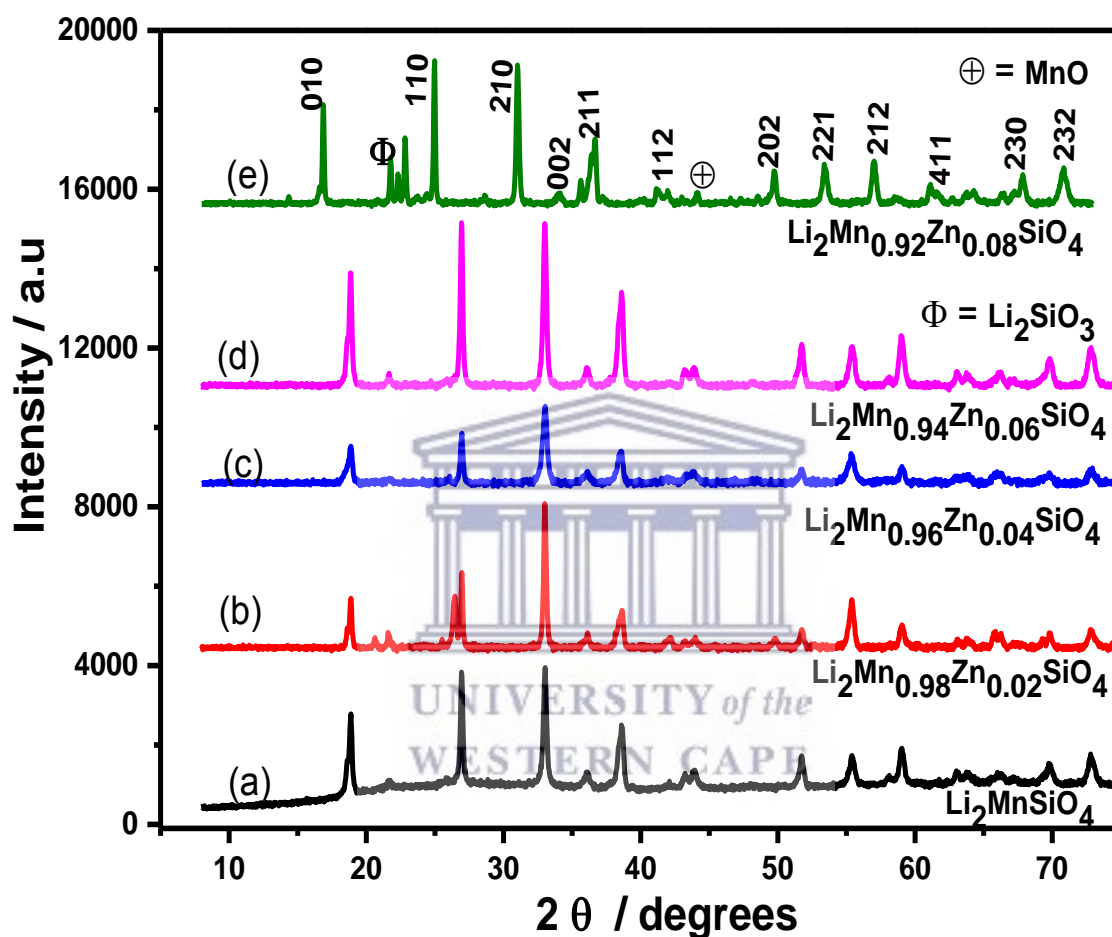


Figure 5.3: XRD spectra of $\text{Li}_2\text{MnSiO}_4$ (a), $\text{Li}_2\text{Mn}_{0.98}\text{Zn}_{0.02}\text{SiO}_4$ (b), $\text{Li}_2\text{Mn}_{0.96}\text{Zn}_{0.04}\text{SiO}_4$ (c), $\text{Li}_2\text{Mn}_{0.94}\text{Zn}_{0.06}\text{SiO}_4$ (d), and $\text{Li}_2\text{Mn}_{0.92}\text{Zn}_{0.08}\text{SiO}_4$ (e)

5.3.3 (b) Crystal structure models and atom connectivity

Crystal structure simulations to reveal atomic bonds and unit cell properties of the electrode materials were performed by a combined study involving Match and Endeavour structure solution softwares. Figure 5.4 displays the crystal structure models, unit cells and cell axes of undoped and Zn-doped $\text{Li}_2\text{MnSiO}_4$ electrode materials. As earlier mentioned, the orthosilicate-based electrode materials were all indexed to the orthorhombic $\text{Pmn}2_1$ space group which is isostructural to the low temperature form of Li_3PO_4 . The crystal structure of $\text{Li}_2\text{MnSiO}_4$ is reported to consist of infinite ridged layers of MnSiO_4 subunits which lie on the ac -plane and linked by LiO_4 tetrahedra along the b -axis. SiO_4 tetrahedra share four corners with four neighboring MO_4 tetrahedra and vice versa, within the layers of MnSiO_4 . Li ions occupy tetrahedral sites located between two of the MnSiO_4 layers, with a pathway for lithium motion to facilitating the extraction/ insertion process [37–39].

As shown by the simulated crystal structure model of $\text{Li}_2\text{MnSiO}_4$ displayed in Figure 5.4 (a), viewing along the b -plane shows primary Mn, Li and Si sites as ball (atomic spheres) lying on the ac -plane and tetrahedrally connected to oxygen atoms through thin bonds, which is similar to literature reports [38]. It is also worth noting that Li atoms are aligned in a dimensional pathway along the ac -plane, which is beneficial to facilitate movement during charge and discharge processes. Zn-doped $\text{Li}_2\text{MnSiO}_4$ electrode materials all display the same atomic arrangements observed in $\text{Li}_2\text{MnSiO}_4$ as shown in Figure 5.4 (b), (c) and (d). However, $\text{Li}_2\text{Mn}_{0.92}\text{Zn}_{0.08}\text{SiO}_4$ (8 % Zn-dopant ratio) showed some disorder in the atomic connections as displayed in Figure 5.4 (e) which may be associated with the increased nucleation/ reduction in the d -spacing observed in section 5.3.3 (a).

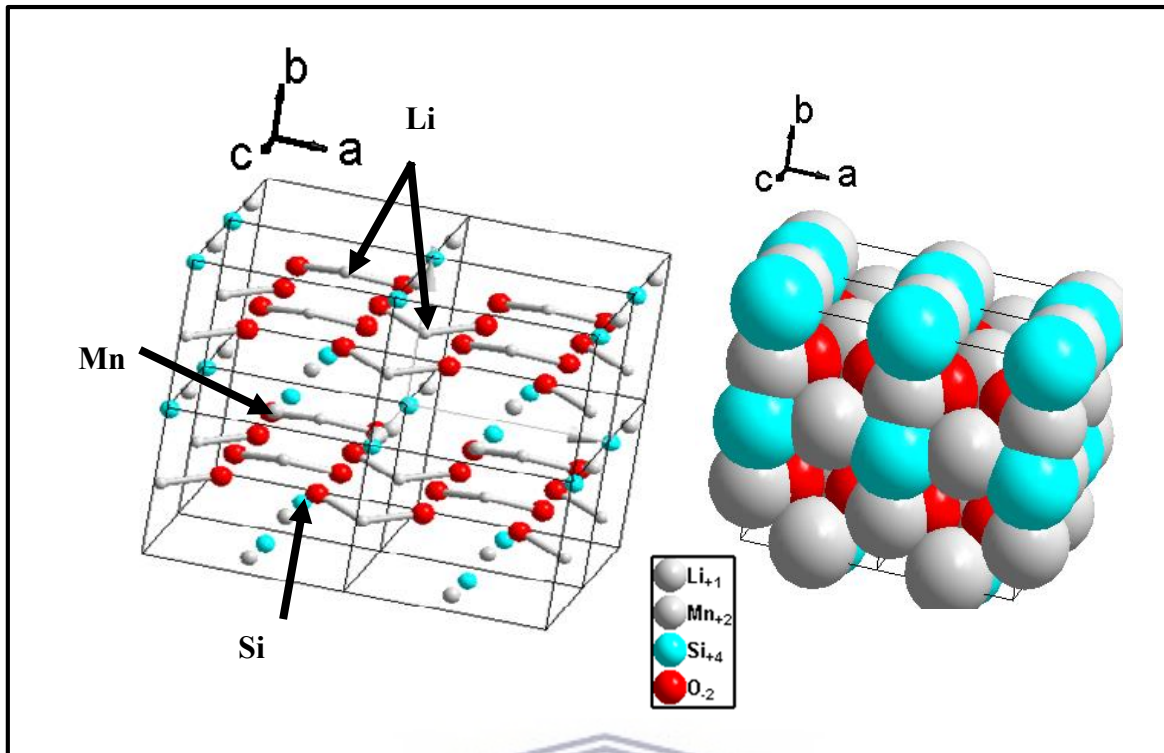


Figure 5.4 (a): Crystal structure models of $\text{Li}_2\text{MnSiO}_4$ nanocrystals

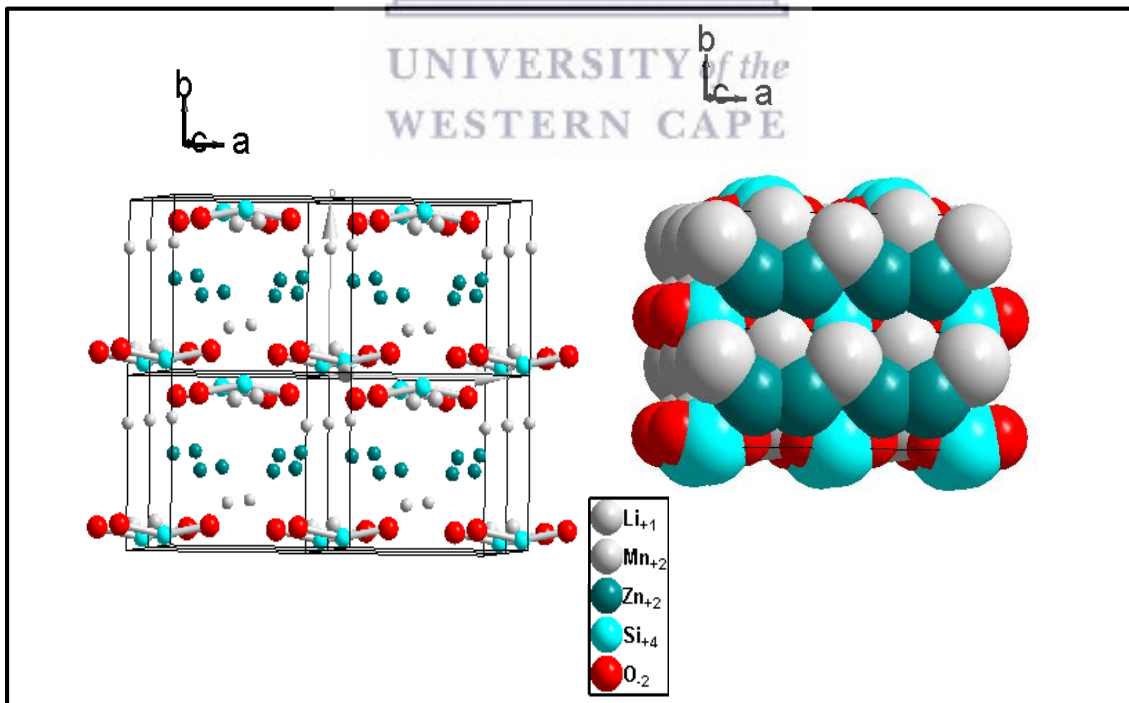


Figure 5.4 (b): Crystal structure models of $\text{Li}_2\text{Mn}_{0.98}\text{Zn}_{0.02}\text{SiO}_4$ nanocrystals

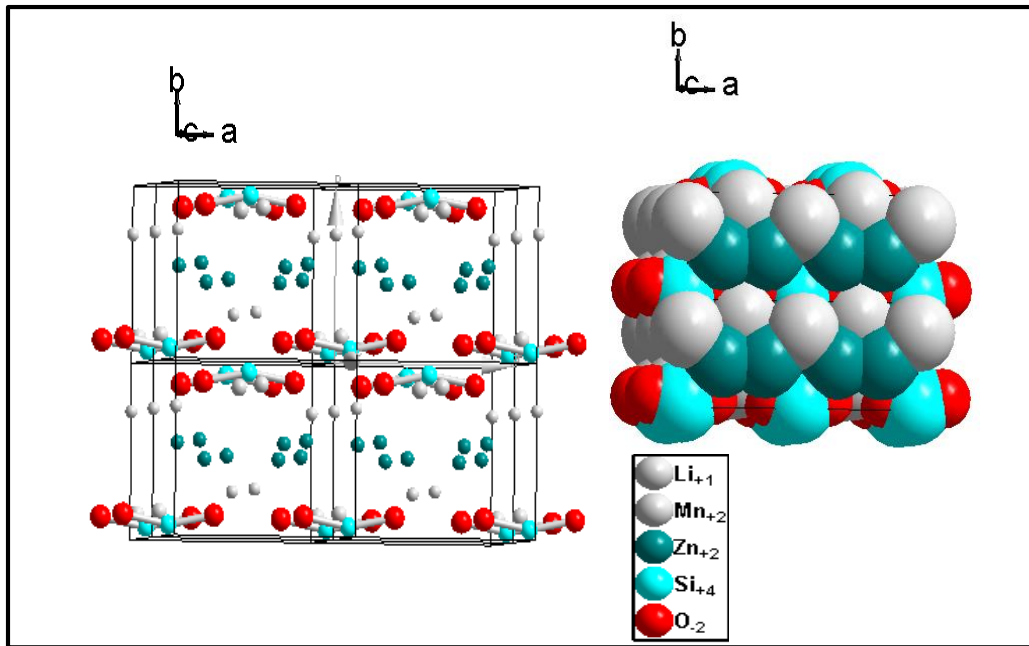


Figure 5.4 (c): Crystal structure models of $\text{Li}_2\text{Mn}_{0.96}\text{Zn}_{0.04}\text{SiO}_4$ nanocrystals

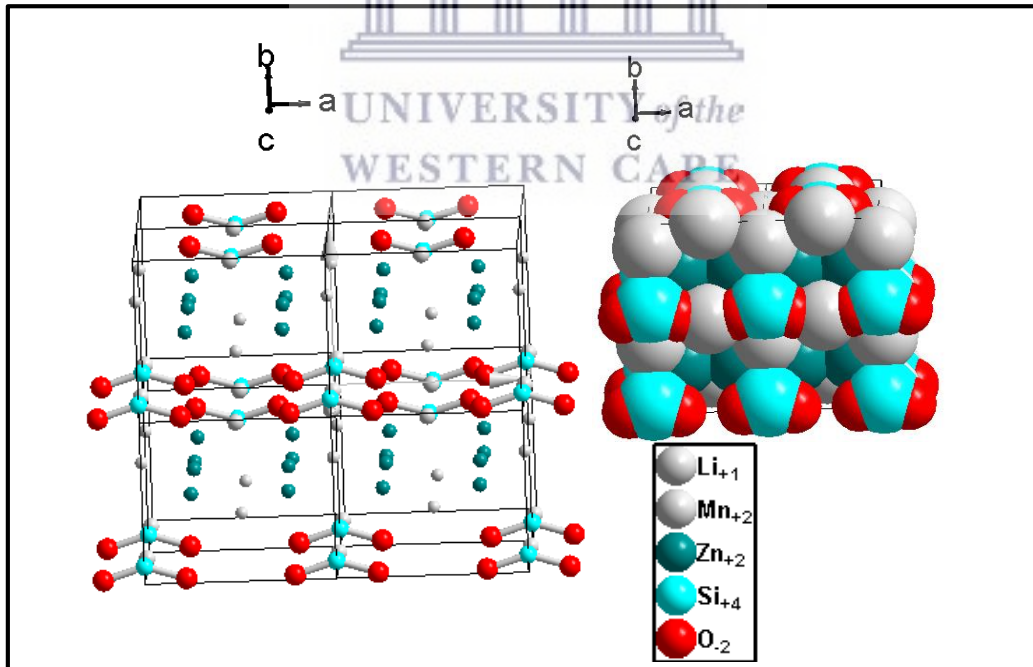


Figure 5.4 (d): Crystal structure models of $\text{Li}_2\text{Mn}_{0.94}\text{Zn}_{0.06}\text{SiO}_4$ nanocrystals

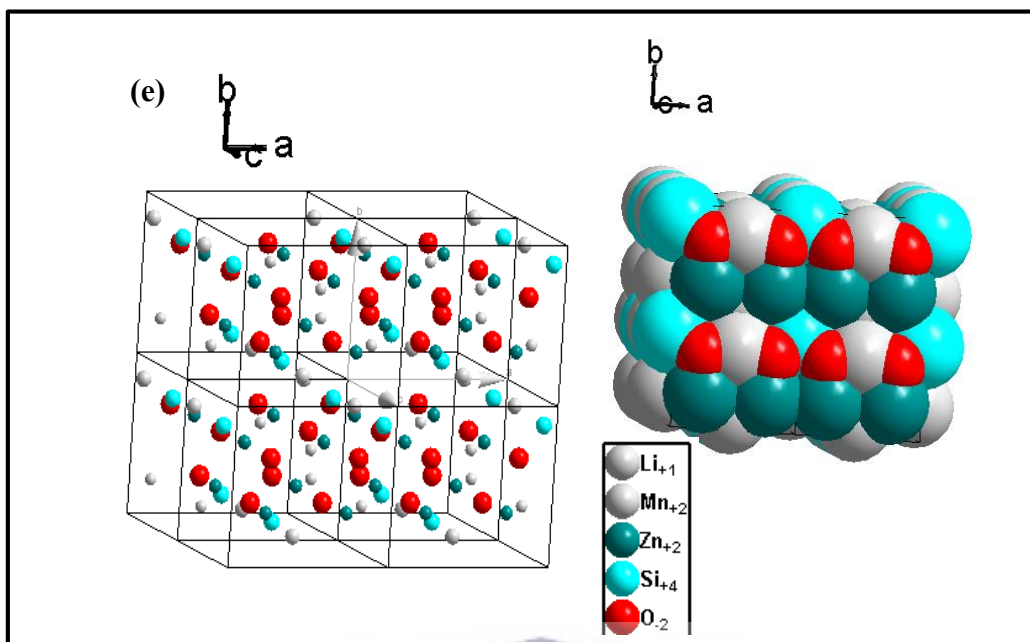


Figure 5.4 (e): Crystal structure models of $\text{Li}_2\text{Mn}_{0.92}\text{Zn}_{0.08}\text{SiO}_4$ nanocrystals



5.3.4 Functional group Analysis by Fourier transform Infrared (FTIR) Spectroscopy

FTIR spectroscopy was used to obtain more structural information on the symmetric and asymmetric vibrations/ rotations within $\text{Li}_2\text{MnSiO}_4$ and the various ratios of Zn-doped $\text{Li}_2\text{MnSiO}_4$ electrode materials. Figure 5.5 (a) and (b) presents the FTIR spectra of undoped and Zn-doped $\text{Li}_2\text{MnSiO}_4$ materials and an enlarge spectrum of $\text{Li}_2\text{MnSiO}_4$ with 4 % Zn doping. The vibrational peaks in the region of 400 cm^{-1} - 1100 cm^{-1} are in agreement with those reported for $\text{Li}_2\text{MnSiO}_4$ [40,41]. Bands appearing at 1073 cm^{-1} and around $750 - 590\text{ cm}^{-1}$ can be assigned to the asymmetric and symmetric vibrations of Si-O-Si bonds in the silicate tetrahedra (SiO_4^{4-}). The band at 850 cm^{-1} can be assigned to the vibration of the Si-O-Mn

linkage, thus confirming the complete incorporation of Mn ions into the Si-O framework. The vibrational peaks around 540- 420 cm^{-1} correspond to stretching motion of $[\text{LiO}_4]$ tetrahedron. Additionally, the blue shift in the position of the Si-O-Mn bond as well as a reduction of its intensity in the Zn-doped materials confirm the insertion of Zn ions into the Mn site.

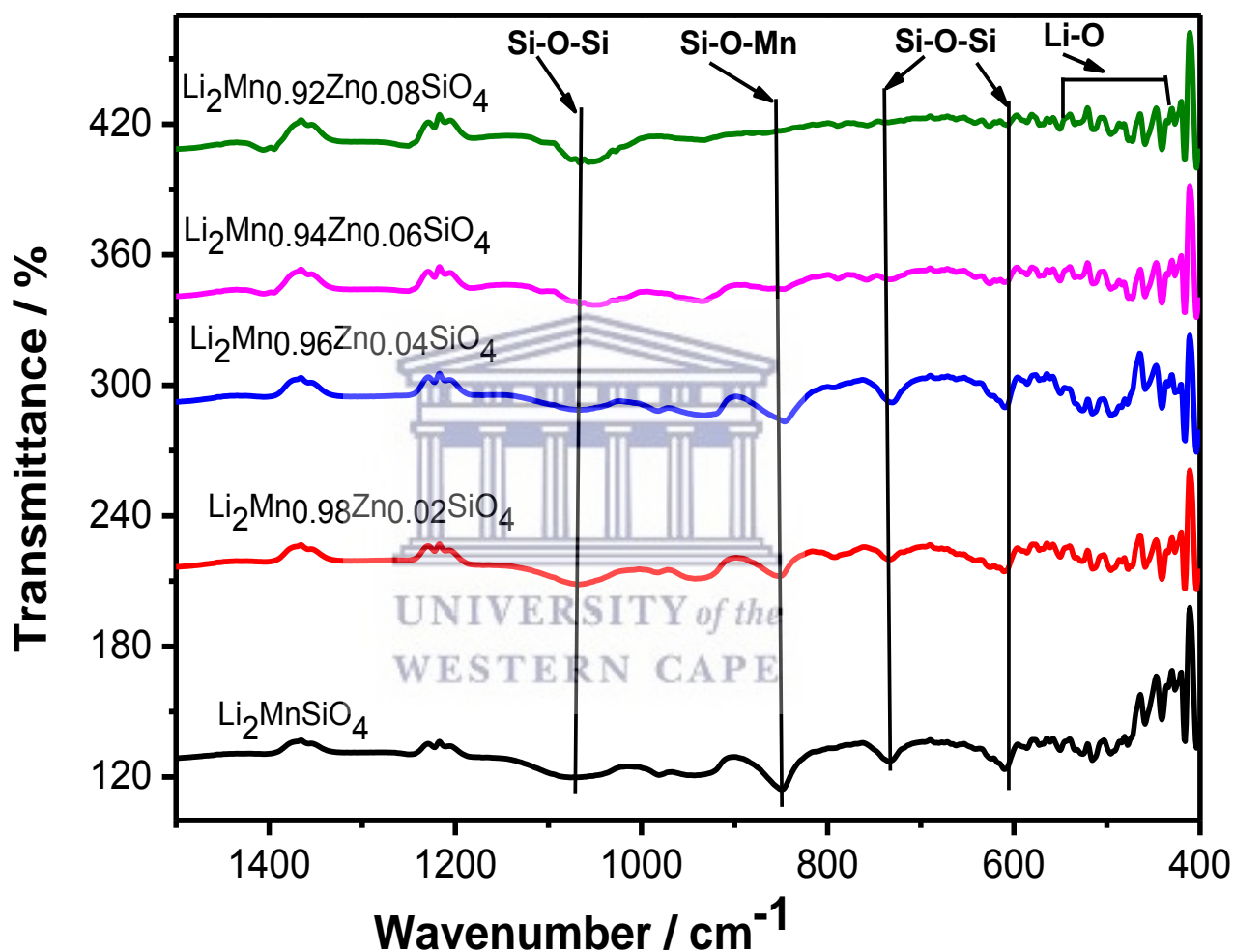


Figure 5.5 (a): FTIR spectra of undoped and Zn-doped $\text{Li}_2\text{MnSiO}_4$ electrode materials

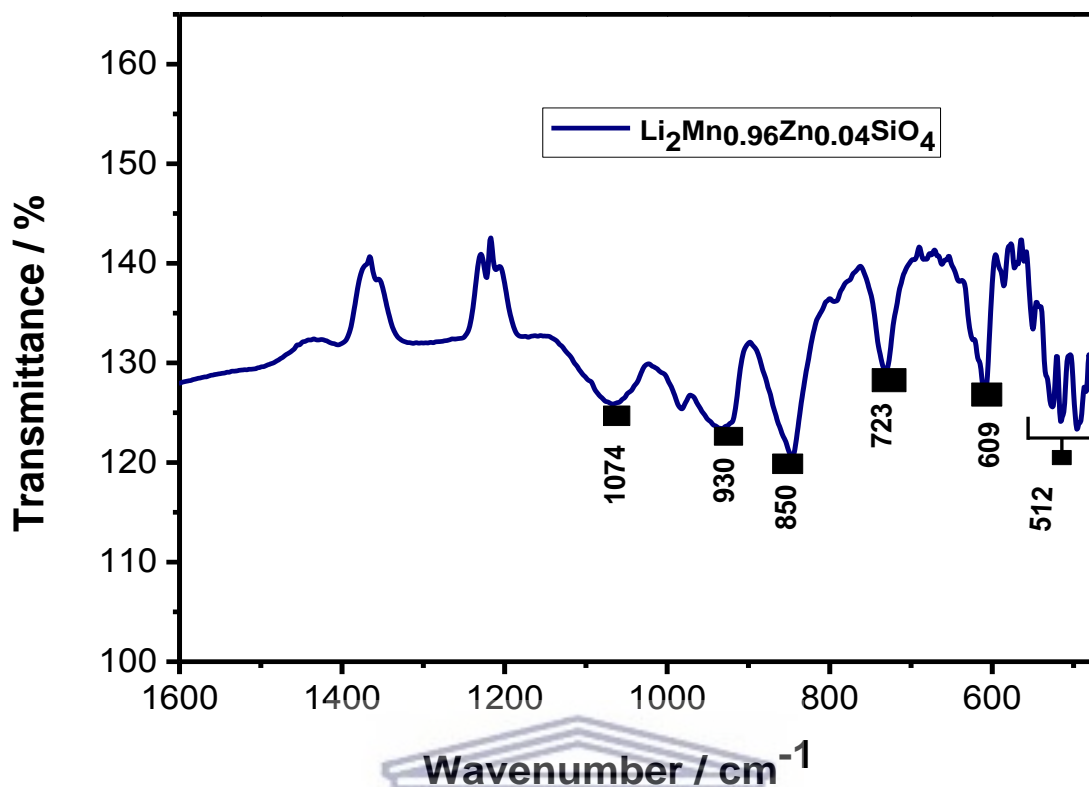


Figure 5.5 (b): FTIR spectrum of $\text{Li}_2\text{Mn}_{0.96}\text{Zn}_{0.04}\text{SiO}_4$ nanocrystals

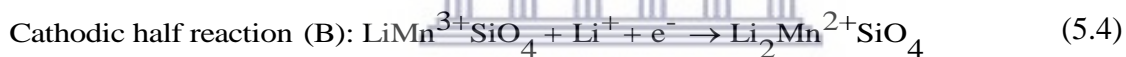
5.3.5 (a) Electrochemical characterization

Electrochemical properties of undoped and Zn-doped $\text{Li}_2\text{MnSiO}_4$ electrode materials were investigated using cyclic voltammetry (CV), electrochemical impedance spectroscopy (EIS) and galvanostatic charge-discharge experiments in 1 M sodium sulfate (Na_2SO_4) aqueous electrolyte.

i) Cyclic Voltammetric (CV) studies

CV studies were conducted at a potential window of 0.1 – 0.8 V at scan rates of 10 – 150 mV s^{-1} to determine the redox behavior of the electro-active species and the energy storage mechanism occurring in undoped and Zn-doped $\text{Li}_2\text{MnSiO}_4$ electrode materials. Figure 5.6 (a)

shows a comparative CV plot of the materials at a scan rate of 50 mV s⁻¹. As observed, the CV curves present peak-shaped voltammograms which is characteristic of battery –type materials [42]. These materials are reported to exhibit Nernstian processes with non-capacitive faradaic charge storage mechanism [43,44]. The Nernstian processes governing Li⁺ ion insertion and de-insertion in these materials are illustrated by Equations 5.3 and 5.4, respectively. Equation 5.3 describes the removal of Li⁺ ions from the orthosilicate lattice with associated oxidation of Mn²⁺ to Mn³⁺ ions. While Equation 5.4 represents the insertion of Li⁺ ions into the LiMnSiO₄ framework with the concomitant reduction of Mn³⁺ to Mn²⁺ ions [35].



The redox properties of undoped and Zn-doped Li₂MnSiO₄ electrode nanomaterials are outlined in Table 5.3. An increase in peak cathodic and anodic currents illustrated by the Zn doped counterparts especially that of 4 % Zn dopant ratio (Li₂Mn_{0.96}Zn_{0.04}SiO₄) depicts better electrochemical performance. It is observed that the CV profiles exhibit a peak-to-peak separation (ΔE_p) larger than the 57 mV predicted for an electrochemically reversible one-electron redox couple. A quasi-reversible electron transfer process is therefore exhibited by these materials due to their comparatively slow kinetics and peak overlapping with increase in scan rate as shown in Figure 5.6 (b) [45,46]. The specific capacity values reported in Table 5.3

were calculated from the CV profiles according to Equation 5.6 by integrating the area under the CV curves [47].

$$C_{sp} = \frac{1}{2} \int \frac{I.dV}{mv} \quad (5.6)$$

Where I represents the current, V is the potential window, v is the scan rate and m is the active electrode mass. The higher specific capacity values obtained for the Zn-doped electrodes especially that of 4 % Zn ratio ($\text{Li}_2\text{Mn}_{0.96}\text{Zn}_{0.04}\text{SiO}_4$) may be attributed to the high nucleation density observed in XRD investigations and well-defined rhombohedra nanostructures obtained from morphological characterization. These vital features provided a larger surface area, more available sites for electrolyte penetration and faster diffusion of Li-ions, leading to high energy storage performance.

The scan rate is known to control how fast the applied potential is scanned. A faster scan rate will lead to a decrease in the size of the diffusion layer; resulting in higher currents as observed in Figure 5.6 (b) [45]. Figure 5.6 (c) displays the linear relationship between the peak current and the square root of the scan rate indicating a diffusion controlled process, which is usually governed by the Randles-Sevcik equation (Equation 5.7).

$$I_{pa} = 2.69 \times 10^5 \text{ n}^{3/2} \text{ A D}_{Li}^{1/2} \text{ C v}^{1/2} \quad (5.7)$$

Where n represents the number of electrons transferred in the redox process, A (cm^2) is the area of the electrode, D_{Li} ($\text{cm}^2 \text{s}^{-1}$) is the diffusion coefficient of Li^+ , C (mol cm^{-3}) is the bulk analyte concentration, and ν (V s^{-1}) is the rate at which the potential is scanned.

The variation of specific capacity with scan rate of $\text{Li}_2\text{Mn}_{0.96}\text{Zn}_{0.04}\text{SiO}_4$ electrode material is displayed in Figure 5.6 (d). As expected, the specific capacity decreases with increasing scan rate due to the fact that only a limited diffusion layer is available for redox activity at higher scan rates [45]. The $\text{Li}_2\text{Mn}_{0.96}\text{Zn}_{0.04}\text{SiO}_4$ majority rhombohedra electrode delivers a specific capacity of 110.7 C g^{-1} at a scan rate of 10 mV s^{-1} and maintains a specific capacity of 38.1 C g^{-1} at a scan rate of 150 mV s^{-1} , thus ascertaining the noticeable electrochemical performance of $\text{Li}_2\text{Mn}_{0.96}\text{Zn}_{0.04}\text{SiO}_4$ electrode material.



Table 5.3: Redox and charge storage properties of undoped and Zn-doped $\text{Li}_2\text{MnSiO}_4$ electrode materials obtained from CV investigations

Electrode material	E_{pa} / V	E_{pc} / V	$I_{\text{pa}} / \mu\text{A}$	$I_{\text{pc}} / \mu\text{A}$	$\Delta E_{\text{p}} / \text{V}$	E^0 / V	$C_{\text{sp}} / \text{C g}^{-1}$
$\text{Li}_2\text{MnSiO}_4$	0.54	0.39	4.84	-5.63	0.15	0.47	29.42
$\text{Li}_2\text{Mn}_{0.98}\text{Zn}_{0.02}\text{SiO}_4$	0.60	0.32	13.2	-5.99	0.28	0.46	71.42
$\text{Li}_2\text{Mn}_{0.94}\text{Zn}_{0.04}\text{SiO}_4$	0.62	0.33	23.4	-1.31	0.29	0.48	80.46
$\text{Li}_2\text{Mn}_{0.92}\text{Zn}_{0.08}\text{SiO}_4$	0.60	0.36	10.9	3.93	0.24	0.48	10.05
$\text{Li}_2\text{Mn}_{0.90}\text{Zn}_{0.1}\text{SiO}_4$	0.52	0.35	15.9	-1.34	0.17	0.44	64.07

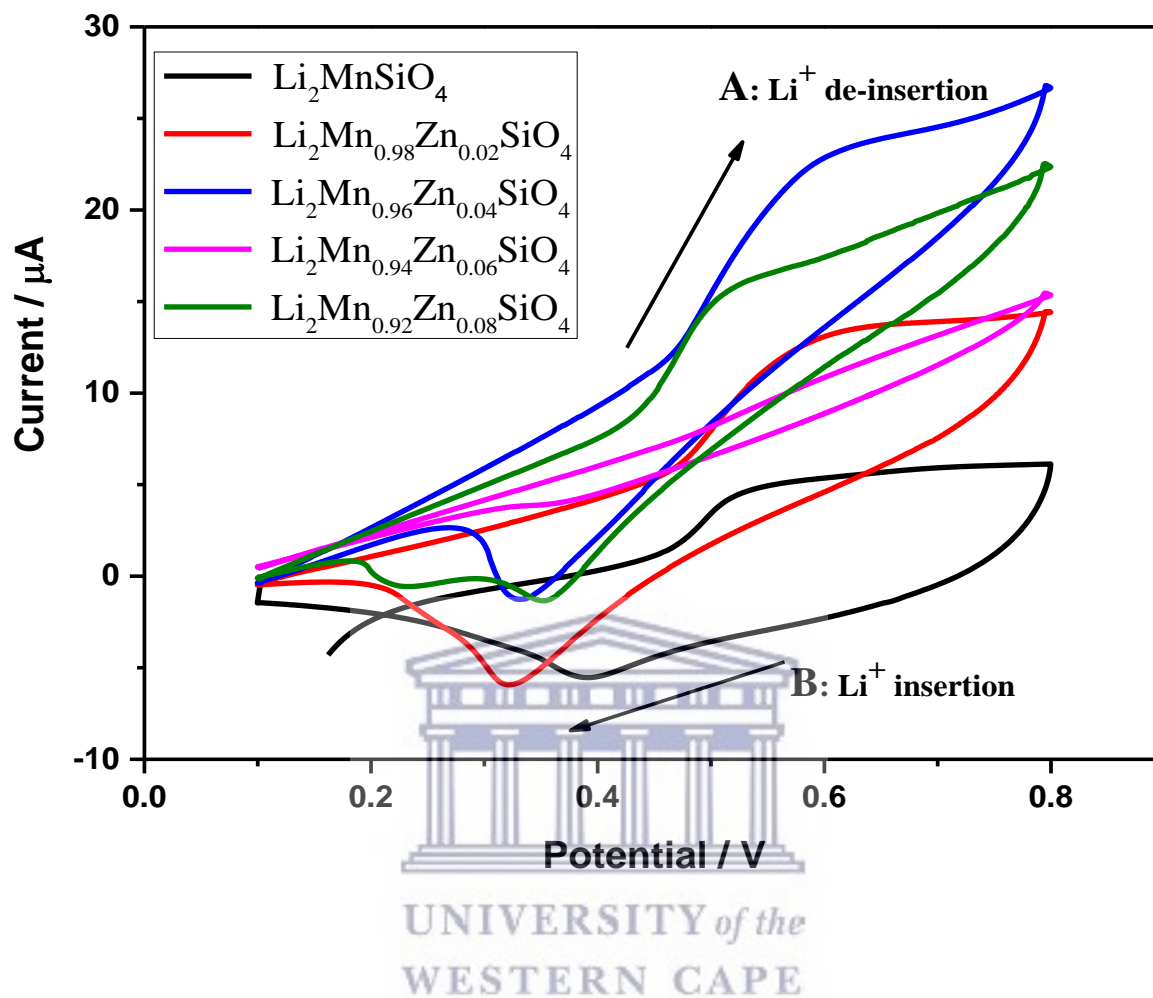


Figure 5.6 (a): Comparative CV curves of pure and Zn-doped $\text{Li}_2\text{MnSiO}_4$ nanomaterials at a scan rate of 50 mV s^{-1} in 1 M sodium sulfate (Na_2SO_4) aqueous electrolyte

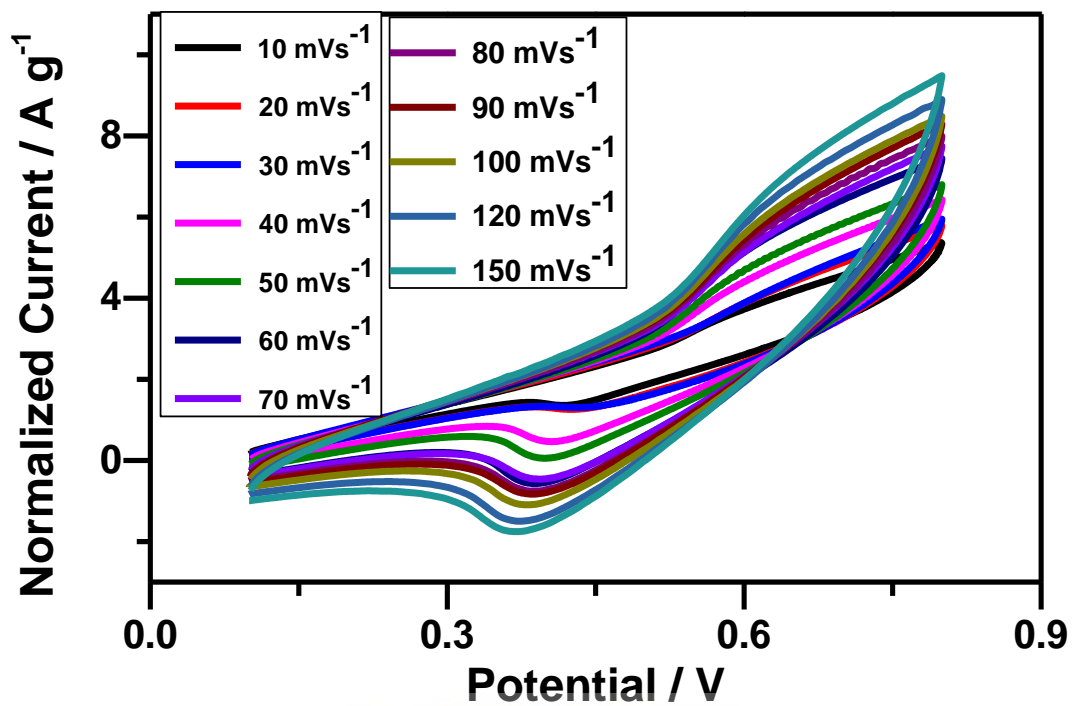


Figure 5.6 (b): CV curves of $\text{Li}_2\text{Mn}_{0.96}\text{Zn}_{0.04}\text{SiO}_4$ at scan rates of $10 - 150 \text{ mV s}^{-1}$ in 1 M sodium sulfate (Na_2SO_4) aqueous electrolyte



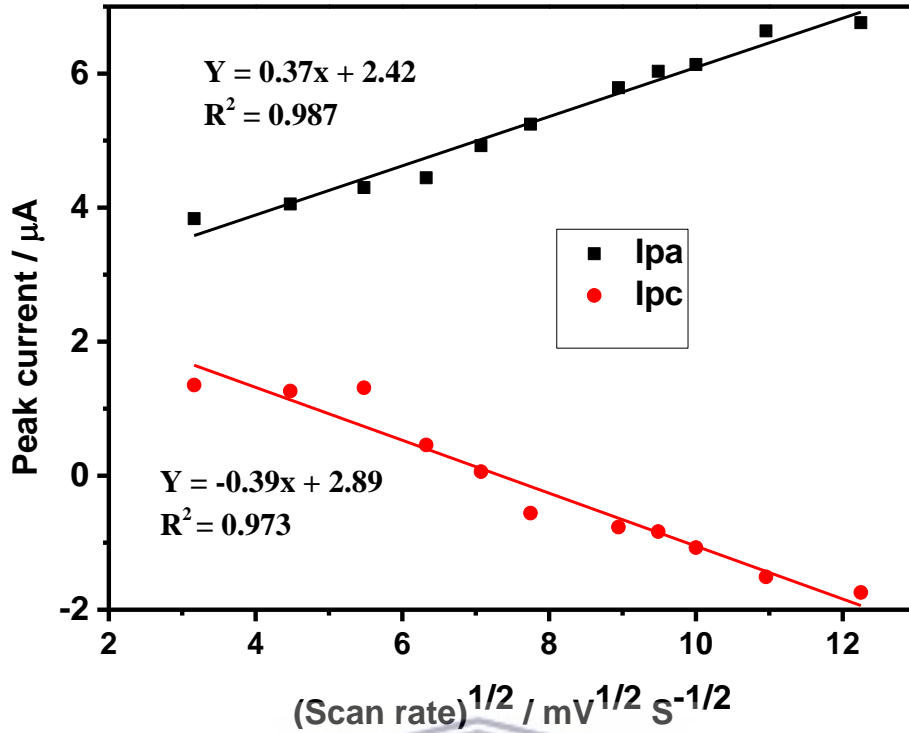


Figure 5.6 (c): Linear relationship between the peak current (I_{pa} and I_{pc}) versus the square root of the scan rate of $\text{Li}_2\text{Mn}_{0.96}\text{Zn}_{0.04}\text{SiO}_4$ electrode material

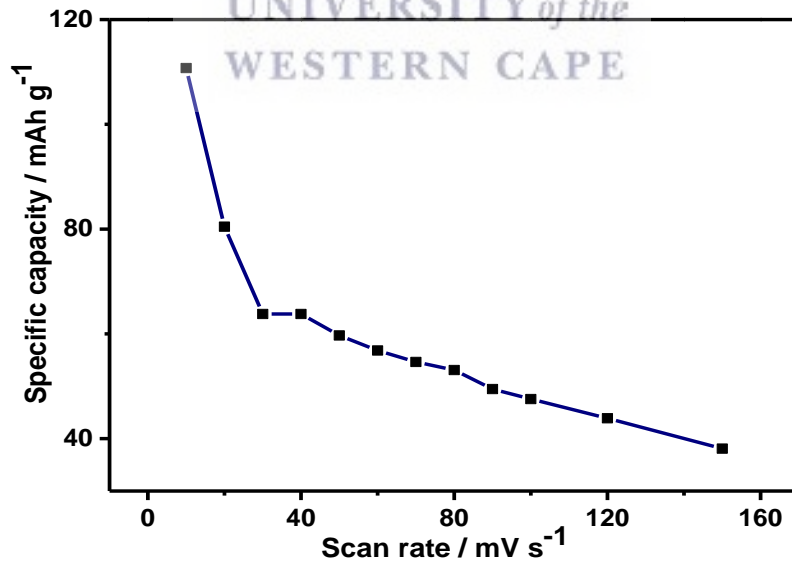


Figure 5.6 (d): Variation of specific capacity with scan rate of $\text{Li}_2\text{Mn}_{0.96}\text{Zn}_{0.04}\text{SiO}_4$ electrode material in 1 M sodium sulfate (Na_2SO_4) aqueous electrolyte at a potential window of 0.1 – 0.8 V

ii) Electrochemical impedance spectroscopic (EIS) measurements

EIS studies were further conducted to elucidate the kinetic and diffusive properties occurring at the electrode/electrolyte interfaces of the orthosilicate-based electrode materials. The measurements were recorded at open circuit voltage (OCV) in the frequency range of 0.1 MHz to 100 KHz at an amplitude of 5 mV. Figure 5.7 (a) shows the Nyquist plots of undoped and Zn-doped $\text{Li}_2\text{MnSiO}_4$ electrode materials. The non-capacitive faradaic charge storage mechanism observed in CV studies is further confirmed by the deviation of the Nyquist curves from being perpendicular to the Z_{re} axis. This is ascribed to the fact that capacitive materials exhibit Nyquist curves parallel to the Z_{img} axis and perpendicular to the Z_{re} axis [47]. The curves present a semi-circle (more pronounced in the pure $\text{Li}_2\text{MnSiO}_4$ electrode) at the high frequency domain which describes the charge transfer resistance (R_{ct}) in the materials. An inclined line observed at the middle to low frequency region is ascribed to the frequency dependent Warburg diffusion (W_o) of Li-ions in the bulk of the electrode materials. Z-view software was used in EIS curve fitting using the circuit models shown in Figure 5.7 (b). Values obtained for the solution resistance (R_s), constant phase element (CPE), Warburg diffusion (W_o), R_{ct} and phase angle for pure and Zn-doped $\text{Li}_2\text{MnSiO}_4$ electrodes are outlined in Table 5.4. It is observed that R_{ct} values increased with Zn doping except for the $\text{Li}_2\text{Mn}_{0.96}\text{Zn}_{0.04}\text{SiO}_4$ (Zn doping ratio of 4 %) electrode which has demonstrated superior performance in CV investigations and also showed an almost uniform particle size distribution. As shown in Figure 5.7 (c), it is worth noting that the electrode materials portray a near-semiconductor and semiconductor properties with phase angles ranging from $38.8 - 54.2^\circ$, which will enable faster movement of Li-ions and electrons resulting in high electrochemical performance. Zn-doped $\text{Li}_2\text{MnSiO}_4$ electrode materials show higher phase angles over the pristine $\text{Li}_2\text{MnSiO}_4$ electrode materials indicating that Zn doping modified the electrical properties of pure $\text{Li}_2\text{MnSiO}_4$ electrode [25]. The double

layer capacitance contributions of the materials towards the total energy storage mechanism of the materials are shown by the *CPE* values with pure $\text{Li}_2\text{MnSiO}_4$ having maximum at $0.73 \mu\text{F}$ and minimum shown by $\text{Li}_2\text{Mn}_{0.96}\text{Zn}_{0.04}\text{SiO}_4$ to be $0.58 \mu\text{F}$.

Table 5.4: EIS curve fitting data of pure and Zn-doped $\text{Li}_2\text{MnSiO}_4$ electrode materials

Electrode material	R_s / Ω	$CPE / \mu\text{F}$	R_{ct} / Ω	$W_o / \Omega \text{ s}^{-1/2}$	Phase angle / °
$\text{Li}_2\text{MnSiO}_4$	1.81	0.73	17.03	0.68	38.8
$\text{Li}_2\text{Mn}_{0.98}\text{Zn}_{0.02}\text{SiO}_4$	4.75	0.67	177.7	-	46.8
$\text{Li}_2\text{Mn}_{0.96}\text{Zn}_{0.04}\text{SiO}_4$	2.78	0.58	89.7	-	39.2
$\text{Li}_2\text{Mn}_{0.94}\text{Zn}_{0.06}\text{SiO}_4$	7.12	0.63	495	-	54.2
$\text{Li}_2\text{Mn}_{0.92}\text{Zn}_{0.08}\text{SiO}_4$	1.269	0.74	392.7	-	52.1

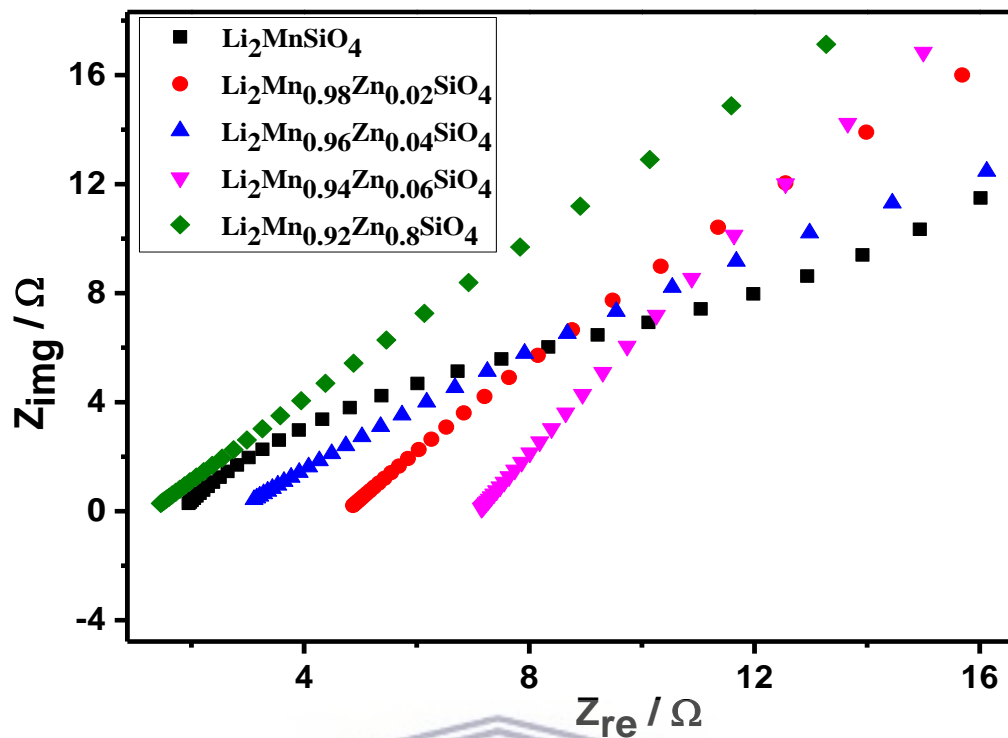


Figure 5.7 (a): Nyquist plots of pure and Zn-doped $\text{Li}_2\text{MnSiO}_4$ electrode materials

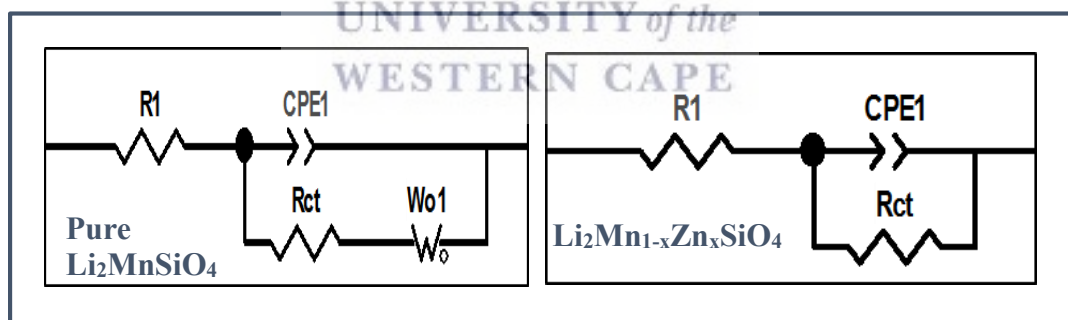


Figure 5.7 (b): Circuit models used to fit EIS data of pure and Zn-doped $\text{Li}_2\text{MnSiO}_4$ electrode

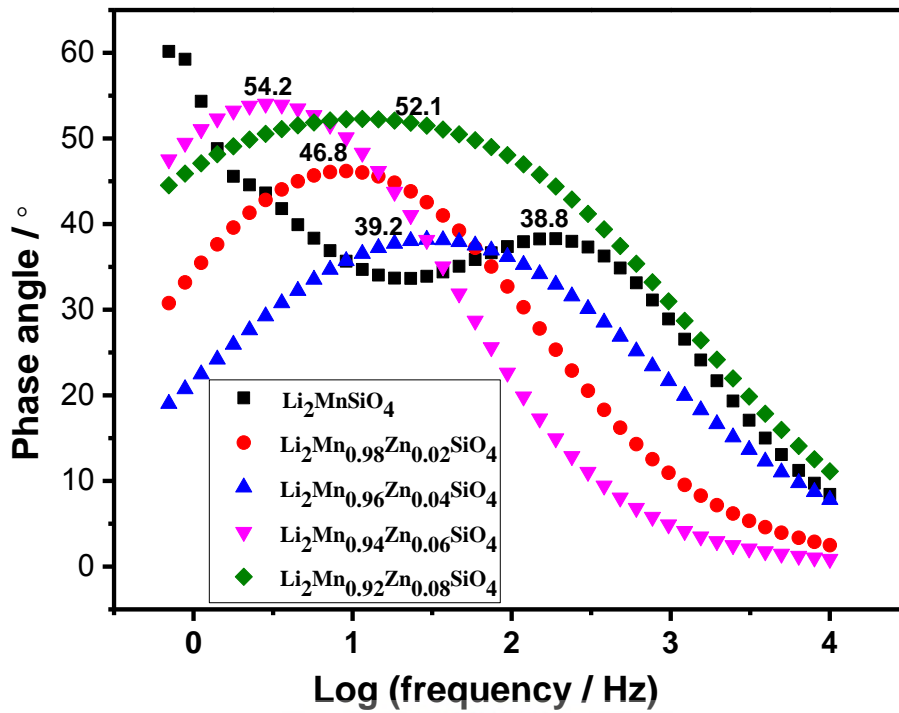


Figure 5.7 (c): Phase angle Bode plots of pure and Zn-doped $\text{Li}_2\text{MnSiO}_4$ electrodes

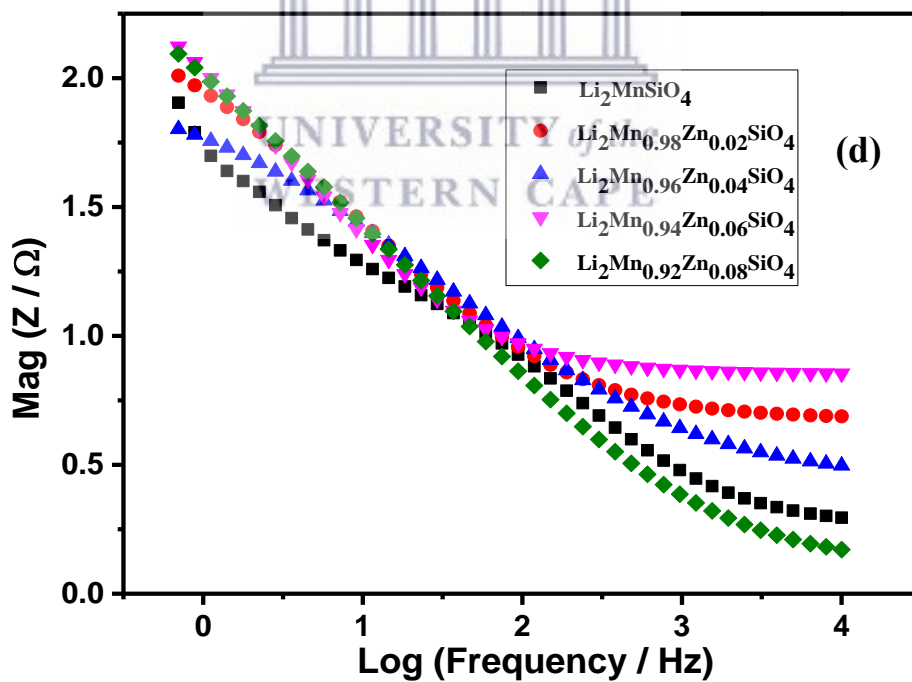


Figure 5.7 (d): Total impedance Bode plots of pure and Zn-doped $\text{Li}_2\text{MnSiO}_4$ electrode materials

5.3.5 (b) Electrochemical Performance of the fabricated supercapattery devices

The practical energy storage applications of pure and Zn-doped $\text{Li}_2\text{MnSiO}_4$ electrode materials were investigated by fabricating aqueous supercapattery devices using the orthosilicate-based materials as positive electrodes and activated carbon as the negative electrode. Studies were performed in 1 M Na_2SO_4 aqueous electrolyte at a voltage window of 1.6 V. Due to electrochemical performance in three electrode cells, only three Zn-doped $\text{Li}_2\text{MnSiO}_4$ samples (2 %, 4 % and 8 %) and pure $\text{Li}_2\text{MnSiO}_4$ were further investigated for supercapattery applications.

i) Cyclic Voltammetric studies of supercapattery devices

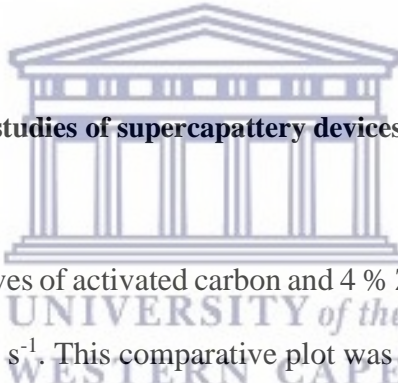


Figure 5.8 (a) shows the CV curves of activated carbon and 4 % Zn-doped $\text{Li}_2\text{MnSiO}_4$ electrode material at a scan rate of 50 mV s^{-1} . This comparative plot was used to ascertain the use of the orthosilicate-based electrode as the positive electrode and activated carbon as the negative electrodes and the voltage window of the supercapattery devices. The activated carbon electrode exhibited capacitive behavior in the potential window of $-0.8 - 0.1 \text{ V}$ due to the physical electrostatic adsorption of ions at the interface between electrode and electrolyte [48]. Meanwhile the orthosilicate-based electrodes showed well defined peak-shaped battery-like character in the potential range of $0.1 - 0.8 \text{ V}$. A voltage window of 1.6 V was therefore achieved for the supercapattery cells as shown in Figure 5.8 (b).

To achieve optimum capacitive performance of the supercapattery devices, the balance of the masses as well as the charges of the positive and negative electrodes is very important. In order

to keep the charges flowing through both electrodes, the masses of both electrodes must be adjusted accordingly. The mass loading of the positive and negative electrodes were adjusted according to the mass-charge balance equation, Equation 5.8 [49].

$$\frac{M^+}{M^-} = \left(\frac{C_{sp}^-}{C_{sp}^+} \right) \left(\frac{\Delta V^-}{\Delta V^+} \right) \quad (5.8)$$

Where, M , C_{sp} and ΔV denote the active mass, specific capacitance and the potential window obtained from the half cells, respectively. The mass loading of AC//Li₂MnSiO₄ supercapattery device was adjusted to 11.97 mg, while those of AC//Li₂Mn_{0.98}Zn_{0.02}SiO₄, AC//Li₂Mn_{0.96}Zn_{0.04}SiO₄ and AC//Li₂Mn_{0.92}Zn_{0.08}SiO₄ devices were at 15.40 mg, 14.07 mg and 11.41 mg, respectively.

Figure 5.8 (b) depicts CV curves of activated carbon with pure/Zn-doped Li₂MnSiO₄ supercapatteries. The devices present quasi-rectangular-shaped voltammograms which indicate the prevailing pseudo-capacitance response in the devices as opposed to the purely battery behavior (well defined peak-shaped CVs) observed in the three electrode cells [43]. An increase in the normalized current output of the 4 % Zn-doped Li₂MnSiO₄ device (AC//Li₂Mn_{0.96}Zn_{0.04}SiO₄) reveals a significant increase in the specific capacitance as well as a higher electrochemical performance over pure Li₂MnSiO₄, 2 % and 8 % Zn-doped Li₂MnSiO₄ devices.

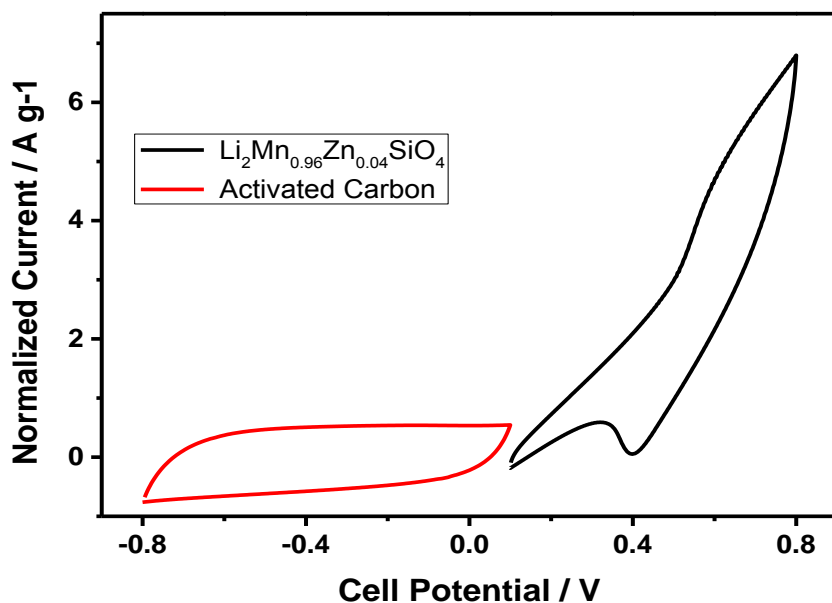


Figure 5.8 (a): CV curves of activated carbon and $\text{Li}_2\text{Mn}_{0.96}\text{Zn}_{0.04}\text{SiO}_4$ at a scan rate of 50 mV s^{-1} in $1 \text{ M Na}_2\text{SO}_4$ aqueous electrolyte

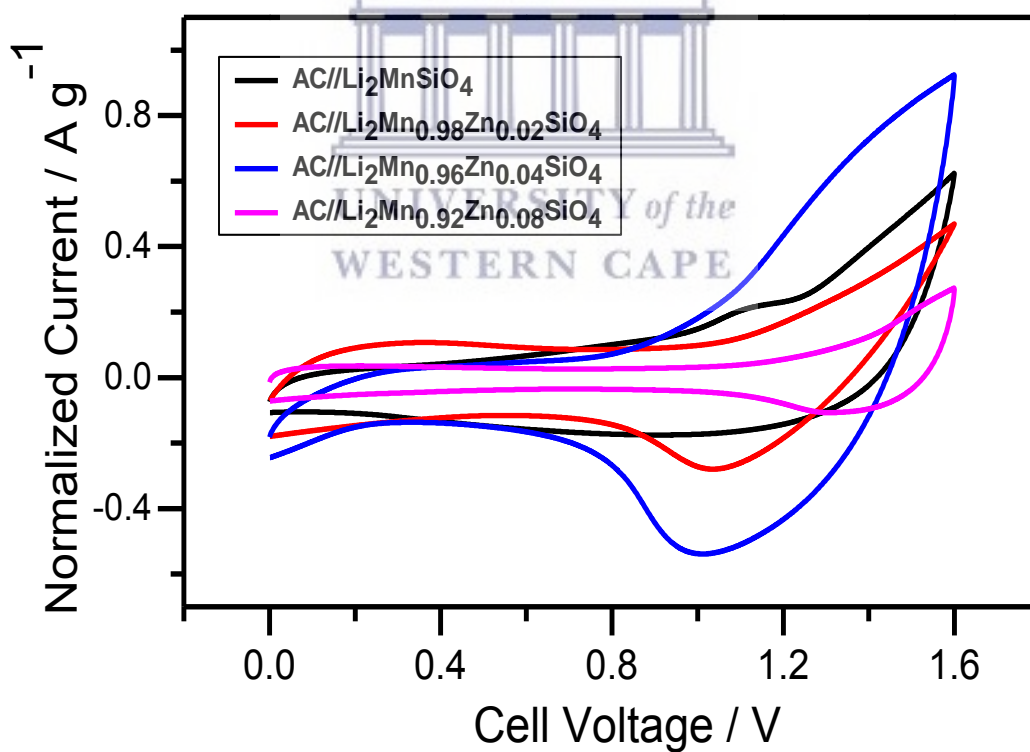


Figure 5.8 (b): CV curves of AC//Li₂MnSiO₄ and AC// Li₂Mn_{1-x}Zn_xSiO₄ supercapattery devices in $1 \text{ M Na}_2\text{SO}_4$ aqueous electrolyte at a potential window of $0.1 - 0.8 \text{ V}$

ii) Galvanostatic charge-discharge (GCD) studies of supercapattery devices

Figure 5.9 (a) displays the GCD profiles of pure and Zn-doped $\text{Li}_2\text{MnSiO}_4$ supercapattery devices with activated carbon at a current load of 0.1 A g^{-1} and a cell voltage of 1.6 V. Quasi-triangular GCD curves are observed which are consistent with the CV profiles. The slight deviation of potential plateaus observed in majority battery behavior and non-linear nature of the GCD profiles indicates that the devices exhibit hybrid (battery-capacitive) charge storage [35,50]. The specific capacitance of the various devices were calculated based on the total mass of the two electrodes according to Equation 5.9 [35].

$$C_{\text{sp}} = \frac{4I}{m \Delta V / \Delta t} \quad (5.9)$$

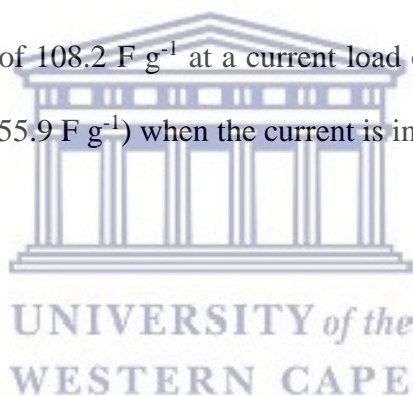


Where I is the applied current (A), m is the total mass of positive and negative electrodes (g), ΔV is the voltage window (V) and Δt is the discharge time (s)

The AC// $\text{Li}_2\text{Mn}_{0.96}\text{Zn}_{0.04}\text{SiO}_4$ supercapattery device delivered a high specific capacitance of 108.2 F g^{-1} which is almost twice that of the AC// $\text{Li}_2\text{MnSiO}_4$ device at 59.8 F g^{-1} and AC// $\text{Li}_2\text{Mn}_{0.98}\text{Zn}_{0.02}\text{SiO}_4$ at 52.3 F g^{-1} and about five times higher than the AC// $\text{Li}_2\text{Mn}_{0.92}\text{Zn}_{0.08}\text{SiO}_4$ device at 23.98 F g^{-1} . The higher specific capacitance observed in the AC// $\text{Li}_2\text{Mn}_{0.96}\text{Zn}_{0.04}\text{SiO}_4$ supercapattery can be attributed to the significant change in the morphology of the $\text{Li}_2\text{Mn}_{0.96}\text{Zn}_{0.04}\text{SiO}_4$ electrode material and a pillar effect of Zn doping which provided more volume for the movement of Li-ions and an enhanced electrical

conductivity. These changes are favorable for the electrochemical performance of $\text{Li}_2\text{MnSiO}_4$ including discharge capacitance and rate capability. However, these beneficial properties are traded off with increasing Zn doping. These results are in good agreement with various literature reports [27,51,52].

Figure 5.9 (b) depicts the GCD curves of the AC// $\text{Li}_2\text{Mn}_{0.96}\text{Zn}_{0.04}\text{SiO}_4$ supercapattery device at current loads of 0.1 to 2 A g^{-1} . The almost symmetric profiles with no ohmic drops reveals the good electrochemical performance of the devices. The variation of specific capacitance with increasing current load is presented in Figure 5.9 (c). It is observed that the specific capacitance decreases with an increase in current load due to the fact that not enough active material is involved in the redox reaction [53]. The AC// $\text{Li}_2\text{Mn}_{0.96}\text{Zn}_{0.04}\text{SiO}_4$ supercapattery device delivers a specific capacitance of 108.2 F g^{-1} at a current load of 0.1 A g^{-1} and still retains a specific capacitance of ~52 % (55.9 F g^{-1}) when the current is increased by a factor of 20 (2 A g^{-1}).



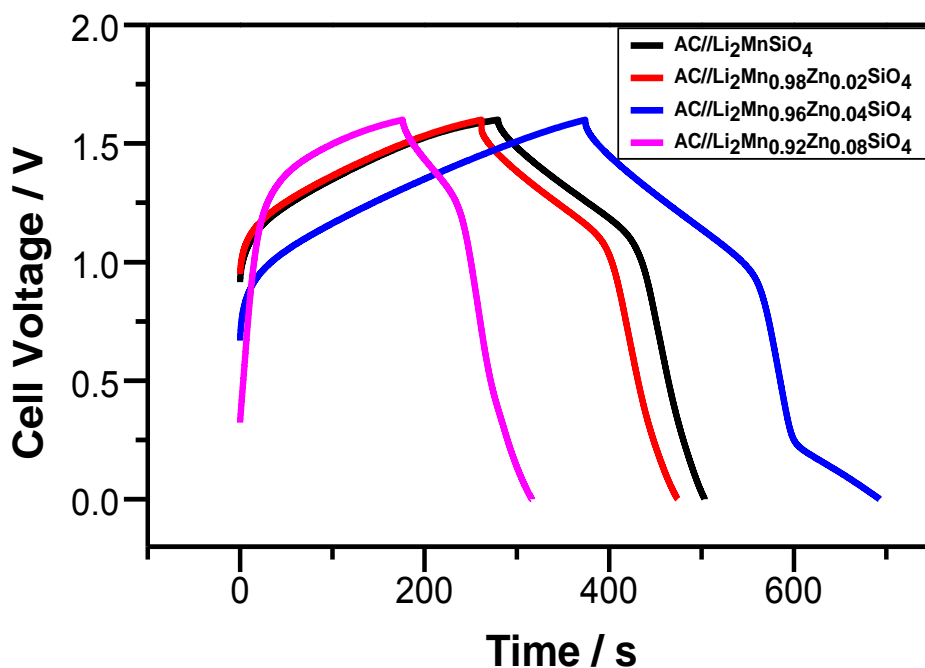


Figure 5.9 (a): GCD profiles of AC//Li₂MnSiO₄ and AC// Li₂Mn_{1-x}Zn_xSiO₄ supercapattery devices at a current load of 0.1 A g⁻¹ at a voltage window of 1.6 V

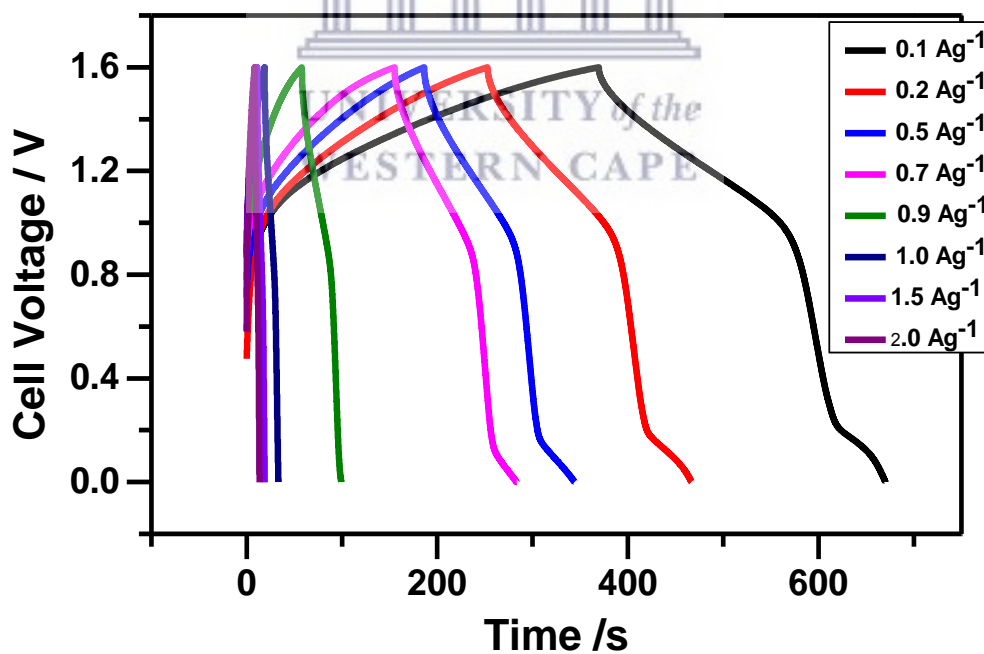


Figure 5.9 (b): GCD profiles of AC//Li₂Mn_{0.96}Zn_{0.04}SiO₄ device at varying current loads 0.1 – 2 A g⁻¹ in 1 M Na₂SO₄ aqueous electrolyte

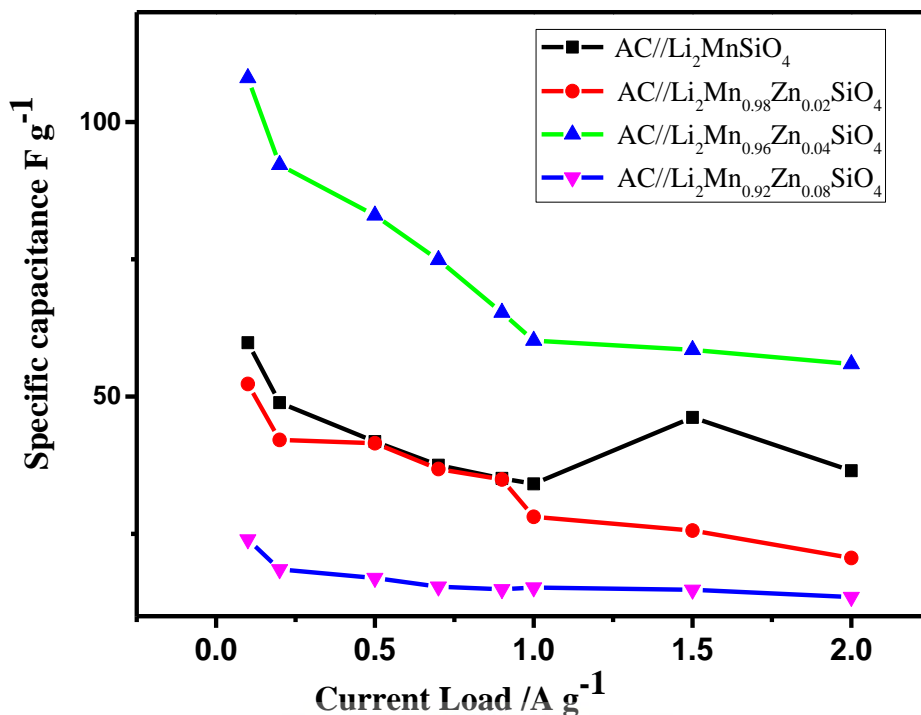


Figure 5.9 (c): Variation of specific capacitance with current load of AC//Li₂MnSiO₄ and AC//Li₂Mn_{1-x}Zn_xSiO₄ supercapattery devices in 1 M Na₂SO₄ aqueous electrolyte and voltage window of 1.6 V



iii) Electrochemical cycling / stability studies

The stability of the supercapattery devices over repeated charge-discharge cycling was achieved over 3000 cycles at a current load of 0.2 A g⁻¹. Figure 5.10 (a) presents the capacitance retention of the AC//Li₂Mn_{0.96}Zn_{0.04}SiO₄ and AC//Li₂Mn_{0.92}Zn_{0.08}SiO₄ supercapatteries over 3000 cycles and that of AC//Li₂MnSiO₄ and AC//Li₂Mn_{0.92}Zn_{0.08}SiO₄ devices over 1000 cycles as the inset. The AC//Li₂Mn_{0.96}Zn_{0.04}SiO₄ and AC//Li₂Mn_{0.92}Zn_{0.08}SiO₄ devices exhibited good capacitance retention of 72.5 % and 85.4 % respectively over 3000 cycles. While the AC//Li₂MnSiO₄ and AC//Li₂Mn_{0.92}Zn_{0.08}SiO₄ devices delivered a capacitance retention of 69.7 % and 66.8 %, respectively over 1000 cycles. The cycling stability of the AC//Li₂MnSiO₄ and

AC//Li₂Mn_{0.92}Zn_{0.08}SiO₄ devices is only reported for 1000 cycles because the supercapattery cells became completely unstable after 1000 cycles with a “noisy voltage versus time output”. The coulombic efficiency per cycle is shown in Figure 5.10 (b). Notably, the AC//Li₂Mn_{0.96}Zn_{0.04}SiO₄ supercapattery exhibits an excellent coulombic efficiency of 90.1 % for the 1st cycle to 99.7 % at 3000 cycles. AC//Li₂Mn_{0.98}Zn_{0.02}SiO₄ device showed a coulombic efficiency of 97.3 % at cycle 1 and up to 99.6 % at cycle 3000. Meanwhile the AC//Li₂MnSiO₄ device delivered 83.7 % coulombic efficiency at cycle 1 and 98.4 % at 1000 cycles over 89.8 % at cycle 1 and 99.5 at cycle 3000 by the AC//Li₂Mn_{0.92}Zn_{0.08}SiO₄. The superior cycling stability and overall performance of the AC//Li₂Mn_{0.96}Zn_{0.04}SiO₄ supercapattery device can be ascribed to the increased interlayer spacing observed in XRD studies which accommodated volume expansion during repeated charge-discharge studies. During the process of Li⁺ ion removal, the orthosilicate lattice is exposed to structural collapse due to the oxidation of Mn²⁺ ions to unstable and smaller Jahn-teller active Mn³⁺ ions. However in the presence Zn²⁺ dopant ions, lattice shrinking is prevented by the unchangeable radius of Zn²⁺. As a result, the Zn²⁺ in the lattice will act as a pillar to prevent the collapse of the crystal during cycling. The favourable Zn doping ratio is observed to be 4 %, after which more Zn²⁺ ions acted as a barrier to the movement of Li⁺ ions leading to a reduction in electrochemical performance.

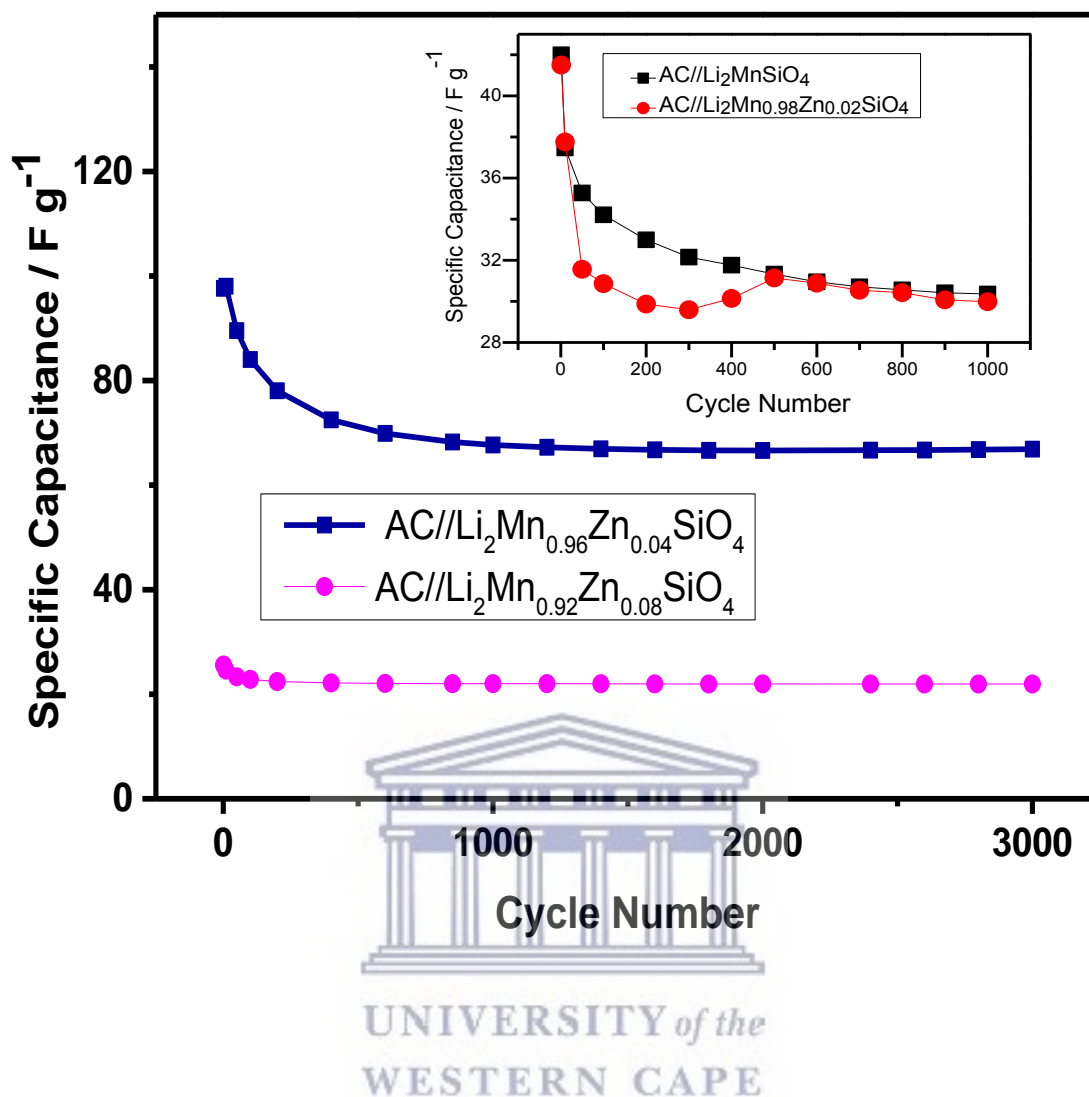


Figure 5.10 (a): Cycling stability of AC//Li₂MnSiO₄ and AC// Li₂Mn_{1-x}Zn_xSiO₄ supercapattery devices over 1000 and 3000 cycles

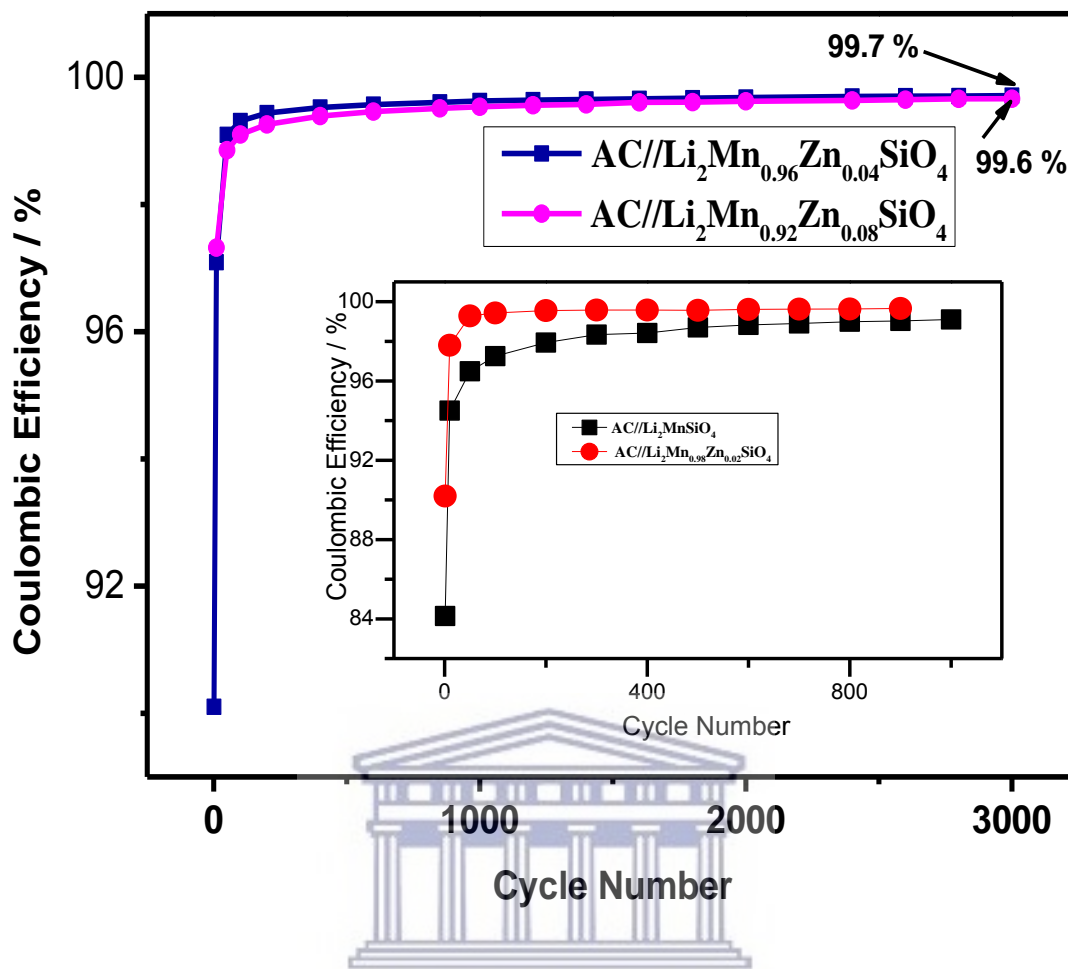


Figure 5.10 (b): Coulombic efficiency of AC//Li₂MnSiO₄ and AC// Li₂Mn_{1-x}Zn_xSiO₄ supercapattery devices

5.3.5 (c) Specific Energy and Specific Power

The most important characteristics of an energy storage device are the specific energy and power, usually expressed as the Ragone plot. Figure 5.11 presents the Ragone plot of the supercapattery devices at increasing current loads. The specific energy (W h kg⁻¹) and specific

power (W kg^{-1}) of the devices at different current loads were calculated according to Equation 5.10 and 5.11 [54].

$$E = \frac{1}{2} C_{\text{sp}} \times \Delta V^2 \times \frac{1}{3.6} \quad (5.10)$$

$$P = \frac{E}{\Delta t} \times 3600 \quad (5.11)$$

Where C_{sp} denotes the specific capacitance of the device (F g^{-1}), ΔV is the applied voltage (V) and Δt is the supercapattery discharge time (s).

It was observed that the AC// $\text{Li}_2\text{Mn}_{0.96}\text{Zn}_{0.04}\text{SiO}_4$ supercapattery could deliver a specific energy of 38.4 W h kg^{-1} when the specific power was at 516 W kg^{-1} and even maintained a specific energy of 19.9 W h kg^{-1} when the specific power increased to 14429 W kg^{-1} . On the other hand, the AC// $\text{Li}_2\text{MnSiO}_4$ device could deliver a specific energy of 21.3 W h kg^{-1} at a specific power of 482.2 W kg^{-1} and could attain a specific energy of 13 W kg^{-1} at a specific power of 4978.6 W kg^{-1} . These results are comparable to recently reported supercapattery devices such as MWCNT- Co_3O_4 -Ag//AC (16.5 W h kg^{-1} at 297.5 W kg^{-1}) [55], KCoPO₄//AC (19 W h kg^{-1} at 214 W kg^{-1}) [6], Ni(OH)₂/CuCo₂S₄/Ni//AC (39.7 W h kg^{-1} at 365.3 W kg^{-1}) [56] and AC//2D- MnCo_2O_4 (33.8 W h kg^{-1} at 318.9 W kg^{-1}) [57]. The commendable electrochemical performance of the supercapatteries especially the AC// $\text{Li}_2\text{Mn}_{0.96}\text{Zn}_{0.04}\text{SiO}_4$ is due to the large surface area of nanostructured $\text{Li}_2\text{Mn}_{0.96}\text{Zn}_{0.04}\text{SiO}_4$ electrode material which provided high

contact volume with electrolyte ions and the pillar effect of Zn doping which accommodated volume expansion during charge and discharge processes leading high rate performance.

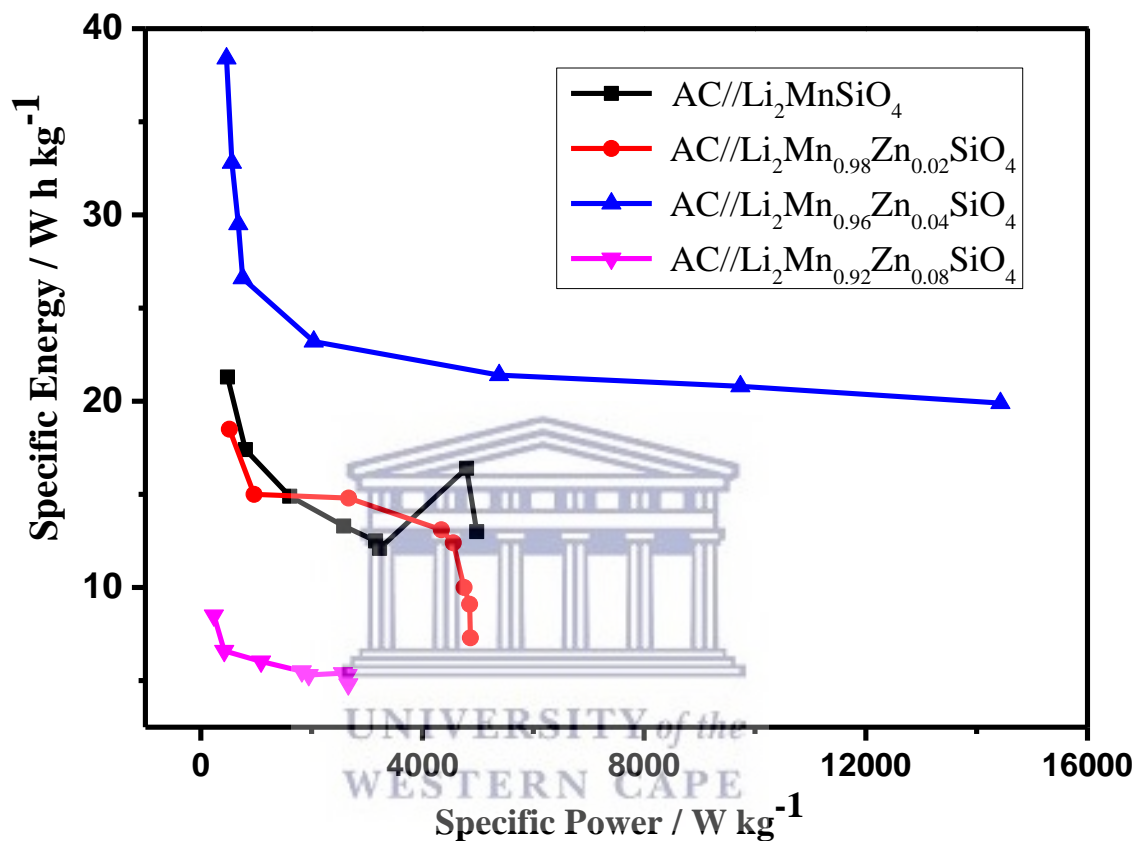


Figure 5.11: Ragone plot of AC//Li₂MnSiO₄ and AC// Li₂Mn_{1-x}Zn_xSiO₄ supercapattery devices in 1 M Na₂SO₄ aqueous electrolyte and voltage window of 1.6 V

5.4 Conclusion

Crystalline and orthorhombic Zn-doped $\text{Li}_2\text{MnSiO}_4$ nanomaterials were prepared in this study by a solvothermal synthesis in ethylene glycol. SEM and TEM investigations revealed mixed rhombohedral and spherically-shaped nanocrystals with average diameters in the range of 22.5 – 30.7 nm. SAXS studies showed skewed to bell-shaped particle size distributions with primary particles in the range of 14.7 – 23.1 nm. The vibration of the Si-O-Mn linkage was revealed by FTIR investigations at 850 cm^{-1} while the stretching motion of LiO_4 were observed around $540\text{--}420\text{ cm}^{-1}$. Electrochemical studies by CV showed that the 4 % Zn dopant ratio ($\text{Li}_2\text{Mn}_{0.96}\text{Zn}_{0.04}\text{SiO}_4$) depicts better electrochemical performance with specific capacity of 80 C g^{-1} . Supercapatteries assembled with activated carbon as negative electrode and the orthosilicate-based electrodes as the positive electrodes delivered a specific capacitances from $108.2\text{--}23.98\text{ F g}^{-1}$ at 0.1 A g^{-1} and capacitance retention of 72.5 % - 84.5 % over 3000 cycles at 0.2 A g^{-1} . The supercapatteries delivered excellent coulombic efficiency of 99.6 – 99.7 % at 3000 cycles. A commendable specific energy of 38.4 W h kg^{-1} at a specific power of 516 W kg^{-1} and up to 19.9 W h kg^{-1} retained at specific power of 14429 W kg^{-1} was delivered by the AC// $\text{Li}_2\text{Mn}_{0.96}\text{Zn}_{0.04}\text{SiO}_4$ supercapattery. The superior electrochemical performance of the AC// $\text{Li}_2\text{Mn}_{0.96}\text{Zn}_{0.04}\text{SiO}_4$ supercapattery is attributed to the high contact volume of the electrode material with the electrolyte provided by the nano-morphology and high surface area of the electrode. The pillar effect of Zn doping also provided more volume for the movement of Li-ions and enhanced the electrical conductivity of the material leading an increased rate performance. These results are comparable to recently reported supercapattery devices. With further development, the Zn-doped $\text{Li}_2\text{MnSiO}_4$ rhombohedral nanostructures may find wide applications in advanced energy storage systems.

References

- [1] J. Lin, Y. Yan, X. Zheng, Z. Zhong, Y. Wang, J. Qi, J. Cao, W. Fei, Y. Huang, J. Feng, Designing and constructing core-shell NiCo₂S₄@Ni₃S₂ on Ni foam by facile one-step strategy as advanced battery-type electrodes for supercapattery, *J. Colloid Interface Sci.* 536 (2019) 456–462. doi:10.1016/j.jcis.2018.10.072.
- [2] A. Muzaffar, M.B. Ahamed, K. Deshmukh, J. Thirumalai, A review on recent advances in hybrid supercapacitors: Design, fabrication and applications, *Renew. Sustain. Energy Rev.* 101 (2019) 123–145. doi:10.1016/j.rser.2018.10.026.
- [3] J.R. Croy, A. Abouimrane, Z. Zhang, Next-generation lithium-ion batteries: The promise of near-term advancements, *MRS Bull.* 39 (2014) 407–415. doi:10.1557/mrs.2014.84.
- [4] N. Priyadharsini, S. Surendran, B. Senthilkumar, L. Vasylechko, R.K. Selvan, Synthesis and Electrochemical Performances of γ -KCoPO₄ Nanocrystals as Promising Electrode for Aqueous Supercapatteries, *ChemElectroChem.* 6 (2019) 369–377. doi:10.1002/celc.201801440.
- [5] D. Kaufman, K.L. Hudson, R. Mcclamrock, Where Do Batteries End and Supercapacitors Begin, *Science* (80-). 343 (2014) 1210–1211. doi:10.1126/science.1249625.
- [6] K.V. Sankar, S. Shanmugapriya, S. Surendran, S.C. Jun, R.K. Selvan, Facile hydrothermal synthesis of carbon-coated cobalt ferrite spherical nanoparticles as a

-
- potential negative electrode for flexible supercapattery, *J. Colloid Interface Sci.* 513 (2018) 480–488. doi:10.1016/j.jcis.2017.11.054.
- [7] G.Z. Chen, Understanding supercapacitors based on nano-hybrid materials with interfacial conjugation, *Prog. Nat. Sci. Mater. Int.* 23 (2013) 245–255. doi:10.1016/j.pnsc.2013.04.001.
- [8] M. Swietoslowski, M. Molenda, M. Gajewska, Preliminary study of structural changes in $\text{Li}_2\text{MnSiO}_4$ cathode material during electrochemical reaction, *Funct. Mater. Lett.* 9 (2016) 2–5. doi:10.1142/S1793604716410034.
- [9] A. Kilic, E. Serife, E. Stojanovska, A review of nanofibrous structures in lithium ion batteries, 300 (2015). doi:10.1016/j.jpowsour.2015.09.059.
- [10] R. Chen, R. Luo, Y. Huang, F. Wu, L. Li, Advanced High Energy Density Secondary Batteries with Multi-Electron Reaction Materials, *Adv. Sci.* 3 (2016) 1–39. doi:10.1002/advs.201600051.
- [11] M.S. Whittingham, C. Siu, J. Ding, Can Multielectron Intercalation Reactions Be the Basis of Next Generation Batteries?, *Acc. Chem. Res.* 51 (2018) 258–264. doi:10.1021/acs.accounts.7b00527.
- [12] R.J. Gummow, Y. He, Recent progress in the development of $\text{Li}_2\text{MnSiO}_4$ cathode materials, *J. Power Sources.* 253 (2014) 315–331. doi:10.1016/j.jpowsour.2013.11.082.
- [13] Q. Cheng, W. He, X. Zhang, M. Li, L. Wang, Modification of $\text{Li}_2\text{MnSiO}_4$ cathode materials for lithium-ion batteries: a review, *J. Mater. Chem. A.* 5 (2017) 10772–10797. doi:10.1039/C7TA00034K.
- [14] T. Peng, W. Guo, Q. Zhang, Y. Zhang, M. Chen, Uniform coaxial $\text{CNT@Li}_2\text{MnSiO}_4\text{@C}$

-
- as advanced cathode material for lithium-ion battery, *Electrochim. Acta.* 291 (2018) 1–8. doi:10.1016/j.electacta.2018.08.143.
- [15] H. Park, T. Song, R. Tripathi, L.F. Nazar, U. Paik, $\text{Li}_2\text{MnSiO}_4$ /carbon nanofiber cathodes for Li-ion batteries, *Ionics (Kiel)*. 20 (2014) 1351–1359. doi:10.1007/s11581-014-1105-4.
- [16] H.J. Song, J.-C. Kim, M. Choi, C. Choi, M.A. Dar, C.W. Lee, S. Park, D.-W. Kim, $\text{Li}_2\text{MnSiO}_4$ nanorods-embedded carbon nanofibers for lithium-ion battery electrodes, *Electrochim. Acta.* 180 (2015) 756–762. doi:10.1016/j.electacta.2015.08.161.
- [17] F. Wang, J. Chen, C. Wang, B. Yi, Fast sol-gel synthesis of mesoporous $\text{Li}_2\text{MnSiO}_4$ /C nanocomposite with improved electrochemical performance for lithium-ion batteries, *J. Electroanal. Chem.* 688 (2013) 123–129. doi:10.1016/j.jelechem.2012.10.014.
- [18] H. Zhu, W. Deng, L. Chen, S. Zhang, Nitrogen doped carbon layer of $\text{Li}_2\text{MnSiO}_4$ with enhanced electrochemical performance for lithium ion batteries, *Electrochim. Acta.* 295 (2019) 956–965. doi:10.1016/j.electacta.2018.11.133.
- [19] C. Deng, S. Zhang, Y.X. Wu, B.D. Zhao, Partial substitution of Mn/Si with V, Cr or Al in $\text{Li}_2\text{MnSiO}_4$ nanoparticle: Dependence of the physical and electrochemical properties on the substitution strategy, *J. Electroanal. Chem.* 719 (2014) 150–157. doi:10.1016/j.jelechem.2014.02.022.
- [20] Z. Ding, Y. Feng, D. Zhang, R. Ji, L. Chen, D.G. Ivey, W. Wei, Crystallographic Habit Tuning of $\text{Li}_2\text{MnSiO}_4$ Nanoplates for High-Capacity Lithium Battery Cathodes, *ACS Appl. Mater. Interfaces.* 10 (2018) 6309–6316. doi:10.1021/acsami.7b17587.
- [21] S. Choi, S.J. Kim, Y.J. Yun, S.S. Lee, S.Y. Choi, H.K. Jung, Controlled shape with enhanced electrochemical performance of various ions doped $\text{Li}_2\text{MnSiO}_4$ cathode

-
- nanoparticles, *Mater. Lett.* 105 (2013) 113–116. doi:10.1016/j.matlet.2013.04.045.
- [22] C. Hwang, T. Kim, Y. Noh, W. Cha, J. Shim, K. Kwak, K.M. Ok, K.-K. Lee, Synthesis, characterization, and electrochemical performance of V-doped $\text{Li}_2\text{MnSiO}_4/\text{C}$ composites for Li-ion battery, 2016. doi:10.1016/j.matlet.2015.10.113.
- [23] Y. Dong, W.L. Zhang, C.M. Wang, T. Shi, L. Chen, Synthesis of La-doped $\text{Li}_2\text{MnSiO}_4$ nano-particle with high-capacity via polyol-assisted hydrothermal method, *Electrochim. Acta.* 166 (2015) 40–46. doi:10.1016/j.electacta.2015.02.236.
- [24] A.Y. Shenouda, N. Munichandraih, The electrochemical properties of $\text{Li}_2\text{Ni}_x\text{Mn}_{1-x}\text{SiO}_4$ cathode material for lithium batteries, *Int. J. Electrochem. Sci.* 11 (2016) 8123–8131. doi:10.20964/2016.10.43.
- [25] A.Y. Shenouda, H.K. Liu, Studies on electrochemical behaviour of zinc-doped LiFePO_4 for lithium battery positive electrode, *J. Alloys Compd.* 477 (2009) 498–503. doi:10.1016/j.jallcom.2008.10.077.
- [26] J.W. Lee, M.S. Park, B. Anass, J.H. Park, M.S. Paik, S.G. Doo, Electrochemical lithiation and delithiation of LiMnPO_4 : Effect of cation substitution, *Electrochim. Acta.* 55 (2010) 4162–4169. doi:10.1016/j.electacta.2010.02.097.
- [27] R. Poonguzhali, N. Shanmugam, R. Gobi, A. Senthilkumar, R. Shanmugam, K. Sathishkumar, Influence of Zn doping on the electrochemical capacitor behavior of MnO_2 nanocrystals, *RSC Adv.* 5 (2015) 45407–45415. doi:10.1039/c5ra01326g.
- [28] X. Wu, G.L. Xu, G. Zhong, Z. Gong, M.J. McDonald, S. Zheng, R. Fu, Z. Chen, K. Amine, Y. Yang, Insights into the Effects of Zinc Doping on Structural Phase Transition of P2-Type Sodium Nickel Manganese Oxide Cathodes for High-Energy Sodium Ion Batteries, *ACS Appl. Mater. Interfaces.* 8 (2016) 22227–22237.

-
- doi:10.1021/acsami.6b06701.
- [29] G. Li, X. Xu, R. Han, J. Ma, Synthesis and superior electrochemical properties of shaggy hollow Zn-doped Fe₂O₃ nanospheres for high-performance lithium-ion batteries, *Cryst Eng Comm.* 18 (2016) 2949–2955. doi:10.1039/c5ce02408k.
- [30] Q. Mao, C. Zhang, W. Yang, J. Yang, L. Sun, Y. Hao, X. Liu, Mitigating the voltage fading and lattice cell variations of O₃-NaNi_{0.2}Fe_{0.35}Mn_{0.45}O₂ for high performance Na-ion battery cathode by Zn doping, *J. Alloys Compd.* 794 (2019) 509–517. doi:10.1016/j.jallcom.2019.04.271.
- [31] H. Zhao, X. Gao, Y. Li, Q. Ran, C. Fu, Y. Feng, J. Liu, X. Liu, J. Su, Synergistic effects of zinc-doping and nano-rod morphology on enhancing the electrochemical properties of spinel Li-Mn-O material, *Ceram. Int.* (2019) 0–1. doi:10.1016/j.ceramint.2019.05.324.
- [32] M.M. Ndipingwi, C.O. Ikpo, N.W. Hlongwa, N. Dywili, A.L. Djoumessi Yonkeu, E.I. Iwuoha, Crystal chemistry and lithium-ion intercalation properties of lithium manganese silicate cathode for aqueous rechargeable Li-ion batteries, *J. Appl. Electrochem.* (2019). doi:10.1007/s10800-019-01296-0.
- [33] S. Liu, J. Xu, D. Li, Y. Hu, X. Liu, K. Xie, High capacity Li₂MnSiO₄/C nanocomposite prepared by sol-gel method for lithium-ion batteries, *J. Power Sources.* 232 (2013) 258–263. doi:10.1016/j.jpowsour.2012.12.126.
- [34] D. Rangappa, K.D. Murukanahally, T. Tomai, A. Unemoto, I. Honma, Ultrathin Nanosheets of Li₂MSiO₄ (M = Fe, Mn) as High-Capacity Li-Ion Battery Electrode, *Nano Lett.* 12 (2012) 1146–1151. doi:10.1021/nl202681b.
- [35] M.M. Ndipingwi, C.O. Ikpo, N.W. Hlongwa, Z. Myalo, N. Ross, M. Masikini, S. V.

-
- John, P.G. Baker, W.D. Roos, E.I. Iwuoha, Orthorhombic Nanostructured $\text{Li}_2\text{MnSiO}_4/\text{Al}_2\text{O}_3$ Supercapattery Electrode with Efficient Lithium-Ion Migratory Pathway , *Battery-Supercaps.* 1 (2018) 223–235. doi:10.1002/batt.201800045.
- [36] W. Bras, I.P. Dolbnya, D. Detollenaere, R. Van Tol, M. Malfois, G.N. Greaves, A.J. Ryan, E. Heeley, Recent experiments on a combined small-angle/wide-angle X-ray scattering beam line at the ESRF, *J. Appl. Crystallogr.* 36 (2003) 791–794. doi:10.1107/S002188980300400X.
- [37] M. Arroyo-deDompablo, On the energetic stability and electrochemistry of $\text{Li}_2\text{MnSiO}_4$ polymorphs, *Chem.* 20 (2008) 5574–5584. doi:10.1021/cm801036k.
- [38] R. Dominko, M. Bele, M. Gaberšček, A. Meden, M. Remškar, J. Jamnik, Structure and electrochemical performance of $\text{Li}_2\text{MnSiO}_4$ and $\text{Li}_2\text{FeSiO}_4$ as potential Li-battery cathode materials, *Electrochem. Commun.* 8 (2006) 217–222. doi:10.1016/j.elecom.2005.11.010.
- [39] Z. Ding, Y. Feng, D. Zhang, R. Ji, L. Chen, D.G. Ivey, W. Wei, Crystallographic Habit Tuning of $\text{Li}_2\text{MnSiO}_4$ Nanoplates for High- Capacity Lithium Battery Cathodes, *ACS Appl. Mater. Interfaces.* 10 (2018) 6309–6316. doi:10.1021/acsami.7b17587.
- [40] X. Wu, S.X. Zhao, L.Q. Yu, J.L. Yang, C.W. Nan, Effect of sulfur doping on structural reversibility and cycling stability of a $\text{Li}_2\text{MnSiO}_4$ cathode material, *Dalt. Trans.* 47 (2018) 12337–12344. doi:10.1039/c8dt02226g.
- [41] C. Wang, Y. Xu, X. Sun, B. Zhang, Y. Chen, S. He, Enhanced electrochemical properties of F-doped $\text{Li}_2\text{MnSiO}_4/\text{C}$ for lithium ion batteries, *J. Power Sources.* 378 (2018) 345–352. doi:10.1016/j.jpowsour.2017.12.004.
- [42] D. Tie, S. Huang, J. Wang, J. Ma, J. Zhang, Y. Zhao, Hybrid energy storage devices :

-
- Advanced electrode materials and matching principles, *Energy Storage Mater.* (2019) 1–20. doi:10.1016/j.ensm.2018.12.018.
- [43] L. Guan, L. Yu, G.Z. Chen, Capacitive and non-capacitive faradaic charge storage, *Electrochim. Acta.* 206 (2016) 464–478. doi:10.1016/j.electacta.2016.01.213.
- [44] B. Akinwolemiwa, G.Z. Chen, Fundamental consideration for electrochemical engineering of supercapattery, *J. Braz. Chem. Soc.* 29 (2018) 960–972. doi:10.21577/0103-5053.20180010.
- [45] N. Elgrishi, K.J. Rountree, B.D. McCarthy, E.S. Rountree, T.T. Eisenhart, J.L. Dempsey, A Practical Beginner's Guide to Cyclic Voltammetry, *J. Chem. Educ.* 95 (2018) 197–206. doi:10.1021/acs.jchemed.7b00361.
- [46] T. Pajkossy, S. Vesztegom, Analysis of voltammograms of quasi-reversible redox systems: Transformation to potential program invariant form, *Electrochim. Acta.* 297 (2019) 1121–1129. doi:10.1016/j.electacta.2018.12.023.
- [47] A.C. Nwanya, D. Obi, R.U. Osuji, R. Bucher, M. Maaza, F.I. Ezema, Simple chemical route for nanorod-like cobalt oxide films for electrochemical energy storage applications, *J. Solid State Electrochem.* 21 (2017) 2567–2576. doi:10.1007/s10008-017-3520-8.
- [48] H. Shao, N. Padmanathan, D. McNulty, Cobalt Phosphate-Based Supercapattery as Alternative Power Source for Implantable Medical Devices, *ACS Appl. Energy Mater.* 2 (2019) 569–578. doi:10.1021/acsaem.8b01612.
- [49] G.Z. Chen, G.Z. Chen, Supercapacitor and supercapattery as emerging electrochemical energy stores Supercapacitor and supercapattery as emerging electrochemical energy stores, *Int. Mater. Rev.* 0 (2016) 1–30. doi:10.1080/09506608.2016.1240914.

-
- [50] A. Noori, M.F. El-kady, M.S. Rahmanifar, R.B. Kaner, M.F. Mousavi, Towards establishing performance metrics for batteries, supercapacitors and beyond, *Chem. Soc. Rev.* (2019). doi:10.1039/c8cs00581h.
- [51] H. Fang, H. Yi, C. Hu, B. Yang, Y. Yao, W. Ma, Y. Dai, Effect of Zn doping on the performance of LiMnPO₄ cathode for lithium ion batteries, *Electrochim. Acta.* 71 (2012) 266–269. doi:10.1016/j.electacta.2012.03.160.
- [52] H. Liu, Q. Cao, L.J. Fu, C. Li, Y.P. Wu, H.Q. Wu, Doping effects of zinc on LiFePO₄ cathode material for lithium ion batteries, *Electrochem. Commun.* 8 (2006) 1553–1557. doi:10.1016/j.elecom.2006.07.014.
- [53] C.O. and K.M.R. N. Padmanathan, Han Shao, David McNulty, Hierarchical NiO–In₂O₃ microflower (3D)/ nanorod (1D) hetero-architecture as a supercapattery electrode with excellent cyclic stability, *J. Mater. Chem. A.* 4 (2016) 4820–4830. doi:10.1039/C5TA10407F.
- [54] A.S. Rajpurohit, N.S. Punde, C.R. Rawool, A.K. Srivastava, Fabrication of high energy density symmetric supercapacitor based on cobalt-nickel bimetallic tungstate nanoparticles decorated phosphorus-sulphur co-doped graphene nanosheets with extended voltage, *Chem. Eng. J.* (2019) 679–692. doi:10.1016/j.cej.2019.04.100.
- [55] J. Iqbal, A. Numan, S. Rafique, R. Jafer, S. Mohamad, K. Ramesh, S. Ramesh, High performance supercapattery incorporating ternary nanocomposite of multiwalled carbon nanotubes decorated with Co₃O₄ nanograins and silver nanoparticles as electrode material, *Electrochim. Acta.* 278 (2018) 72–82. doi:10.1016/j.electacta.2018.05.040.
- [56] N. Tang, H. You, M. Li, G.Z. Chen, L. Zhang, Cross-linked Ni(OH)₂/CuCo₂S₄/Ni networks as binder-free electrodes for high performance supercapatteries, *Nanoscale.* 10

(2018) 20526–20532. doi:10.1039/c8nr05662e.

- [57] B. Saravanakumar, X. Wang, W. Zhang, L. Xing, W. Li, Holey two dimensional manganese cobalt oxide nanosheets as a high-performance electrode for supercapattery, *Chem. Eng. J.* 373 (2019) 547–555. doi:10.1016/j.cej.2019.05.080.

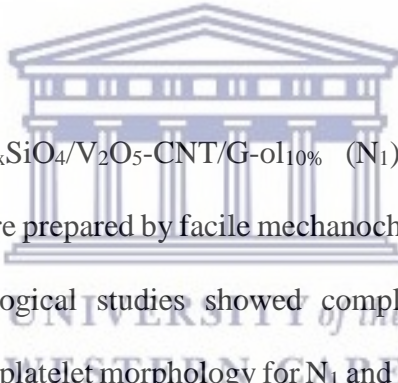


CHAPTER SIX

RESULTS AND DISCUSSION – MANUSCRIPT 4

Fabrication of Zinc doped Lithium Manganese Silicate/Vanadium Pentoxide/Graphol Composite Nanoarchitectures for Supercapattery Energy Storage (Prepared for Energy Storage Materials)

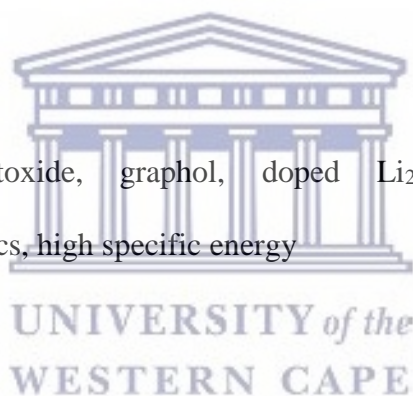
Abstract



Nanoarchitected $\text{Li}_2\text{Mn}_{1-x}\text{Zn}_x\text{SiO}_4/\text{V}_2\text{O}_5\text{-CNT/G-ol}_{10\%}$ (N_1) and $\text{Li}_2\text{Mn}_{1-x}\text{Zn}_x\text{SiO}_4/\text{V}_2\text{O}_5\text{-CNT/G-ol}_{5\%}$ (N_2) electrodes were prepared by facile mechanochemical reactions and annealing for 2 h at 350°C . Morphological studies showed completely hybridized mesoporous nanoarchitectures with majority platelet morphology for N_1 and further elongation in N_2 . SAXS investigations revealed mean primary particle sizes of 12.3 nm and aggregates at 29.4 and 48.1 nm for N_1 . N_2 showed similar form of aggregation with a single peak at 65.1 nm. Majority peaks in the X-ray diffraction patterns of N_1 and N_2 were indexed to orthorhombic $\text{Pmn}2_1$ space group of $\text{Li}_2\text{MnSiO}_4$, with minor peaks belonging to the 001 and 002 planes of oxygenated graphene sheets. Fourier transform infrared spectroscopy (FTIR) showed the asymmetric and symmetric vibrations of Si-O-Si and V-O-V bonds as well as the stretching motion of $[\text{LiO}_4]$ tetrahedra around $511 - 933\text{ cm}^{-1}$ and $420 - 494\text{ cm}^{-1}$, respectively. The vibration of Mn-O-Si layers, C=C and C-O bonds from the graphitic domains and OH characteristic band were also observed around $1060 - 1164\text{ cm}^{-1}$, 1641.4 cm^{-1} and 1371.8 cm^{-1} in FTIR analysis. Electrochemical studies by cyclic voltammetry in 1 M Na_2SO_4 at a potential window of 0.1 –

0.8 V revealed a charge storage mechanism of the electrodes involving surface bound faradaic reactions such as oxidation/reduction of manganese and vanadium ions together with intercalation processes of Li^+ ion. Electrochemical impedance spectroscopic studies showed a smaller R_{ct} value for N_2 (2.29 Ω) over N_1 (4.02 Ω), indicating faster movements of electro-active species in N_2 . Assembled AC// N_1 and AC// N_2 supercapatteries with activated carbon delivered specific capacitance of 205 F g^{-1} and 126 F g^{-1} , as well as specific energy and power of 92.3 W h kg^{-1} , 769.8 W kg^{-1} and 56.8 W h kg^{-1} , 427.8 W kg^{-1} , respectively at voltage of 1.8 V and current load of 0.1 A g^{-1} . The commendable electrochemical performance of the AC// N_1 and AC// N_2 supercapatteries can be attributed to the existence of nanoholes in the hybridized nanoarchitectures which enabled faster ionic movements.

Keywords: Vanadium pentoxide, graphol, doped $\text{Li}_2\text{MnSiO}_4$, nanoarchitectures, supercapattery, naoarchitectonics, high specific energy



6.1 Introduction

The global rise in energy demand and environmental issues associated with the existing energy production processes have necessitated the move towards clean and renewable energies based on alternative sources such as solar energy as well as the development of high-efficient energy conversion and storage devices. Electrochemical energy storage is an un-avoidable part of the clean energy portfolio. In the past decade, significant progress has been achieved in developing advanced technologies to face these challenges [1–4]. However, further improvement of performance and efficiency of current technologies is strongly needed to facilitate cost-

effective energy production and storage. The advent of nanotechnology and its rapid progress projects the potentials for accelerated improvements in many fields including advanced materials, energy devices and medicine. In recent times, nanotechnology has made impressive advances and has become an important pillar in the development of new materials and devices. The performance and lifetime of energy devices are critically dependent on nanoscale interfacial phenomena [5–7]. Nanoarchitectonics, a new paradigm of materials science and technology at the nanoscale, also known as the “rising tide on the horizon of current materials research” was proposed by Masakazu Aono in 2000 [8–11]. This concept enables the integration of predefined molecular functionalities, such as electrochemical, optical, catalytic or biological properties, into bulk materials, thin films and devices. Nanoarchitectonics results in creation of novel and reliable materials/systems where some inevitable uncertainties in nanoscale phenomena are accommodated by balanced harmonization. This harmonization can be done using known strategies such as chemical synthesis, atomic/molecular manipulation, field-induced material control and self-assembly [3,12,13]. Oldacre *et al.*, harmonized cofacial cobalt porphyrin prisms - $[\text{Ru}_8(\eta^6\text{-iPrC}_6\text{H}_4\text{Me})_8(2,5\text{-dihydroxy-1,4-benzoquinato})_4(\text{cobalt(II) tetra-4-pyridyl porphyrinate})_2][\text{triflate}]_8$ by discrete self-assembly for oxygen reduction catalysis. The Co prisms showed enhanced turnover frequency and catalyzed about 90 % oxygen reduction to hydrogen peroxide in the chemical reduction [14]. Lee *et al.* prepared densely packed functionalised multiwalled carbon nanotubes - $(\text{MWNT-NH}_2/\text{MWNT-COOH})_n$ electrodes for lithium ion battery applications through layer-by-layer assembly on indium tin oxide glass. The nanoarray electrodes, with thickness of up to several micrometres, delivered high reversible capacity of $\sim 200 \text{ mA h g}^{-1}$, specific power of 100 k W kg^{-1} and excellent cycling stability after 1000 cycles [15]. Also, Rajendran *et al.* synthesized a ternary nanocomposite for supercapacitive applications based on nickel oxide (NiO), multi-walled carbon nanotubes (CNTs), and reduced graphene oxide (RGO) by solvothermal synthesis,

using the concept of nanoarchitectonics. The RGO/CNT/NiO ternary nanocomposite exhibited good synergistic effect and delivered a high specific capacitance of 367 F g^{-1} at a current density of 1 A g^{-1} in 6 M KOH electrolyte, with a good capacitance retention of 94% after $1,000$ cycles [16]. More recently, Ariga and co-workers reviewed various approaches to low dimensional material (nanoparticles, nanorods, nanowires, nanosheets, cubic particles) nanoarchitectonics ranging from metal to covalent-organic frameworks, structured nanocarbons, block-copolymers and molecular receptors. The nanoarchitected materials prepared by methods such as layer-by-layer assembly, liquid interfacial precipitation and self-assembly can be used for several applications including supercapacitors, sensors, photodetectors, supramolecular differentiation, and enzyme reactors [1]. However, the control of functional constituents within low-dimensional materials and the development of large scale production is regarded as the key requirements of nanoarchitectonics.

Mechanochemistry, a solvent free technique has recently gained wide attention in organic and inorganic synthesis due to its superior sustainability metrics such as low cost, reduced reaction times, high yields and good selectivity [17–19]. Mechanochemical reactions enable formation of materials with low agglomeration, uniform morphology and crystal structure, making it a promising approach to harmonize nanoarchitectures.

Battery and supercapacitor hybrids known as supercapatteries, which combine the advantages of supercapacitors and rechargeable batteries such as higher power densities, fast charge-discharge rates and longer cycle life are currently considered to be excellent candidates to meet the increasing energy demands of the energy intensive environment [20–22].

Herein, we discuss the hybridization of hydroxylated graphene (graphol) sheets into vanadia and Zinc-doped lithium manganese nanonetworks and their harmonization into nanoarchitectonic electrodes for supercapattery applications. The nanoarchitected electrodes

were prepared using straight forward and sustainable mechanochemical reactions involving hand-milling and ultrasonication in a very short time.

6.2 Experimental details

6.2.1 Materials

Microcrystalline graphite (2- 15 μm , 99.99 %) was purchased from Alfar Aesar, while the rest of the chemicals used were supplied by Sigma-Aldrich and were all used without further purification. These include, vanadium (V) oxide (> 98 % reagent grade), sodium sulfate (\geq 99.99 % trace metal basis), manganese (II) chloride tetrahydrate (99.99 % trace metal basis), oxalic acid dihydrate (\geq 99 % ACS reagent). Ethylene glycol (anhydrous, \geq 99.8 %), lithium hydroxide (98 % reagent grade), isopropanol (70 % in water), ethanol (absolute, \geq 99.8 %) and hydrogen peroxide solution (30 wt. % in water, ACS reagent) were also used. Carbon nanotubes, multiwalled (> 98% carbon basis, 6 - 13 nm x 2.5 - 20 μm), tetraethyl orthosilicate (\geq 99.0 %), zinc acetate dihydrate (99.999 % trace metal basis) and sodium hydroxide (98 – 100.5 %) were also included. Furthermore, tetrahydrofuran (THF, > 99.8 %), Borane in THF complex (1 M), ethanol (absolute, \geq 99.8 %), polytetrafluoroethylene (mean particle size 20 μm), activated charcoal (Norit $\text{\textcircled{R}}$ pellets), carbon black (4 μm mesoporous carbon matrix, \geq 99.95 % metal basis). lithium nitrate (99.99 %), chloroform and N-methyl-2-pyrrolidone (anhydrous , 99.5 %) were also used. Hydrochloric acid (reagent grade and assay 36.5 – 38.0 %) was obtained from Kimix chemicals and nickel foam (1.6 mm thick, 0.25 μm pore diameter) purchased from MTI Corporation.

6.2.2. Synthesis of $\text{Li}_2\text{Mn}_{1-x}\text{Zn}_x\text{SiO}_4/\text{V}_2\text{O}_5\text{-CNT}/\text{G-ol}$ Nanoarchitectures

The synthesis of graphol (G-ol), V_2O_5 , $\text{V}_2\text{O}_5\text{-CNT}$ and zinc doped lithium manganese silicate ($\text{Li}_2\text{Mn}_{1-x}\text{Zn}_x\text{SiO}_4$) nanomaterials have been discussed in previous chapters of this work. In summary, graphol (G-ol) was prepared by hydroboration of graphene oxide and subsequent oxidation with NaOH and 30 % H_2O_2 . Pristine V_2O_5 and $\text{V}_2\text{O}_5\text{-CNT}$ nanorods were prepared by oxalic acid-assisted hydrothermal synthesis while $\text{Li}_2\text{Mn}_{1-x}\text{Zn}_x\text{SiO}_4$ nanocrystals were prepared by solvothermal synthesis in ethylene glycol.

The nanoarchitectonic electrodes were prepared by mechanochemical reactions involving a combination of hand-milling and ultrasonication processes with annealing at 350°C for 2 h. Two nanoarchitectonic electrodes were prepared with same amounts of $\text{V}_2\text{O}_5\text{-CNT}$ and $\text{Li}_2\text{Mn}_{1-x}\text{Zn}_x\text{SiO}_4$ nanostructures while varying the ratios of G-ol nanosheets. 375 mg of $\text{Li}_2\text{Mn}_{1-x}\text{Zn}_x\text{SiO}_4$ nanomaterials (75 % of total amount), 50 mg of $\text{V}_2\text{O}_5\text{-CNT}$ nanocomposite (10 %) were carefully hand-milled with 60 mg (12 %) and 30 mg (6 %) of G-ol nanosheets separately using an agate mortar and pestle. The finely ground materials were further hybridized sonochemically in chloroform using an ultrasonic bath for 4 h. The mixtures were evaporated at room temperature and the nanoarchitectonic electrodes were obtained by annealing the materials at 350°C in a muffle furnace for 2 h at a heating rate of 5°C per minute. This was to remove any strain effects offered by the different nanomaterials on each other and to avoid variation in morphology from region to region. The synthesis scheme is displayed in Figure 6.1.

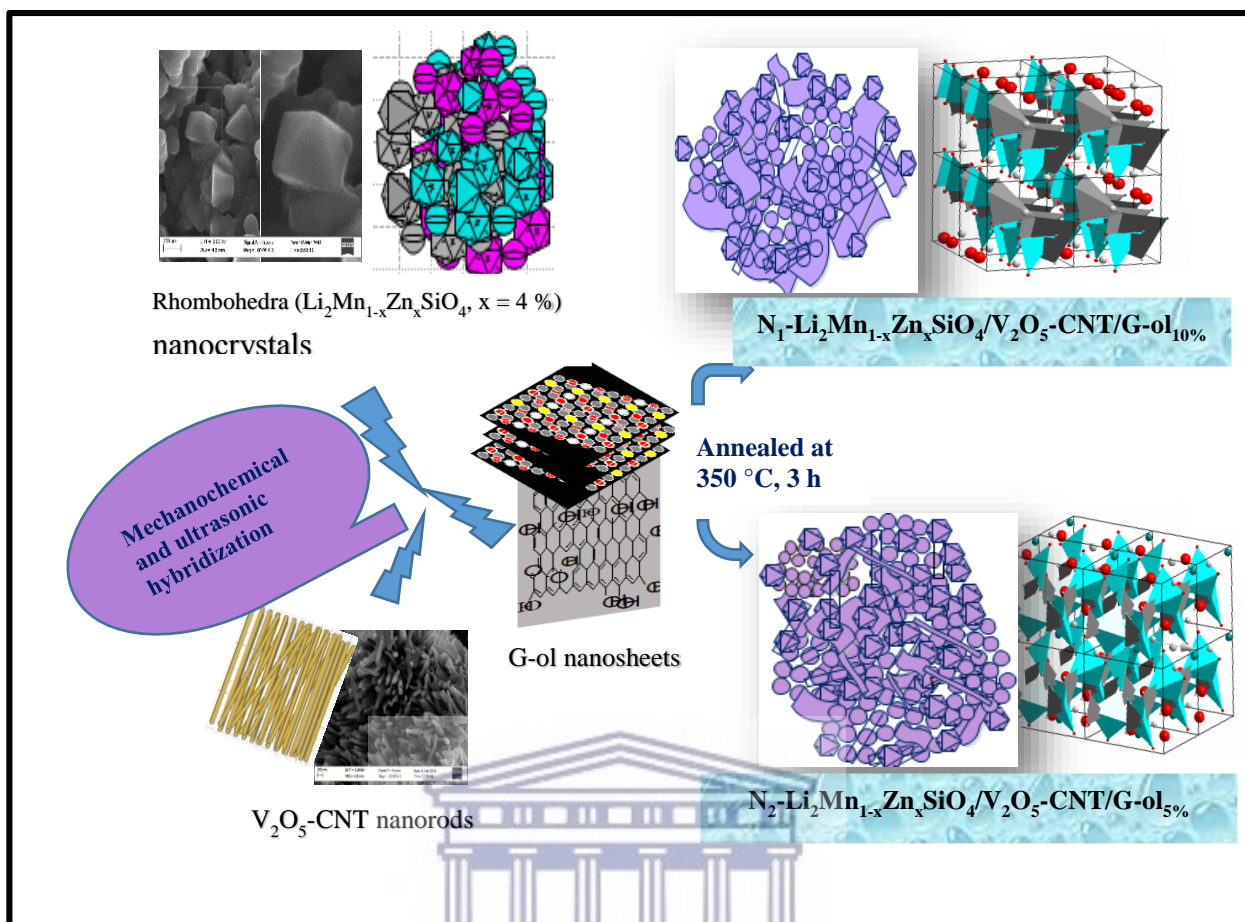


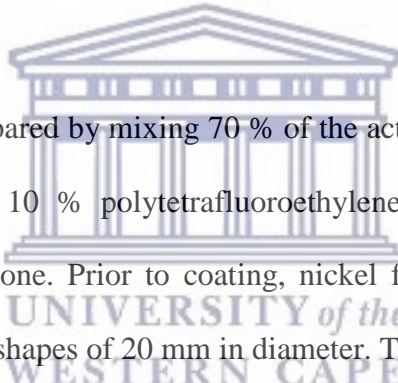
Figure 6.1: Synthesis scheme of N_1 and N_2 nanoarchitectonic electrode materials

6.2.3 Material Characterization

Structural and morphological features of the nanoarchitectures were characterized using ZEISS ULTRA scanning electron microscope equipped with an energy dispersive spectrometer and a Tecnai G^2 F_2O X-Twin MAT 200 kV field emission transmission electron microscope from FEI. Analyses were performed on a nickel-copper grid. The particle size distribution of the nanomaterials were obtained by small-angle X-ray scattering experiments performed on an Anton Paar SAXSpace system. Copper $\text{K}\alpha$ radiation (0,154 nm) was used and the instrument

is equipped with a 1 D mythen 2 position sensitive detector and a beamstop alignment. Powder X-ray diffraction studies were obtained using a D8 advance diffractometer from BRUKER-AXS using copper $K\alpha_1$ radiation ($\lambda \sim 0.154$ nm) operating at 40 kV and 40 mA. A Perkin Elmer Spectrum 100 series Attenuated Total Reflection (ATR) Fourier Transform Infrared spectrometer with a resolution of 4 cm^{-1} was used to obtain the functional groups present in the materials. Electrochemical studies were performed using both three and two-electrode cells on a VMP-300 potentiostat from Bio-Logic instruments.

6.2.4 Electrode preparation and electrochemical measurements



The working electrode was prepared by mixing 70 % of the active material with 20 % carbon black (conducting agent) and 10 % polytetrafluoroethylene (binder) in a few drops of anhydrous N-methyl-2-pyrrolidone. Prior to coating, nickel foam was cut into rectangular shapes of $0.5 \times 1\text{ cm}^2$ and coin-shapes of 20 mm in diameter. The different sizes were cleaned and etched to remove surface oxide layers using 1 M HCl solution in an ultrasonic bath for 15 mins, then cleaned in absolute ethanol and deionized water for 15 min in sequence by ultrasonication and finally dried at $90\text{ }^\circ\text{C}$ for 12 h. A homogenous paste was obtained using a mortar and pestle and coated on nickel foam with a diameter of 0.5 cm^2 using a spatula and dried at $80\text{ }^\circ\text{C}$ for 12 h. Ag/AgCl and Pt wire were used as the reference and counter electrodes, respectively for studies in three-electrode system. For two-electrode cell analysis, the homogenous paste was coated on coin-shaped nickel foam with a diameter of 20 mm and supercapattery cells were assembled in a Swagelok using nanoarchitected samples as the positive electrodes and activated carbon as the negative electrode. Cyclic voltammograms were recorded in a potential window of 0.1 to 0,8 V at different scan rates and electrochemical

impedance measurements were obtained at a frequency range of 0.1 MHz –100 kHz with 10 points per decade. CV curves, galvanostatic charge-discharge profiles and the cycling performance of the supercapattery cells were obtained in aqueous 1 M Na₂SO₄ electrolyte at a voltage of 1.8 V.

6.3 Results and Discussion

6.3.1 Structure and morphological Analysis by Scanning and Transmission Electron Microscopies (SEM and HRTEM)

The morphology of Li₂Mn_{1-x}Zn_xSiO₄/V₂O₅-CNT/G-ol_{10%} (N₁) and Li₂Mn_{1-x}Zn_xSiO₄/V₂O₅-CNT/G-ol_{5%} (N₂) nanoarchitected electrode materials were examined by SEM and HRTEM microscopies. Figure 6.2 (a) and (b) display the SEM and HRTEM micrographs of N₁ and N₂, respectively with their corresponding lattice fringes and selected area electron diffraction (SAED) images. SEM micrographs revealed that the zinc-doped Li₂MnSiO₄ (Li₂Mn_{1-x}Zn_xSiO₄, x = 4 %) mixed spherical and rhombedral nanoparticles, V₂O₅-CNT nanonetwork and G-ol nanosheets were completely hybridized to give mesoporous nanohybrids with a majority platelet morphology and some elongation especially in the case of N₂ with 5 % G-ol content. HRTEM images further highlighted the nanoarchitectural nature of the nanohybrids. The lattice fringes and SAED images are displayed as insets in the HRTEM images. The observed clear diffraction rings together with the very prominent lattice lines reveal the crystallinity of the materials. Crystallite sizes obtained using ImageJ ranged from 55.4 -159.8 nm for N₁ and from 35.8 – 92.7 nm for N₂. These results are shown in Table 6.1.

The elemental composition of N₁ and N₂ were confirmed using energy dispersive X-ray spectroscopy (EDS). Figure 6.2 (c) and (d) represent the EDS spectra and maps of N₁ and N₂, respectively. All expected elements are observed as well as the atomic and weight percentages represented as an overlaid layer on the electron images. As observed, the maps portray a homogenous distribution of all expected elements.

Table 6.1: Average crystallite sizes of N₁ and N₂ nanohybrid electrodes obtained from SEM micrographs

Electrode material	Average diameter	Standard deviation
	/ nm	/ nm
N ₁ -Li ₂ Mn _{1-x} Zn _x SiO ₄ /V ₂ O ₅ -CNT/G-ol ₁₀ %	106.7	± 25.1
N ₂ -Li ₂ Mn _{1-x} Zn _x SiO ₄ /V ₂ O ₅ -CNT/G-ol ₁₅ %	66.1	± 13.8



Figure 6.2 (a): SEM and HRTEM micrographs of N_1 with SAED and lattice fringes as insets

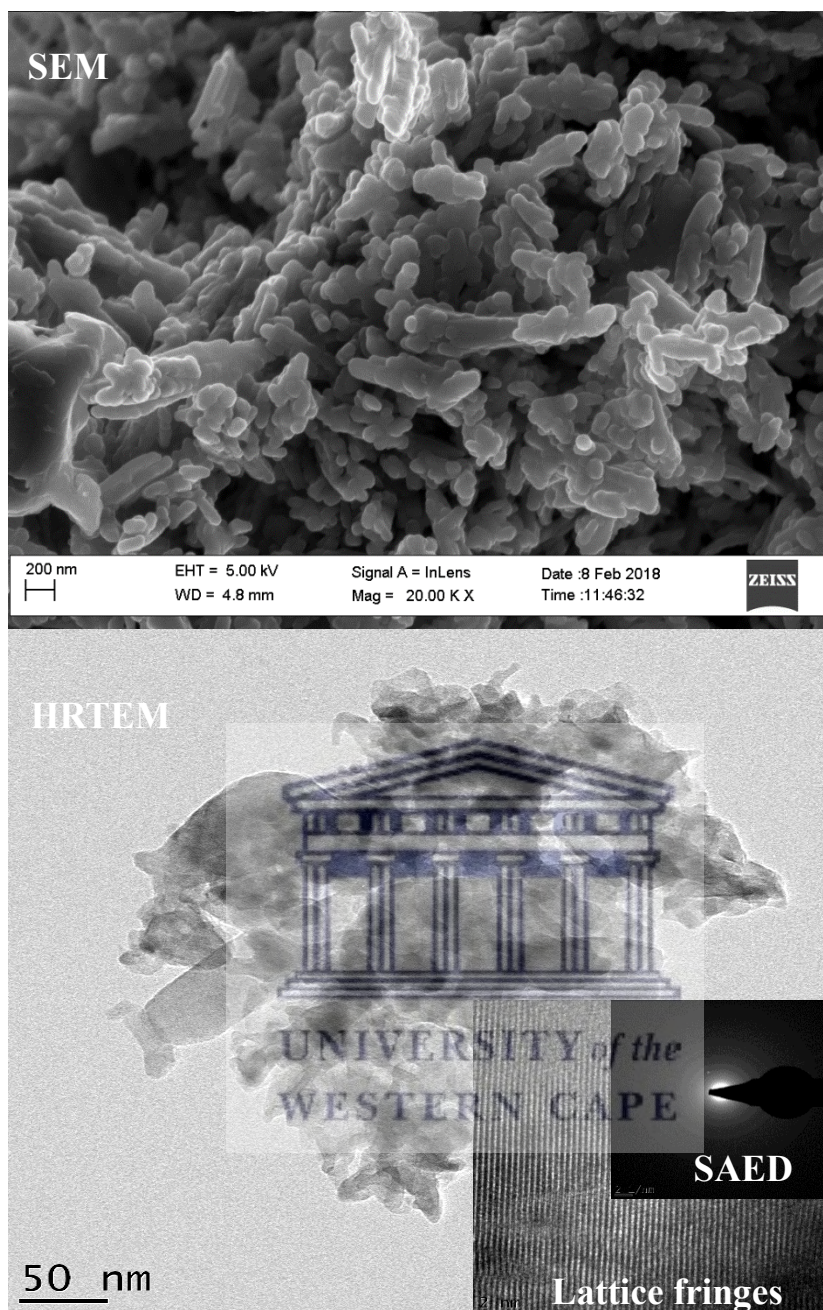


Figure 6.2 (b): SEM and HRTEM micrographs of N₂ with SAED and lattice fringes as insets

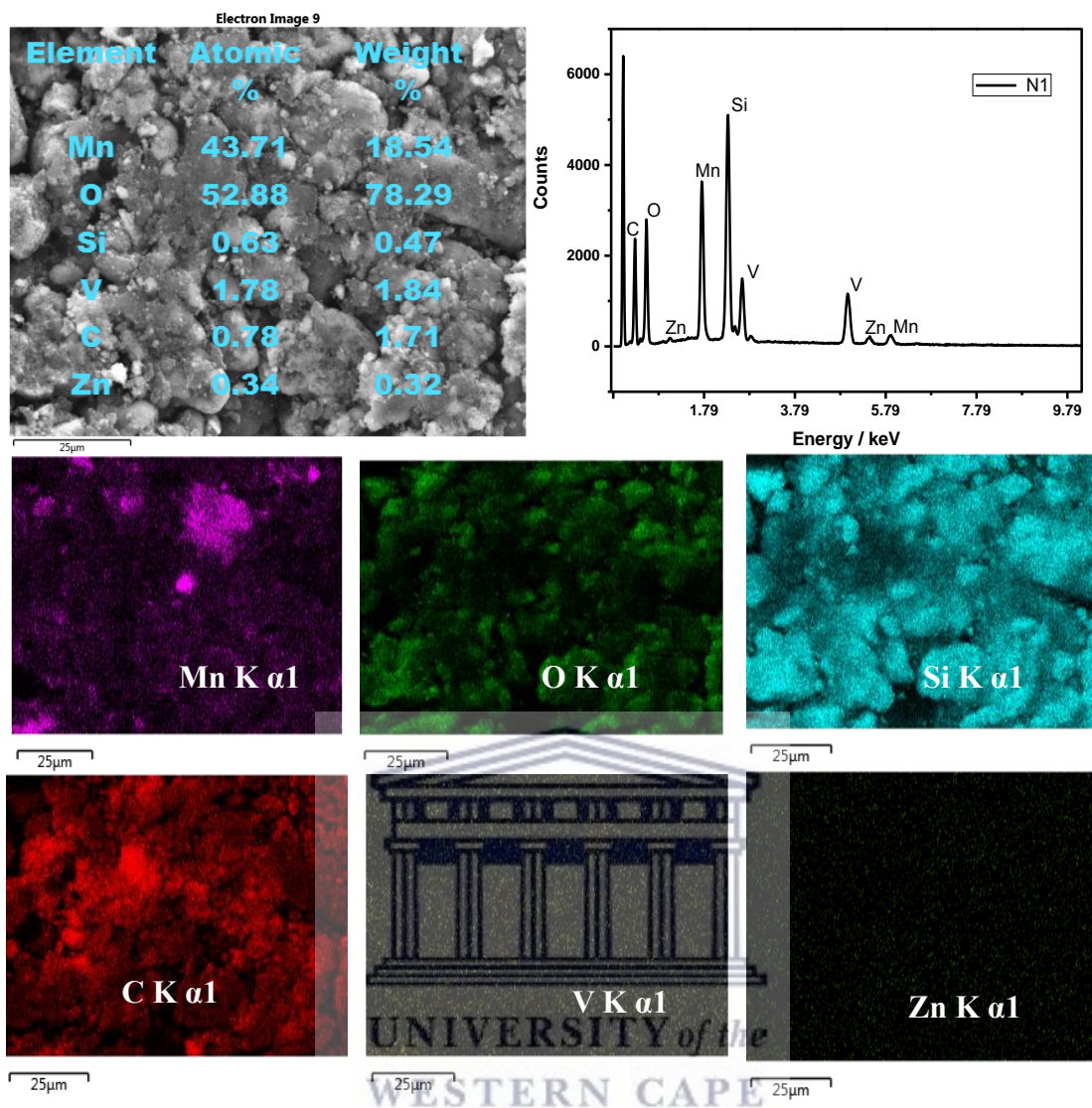


Figure 6.2 (c): EDS spectra and EDS maps of N₁ with elemental mass ratios overlaid on the electron images

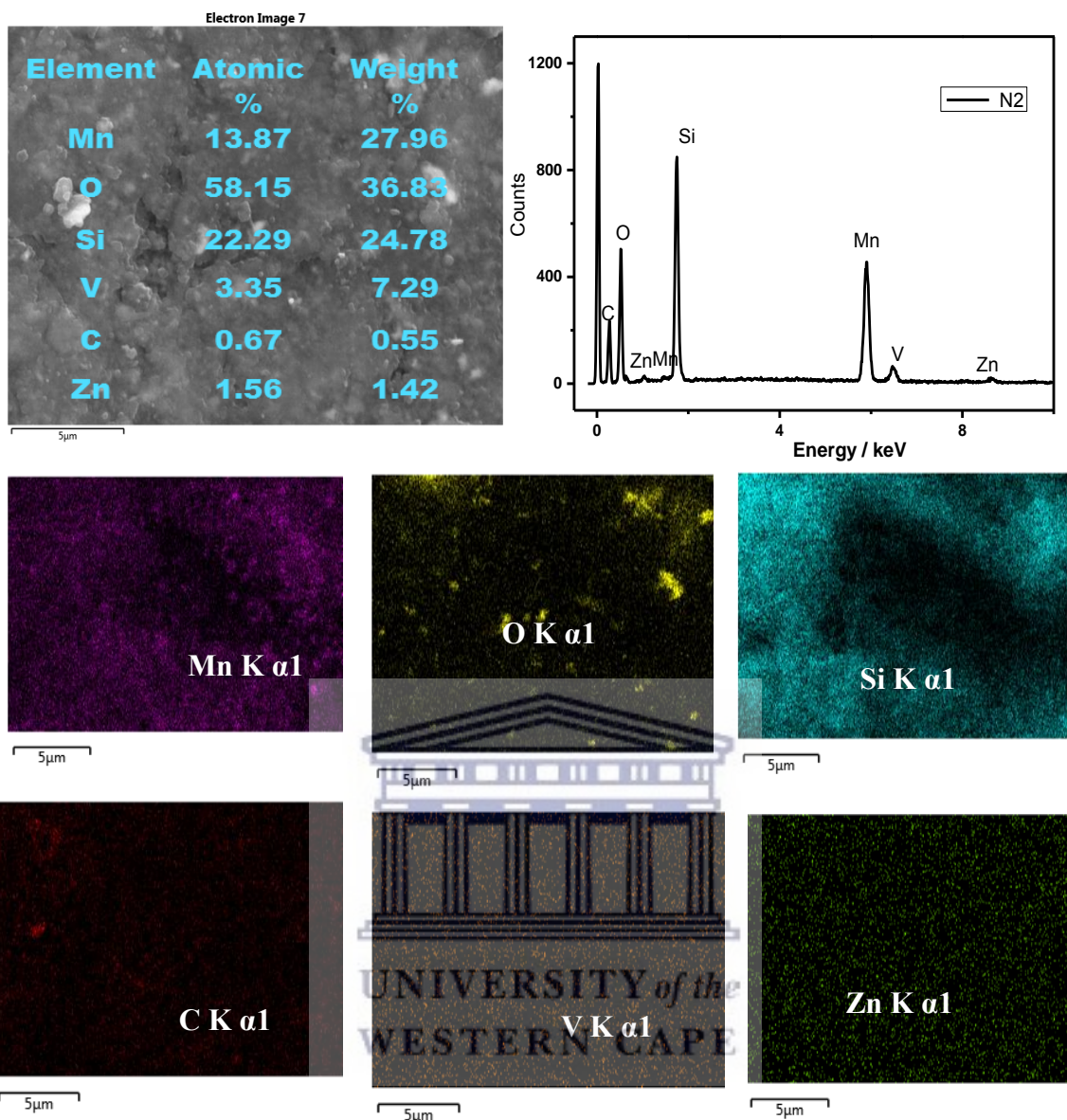


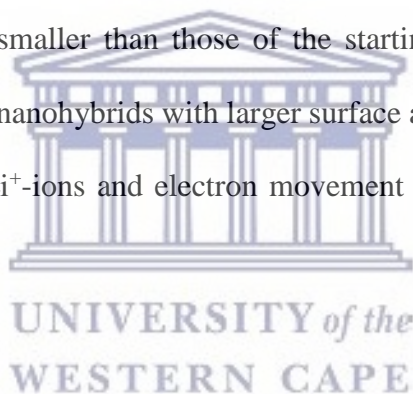
Figure 6.2 (d): EDS spectra and EDS maps of N₂ with elemental mass ratios overlaid on the electron images

6.3.2 Particle size distribution by Small Angle X-ray Scattering (SAXS)

The primary particle sizes and the size distribution of the different nanodomains in the nanomaterials were investigated using SAXS experiments. The scattering data was analyzed and displayed in the form of pair distance distribution functions with respect to the intensity and physical volume of the particles. Figure 6.3 (a) and (b) display the scattering profiles of the nanomaterials as a function of the scattered intensity and physical volume of the scattered particles, respectively. As shown in Figure 6.3 (a) the scattering curves of the intensity particle size distribution show N_1 to consist of an almost bell-shaped distribution with primary particles having center-peak (mean) at 12.3 nm and aggregates at 29.4 and 48.1 nm. This particle size range is lower than that obtained from morphological studies. This is due to the fact that morphological analysis provides information based on a small sample size which does not always account for the entire sample. While SAXS examines comparatively large portions of materials, and generally do not suffer from insufficient sampling [23,24]. The intensity particle size distribution of N_2 exhibits a bell-shaped distribution with mean particle sizes at 65.1 nm, indicating that the hierarchical nanomaterials show a similar form of aggregation [25].

Figure 6.3 (b) shows the pair distance distribution function of the nanomaterials with respect to the physical volume of scattered particles. In volume particle size distribution functions, each particle is considered as a sphere irrespective of its morphology. The obtained mean volume of the particle is therefore converted to the mean diameter of the particle. As such, aggregates of primary particles are measured as one big particle leading to a larger volume. In this regard, the volume of secondary particles (aggregates of primary particles) in G-ol, V_2O_5 -CNT and $Li_2Mn_{1-x}Zn_xSiO_4$ are unusually high as compared to the particle size distribution by intensity [26]. The particle size distribution by volume of G-ol and V_2O_5 -CNT display almost

dumbbell-shaped distributions with center-peaks of primary particles at 22.9 and 26.8 nm and secondary particles at 131.8 and 130.1 nm, respectively. The zinc doped electrode material ($\text{Li}_2\text{Mn}_{1-x}\text{Zn}_x\text{SiO}_4$) and N_1 nanohybrid displayed bell-shaped particle size distributions by volume for the primary particles with mean sizes at 23.5 and 24.2 nm, respectively as shown in Figure 6.3 (b₂). Agglomerates of $\text{Li}_2\text{Mn}_{1-x}\text{Zn}_x\text{SiO}_4$ particles showed a left-skewed distribution while secondary particles in N_1 showed a dumbbell-shaped distribution. This indicates the presence of size variations that were “seen” as larger spheres as observed in Figure 6.3 (a). N_2 nanohybrid also showed a bell-shaped particle size distribution by volume with mean size at 65.2 nm which further agrees with the similar aggregation of particles as observed in the intensity particle size distribution. It is worth noting that the particle sizes obtained for N_1 and N_2 are comparatively smaller than those of the starting materials indicating better hybridization and formation of nanohybrids with larger surface area and high packing density, essential for the diffusion of Li^+ -ions and electron movement for enhanced electrochemical performance.



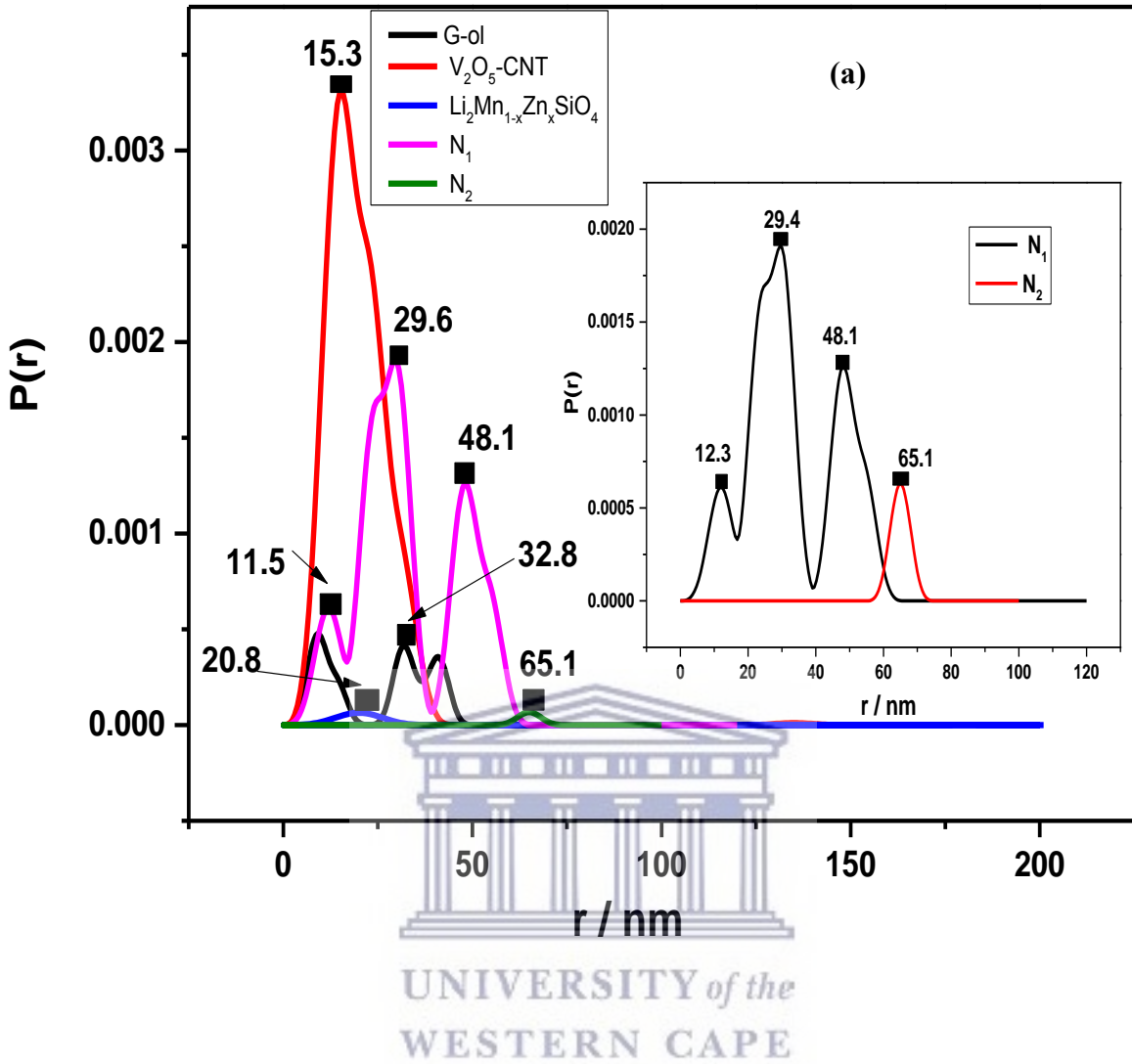


Figure 6.3 (a): SAXS pair distance distribution functions of G-ol, V_2O_5 -CNT, $Li_2Mn_{1-x}Zn_xSiO_4$, N_1 and N_2 nanomaterials by intensity of scattered particles

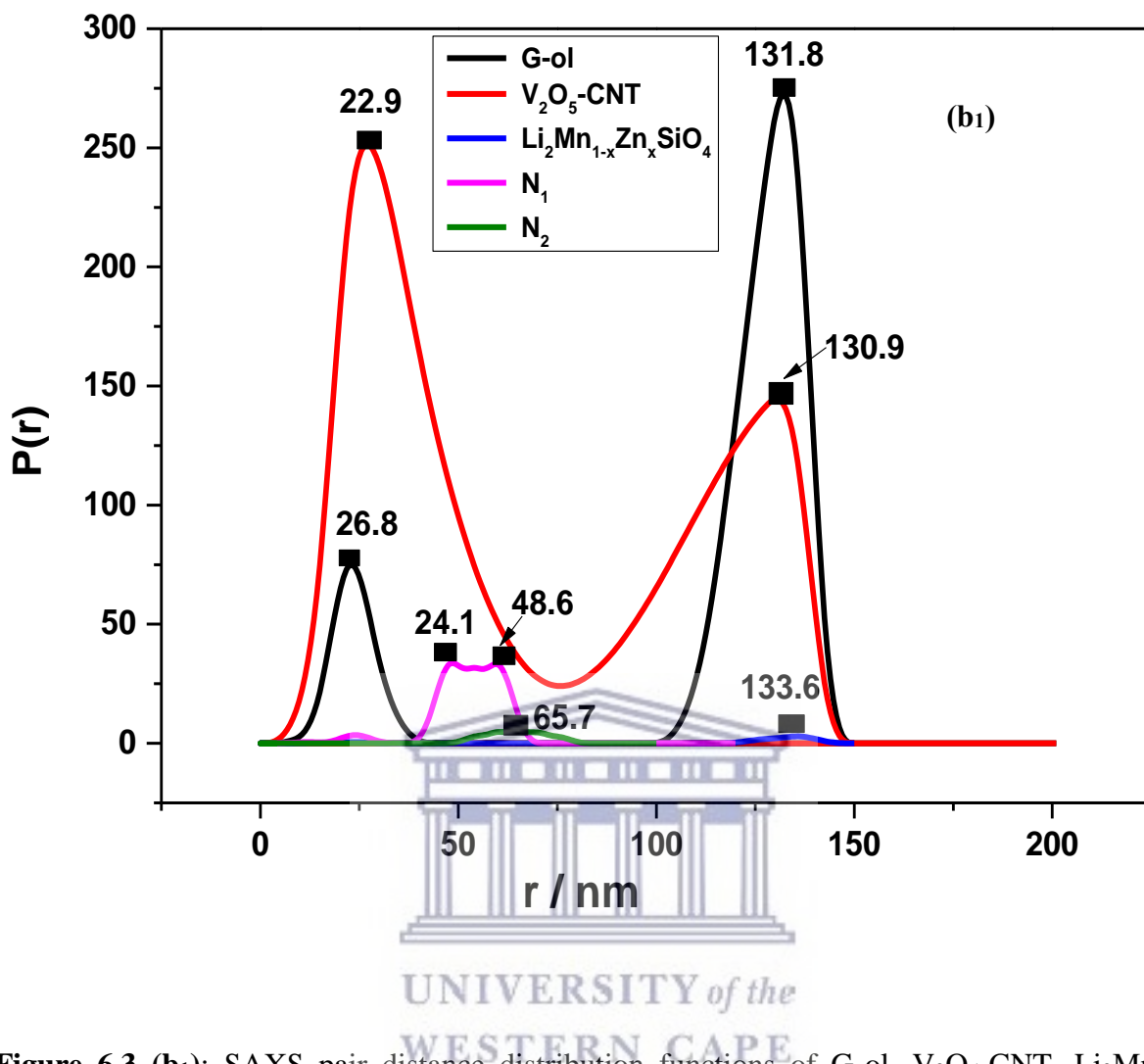


Figure 6.3 (b₁): SAXS pair distance distribution functions of G-ol, V₂O₅-CNT, Li₂Mn_{1-x}Zn_xSiO₄, N₁ and N₂ nanomaterials by physical volume of particles scattered

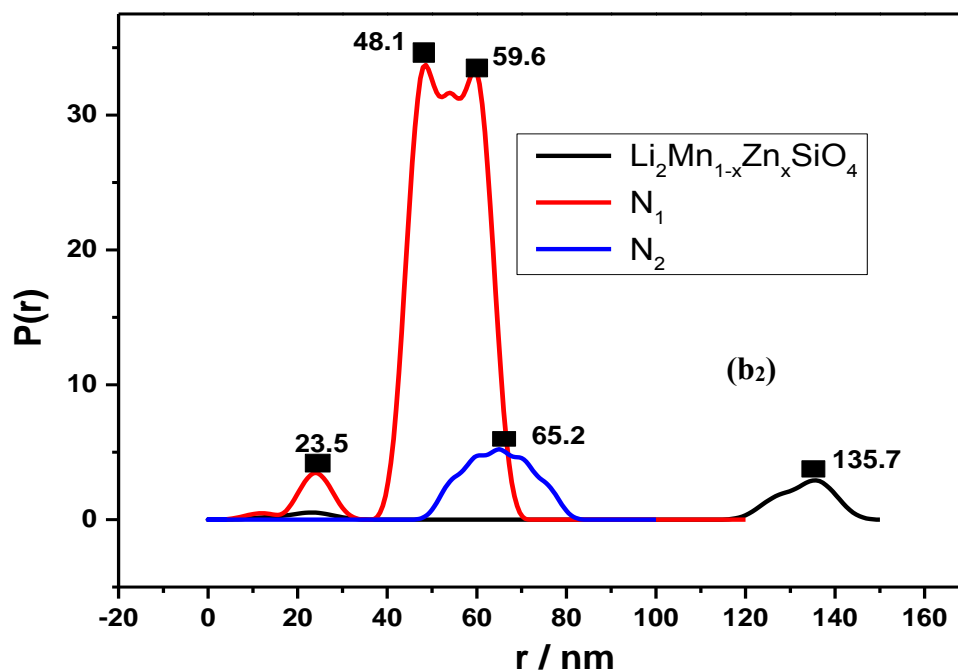


Figure 6.3 (b2): SAXS pair distance distribution functions of G-ol, $\text{V}_2\text{O}_5\text{-CNT}$, $\text{Li}_2\text{Mn}_{1-x}\text{Zn}_x\text{SiO}_4$, N_1 and N_2 nanomaterials by physical volume of particles scattered



6.3.3 Crystallography by X-ray Diffraction Studies (XRD)

6.3.3 (a) Crystal structure and phase identification

XRD was used to obtain further structural information such as the crystallite size, interplanar spacing, crystalline phase and purity of the nanoarchitected N_1 and N_2 electrode materials in addition to results discussed in previous chapters on G-ol, $\text{V}_2\text{O}_5\text{-CNT}$, $\text{Li}_2\text{Mn}_{1-x}\text{Zn}_x\text{SiO}_4$ nanomaterials. Figure 6.4 presents the XRD patterns of N_1 and N_2 nanohybrids compared with the starting nanomaterials (G-ol, $\text{V}_2\text{O}_5\text{-CNT}$ and $\text{Li}_2\text{Mn}_{1-x}\text{Zn}_x\text{SiO}_4$) at a 2θ range of $5 - 80^\circ$.

The diffraction peaks at 2θ values of 17.8° , 26.6° , 32.8° , 38.4° , 59.1° and 73.2° in the XRD spectrum of N_2 are well indexed to the orthorhombic $Pmn2_1$ space group, belonging to the (010), (110), (210), (002), (212) and (232) crystalline planes of Li_2MnSiO_4 . These diffraction peaks are slightly blue-shifted in N_1 nanohybrid due to the higher G-ol content. Minor peaks observed at 2θ values of 10.2° and 25.2° in N_1 and 10.3° in N_2 can be assigned to the 001 and 002 planes of oxygenated graphene sheets found in G-ol [27,28]. The disorder feature of graphitic materials which is indicated by the broadening of the 002 plane [29] is also observed in the N_1 nanohybrid, thus confirming the higher content of G-ol in N_1 (10 %) over N_2 (5 %). N_2 nanohybrid also presents lower peak intensities, indicating the smaller crystallite sizes compared to N_1 . No peaks were observed that could be assigned to V_2O_5 . The average crystallite sizes of N_1 and N_2 were calculated based on the Scherrer's formula [30] as shown in Equation 6.1.



$$D = \frac{K\lambda}{\beta \cos \theta} \quad (6.1)$$

Where D represents the mean crystallite size (nm), K , is the Scherrer's constant (0.89), λ is the wavelength of the X-rays (Cu $K\alpha_1 = 1.54 \text{ \AA}$), β is the peak width at half height of the (010) diffraction peak (rads), and θ is the angle of reflection of the crystalline plane (degrees).

The interlayer spacing plays an important part in the insertion and removal of Li-ions into the crystal lattice of electrode materials. The interlayer spacing of N_1 and N_2 nanohybrids were calculated according to Bragg's law [29], represented by Equation 6.2. These values are displayed in Table 6.2.

$$n\lambda = 2d\sin\theta \quad (6.2)$$

Where, n denotes the order of diffraction ($n = 1$), λ ; the wavelength of the X-ray beam (1.54 Å), d ; the distance between MnSiO₄ and LiO₄ layers (nm) and θ is the diffraction angle (degrees).

Table 6.2: Structural parameters of N₁ and N₂ nanohybrids obtained from XRD analysis

Electrode material	Average crystallite size / nm	Interlayer spacing / nm
N ₁ -Li ₂ Mn _{1-x} Zn _x SiO ₄ /V ₂ O ₅ -CNT/G-0h10%	67.2	0.495
N ₂ -Li ₂ Mn _{1-x} Zn _x SiO ₄ /V ₂ O ₅ -CNT/G-0l5%/	62.1	0.473

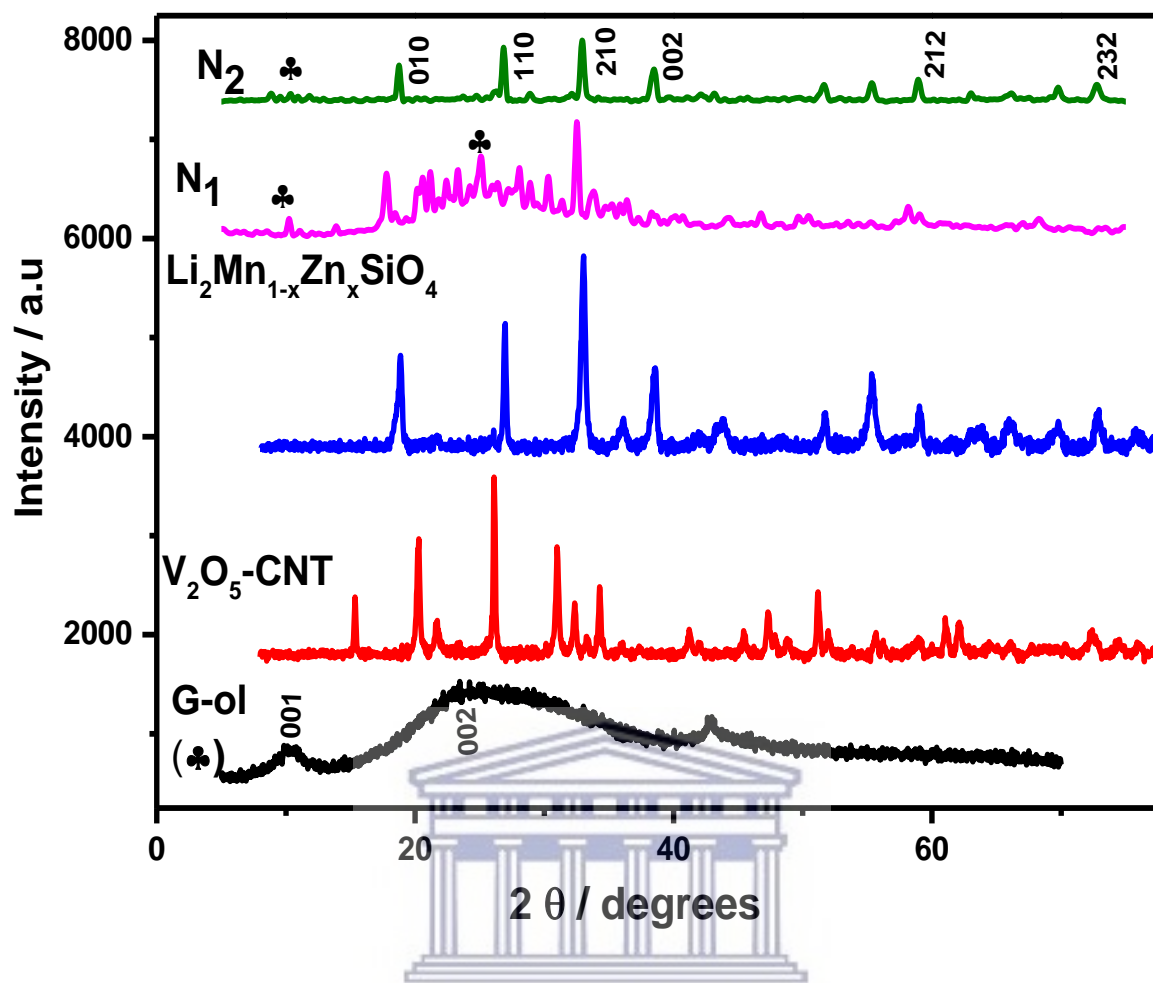


Figure 6.4: XRD spectra of G-ol, V_2O_5 -CNT, $Li_2Mn_{1-x}Zn_xSiO_4$ nanomaterials and N_1 and N_2 nanohybrids

6.3.3 (b) Crystal structure models and atom connectivity

Crystal structure simulations to reveal atomic arrangements or orientations of the crystal subunits of N_1 and N_2 nanohybrid electrode materials were performed by a combined study involving Match and Endeavour structure solution softwares. Figure 6.5 displays the crystal structure models, unit cells and cell axes of N_1 and N_2 nanohybrid electrodes. As discussed in section 6.3.3 (a), major diffraction peaks in N_1 and N_2 nanohybrids were indexed to the orthorhombic $Pmn2_1$ space group of Li_2MnSiO_4 which is isostructural to the low temperature

form of Li_3PO_4 structure. The orthorhombic $\text{Pmn}2_1$ space group is reported to be the most stable form of $\text{Li}_2\text{MnSiO}_4$ and consists of corner-sharing tetrahedra pointing towards the same orientation along the c axis. The crystal structure consists of layers of MnSiO_4 which lie on the ac -plane and linked by LiO_4 tetrahedra along the b -axis. Li ions occupy tetrahedral sites located between two of the MnSiO_4 layers, with a pathway for lithium motion to facilitating the extraction/insertion process [31–33]. The crystal model structure of N_1 with 10 % G-ol content is displayed in Figure 6.5 (a), the introduction of the conductive carbon layer into the nanohybrid crystal displaces some MnSiO_4 layers from the ac -plane towards the b -plane and thus changing the orientation of some of the MnSiO_4 layers. This may be detrimental to the electrochemical performance of N_1 nanohybrid electrode since the dimensional movement of Li-ions is impeded. Figure 6.5 (b) presents the crystal model structure of N_2 . The conductive carbon layer is also observed but without displacing the MnSiO_4 layers along the ac -plane. However, a slight disorientation of the SiO_4 tetrahedra is also observed which may be attributed to the presence of other nanomaterials like V_2O_5 and CNTs in the crystal lattice. The N_2 nanohybrid crystal model also shows a higher degree of nucleation which will enable a higher packing density and high surface area of the electrode, resulting in enhanced electrochemical performance.

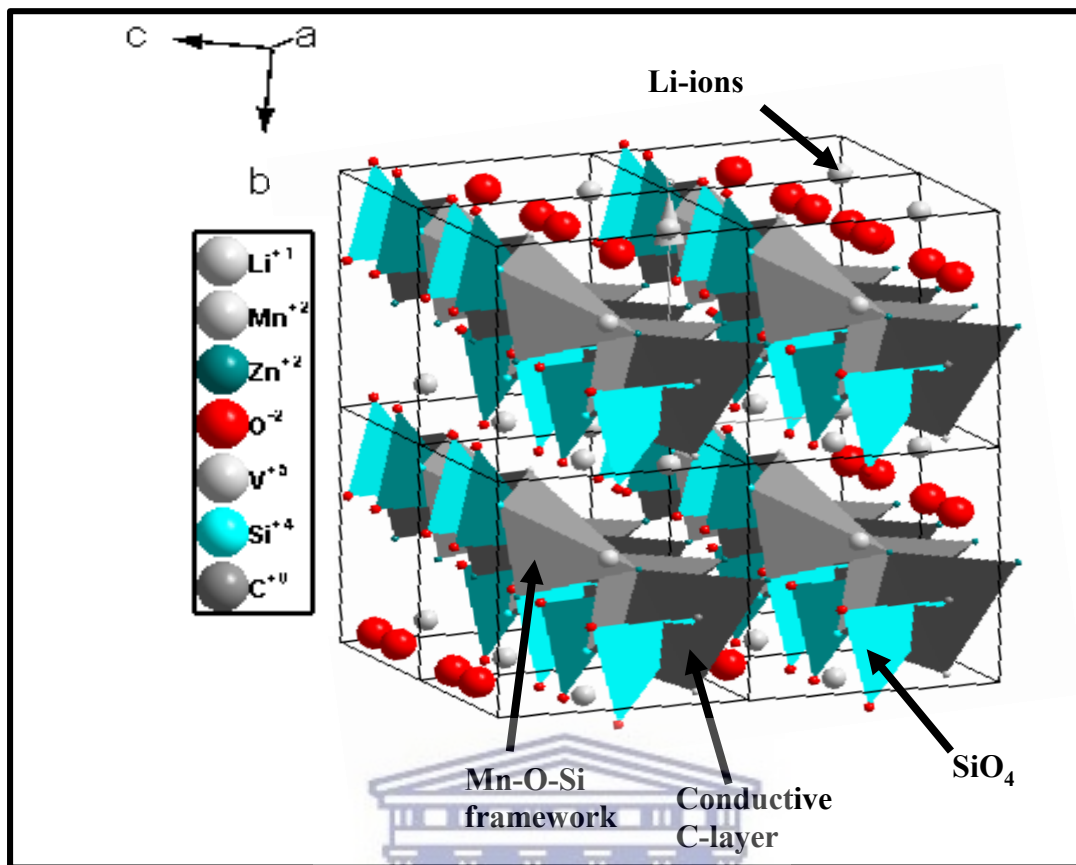


Figure 6.5 (a): Crystal structure model of N₁ nanohybrid electrode material

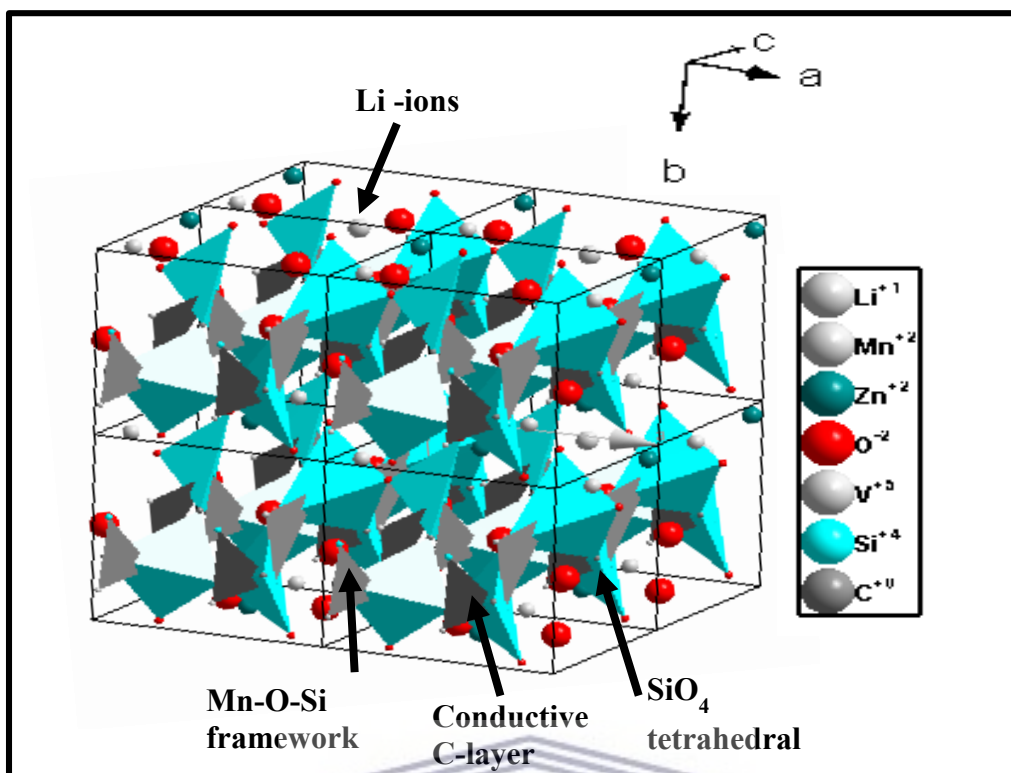
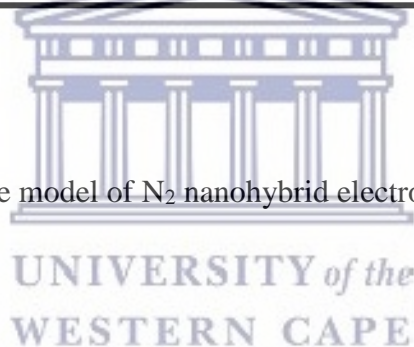


Figure 6.5 (b): Crystal structure model of N₂ nano hybrid electrode material



6.3.4 Functional group Analysis by Fourier transform Infrared (FTIR) Spectroscopy

Further structural characterization of N₁ and N₂ electrode materials were performed using FTIR spectroscopy to investigate the nature of functional groups/bond vibrations present in N₁ and N₂ electrodes. Figure 6.6 displays the FTIR spectra of G-ol, V₂O₅-CNT, Li₂Mn_{1-x}Zn_xSiO₄, N₁ and N₂ electrode nanomaterials. Bands are presented in the region of 400 cm⁻¹ - 4000 cm⁻¹. The bands around 420 - 494 cm⁻¹ are assigned to the stretching motion of [LiO₄] tetrahedra. Asymmetric and symmetric vibrations of Si-O-Si and V-O-V bonds are observed in the region of 511 - 933 cm⁻¹. Bands around 1060 - 1164 cm⁻¹ are assigned to the vibration of Mn-O-Si

layers observed in the crystal structure models and the stretching of epoxy and alkoxy groups in G-ol. The peaks at 1641.4 cm^{-1} and 1371.8 cm^{-1} are assigned to C=C and C-O bonds from the graphitic domains in the nanomaterials. The symmetric and asymmetric vibrations of the C-H bonds are observed at 2828.6 and 2955.7 cm^{-1} , respectively. These bands also show a higher intensity in N_1 nanohybrid electrode compared to N_2 , indicating the higher content of G-ol in N_1 over N_2 . The peaks at 1641.4 cm^{-1} and 1371.8 cm^{-1} are assigned to C=C and C-O bonds from the graphitic domains in the nanomaterials. The symmetric and asymmetric vibrations of the C-H bonds are observed at 2828.6 and 2955.7 cm^{-1} , respectively. A strong OH characteristic band is observed in the nanomaterials in the region of $3000 - 3500\text{ cm}^{-1}$.

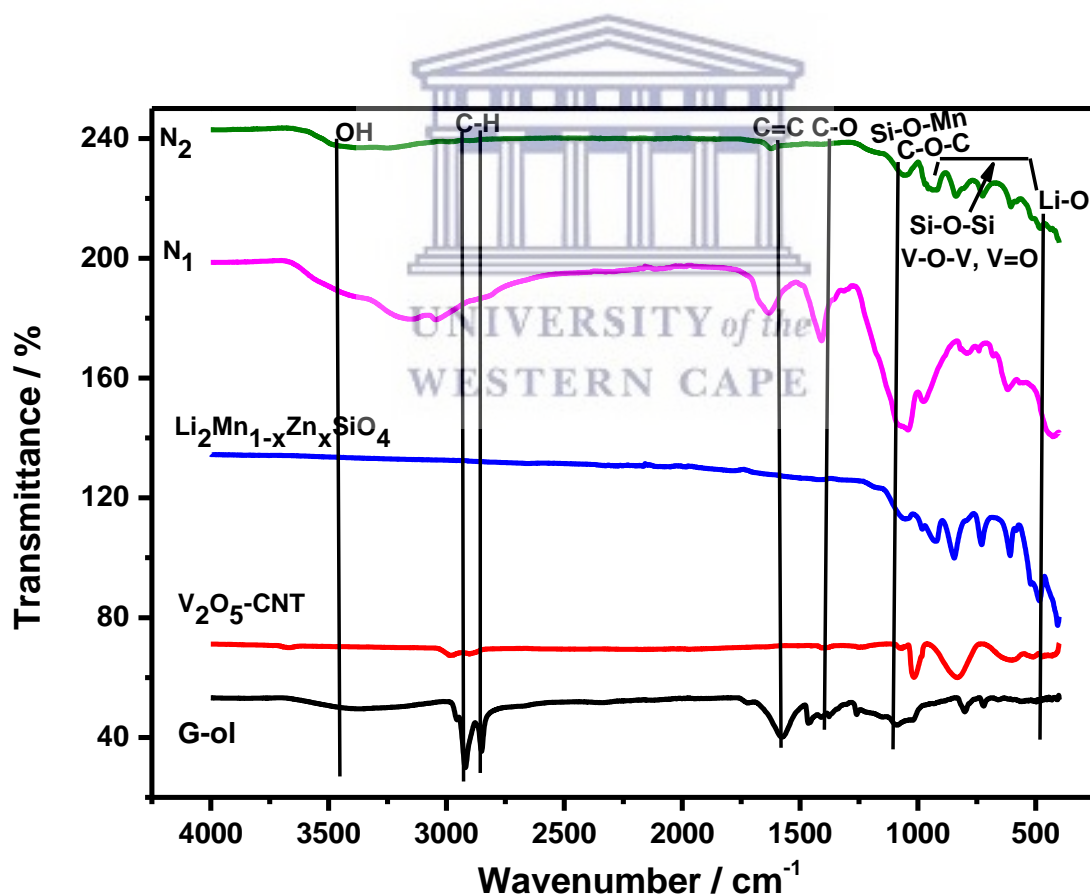


Figure 6.6: FTIR spectra of G-ol, V₂O₅-CNT, Li₂Mn_{1-x}Zn_xSiO₄, N₁ and N₂ electrode nanomaterials.

6.4 Raman Spectroscopy

Raman spectroscopy was used to obtain more structural information especially that of the disordered sp² carbon sites found in the nanomaterials. Figure 6.7 displays the Raman spectra of G-ol, V₂O₅-CNT, Li₂Mn_{1-x}Zn_xSiO₄, N₁ and N₂ electrode nanomaterials obtained with an excitation laser of 514.9 nm. The peak observed around 324.8 cm⁻¹ is ascribed to the metal-oxygen bending vibrations such as Mn-O and V-O bonds [34]. The peak appearing at ~483.9 cm⁻¹ comes from the silicon background used for Raman analysis [35]. The defect band (D-band) of graphitic carbon was observed at ~1448.7 cm⁻¹ while the band related to the planar configuration of graphitic sp² carbon sites (G-band) was observed at ~1527.3 cm⁻¹. The presence of graphitic nanomaterials like CNT and graphol in the nanohybrid electrode materials are further confirmed by the presence of the 2D-band (double overtone of the D-band) and the D+G-band (band indicating the presence of edge-like defects in the basal planes of the graphitic materials) at 2441.5 cm⁻¹ and 2910.2 cm⁻¹, respectively [36].

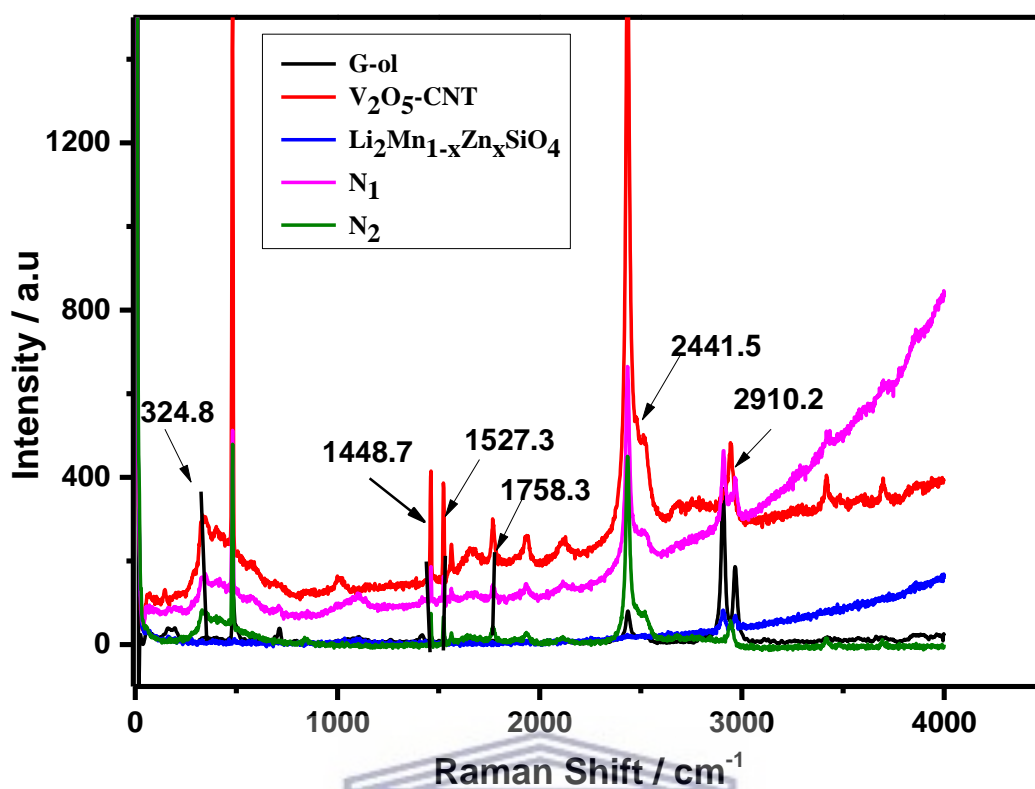


Figure 6.7: Raman spectra of G-ol, V_2O_5 -CNT, $Li_2Mn_{1-x}Zn_xSiO_4$, N_1 and N_2 electrode nanomaterials with excitation laser of 514.9 nm.

6.5 (a) Electrochemical Performance

Electrochemical properties of the electrode materials were investigated using cyclic voltammetry (CV), electrochemical impedance spectroscopy (EIS) and galvanostatic charge-discharge experiments in 1 M sodium sulfate (Na_2SO_4) aqueous electrolyte. Electrochemical properties of $Li_2Mn_{1-x}Zn_xSiO_4$, G-ol and V_2O_5 -CNT electrode materials have been discussed comprehensively as individual electrodes in previous chapters of this work, hence more emphasis will be laid on N_1 and N_2 nanohybrid electrode materials in the succeeding sections.

i) Cyclic Voltammetric (CV) studies

CV experiments in three electrode configuration were performed at a potential window of 0.1 – 0.8 V at scan rates of 5 – 100 mV s⁻¹ to determine the intercalation processes of the electro-active species and surface bound reactions. Figure 6.8 (a) displays a comparative CV plot of Li₂Mn_{1-x}Zn_xSiO₄, N₁ and N₂ nanohybrid electrode materials at a scan rate of 80 mV s⁻¹ with G-ol and V₂O₅-CNT as the inset. As observed, the N₂ nanohybrid electrode demonstrates better charge storage capability as evidenced by its higher current and area of the CV curve due to the presence of better electron transport channels endowed by the particle morphology and conductive frameworks, which facilitates the rapid transfer of electrons.

The CV curves of N₂ nanohybrid electrode at different scan rates are shown in Figure 6.8 (b). It is worth noting that the current increases with increasing scan rate and the shape of the CV curves remains unchanged even at higher scan rates, suggesting a good reversibility of the nanohybrid electrode. The shape of the CV curves suggests a charge storage mechanism of the electrode involving surface bound faradaic reactions such as oxidation/reduction of manganese and vanadium ions together with Li⁺ ion insertion/de-insertion [37].

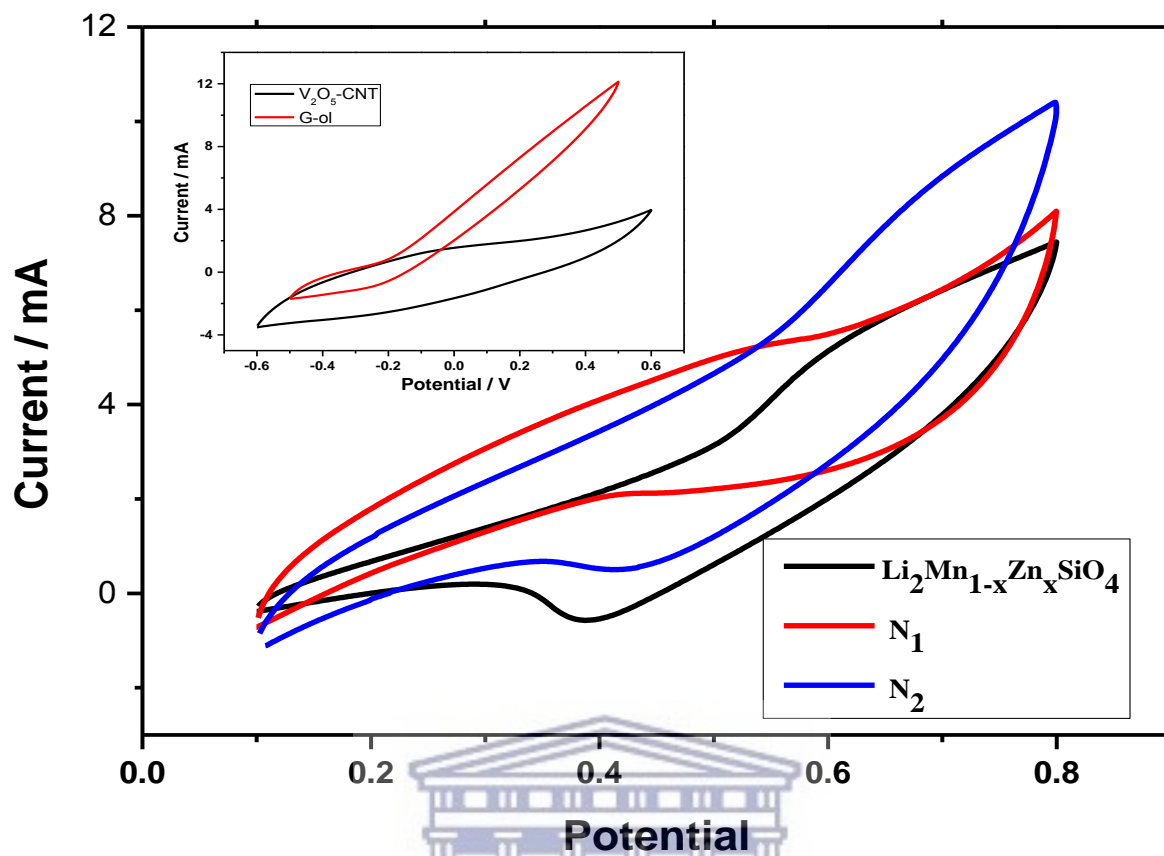


Figure 6.8 (a): Comparative CV curves of $\text{Li}_2\text{Mn}_{1-x}\text{Zn}_x\text{SiO}_4$, N_1 and N_2 electrodes with G-ol and $\text{V}_2\text{O}_5\text{-CNT}$ as inset at a scan rate of 80 mV s^{-1} in 1 M sodium sulfate (Na_2SO_4) aqueous electrolyte

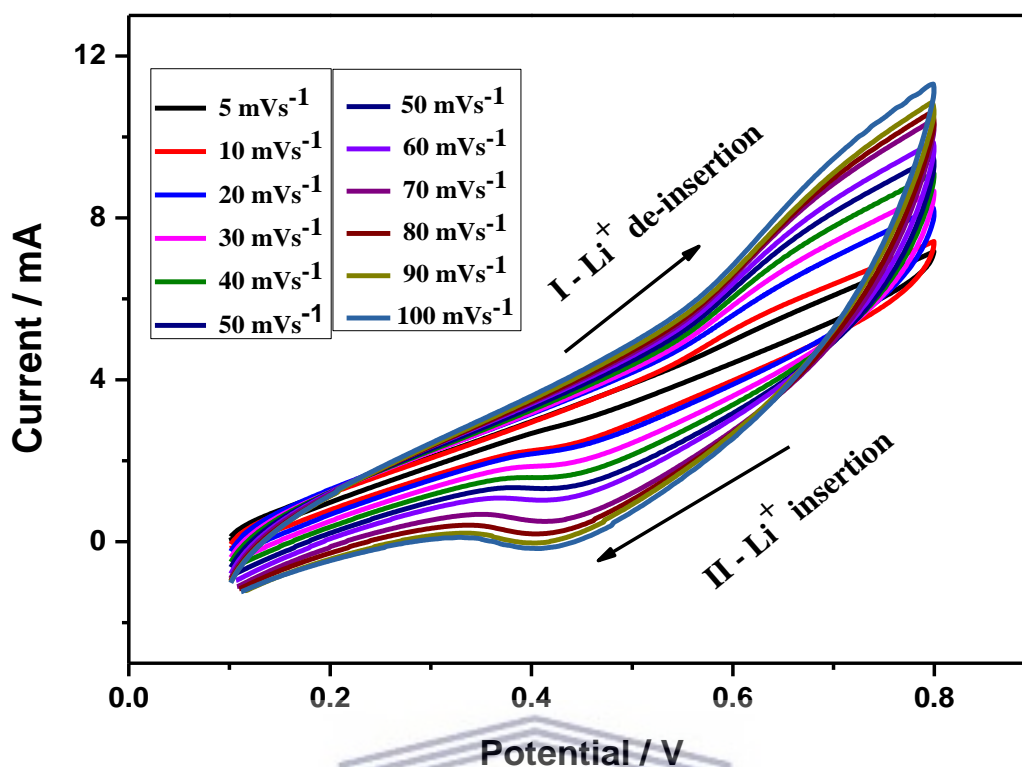
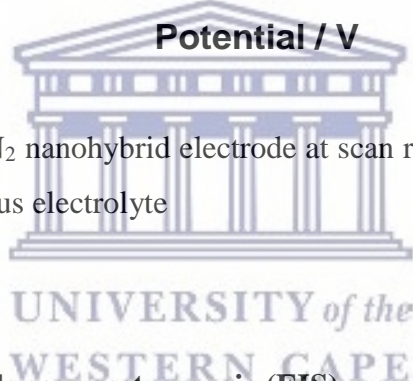


Figure 6.8 (b): CV curves of N₂ nanohybrid electrode at scan rates of 5 – 100 mV s⁻¹ in 1 M sodium sulfate (Na₂SO₄) aqueous electrolyte



ii) Electrochemical impedance spectroscopic (EIS) measurements

EIS studies were employed to evaluate ion diffusion processes in the N₁ and N₂ nanohybrid electrodes. Figure 6.9 (a) presents comparative Nyquist plots of N₁ and N₂ nanohybrid electrode materials at open circuit voltage in 1 M Na₂SO₄ electrolyte. The plots consists of a semicircle in the high-medium frequency region, which describes the charge transfer resistance (R_{ct}) followed by a vertical line parallel to the imaginary axis, the frequency dependent Warburg diffusion (W_o) of Li-ions which is typical of capacitive behavior [38,39]. The very inclined line of N₁ suggests capacitance contribution, indicating the higher content of G-ol nanosheets. EIS curves were fitted using Z-view circuit models shown in Figure 6.9 (b). Values

obtained for the internal resistance (R_s), capacitance contribution (C_1), constant phase element (CPE), Warburg diffusion (W_o), R_{ct} and phase angle for the nanohybrid electrodes are outlined in Table 6.3. Even though N_2 possesses a lower phase angle (7.1°) compared to N_1 (17.8°) which suggest lower conductivity as shown in Figure 6.10 (b), the R_{ct} value of N_2 (2.29Ω) is lower than that of N_1 (4.02Ω), indicating faster movements electro-active species in the electrode.

Table 6.3: EIS curve fitting data of N_1 and N_2 nanohybrid electrodes

Electrode material	R_s / Ω	$C_1, CPE / \mu F$	R_{ct} / Ω	$W_s, W_o / \Omega s^{-1/2}$	Phase angle / $^\circ$
N_1	2.14	$1.42 E^{-05}$	4.02	0.47	17.8
N_2	8.83	0.62	2.29	0.69-	7.1

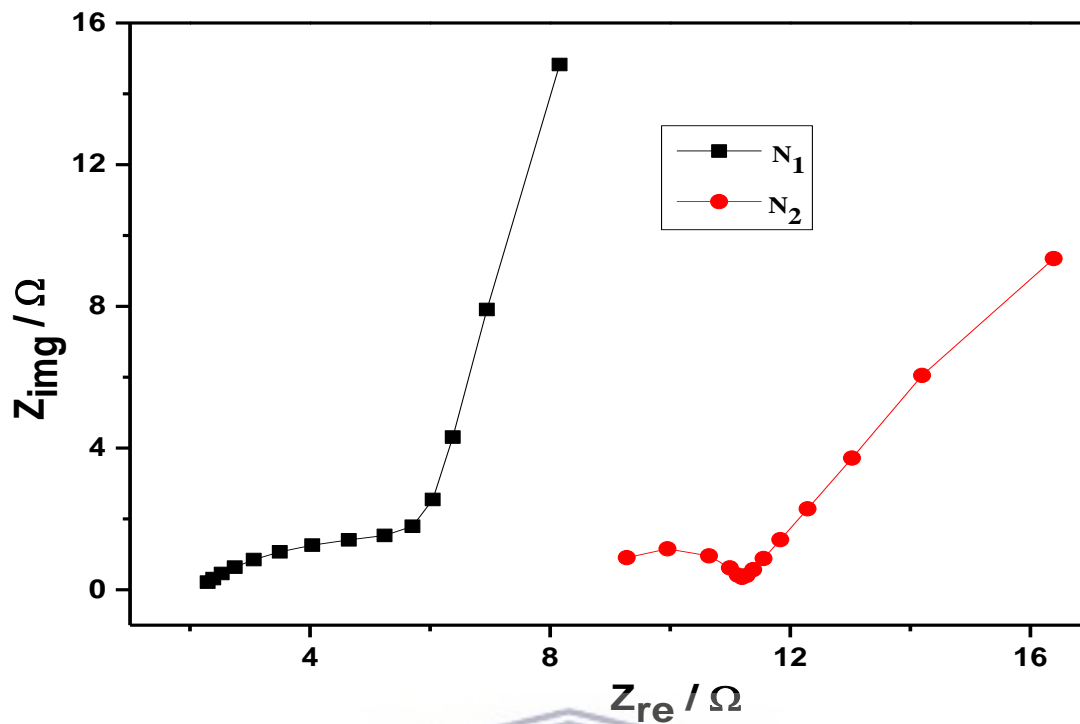


Figure 6.9 (a): Nyquist plots of N_1 and N_2 nanohybrid electrodes at OCV

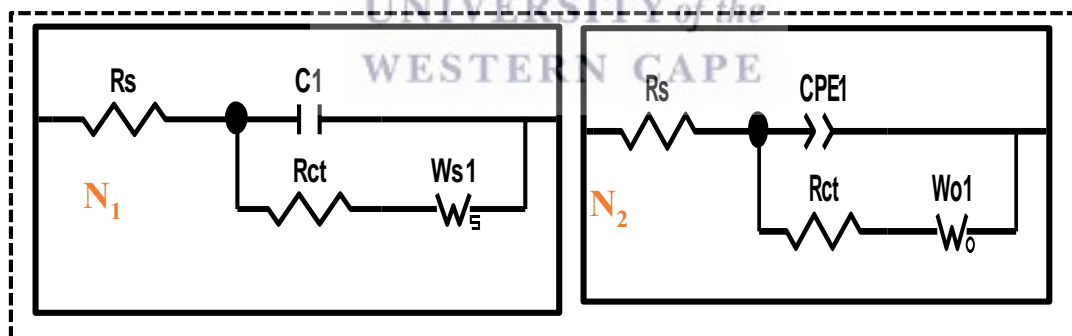


Figure 6.9 (b): Circuit models used to fit EIS data

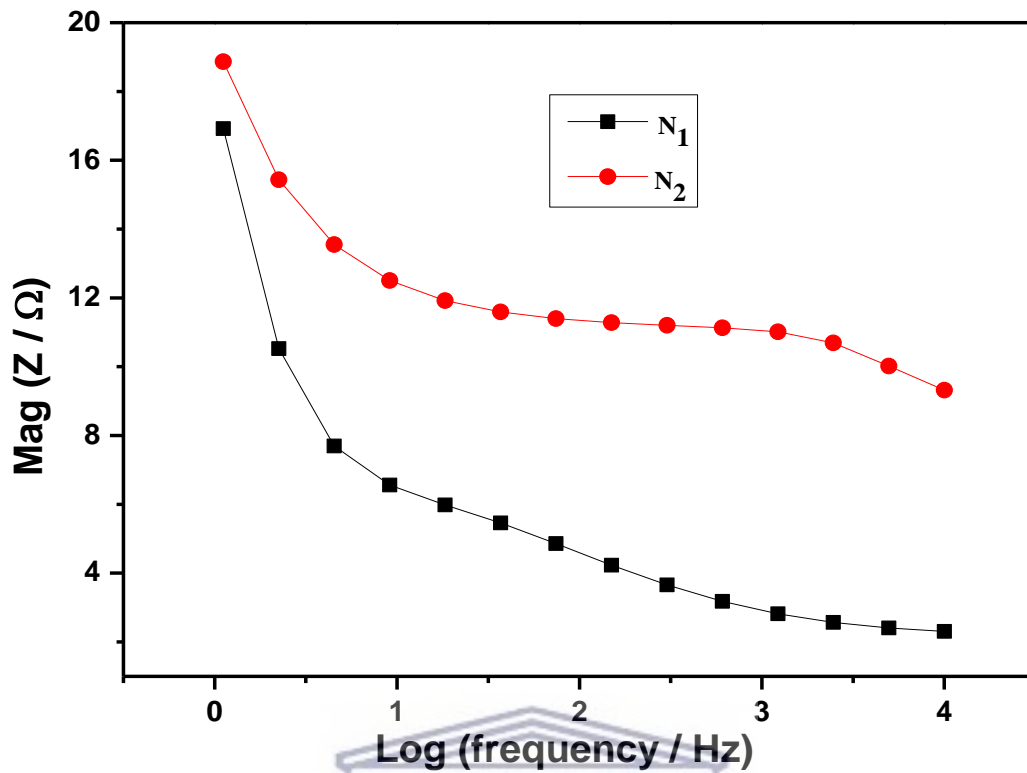


Figure 6.10 (a): Total impedance Bode plots of N₁ and N₂ nano hybrid electrode materials

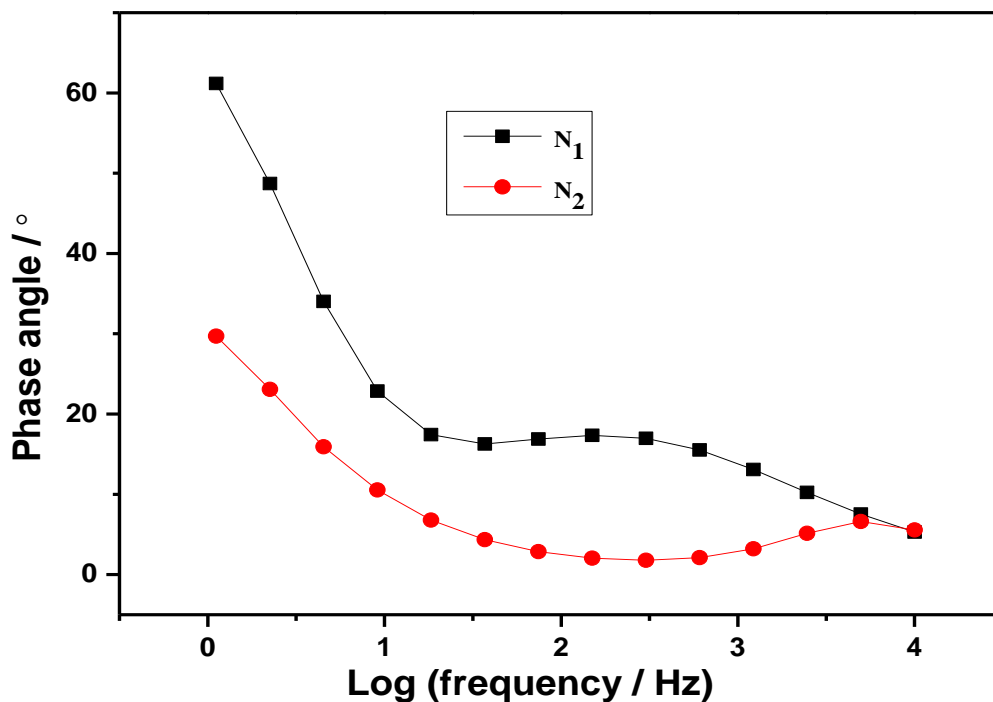


Figure 6.10 (b): Phase angle Bode plots of N₁ and N₂ nanohybrid electrode materials



6.5 (b) Electrochemical Performance of the fabricated asymmetric supercapacitor devices

The energy storage capabilities of the nanohybridized electrodes were evaluated by fabricating Swagelok-type supercapattery devices using N₁ and N₂ nanohybrid electrode materials as positive electrodes and activated carbon as the negative electrode. Studies were performed in 1 M Na₂SO₄ aqueous electrolyte at a voltage window of 1.6 V and extended to 1.8 V to increase the specific energy.

iv) Cyclic Voltammetric studies of supercapattery devices

Figure 6.11 (a) shows the CV curves of activated carbon and N₂ nanohybrid electrode at a scan rate of 50 mV s⁻¹. The comparative plot was used to establish the use of the the nanohybrid electrodes as the positive electrode and activated carbon as the negative electrode. The activated carbon electrode exhibited rectangular shaped CV curves which are very indicative of capacitive behavior in the potential range of -0.8 – 0.1 V. Meanwhile N₂ showed surface bound interconversion reactions as earlier mentioned.

To confirm the optimum or stable voltage window of the device to maximize its specific energy in 1 M Na₂SO₄ aqueous electrolyte, the device was investigated at different voltages ranges from 0 – 1.8 V at a scan rate of 80 mV s⁻¹ as shown in Figure 6.11 (b). It is observed that the CV curves retain a rectangular shape up to 1.4 V, with a slight increase in anodic current at 1.8 V, indicating some electrolyte decomposition or unwanted side reactions [40].

A comparative plot of the N₁ and N₂ based supercapatteries with AC is shown in Figure 6.11 (c). AC//N₂ exhibits noticeable increase in the current response, signifying better specific capacitance as well as a higher electrochemical performance over the AC//N₁ device as observed in studies in the three electrode cell design.

CV curves of the AC//N₂ supercapattery at different scan rates are exhibited in Figure 6.11 (d). It is observed that with increasing scan rate, the area of the AC//N₂ device gradually becomes larger due to the effective combination of EDLCs and pseudocapacitance, implying that a hybrid device (supercapattery) has been successfully assembled [41].

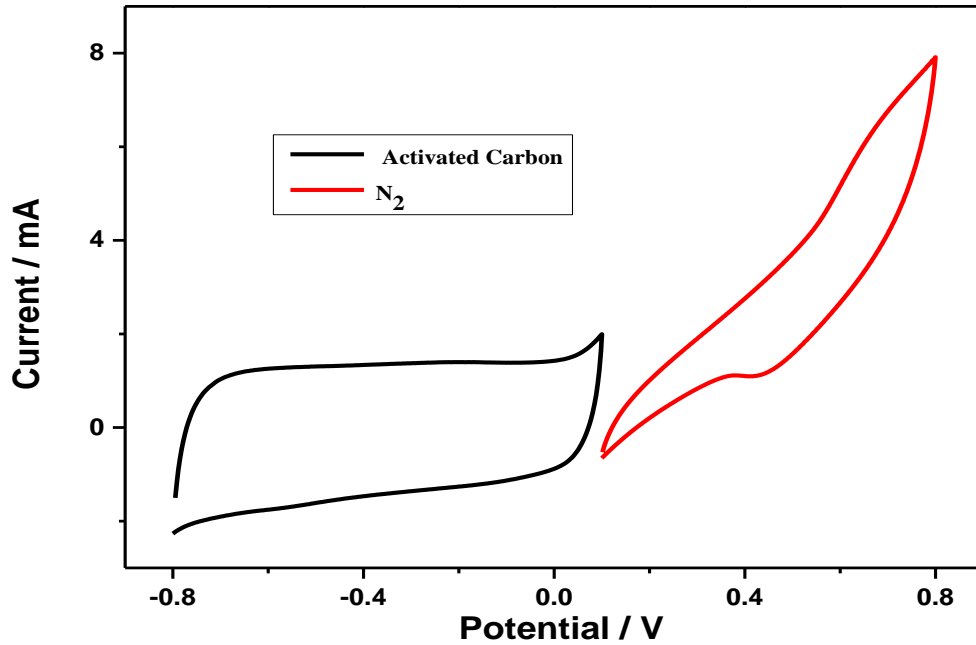


Figure 6.11 (a): CV curves of activated carbon and N₂ nano hybrid electrodes at a scan rate of 50 mV s⁻¹ in 1 M Na₂SO₄ aqueous electrolyte

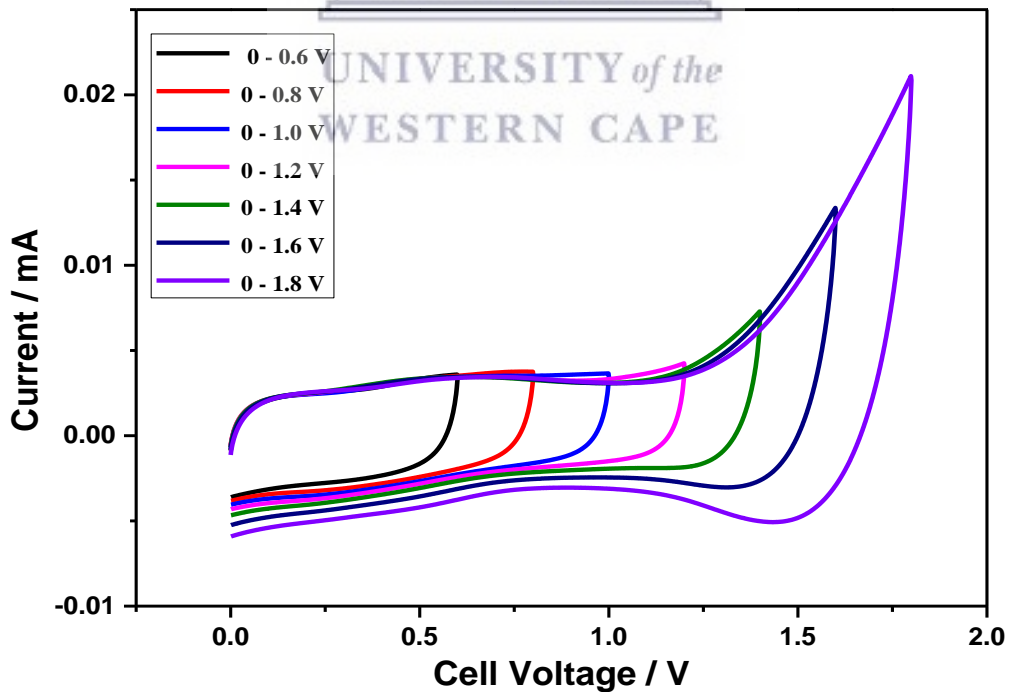


Figure 6.11 (b): CV curves of AC/N₂ supercapattery at various potential ranges from 0 – 1.8 V at a scan rate of 80 mV s⁻¹ in 1 M Na₂SO₄ aqueous electrolyte

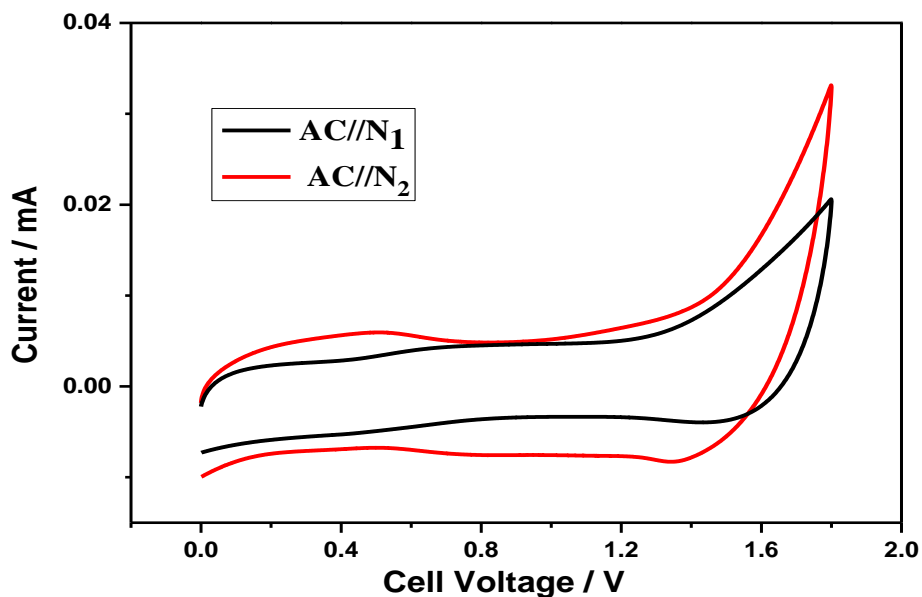


Figure 6.11 (c): Comparative plot of AC// N₁ and AC//N₂ supercapattery devices at 50 mVs⁻¹ in 1 M Na₂SO₄ aqueous electrolyte at voltage window of 1.8 V

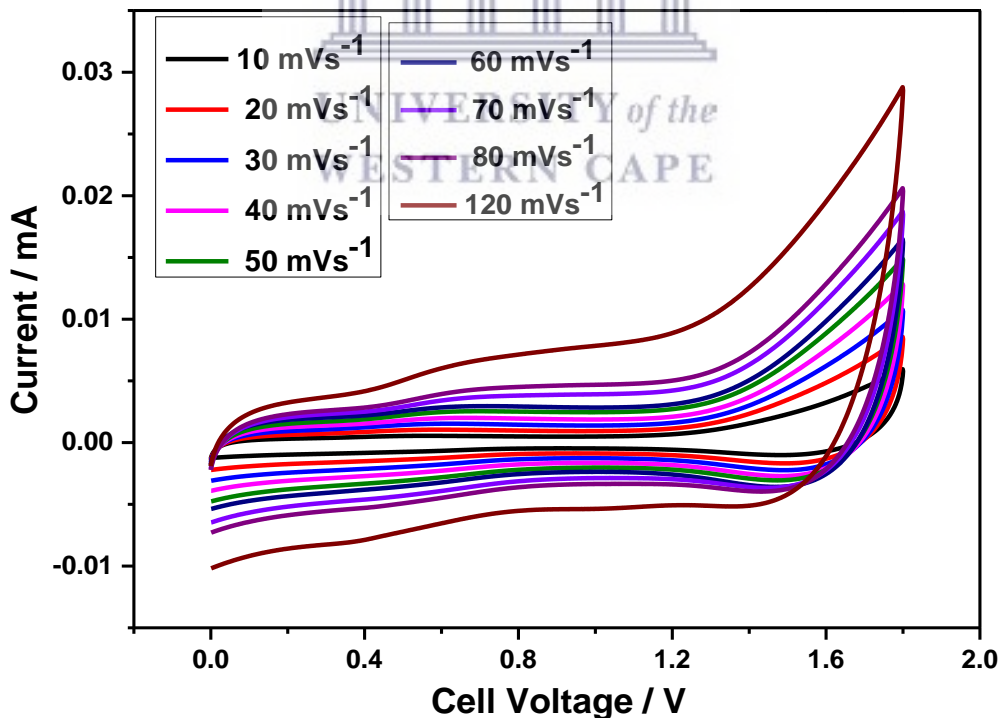


Figure 6.11 (d): CV curves of AC//N₂ supercapattery at scan rates of 10 -120 mVs⁻¹ in 1 M Na₂SO₄ aqueous electrolyte at voltage window of 1.8 V

v) **Galvanostatic charge-discharge (GCD) studies of supercapattery devices**

To increase the energy storage capabilities of the nanohybrid electrode supercapatteries, the maximum cell voltage was set at 1.8 V. Figure 6.12 (a) shows comparative GCD profiles of AC//N₁ and AC//N₂ supercapattery devices at cell voltages of 1.8 V (i) and 1.6 V (ii) and current loads of 0.1 A g⁻¹ and 0.05 A g⁻¹, respectively. The near symmetric nature of the curves indicates the high electrochemical reversibility of the devices. Quasi-triangular line curves and the slight deviation from potential plateaus further indicates that the devices exhibit hybrid (battery-capacitive) energy storage.

The specific capacitance of the various devices at the different voltage windows were calculated based on the balanced total masses of the two electrodes according to Equation 6.3. (Mass balancing has been discussed in previous chapters of this work).


$$C_{sp} = \frac{4I}{m \Delta V / \Delta t} \quad (6.3)$$

Where I represents the applied current (A), m is the total mass of both positive and negative electrodes (g), ΔV is the voltage window (V) and Δt is the discharge time (s)

At a cell voltage of 1.8 V, the AC//N₂ supercapattery device delivered a high specific capacitance of 205 F g⁻¹ which is almost 1.6 times greater than that of the AC//N₁ device with 126 F g⁻¹ at a current load of 0.1 A g⁻¹. A lower electrochemical performance was obtained for the supercapattery devices at 1.6 V. AC//N₂ showed a specific capacitance of 64.7 F g⁻¹ while

AC//N₁ delivered 53.5 F g⁻¹ at 0.05 A g⁻¹. The higher specific capacitance of AC//N₂ supercapattery can be attributed to better hybridization of V₂O₅-CNT, Li₂Mn_{1-x}Zn_xSiO₄ and 5 % G-ol nanomaterials which provided conductive channels and large surface area for ion diffusion and enhanced electrical conductivity. N₁ nanohybrid based supercapattery showed decreased electrochemical performance due to the higher content of G-ol which was in tune with V₂O₅-CNT, Li₂Mn_{1-x}Zn_xSiO₄ nanomaterials leading to slight sheltering of conduction channels and impeding electron/ion flow. Figure 6.12 (b) - (c) display the GCD curves of the AC//N₂ and AC//N₁ supercapattery devices at cell voltages of 1.8 V (i) and 1.6 V (ii) at various current loads. The almost symmetric profiles with absence of the ohmic drop reveal the good electrochemical performance of the devices.

The variation of discharge capacitance with increasing current load at 1.8 V for the AC//N₂ device is shown in Figure 6.12 (d). It is observed that the specific capacitance decreases with an increase in current load due to lack of active material accessibility at higher scan rates. The AC//N₂ device supercapattery device delivered a specific capacitance of 205 F g⁻¹ at a current load of 0.1 A g⁻¹ and still retains a specific capacitance of ~26 % (52.6 F g⁻¹) when the current is increased by a factor of 20 (2 A g⁻¹). The AC//N₁ device delivered a specific capacitance of 126 F g⁻¹ at 0.1 A g⁻¹ with a capacitance retention of ~18 % (23.3 F g⁻¹) at 2 A g⁻¹.

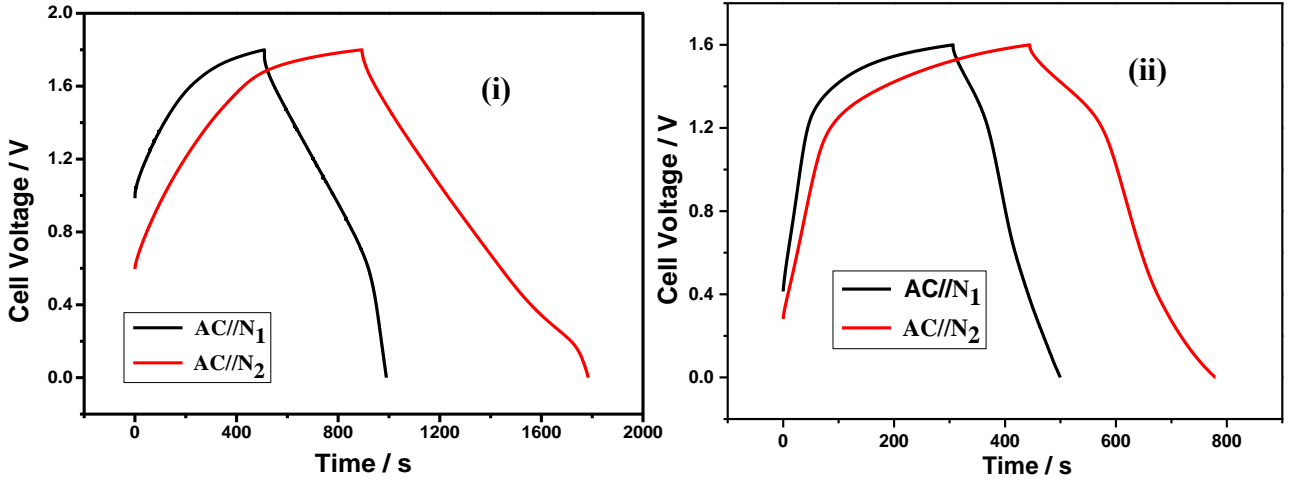


Figure 6.12 (a): Comparative GCD profiles of AC//N₂ and AC// N₁ supercapattery devices at voltage range of 1.8 V and current load of 0.1 A g⁻¹ (i) and 1.6 V and 0.05 A g⁻¹ (ii)

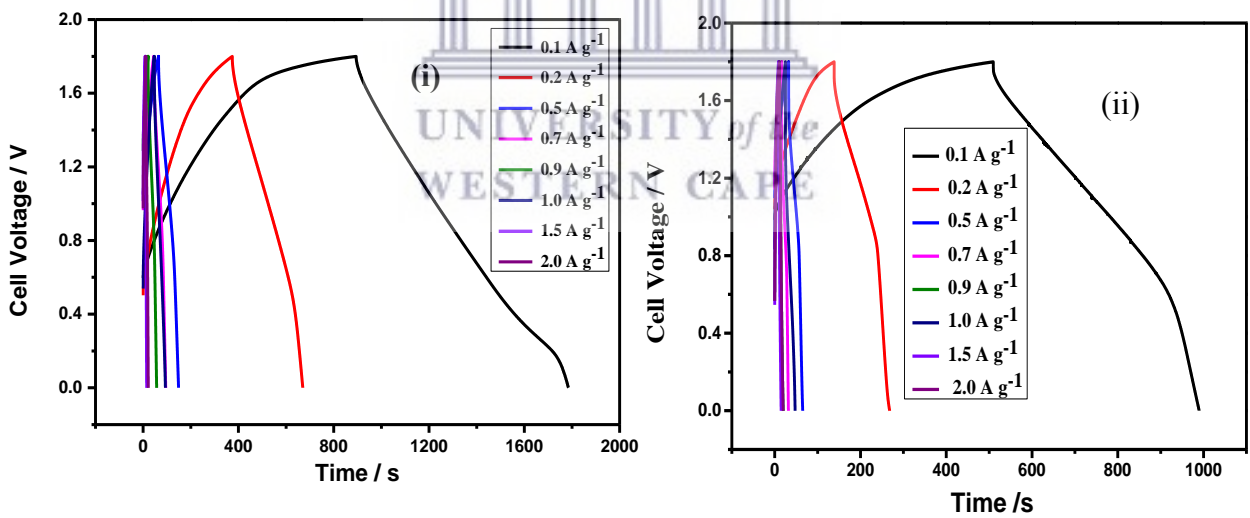


Figure 6.12 (b): GCD curves of AC//N₂ (i) and AC// N₁ (ii) supercapattery devices at various current loads at voltage range of 1.8 V

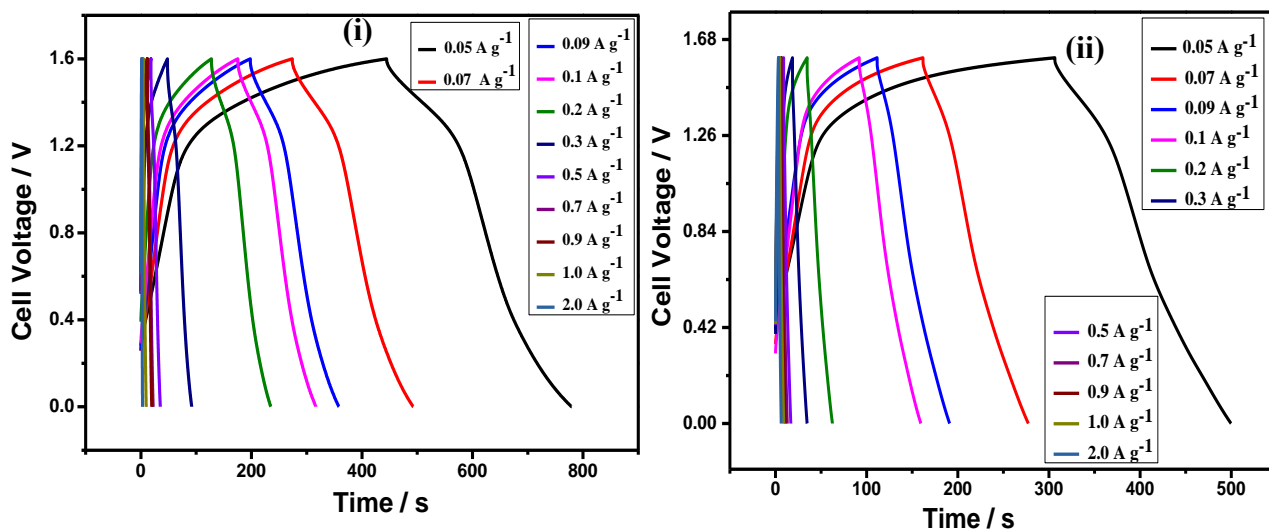


Figure 6.12 (c): GCD curves of AC//N₂ (i) and AC// N₁ (ii) supercapattery devices at various current loads at voltage range of 1.6 V

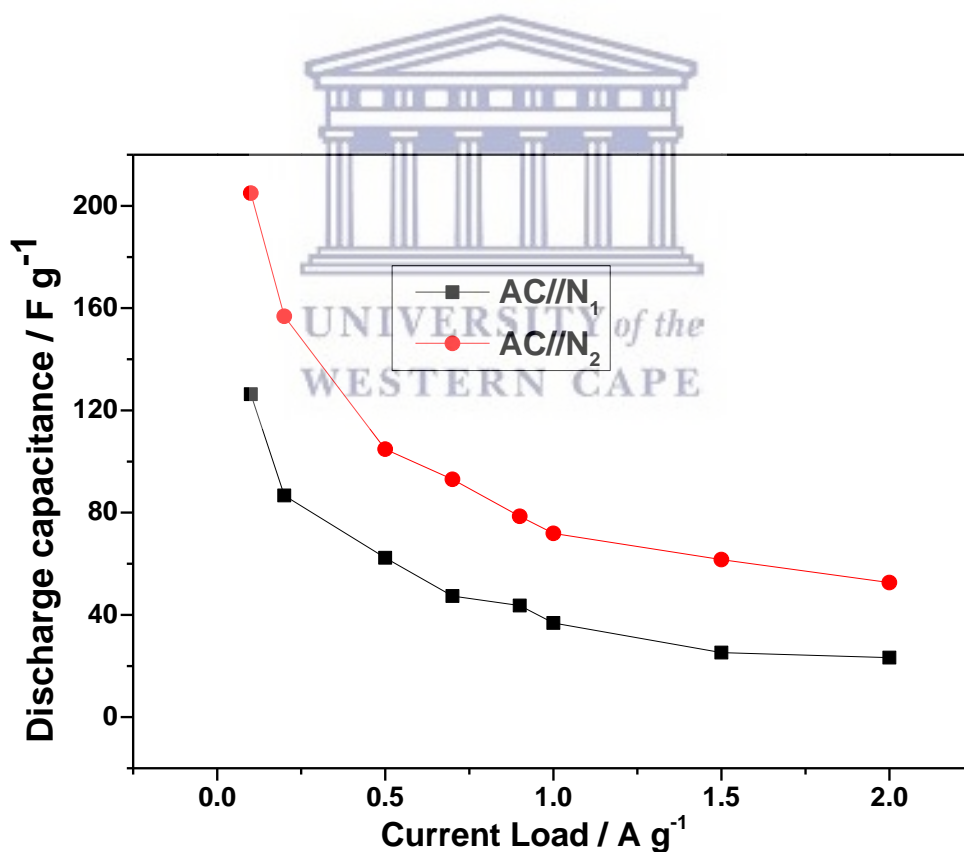


Figure 6.12 (d): Variation of discharge capacitance with current load of AC//N₂ device in 1 M Na₂SO₄ aqueous electrolyte at voltage window of 1.8 V

vi) Electrochemical cycling / stability studies

Long cycling capability is an important parameter used to establish the electrochemical performance of supercapatteries. The stability of the nanohybrid supercapattery devices over repeated charge-discharge cycles was achieved over 5000 cycles at a current load of 0.2 A g^{-1} . Figure 6.13 (a) presents the capacitance retention of AC//N₂ and AC//N₁ supercapatteries over 5000 cycles. The AC//N₂ supercapattery demonstrated a capacitance retention of 55.1 % while the AC//N₁ device showed a capacitance retention of 33.5 % over 5000 cycles.

The coulombic efficiency per cycle is shown in Figure 6.13 (b). It is worth noting that AC//N₂ supercapattery device exhibited an excellent coulombic efficiency of 96.4 % for cycle 1 and up to 98.8 % at 5000 cycles. The AC//N₁ device also showed a coulombic efficiency of 94.5 % at cycle 1 and 98.6 % at cycle 5000.

The superior cycling stability and overall performance of the AC//N₂ supercapattery device can be ascribed to the increased packing density and nucleation observed in XRD crystal structure models which provided a high surface area and shorter diffusion length of Li-ions during repeated charge-discharge studies.

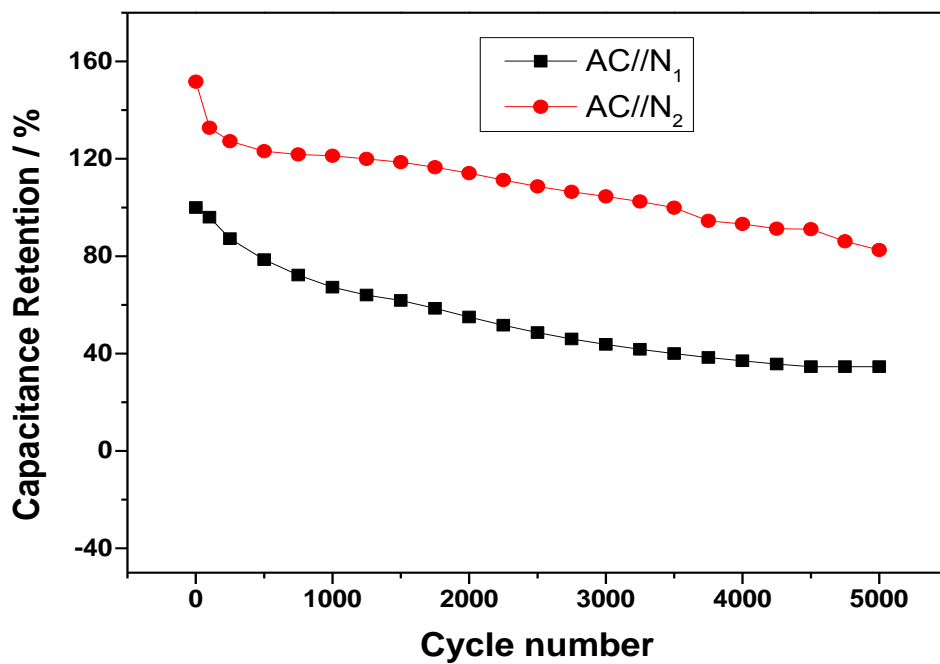


Figure 6.13 (a): Cycling stability of AC//N₁ and AC//N₂ supercapattery devices over 5000 cycles in 1 M Na₂SO₄ aqueous electrolyte at voltage window of 1.8 V

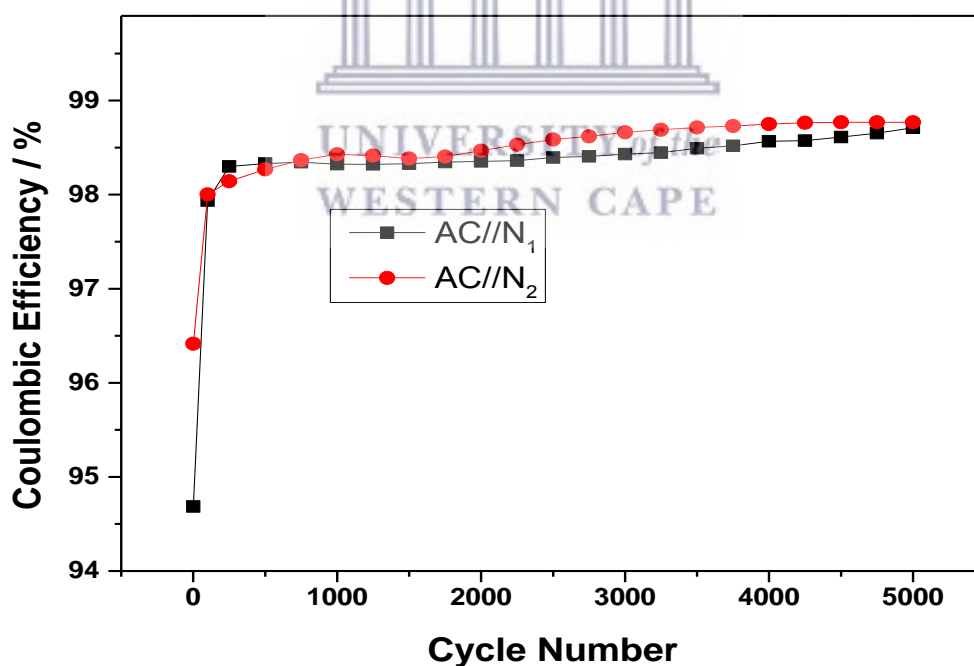


Figure 6.13 (b): Coulombic efficiency of AC//N₁ and AC//N₂ supercapattery devices over 5000 cycles in 1 M Na₂SO₄ aqueous electrolyte at voltage window of 1.8 V

vii) **Electrochemical Impedance studies before and after cycling**

EIS was further used to investigate the effect of cycling degradation on the kinetic properties of the supercapattery cells. Figure 6.14 (a) displays comparative Nyquist plots of the AC//N₁ and AC//N₂ supercapattery devices before and after 5000 cycles at open circuit voltage. As observed in the half cells, the plots consists of semi-circles at the high-medium frequency region and an incline line at the low frequency region. The high-medium frequency region is associated with the internal/electrolyte resistance (R_s) and charge transfer resistance (R_{ct}), while the low frequency region describes the Warburg diffusion of electrolyte ions (W_o). The equivalent circuit model used to fit the obtained data is displayed as the inset in Figure 6.14 (a). Circuit element values obtained from fitting are shown in Table 6.4. The higher electrochemical performance of the AC//N₂ supercapattery device is corroborated by its R_{ct} values which are much lower than those of the AC//N₁ device.

R_s and R_{ct} values of AC//N₂ supercapattery device before and after 5000 cycles are 2.48 and 6.03 Ω , 2.52 and 1.61 Ω , respectively. AC//N₁ supercapattery device also showed values of R_s and R_{ct} to be 3.57 and 45.9 Ω as well as 3.07 and 31.45 Ω before and after 5000 cycles. The slight decrease in the internal/solution and charge transfer resistances after 5000 cycles is mainly due to the slight increase in the wettability of the supercapattery electrodes by repeated electrolyte immersion [42]. A decrease in the phase angle values is noticed before and after cycling as shown in Figure 6.14 (c). This decrease may be attributed to changes in the surface states and transport properties of the supercapattery electrodes due to undesirable site reactions of electrolytic ions with the electrode surface during the continuous charge-discharge process.

Table 6.4: EIS simulation data of AC//N₁ and AC//N₂ supercapattery devices before and after 5000 cycles

Supercapattery device	R _s / Ω	CPE / μF	R _{ct} / Ω	W _o / Ωs ^{-1/2}	Phase angle / °
AC//N ₁ before cycling	3.57	0.57	45.94	0.96	29.2
AC//N ₁ after cycling	3.07	0.69	31.45	0.87	23.9
AC//N ₂ before cycling	2.48	0.50	6.03	0.374	36.7
AC//N ₂ after cycling	2.52	0.48	1.61	0.33	26.9



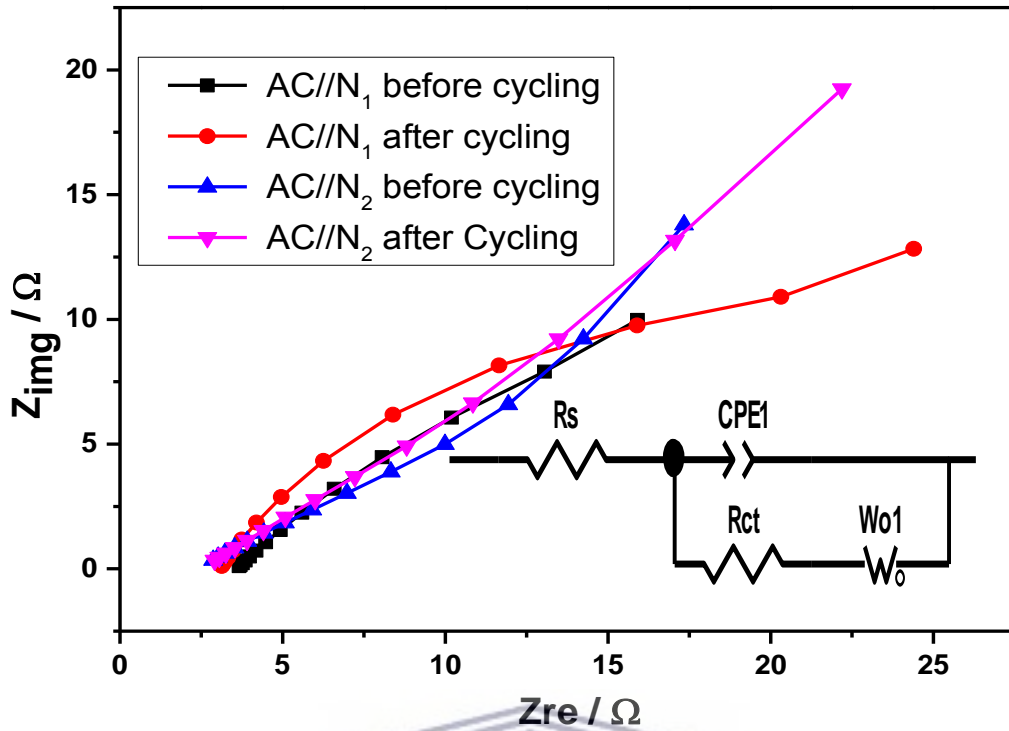


Figure 6.14 (a): Nyquist plots of AC//N₁ and AC//N₂ supercapattery devices before and after cycling with circuit model used to fit EIS data as inset

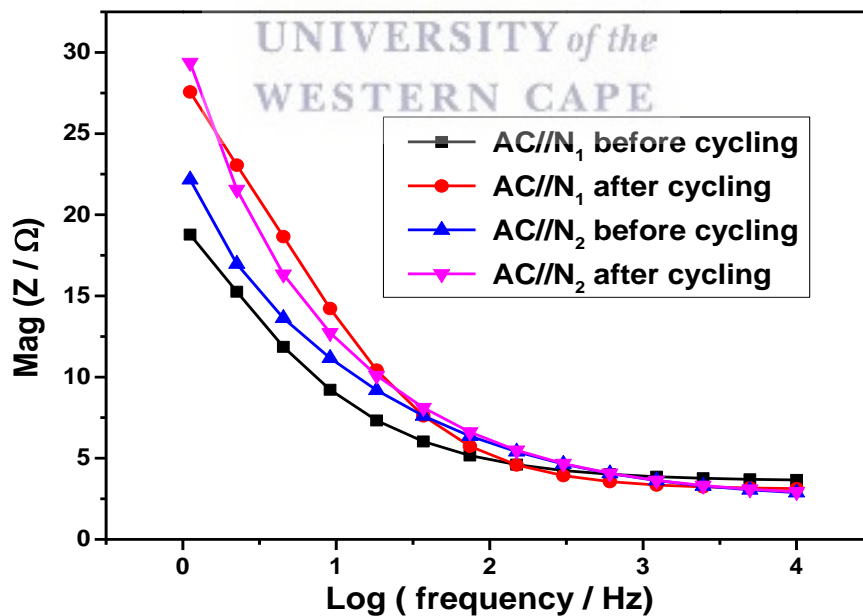


Figure 6.14 (b): Total impedance Bode plots of AC//N₁ and AC//N₂ supercapattery devices before and after cycling

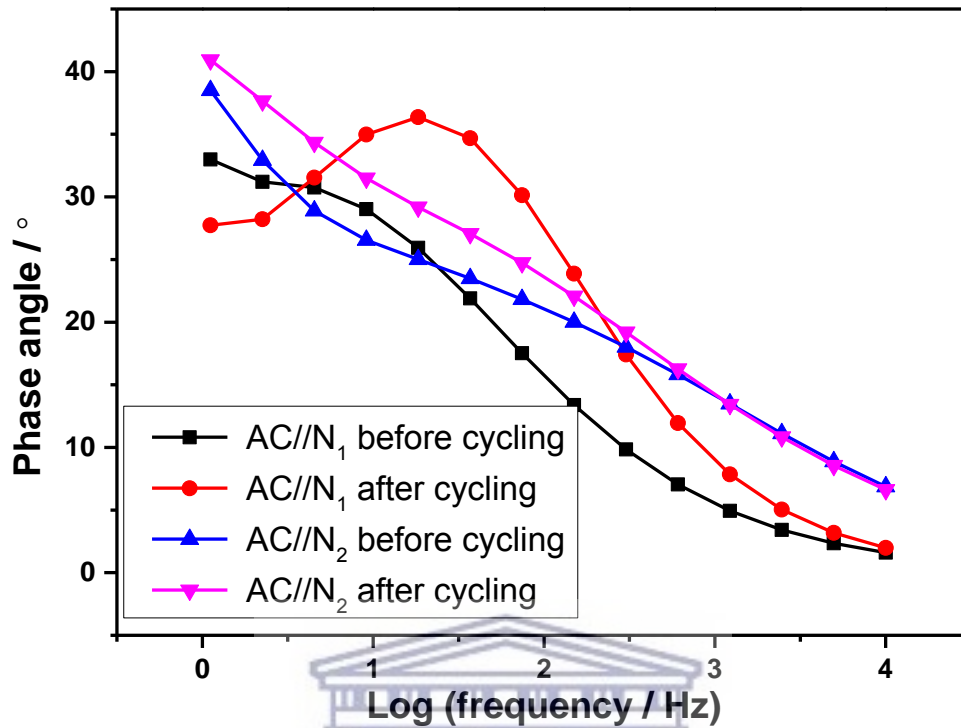


Figure 6.14 (c): Phase angle Bode plots of AC//N₁ and AC//N₂ supercapattery devices before and after cycling

6.5 (c) Specific Energy and Specific Power

Supercapatteries are expected to deliver high energy and power densities due to their hybrid nature (combination of high energy battery electrodes with electrochemical double layer capacitor electrodes). To evaluate the energy storage performance of the assembled supercapatteries, Figure 6.15 shows the Ragone plots of AC//N₁ and AC//N₂ supercapattery devices at increasing current loads. The specific energy and power of AC//N₁ and AC//N₂

supercapattery devices were obtained by discharging the charged devices at increasing current loads at an applied voltage of 1.8 V, according to Equation 6.4 and 6.5.

$$E = \frac{1}{2} C_{sp} \times \Delta V^2 \times \frac{1}{3.6} \quad (6.4)$$

$$P = \frac{E}{\Delta t} \times 3600 \quad (6.5)$$

Where C_{sp} denotes the specific capacitance of the device ($F g^{-1}$), ΔV is the applied voltage (V) and Δt is the supercapattery discharge time (s).

The AC//N₂ supercapattery delivered an excellent specific energy of 92.3 W h kg⁻¹ at a specific power of 769.8 W kg⁻¹ and even maintained a specific energy of 23.67 W h kg⁻¹ at a specific power 13435.2 W kg⁻¹. While AC//N₁ supercapattery device could deliver a specific energy of 56.8 W h kg⁻¹ at a specific power of 427.8 W kg⁻¹ and could retain a specific energy of 10.48 W kg⁻¹ at a specific power of 6039.4 W kg⁻¹. These results are comparable and even higher than recent reported supercapattery devices based on other transition metal nanohybrids. Such as, NiCo-MnO₂//C-FP (48.8 W h kg⁻¹ at 896.9 W kg⁻¹) [43], MWCNT-Co₃O₄-Ag//AC (16.5 W h kg⁻¹ at 297.5 W kg⁻¹) [44], graphene/MnO₂//AC (51.1 W h kg⁻¹ at 198 W kg⁻¹) [38], AC//LiMnPO₄-S (11 W h kg⁻¹ at 198 W kg⁻¹) [45] and 2D MnCo₂O₄//AC (33.8 W h kg⁻¹ at 318.9 W kg⁻¹) [46]. The excellent electrochemical performance of the AC//N₁ and AC//N₂ supercapatteries can be attributed to the existence of nanoholes in the hybridized nanoarchitectures that enabled faster ionic conductivity and reduced internal resistances via the interconnected hybrid structures.

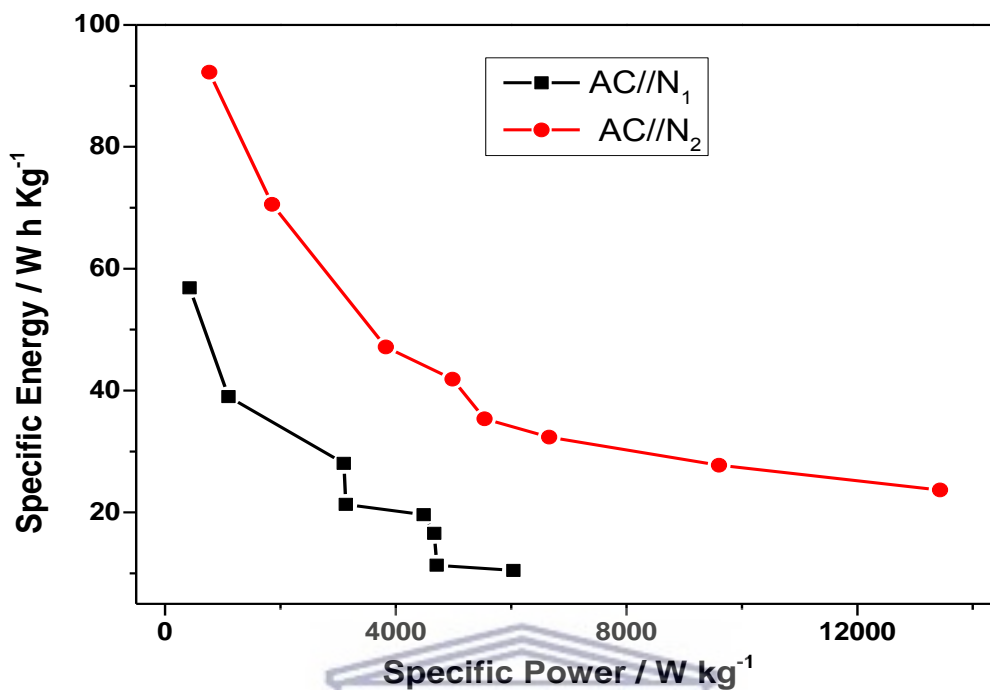


Figure 6.15: Ragone plot of AC/N₁ and AC/N₂ supercapattery devices in 1 M Na₂SO₄ aqueous electrolyte at voltage window of 1.8 V

6.6 Conclusion

In summary, Li₂Mn_{1-x}Zn_xSiO₄/V₂O₅-CNT/G-ol_{10%} (N₁) and Li₂Mn_{1-x}Zn_xSiO₄/V₂O₅-CNT/G-ol_{5%} (N₂) nanohybrid electrodes have been prepared by facile mechanochemical reactions and an annealing step at 350° C for 2 h. Morphological studies by SEM and HRTEM showed completely hybridized mesoporous nanoarchitectures with majority platelet morphology for N₁ and further elongation in N₂ with 5 % G-ol content. SAXS investigations revealed bell-shaped particle size distribution with mean particle sizes at 12.3 nm and aggregates at 29.4 and 48.1

nm for N₁. N₂ showed similar form of aggregation with a single peak at 65.1 nm. XRD studies showed peaks belonging to the (010), (110), (210), (002), (212) and (232) crystalline planes of Li₂MnSiO₄ which were indexed to orthorhombic Pmn2₁ space group, and minor peaks observed for the 001 and 002 planes of oxygenated graphene sheets. Asymmetric and symmetric vibrations of Si-O-Si and V-O-V bonds as well as the stretching motion of [LiO₄] tetrahedra were observed in FTIR analysis around 511 – 933 cm⁻¹ and 420 - 494 cm⁻¹, respectively. The vibration of Mn-O-Si layers, C=C and C-O bonds from the graphitic domains and OH characteristic band were observed around 1060 – 1164 cm⁻¹, 1641.4 cm⁻¹ and 1371.8 cm⁻¹. Electrochemical studies in 1 M Na₂SO₄ revealed CV curves with shapes suggesting a charge storage mechanism of the electrodes involving surface bound faradaic reactions such as oxidation/reduction of manganese and vanadium ions together with intercalation processes of Li⁺ ion. EIS studies showed a smaller R_{ct} value for N₂ (2.29 Ω) over N₁ (4.02 Ω), indicating faster movements of electro-active species in N₂. To evaluate the energy storage performance of the nanoarchitected materials, supercapatteries were assembled with the N₁ and N₂ nanohybrids as positive electrodes and activated carbon as the negative electrode. The AC//N₂ supercapattery device delivered a maximum specific capacitance of 205 F g⁻¹, excellent specific energy of 92.3 W h kg⁻¹ at a specific power of 769.8 W kg⁻¹ at 1.8 V and 0.1 A g⁻¹. While AC//N₁ supercapattery device delivered specific capacitance of 126 F g⁻¹, specific energy of 56.8 W h kg⁻¹ at a specific power of 427.8 W kg⁻¹, voltage of 1.8 V and 0.1 A g⁻¹.

The higher AC//N₂ supercapattery can be attributed to better hybridization of V₂O₅-CNT, Li₂Mn_{1-x}Zn_xSiO₄ and 5 % G-ol nanomaterials which provided conductive channels and large surface area for ions diffusion and enhanced electrical conductivity. Long cycling stability tests demonstrated a capacitance retention of 55.1 % and an excellent coulombic efficiency 98.8 % for AC//N₂ supercapattery and a capacitance retention of 33.5 % and excellent coulombic efficiency of 98.6 % for the AC//N₁ device showed over 5000 cycles. The commendable

electrochemical performance of the AC//N₁ and AC//N₂ supercapatteries can be attributed to the existence of nanoholes in the hybridized nanoarchitectures which enabled faster ionic conductivity and reduced internal resistances via the interconnected hybrid structures. This study serves as a facile and affordable broad-spectrum approach to design high performing nanoarchitectonic electrode platforms for energy storage devices.

References

- [1] K. Ariga, M. Matsumoto, T. Mori, L.K. Shrestha, Materials nanoarchitectonics at two-dimensional liquid interfaces, *Beilstein J. Nanotechnol.* 10 (2019) 1559–1587. doi:10.3762/bjnano.10.153.
- [2] D. Gielen, F. Boshell, D. Saygin, M.D. Bazilian, N. Wagner, R. Gorini, The role of renewable energy in the global energy transformation, *Energy Strateg. Rev.* 24 (2019) 38–50. doi:10.1016/j.esr.2019.01.006.
- [3] W. Raza, F. Ali, N. Raza, Y. Luo, K.H. Kim, J. Yang, S. Kumar, A. Mehmood, E.E. Kwon, Recent advancements in supercapacitor technology, *Nano Energy.* 52 (2018) 441–473. doi:10.1016/j.nanoen.2018.08.013.
- [4] Poonam, K. Sharma, A. Arora, S.K. Tripathi, Review of supercapacitors: Materials and devices, *J. Energy Storage.* 21 (2019) 801–825. doi:10.1016/j.est.2019.01.010.
- [5] E. Serrano, G. Rus, J. García-Martínez, Nanotechnology for sustainable energy, *Renew. Sustain. Energy Rev.* 13 (2009) 2373–2384. doi:10.1016/j.rser.2009.06.003.
- [6] Z.L. Wang, W. Wu, Nanotechnology-enabled energy harvesting for self-powered micro-

-
- /nanosystems, *Angew. Chemie - Int. Ed.* 51 (2012) 11700–11721. doi:10.1002/anie.201201656.
- [7] J.M. Giussi, M.L. Cortez, W.A. Marmisollé, O. Azzaroni, Practical use of polymer brushes in sustainable energy applications: Interfacial nanoarchitectonics for high-efficiency devices, *Chem. Soc. Rev.* 48 (2019) 814–849. doi:10.1039/c8cs00705e.
- [8] M. Aono, Focus on materials nanoarchitectonics, *Sci. Technol. Adv. Mater.* 12 (2011) 10–12. doi:10.1088/1468-6996/12/4/040301.
- [9] K. Ariga, Y. Yamauchi, M. Aono, Commentary: Nanoarchitectonics - Think about NANO again, *APL Mater.* 3 (2015). doi:10.1063/1.4922549.
- [10] O. Azzaroni, K. Ariga, Nanoarchitectonics, now, *Mol. Syst. Des. Eng.* 4 (2019) 9–10. doi:10.1039/c9me90001b.
- [11] K. Ariga, J. Li, Nanoarchitectonics for Advanced Materials: Strategy beyond Nanotechnology, *Adv. Mater.* 28 (2016) 987–988. doi:10.1002/adma.201505715.
- [12] K. Ariga, M. Nishikawa, T. Mori, J. Takeya, L.K. Shrestha, J.P. Hill, Self-assembly as a key player for materials nanoarchitectonics, *Sci. Technol. Adv. Mater.* 20 (2019) 51–95. doi:10.1080/14686996.2018.1553108.
- [13] D. Kim, M. Gu, M. Park, T. Kim, B.S. Kim, Layer-by-layer assembly for photoelectrochemical nanoarchitectonics, *Mol. Syst. Des. Eng.* 4 (2019) 65–77. doi:10.1039/c8me00067k.
- [14] A.N. Oldacre, A.E. Friedman, T.R. Cook, A self-assembled cofacial cobalt porphyrin prism for oxygen reduction catalysis, *J. Am. Chem. Soc.* 139 (2017) 1424–1427. doi:10.1021/jacs.6b12404.

-
- [15] S.W. Lee, N. Yabuuchi, B.M. Gallant, S. Chen, B.S. Kim, P.T. Hammond, Y. Shao-Horn, High-power lithium batteries from functionalized carbon-nanotube electrodes, *Nat. Nanotechnol.* 5 (2010) 531–537. doi:10.1038/nnano.2010.116.
- [16] R. Rajendran, L.K. Shrestha, R.M. Kumar, R. Jayavel, J.P. Hill, K. Ariga, Composite Nanoarchitectonics for Ternary Systems of Reduced Graphene Oxide/Carbon Nanotubes/Nickel Oxide with Enhanced Electrochemical Capacitor Performance, *J. Inorg. Organomet. Polym. Mater.* 25 (2015) 267–274. doi:10.1007/s10904-014-0102-4.
- [17] D. Leistenschneider, N. Jäckel, F. Hippauf, V. Presser, L. Borchardt, Mechanochemistry-assisted synthesis of hierarchical porous carbons applied as supercapacitors, *Beilstein J. Org. Chem.* 13 (2017) 1332–1341. doi:10.3762/bjoc.13.130.
- [18] J.L. Howard, Q. Cao, D.L. Browne, Mechanochemistry as an emerging tool for molecular synthesis: What can it offer?, *Chem. Sci.* 9 (2018) 3080–3094. doi:10.1039/c7sc05371a.
- [19] T. Tsuzuki, P.G. McCormick, Mechanochemical synthesis of nanoparticles, *J. Mater. Sci.* 39 (2004) 5143–5146. doi:10.1023/B:JMSC.0000039199.56155.f9.
- [20] M.M. Ndipingwi, C.O. Ikpo, N.W. Hlongwa, Z. Myalo, N. Ross, M. Masikini, S. V. John, P.G. Baker, W.D. Roos, E.I. Iwuoha, Orthorhombic Nanostructured $\text{Li}_2\text{MnSiO}_4/\text{Al}_2\text{O}_3$ Supercapattery Electrode with Efficient Lithium-Ion Migratory Pathway, *Batter. Supercaps.* 1 (2018) 223–235. doi:10.1002/batt.201800045.
- [21] K.V. Sankar, S. Shanmugapriya, S. Surendran, S.C. Jun, R.K. Selvan, Facile hydrothermal synthesis of carbon-coated cobalt ferrite spherical nanoparticles as a potential negative electrode for flexible supercapattery, *J. Colloid Interface Sci.* 513

-
- (2018) 480–488. doi:10.1016/j.jcis.2017.11.054.
- [22] J. Lin, Y. Yan, X. Zheng, Z. Zhong, Y. Wang, J. Qi, J. Cao, W. Fei, Y. Huang, J. Feng, Designing and constructing core-shell NiCo₂S₄@Ni₃S₂ on Ni foam by facile one-step strategy as advanced battery-type electrodes for supercapattery, *J. Colloid Interface Sci.* 536 (2019) 456–462. doi:10.1016/j.jcis.2018.10.072.
- [23] L.F. Drummy, Y.C. Wang, R. Schoenmakers, K. May, M. Jackson, H. Koerner, B.L. Farmer, B. Mauryama, R.A. Vaia, Morphology of layered silicate- (NanoClay-) polymer nanocomposites by electron tomography and small-angle X-ray scattering, *Macromolecules.* 41 (2008) 2135–2143. doi:10.1021/ma702232f.
- [24] H.K. Kammler, G. Beaucage, D.J. Kohls, N. Agashe, J. Ilavsky, Monitoring simultaneously the growth of nanoparticles and aggregates by in situ ultra-small-angle x-ray scattering, *J. Appl. Phys.* 97 (2005). doi:10.1063/1.1855391.
- [25] S.K. Sharma, J. Bahadur, P.N. Patil, P. Maheshwari, S. Mukherjee, K. Sudarshan, S. Mazumder, P.K. Pujari, Revealing the nano-level molecular packing in chitosan-NiO nanocomposite by using positron annihilation spectroscopy and small-angle X-ray scattering, *ChemPhysChem.* 14 (2013) 1055–1062. doi:10.1002/cphc.201200902.
- [26] A. Singh, J. Vihinen, E. Frankberg, L. Hyvärinen, M. Honkanen, E. Levänen, Pulsed Laser Ablation-Induced Green Synthesis of TiO₂ Nanoparticles and Application of Novel Small Angle X-Ray Scattering Technique for Nanoparticle Size and Size Distribution Analysis, *Nanoscale Res. Lett.* 11 (2016) 1–9. doi:10.1186/s11671-016-1608-1.
- [27] S. Mahalingam, J. Ramasamy, Y.H. Ahn, Synthesis and application of graphene- α MoO₃ nanocomposite for improving visible light irradiated photocatalytic decolorization of

-
- methylene blue dye, *J. Taiwan Inst. Chem. Eng.* 80 (2017) 276–285. doi:10.1016/j.jtice.2017.07.009.
- [28] J. Sun, Y. Deng, J. Li, G. Wang, P. He, S. Tian, X. Bu, Z. Di, S. Yang, G. Ding, X. Xie, A New Graphene Derivative: Hydroxylated Graphene with Excellent Biocompatibility, *ACS Appl. Mater. Interfaces*. 8 (2016) 10226–10233. doi:10.1021/acsami.6b02032.
- [29] J. Chen, B. Yang, H. Hou, H. Li, L. Liu, L. Zhang, X. Yan, Disordered, Large Interlayer Spacing, and Oxygen-Rich Carbon Nanosheets for Potassium Ion Hybrid Capacitor, *Adv. Energy Mater.* 9 (2019) 1–9. doi:10.1002/aenm.201803894.
- [30] Y.Z. Song, J.J. Ding, K.K. Zhang, R.X. Zhao, X.M. Lv, J.M. Xie, Facile Synthesis of Mn_3O_4 @SWCNT Nanoparticles and Their Application in Supercapacitors, *Russ. J. Phys. Chem. A*. 93 (2019) 2072–2078. doi:10.1134/s0036024419100285.
- [31] M.E. Arroyo-DeDompablo, R. Dominko, J.M. Gallardo-Amores, L. Dupont, G. Mali, H. Ehrenberg, J. Jamnik, E. Morán, On the energetic stability and electrochemistry of $\text{Li}_2\text{MnSiO}_4$ polymorphs, *Chem. Mater.* 20 (2008) 5574–5584. doi:10.1021/cm801036k.
- [32] and M.E.A. A. Saracibar, Z. Wang, K. Carroll, Y. S. Meng, Dompablo, New Insights in the Electrochemical Performance of $\text{Li}_2\text{MnSiO}_4$: effect of cationic substitutions, *J. Mater. Chem. A*. 3 (2015) 6004–6011. doi:10.1039/x0xx00000x.
- [33] V. V. Politaev, A.A. Petrenko, V.B. Nalbandyan, B.S. Medvedev, E.S. Shvetsova, Crystal structure, phase relations and electrochemical properties of monoclinic $\text{Li}_2\text{MnSiO}_4$, *J. Solid State Chem.* 180 (2007) 1045–1050. doi:10.1016/j.jssc.2007.01.001.
- [34] H.S. Park, S.J. Hwang, J.H. Choy, Relationship between chemical bonding character and electrochemical performance in nickel-substituted lithium manganese oxides, *J.*

-
- Phys. Chem. B. 105 (2002) 4860–4866. doi:10.1021/jp010079+.
- [35] L.T. Kerr, H.J. Byrne, B.M. Hennelly, Optimal choice of sample substrate and laser wavelength for Raman spectroscopic analysis of biological specimen, *Anal. Methods*. 7 (2015) 5041–5052. doi:10.1039/c5ay00327j.
- [36] S. R. Ahmad, R. J. Young, I. A. Kinloch, Raman Spectra and Mechanical Properties of Graphene/Polypropylene Nanocomposites, *Int. J. Chem. Eng. Appl.* 6 (2015) 1–5. doi:10.7763/ijcea.2015.v6.440.
- [37] A.K. Singh, D. Sarkar, K. Karmakar, K. Mandal, G.G. Khan, High-Performance Supercapacitor Electrode Based on Cobalt Oxide-Manganese Dioxide-Nickel Oxide Ternary 1D Hybrid Nanotubes, *ACS Appl. Mater. Interfaces*. 8 (2016) 20786–20792. doi:10.1021/acsami.6b05933.
- [38] Z. Fan, J. Yan, T. Wei, L. Zhi, G. Ning, T. Li, F. Wei, Asymmetric supercapacitors based on graphene/MnO₂ and activated carbon nanofiber electrodes with high power and energy density, *Adv. Funct. Mater.* 21 (2011) 2366–2375. doi:10.1002/adfm.201100058.
- [39] A.C. Nwanya, D. Obi, R.U. Osuji, R. Bucher, M. Maaza, F.I. Ezema, Simple chemical route for nanorod-like cobalt oxide films for electrochemical energy storage applications, *J. Solid State Electrochem.* 21 (2017) 2567–2576. doi:10.1007/s10008-017-3520-8.
- [40] A.S. Rajpurohit, N.S. Punde, C.R. Rawool, A.K. Srivastava, Fabrication of high energy density symmetric supercapacitor based on cobalt-nickel bimetallic tungstate nanoparticles decorated phosphorus-sulphur co-doped graphene nanosheets with extended voltage, *Chem. Eng. J.* (2019) 679–692. doi:10.1016/j.cej.2019.04.100.

-
- [41] L. Xu, S. Wang, X. Zhang, T. He, F. Lu, H. Li, J. Ye, A facile method of preparing LiMnPO₄/reduced graphene oxide aerogel as cathodic material for aqueous lithium-ion hybrid supercapacitors, *Appl. Surf. Sci.* 428 (2018) 977–985. doi:10.1016/j.apsusc.2017.09.247.
- [42] R. Manikandan, C.J. Raj, M. Rajesh, B. Chul, S. Yeup, B. Cho, K. Hyun, Polycrystalline V₂O₅/Na_{0.33}V₂O₅ electrode material for Li⁺ ion redox supercapacitor, *Electrochim. Acta.* 230 (2017) 492–500. doi:10.1016/j.electacta.2017.02.031.
- [43] K.O. Oyedotun, M.J. Madito, D.Y. Momodu, A.A. Mirghni, T.M. Masikhwa, N. Manyala, Synthesis of ternary NiCo-MnO₂ nanocomposite and its application as a novel high energy supercapattery device, *Chem. Eng. J.* 335 (2018) 416–433. doi:10.1016/j.cej.2017.10.169.
- [44] J. Iqbal, A. Numan, S. Rafique, R. Jafer, S. Mohamad, K. Ramesh, S. Ramesh, High performance supercapattery incorporating ternary nanocomposite of multiwalled carbon nanotubes decorated with Co₃O₄ nanograins and silver nanoparticles as electrode material, *Electrochim. Acta.* 278 (2018) 72–82. doi:10.1016/j.electacta.2018.05.040.
- [45] N. Priyadharsini, A. Shanmugavani, S. Surendran, B. Senthilkumar, L. Vasylechko, R. Kalai Selvan, Improved electrochemical performances of LiMnPO₄ synthesized by a hydrothermal method for Li-ion supercapatteries, *J. Mater. Sci. Mater. Electron.* 29 (2018) 18553–18565. doi:10.1007/s10854-018-9972-5.
- [46] B. Saravanakumar, X. Wang, W. Zhang, L. Xing, W. Li, Holey two dimensional manganese cobalt oxide nanosheets as a high-performance electrode for supercapattery, *Chem. Eng. J.* 373 (2019) 547–555. doi:10.1016/j.cej.2019.05.080.

CHAPTER SEVEN

CONCLUSION AND RECOMMENDATIONS

7.1 Summary of main thesis results

Nanoarchitectonics, also known as the “rising tide on the horizon of current materials research”, enables the creation of novel and reliable systems by integration of predefined molecular functionalities into bulk materials or devices. This work involves the preparation of various nanoarchitectures and their applications in energy storage devices such as supercapacitors and supercapacitor-battery hybrids (supercapatteries). These nanostructures have been prepared by various synthetic routes ranging from hydroboration with oxidation to solvothermal and mechanochemical synthesis. Nanomaterials investigated in this work include hydroxylated graphene nanosheets (G-ol), vanadium pentoxide (V_2O_5) nanorods and composites with carbon nanotubes (CNTs) and G-ol. Pristine lithium manganese silicate (Li_2MnSiO_4) mixed spherical and rhombohedral nanocrystals and zinc doped counterparts ($Li_2Mn_{1-x}Zn_xSiO_4$, $x = 0, 0.02, 0.04, 0.06, 0.08$) as well as hybridized mesoporous nanoarchitectures ($Li_2Mn_{1-x}Zn_xSiO_4/V_2O_5$ -CNT/G-ol_{10%} - N₁) and ($Li_2Mn_{1-x}Zn_xSiO_4/V_2O_5$ -CNT/G-ol_{5%} - N₂) have equally been studied. Morphological, structural and spectroscopic properties of the various nanostructures were investigated using characterization techniques such as scanning and transmission electron microscopies, small-angle X-ray scattering, X-ray diffraction, Fourier transform Infrared and Raman spectroscopies. Electrochemical properties were obtained using cyclic voltammetry, electrochemical impedance spectroscopy and galvanostatic charge-discharge studies. The energy storage capability of the various

nanostructured electrodes were investigated individually and as composite electrodes in supercapacitors and supercapatteries.

Important findings from the study are listed below

- G-ol nanosheets with layers of 14- 23 nm thick, prepared by hydroboration of graphene oxide and subsequent oxidation were tested as freestanding symmetric supercapacitors (G-ol//G-ol) and asymmetric supercapacitor devices with activated carbon. Good electrochemical performance was achieved for the devices at a high voltage of 1.8 V in aqueous 1 M LiClO₄ electrolyte. The symmetric device delivered specific capacitance of 137.7 F g⁻¹, high specific energy of 47.8 Wh Kg⁻¹ and specific power of 377 W kg⁻¹ at a current load of 0.07 A g⁻¹. While the asymmetric supercapacitor cell delivered a specific capacitance of 91.73 F g⁻¹, specific energy of 32.61 Wh Kg⁻¹ and specific power of 286.6 W kg⁻¹ at 0.007 A g⁻¹. The devices demonstrated commendable capacitance retention of 83 % and coulombic efficiency of 99.8 % over 5000 cycles.
- V₂O₅ nanorods, V₂O₅-CNT and nanocapsulate-shaped composite (V₂O₅-CNT-G-ol) nanocrystals with particle sizes in the range of 10.4 – 22.9 nm were prepared via hydrothermal synthesis and fully characterized physically and electrochemically. The energy storage performance of the V₂O₅-based electrode materials were tested as asymmetric supercapacitors with activated carbon as the negative electrode in 1 M LiNO₃ aqueous electrolyte at a voltage window of 1.6 V. The AC//V₂O₅-CNT-G-ol asymmetric device delivered a specific capacitance of 173.4 F g⁻¹ which was 2.3 times greater than that of the AC//V₂O₅-CNT device (75.4 F g⁻¹) and even 7.1 times greater than the AC//V₂O₅ device. A high specific energy of 63.2 W h kg⁻¹ and specific power of 609.2 W kg⁻¹ was obtained for the AC//V₂O₅-CNT-G-ol device and a capacitance retention of 69 % over 4,000 cycles.

-
- Mixed spherical and rhombohedrally-shaped Zn-doped $\text{Li}_2\text{Mn}_{1-x}\text{Zn}_x\text{SiO}_4$ ($\text{Li}_2\text{Mn}_{1-x}\text{Zn}_x\text{SiO}_4$, $x = 0, 0.02, 0.04, 0.06, 0.08$) nanocrystals were prepared by solvothermal synthesis at $180\text{ }^\circ\text{C}$ in ethylene glycol. Skewed and bell-shaped particle size distributions with diameters of $22.5 - 30.7\text{ nm}$ were observed. Supercapattery devices assembled with activated carbon as negative electrode and $\text{Li}_2\text{Mn}_{1-x}\text{Zn}_x\text{SiO}_4$ as the positive electrodes in $1\text{ M Na}_2\text{SO}_4$ at 1.6 V delivered good capacitance retention and coulombic efficiencies over 3000 cycles. The supercapattery devices exhibited specific energies of $38.4\text{ W h kg}^{-1} - 21.3\text{ W h kg}^{-1}$, capacitance retention of $72.5\% - 84.5\%$ and excellent coulombic efficiency of $99.6 - 99.7\%$ over 3000 cycles.
 - Finally, mesoporous nanoarchitectures of $\text{Li}_2\text{Mn}_{1-x}\text{Zn}_x\text{SiO}_4/\text{V}_2\text{O}_5\text{-CNT/G-ol}_{10\%}$ (N_1) and $\text{Li}_2\text{Mn}_{1-x}\text{Zn}_x\text{SiO}_4/\text{V}_2\text{O}_5\text{-CNT/G-ol}_{5\%}$ (N_2) electrodes were prepared by facile mechanochemical reactions and an annealing process at $350\text{ }^\circ\text{C}$. After various physical and electrochemical characterization, the energy storage performance of the nanohybrids were evaluated in $1\text{ M Na}_2\text{SO}_4$ electrolyte at 1.8 V as supercapattery electrodes assembled with activated carbon as the negative electrode. The AC// N_2 supercapattery device delivered a maximum specific capacitance of 205 F g^{-1} , excellent specific energy of 92.3 W h kg^{-1} at a specific power of 769.8 W kg^{-1} . While AC// N_1 supercapattery device delivered specific capacitance of 126 F g^{-1} , specific energy of 56.8 W h kg^{-1} at a specific power of 427.8 W kg^{-1} . Long cycling stability tests demonstrated a capacitance retention of 55.1% and an excellent coulombic efficiency of 98.8% for AC// N_2 supercapattery as well as a capacitance retention of 33.5% and excellent coulombic efficiency of 98.6% for the AC// N_1 device over 5000 cycles.

Overall, the various nanostructured electrode materials prepared and investigated in this study have demonstrated good electrochemical performance and cycling stability as supercapattery and supercapacitor electrode designs. The performance is attributed to various

material/electrochemical dynamics at various stages. Hence with further optimisation of these electrode architectures, this work may serve as a facile and affordable broad-spectrum approach towards the design of high performance nanoarchitectonic electrodes for energy storage devices.

7.2 Recommendations for Future work

- Electrochemical long stability tests such as voltage holding/floating experiments to further confirm the high potentials of the nanostructured electrode materials
- Use of spectroelectrochemical experiments to better understand the storage mechanism of the electrode materials
- Electrochemical tests in various electrolytes such as ionic liquids and organic based electrolytes to maximise the energy density of the supercapattery devices

